

DEPARTMENT OF THE AIR FORCE  
AIR UNIVERSITY  
**AIR FORCE INSTITUTE OF TECHNOLOGY**

Wright-Patterson Air Force Base,

19950206 091

AFIT/WSF/ENP/94-05

THE JUNCTION CHARACTERISTICS  
AND CURRENT CONDUCTION MECHANISMS OF  
 $\text{GaInP}_2$   $n^+p$  DIODES AND SOLAR CELLS

DISSERTATION

Kitt C. Reinhardt

December 1994

Approved for public release; Distribution Unlimited

UNCLASSIFIED  
EXCLUDED FROM AUTOMATIC  
DOWNGRADING AND  
DECLASSIFICATION

THE JUNCTION CHARACTERISTICS AND CURRENT CONDUCTION

MECHANISMS OF GaInP<sub>2</sub> n<sup>+</sup>p DIODES AND SOLAR CELLS

DISSERTATION

Presented to the Faculty of the Graduate School of Engineering

of the Air Force Institute of Technology

Air University

In partial Fulfillment of the

requirements for the Degree of

Doctor of Philosophy

Kitt C. Reinhardt

December 1994

Accession For	
NTIS GRA&I	<input checked="checked" type="checkbox"/>
DTIC TAB	<input type="checkbox"/>
Unannounced	<input type="checkbox"/>
Justification	
By	
Distribution	
Availability Codes	
Dist	Avail and/or Special
A-1	

Approved for public release; Distribution Unlimited

THE JUNCTION CHARACTERISTICS  
AND CURRENT CONDUCTION MECHANISMS OF  
 $\text{GaInP}_2$   $n^+p$  DIODES AND SOLAR CELLS

Kitt C. Reinhardt, B.S., M.S.

Approved:

Yung Kee Yeo 22 Nov. 1994  
Yung Kee Yeo  
Chairman, Advisory Committee

Robert L. Hengehold 22 Nov '94  
Robert L. Hengehold  
Member, Advisory Committee

Paul H. Ostdiek 22 Nov '94  
Paul H. Ostdiek  
Member, Advisory Committee

E. Thomas Mahefkey 22 Nov '94  
E. Thomas Mahefkey  
Member, Advisory Committee

Dennis W. Quinn 22 NOV 94  
Dennis W. Quinn  
Member, Advisory Committee

Donald C. Reynolds 22 Nov 94  
Donald C. Reynolds  
Dean's Representative

Accepted:

Robert A. Calico, Jr.  
Robert A. Calico, Jr.  
Dean, Graduate School of Engineering



## Preface

I would first like to express my deepest gratitude to Professor Yung Kee Yeo for his valued guidance and encouragement throughout my adventure at AFIT. He is one of the most dedicated and hardest working men I have ever known, and his drive and motivation were instrumental in my completing the doctorate program. I am also grateful to Professors Robert Hengehold, Paul Ostdiek, Dennis Quinn, and Don Reynolds for their valued criticism and technical support. Special thanks also goes to Dr Tom Mahefkey and Steve Cloyd for serving on my doctorate advisory and moral support committee, respectively. I will always be grateful guys!

My sincere thanks also goes to the AFIT chicks Diana and Nancy, for all their good humor and invaluable secretarial help. I especially wish to thank my colleagues Roy Calfas, Bonnie (Baaneeson) Riehl, Dan Johnstone, and of course, Dr Dave Elsaesser, for their technical help and all the fun times.

Finally, all my love and sincere thanks goes to my parents, Dave and Elaine, for teaching me the importance of both loving others and working hard to achieve great things. And lastly, I thank God for watching over me these last few years. There were so many uncertain and difficult challenges that I faced during this period of my life, and somehow, he was always there to show me the way.

Kitt C. Reinhardt

Dedicated to my grandmother, Dorthy Dipirro

## Table of Contents

	Page
Preface .....	iii
List of Figures .....	viii
List of Tables .....	xv
Abstract .....	xvi
Chapter	
I. Introduction .....	1
Research Motivation: The GaInP <sub>2</sub> Solar Cell .....	7
Problem Statement .....	10
Approach .....	11
Outline .....	12
II. Theory: P-N Junction Diode and Solar Cell Device Physics .....	13
Solar Cell Basics and the Photovoltaic (PV) Effect .....	13
Solar Cell Conversion Efficiency and Dark Current .....	16
Basic P-N Junction Current Conduction Models .....	25
Diffusion Dark Current - Shockley Diode Theory .....	28
Recombination Dark Current .....	32
Basic Defect Level Terminology .....	34

Bulk Recombination:	
Shockley-Read-Hall Theory .....	40
P-N Junction Bulk Recombination Current .....	45
P-N Junction Perimeter Recombination Current .....	52
Tunneling Dark Current .....	53
Total P-N Junction Dark Current .....	55
Space-Radiation Damage in Solar Cells .....	62
Microscopic Effects of Radiation Damage in Solar Cells .....	64
Conventions for Characterizing Radiation Damage in Solar Cells .....	67
III. Device Fabrication .....	70
GaInP <sub>2</sub> Solar Cell and Mesa Diode Structure .....	70
Device Processing .....	73
Device Packaging .....	82
IV. GaInP <sub>2</sub> Solar Cell Characterization and Analysis .....	86
GaInP <sub>2</sub> Solar Cell Measurements .....	86
Solar Dark Current and Open-Circuit Voltage .....	90
Solar Cell Photocurrent.....	101
Dark Shunting-Current and "Leaky" Solar Cells .....	103
GaInP <sub>2</sub> /GaAs Lattice Mismatch versus Solar Cell Performance .....	106
Localization of Defects and Small Area Test Diodes .....	114

Dark Current versus P-N Junction P/A Ratio in GaInP <sub>2</sub> Devices .....	117
GaInP <sub>2</sub> Solar Cell Temperature Coefficients .....	122
 V. GaInP <sub>2</sub> Mesa Diode Characterization and Analysis .....	 127
Capacitance-Voltage (C-V) Measurements .....	127
Forward-bias Current-Voltage (I-V) Measurements .....	131
Forward-bias Current-Voltage-Temperature (I-V-T) Measurements ....	140
Reverse-bias I-V-T Measurements .....	147
Deep Level Transient Spectroscopy (DLTS) Measurements .....	155
Frenkel-Poole Barrier Lowering .....	163
Capacitance-Frequency-Temperature (C-F-T) Measurements .....	167
Summary of Deep Levels in GaInP <sub>2</sub> .....	174
 VI. Characterization of Electron Irradiated GaInP <sub>2</sub> Solar Cells and Diodes .....	 177
The Response of GaInP <sub>2</sub> Solar Cells to 1 MeV Electron Irradiation and Thermal Annealing .....	 177
The Response of GaInP <sub>2</sub> Diodes to 1 MeV Electron Irradiation and Thermal Annealing .....	 192
The Response of GaInP <sub>2</sub> n <sup>+</sup> p Junction Dark Recombination Current to 1 MeV Electron Irradiation .....	 206

VII. Summary of Results, Contributions, and Recommendations .....	212
Summary of Results .....	212
Summary of Contributions .....	219
Recommendations for Future Work .....	221
Appendix A: Derivation of Solar Cell Light-current .....	223
Appendix B: Tables of Annual Equivalent 1 MeV Electron Fluences .....	226
Appendix C: Plot of Normalized GaAs Solar Cell Power Output versus 1 MeV Electron Fluence .....	228
Appendix D: Solar Insolation .....	229
Bibliography .....	231
Vita .....	235

## List of Figures

Figure	Page
1. A schematic cross section of the GaInP <sub>2</sub> /GaAs tandem solar cell .....	8
2. (a) Schematic of a typical shallow n <sup>+</sup> p junction solar cell, and (b) an energy -band diagram for the illuminated p-n junction solar cell shown in (a) .....	14
3. Typical light and dark I-V characteristics for a p-n solar cell .....	17
4. Power loss chart of a Si n <sup>+</sup> p solar cell operating at AM1.5. Percentage of each of the loss mechanisms is given. ....	20
5. Theoretical solar cell efficiencies versus semiconductor bandgap. Curves for two different mechanisms are shown : (top) A=1 for diffusion dominated current, and (bottom) A=2 for recombination in the junction space-charge region .....	24
6. (a) Equivalent circuit model for a p-n solar cell, and (b) an energy-band diagram for a p-n junction showing three current transport mechanisms: (1) Carrier diffusion, (2) Carrier recombination via defects in the junction, and (3) Multistep carrier tunneling via defects in the junction .....	27
7. (a) Schematic of a semiconductor p-n junction, and (b) an energy-band diagram of a forward-biased p-n junction showing Fermi-level splitting .....	29
8. (a) A plot of log(n) and log(p) versus distance for a Shockley p-n junction at forward biases of zero and 0.5 V, and (b) current density versus distance for a junction at a forward bias of 0.5 V .....	33
9. (a) Definition of the terms "electron trap" and "recombination center" by means of the relative magnitudes of the capture cross sections $\sigma_n$ , and $\sigma_p$ , indicated by the widths of the arrows, and (b) the definition of the terms "majority carrier trap" and "minority carrier trap", and "electron trap" and "hole trap" .....	37
10. A schematic diagram of indirect generation-recombination processes at thermal equilibrium .....	42

11. (a) The function $f(b)$ versus $b$ , and (b) the function $f(b)$ versus normalized bias voltage according to Choo and Sah, Noyce, and Shockley .....	50
12. Ideal dark forward I-V characteristics for a Si p-n junction at room temperature showing the effects of recombination current .....	56
13. Ideal dark forward I-V characteristics for a GaAs p-n junction at room temperature showing the effects of recombination current .....	57
14. Ideal dark forward I-V characteristics for a GaAs p-n junction showing the effect of shunting resistance .....	59
15. Ideal dark forward I-V characteristics for a GaAs p-n junction showing the effects of shunting resistance .....	60
16. Ideal dark forward I-V characteristics as a function of temperature for a GaAs p-n junction showing the effects of shunting resistance .....	61
17. Diagram of the earth's radiation belts as a function of distance in units of the earth's radius.....	63
18. Schematic diagram of GaInP <sub>2</sub> mesa diode structure showing approximate layer thicknesses and doping densities. The GaInP <sub>2</sub> solar cell has a similar structure except for 1 $\mu\text{m}$ thick top and bottom Au contacts. The p-base doping density of the solar cells is $10^{16}\text{cm}^{-3}$ .....	71
19. A photograph of GaInP <sub>2</sub> /GaAs line-defects taken under 200X magnification .....	75
20. A scanning electron microscopy (SEM) image a typical GaInP <sub>2</sub> /GaAs line-defect taken under 1500X magnification .....	76
21. Sequence of the photolithography and metalization processes used to fabricate GaInP <sub>2</sub> mesa diodes .....	79
22. A photograph of a completed mesa diode die mounted and wire-bonded in a 10 pin T05 can .....	84
23. A photograph of a solar cell/diode die mounted and wire-bonded in a 36 pin flat electronics package .....	85
24. A schematic of the 1kW xenon lamp oriel solar simulator .....	87

25. A schematic of the GaInP <sub>2</sub> diode and solar cell test circuit .....	88
26. Forward-bias dark and AM0-light I-V curves for n <sup>+</sup> p GaInP <sub>2</sub> solar cells .....	89
27. Forward-bias dark I-V curves as a function of temperature for a "well-behaved" GaInP <sub>2</sub> solar cell .....	93
28. A plot of recombination coefficient $I_{rec}$ vs. $1000/T$ for a GaInP <sub>2</sub> solar cell .....	94
29. Forward-bias dark I-V curves for single junction n <sup>+</sup> p GaInP <sub>2</sub> solar cells showing a correlation between the magnitude of dark current and AM0 conversion efficiency .....	96
30. GaInP <sub>2</sub> solar cell open-circuit voltage, $V_{oc}$ , and dark current density, $J_{dark}$ , versus dark current recombination coefficient, $J_{rec}$ .....	97
31. Forward-bias dark I-V curves for "leaky" NREL n <sup>+</sup> p GaInP <sub>2</sub> solar cells .....	99
32. Forward-bias dark I-V curves for a "well-behaved" NREL n <sup>+</sup> p GaInP <sub>2</sub> solar cell .....	100
33. GaInP <sub>2</sub> solar cell open-circuit voltage, $V_{oc}$ , and short-circuit current density, $J_{sc}$ , versus dark current density recombination coefficient, $J_{rec}$ .....	102
34. Forward-bias dark I-V curves for GaInP <sub>2</sub> solar cell showing behavior due to carrier diffusion, recombination, and tunneling .....	104
35. Theoretical AM0 light I-V curves for a GaInP <sub>2</sub> solar cell for various recombination current density coefficient, $J_{rec}$ . The maximum power density is represented by the minimums of the pointed curves .....	107
36. A photograph showing a portion of the 13.6% GaInP <sub>2</sub> solar cell die containing line-defects. The line-defects extend across the solar cell and mesa diodes .....	109
37. Solar cell efficiency distribution across the 1" x 1" GaInP <sub>2</sub> /GaAs wafer .....	111
38. Forward-bias dark I-V curves for both "well-behaved" and "leaky" low doped GaInP <sub>2</sub> solar cells and mesa diodes .....	115



39. Forward-bias dark I-V curves for GaInP <sub>2</sub> n <sup>+</sup> p junctions of different area .....	118
40. A plot of total current density vs. perimeter-to-area ratio (P/A) for GaInP <sub>2</sub> n <sup>+</sup> p junctions of different area at a forward-bias voltage of 1.1 V .....	119
41. Forward-bias light-I-V curves as a function of temperature for an n <sup>+</sup> p GaInP <sub>2</sub> solar cell .....	123
42. 1/C <sup>2</sup> vs. reverse-bias voltage for mid and high doped GaInP <sub>2</sub> diodes, where C is the junction capacitance .....	128
43. 1/C <sup>2</sup> vs. reverse-bias voltage for a low doped GaInP <sub>2</sub> diode, where C is the junction capacitance .....	130
44. Forward-bias dark I-V curves for low, mid, and high doped GaInP <sub>2</sub> diodes showing (a) tunneling, (b) recombination, and (c) diffusion current regions .....	132
45. Forward-bias dark I-V curves for low doped GaInP <sub>2</sub> diodes exposed to H <sub>2</sub> O vapor .....	139
46. Forward-bias dark I-V curves plotted as a function of temperature for a typical "well-behaved" mid doped GaInP <sub>2</sub> diode .....	141
47. Forward-bias dark I-V curves plotted as a function of temperature for a "leaky" mid doped GaInP <sub>2</sub> diode .....	142
48. A plot of dark current ideality factor (A <sub>2</sub> ) vs. temperature for typical low, mid, and high doped GaInP <sub>2</sub> diodes .....	144
49. Recombination current coefficient I <sub>rec</sub> vs. (1000/T) for typical low, mid, and high doped GaInP <sub>2</sub> diodes .....	146
50. Reverse-bias dark I-V curves as a function of temperature for a typical low doped GaInP <sub>2</sub> diode showing (a) exponential- (b) and shunting-like behavior .....	149
51. Reverse-bias dark I-V curves as a function of temperature for a typical mid doped GaInP <sub>2</sub> diode showing exponential- and shunting-like behavior .....	150
52. A plot of reverse-bias current vs. (1000/T) for low, mid, and high doped GaInP <sub>2</sub> diodes measured at a reverse-bias voltage of -5.0 V .....	153

53. A schematic showing the detection of a deep level at $E_t$ using DLTS .....	157
54. Junction capacitance transients due to a majority carrier trap in the p-base of a $\text{GaInP}_2$ $n^+p$ diode .....	159
55. A plot of $\ln[T^2/e_p]$ vs $1/T$ for low and mid doped $\text{GaInP}_2$ diodes determined from DLTS spectra, where $e_p$ is the majority hole emission rate in the p- $\text{GaInP}_2$ .....	161
56. The effect at Frenkel-Poole barrier lowering on the measured energy, $E_a$ , of deep levels in $\text{GaInP}_2$ $n^+p$ diodes .....	165
57. (a) Frenkel-Poole emission barrier lowering, showing the electric field emanating from localized charge distribution associated with defect/impurity center. The electric field is shown lowered on right-side of charge distribution by applied field, $F$ , and the resulting emission barrier is lowered by $\Delta E_a$ .....	166
58. Forward-bias I-V curves for the mid doped "leaky" and "well-behaved" $\text{GaInP}_2$ diodes used for C-F-T measurements .....	169
59. Typical capacitance-frequency-temperature data for $\text{GaInP}_2$ $n^+p$ diodes .....	170
60. A plot of $dC/dT$ for the $\text{GaInP}_2$ diodes of Figure 59, used for determining activation energy $E_a = E_t - E_v$ .....	172
61. A summary of deep levels found in $\text{GaInP}_2$ $n^+p$ diodes using reverse-bias I-V-T, DLTS, and C-F-T measurements .....	175
62. Light I-V curves for a $\text{GaInP}_2$ solar cell before and after 1 MeV electron irradiation of fluence $10^{15} \text{ e}^-/\text{cm}^2$ , and subsequent thermal annealing at $250^\circ\text{C}$ .....	180
63. Light I-V curves for a $\text{GaInP}_2$ solar cell before and after 1 MeV electron irradiation of fluence $10^{16} \text{ e}^-/\text{cm}^2$ , and subsequent thermal annealing at $250^\circ\text{C}$ .....	181
64. A comparison in normalized solar conversion efficiency for various solar cells as a function of 1 MeV electron fluence, where $\text{Eff}_0$ and $\text{Eff}$ are pre- and post-irradiation efficiencies, respectively .....	184

65. A comparison of forward-bias dark I-V curves for GaInP <sub>2</sub> n <sup>+</sup> p solar cells before and after 1 MeV electron irradiation of fluence 10 <sup>15</sup> and 10 <sup>16</sup> e <sup>-</sup> /cm <sup>2</sup> .....	186
66. A plot of normalized values of GaInP <sub>2</sub> solar cell V <sub>oc</sub> , I <sub>sc</sub> , FF, and Eff following 1 MeV electron irradiation of fluence 10 <sup>16</sup> e <sup>-</sup> /cm <sup>2</sup> and multiple hotplate thermal annealing at 250°C for 10 min .....	189
67. Forward-bias dark I-V curves for a GaInP <sub>2</sub> n <sup>+</sup> p solar cell before and after 1 MeV electron irradiation and thermal annealing at 250°C .....	190
68. A comparison of forward-bias dark I-V curves for GaInP <sub>2</sub> n <sup>+</sup> p diodes following exposure to 1 MeV electron irradiation of fluence of 10 <sup>15</sup> and 10 <sup>16</sup> e <sup>-</sup> /cm <sup>2</sup> .....	193
69. Forward-bias dark I-V curves for a low doped GaInP <sub>2</sub> n <sup>+</sup> p before and after 1 MeV electron irradiation and thermal annealing at 250°C .....	195
70. A comparison of dark current annealing behavior in GaInP <sub>2</sub> n <sup>+</sup> p solar cells and diodes following 1 MeV electron irradiation, and multiple thermal annealing at 250°C for 10 min. ....	197
71. Comparison of dark I-V curves for a mid doped GaInP <sub>2</sub> n <sup>+</sup> p diode before and after 1 MeV electron irradiation, and the dark I-V curve for a pre-irradiated low doped GaInP <sub>2</sub> n <sup>+</sup> p diode .....	198
72. Comparison of forward-bias dark I-V curves for a high doped GaInP <sub>2</sub> n <sup>+</sup> p diode before and after 1 MeV electron irradiation, and after room temperature (~25°C) and hotplate annealing (250°C) .....	200
73. A comparison of dark current annealing behavior in GaInP <sub>2</sub> n <sup>+</sup> p diodes versus doping density following 1 MeV electron irradiation and thermal annealing at ~25 and 250°C .....	201
74. A plot of 1/C <sub>2</sub> vs. reverse-bias voltage for a mid and high doped GaInP <sub>2</sub> n <sup>+</sup> p diode before and after 1 MeV electron irradiation and thermal annealing at 250°C twice for 10 min. ....	205
75. Arrhenius plots of I <sub>rec</sub> vs. 1000/T for GaInP <sub>2</sub> n <sup>+</sup> p diodes before and after 1 MeV electron irradiation and thermal annealing at 250°C twice for 10 min. ....	207

76. Forward-bias dark current ideality factor versus temperature for low, mid, and high doped GaInP <sub>2</sub> n <sup>+</sup> p diodes before, and after 1 Mev electron irradiation and thermal annealing at 250°C twice for 10 min .....	209
77. Arrhenious plot of I <sub>rec</sub> vs. 1000/T and 1000/(A/2)T for GaInP <sub>2</sub> n <sup>+</sup> p diode before and after 1Mev electron irradiation and thermal annealing .....	210
78. A plot of the average AM1.5 and AM0 solar spectrum.....	230

## List of Tables

Table	page
I. Trade study showing the effects of solar cell efficiency on solar array area, power density, and mass for a typical space mission .....	4
II. Summary of GaInP <sub>2</sub> solar cell photovoltaic parameters measured at ~ 290 K .....	91
III. GaInP <sub>2</sub> n <sup>+</sup> p solar cell photovoltaic parameters versus dark recombination current density, J <sub>rec</sub> .....	108
IV. Summary of GaInP <sub>2</sub> solar cell photovoltaic parameters measured as a function of temperature .....	125
V. Summary of GaInP <sub>2</sub> n <sup>+</sup> p junction parameters for low, mid, and high doped diodes .....	133
VI. Summary of forward- and reverse-bias measured current densities and generation/recombination center activation energies, E <sub>a</sub> , for the low, mid, and high doped GaInP <sub>2</sub> diodes .....	152
VII. Summary of deep energy levels measured in GaInP <sub>2</sub> using reverse-bias I-V-T and DLTS measurements .....	162
VIII. Summary of activation energies obtained using reverse-bias I-V-T and C-F-T measurements .....	173
IX. Summary of GaInP <sub>2</sub> solar cell photovoltaic parameters before and after exposure to 1 MeV electrons of fluence 10 <sup>15</sup> e <sup>-</sup> /cm <sup>2</sup> , and subsequent multiple thermal annealing at 250°C for 10 min. ....	182
X. Summary of GaInP <sub>2</sub> solar cell photovoltaic parameters before and after exposure to 1 MeV electrons of fluence 10 <sup>16</sup> e <sup>-</sup> /cm <sup>2</sup> , and subsequent multiple thermal annealing at 250°C for 10 min. ....	183

### Abstract

The GaInP<sub>2</sub>/GaAs tandem solar cell currently exhibits the greatest potential of achieving AM1.5 solar conversion efficiencies in excess of 30%. The present work involves an investigation of GaInP<sub>2</sub> n<sup>+</sup>p diode and solar cell dark current mechanisms, the defect centers that affect these mechanisms, and the response of dark current and solar cell photovoltaic parameters to 1 MeV electron irradiation and thermal annealing.

Dark current characteristics of n<sup>+</sup>p mesa diode and solar cells fabricated from MOCVD grown GaInP<sub>2</sub> have been examined and correlated with GaInP<sub>2</sub> solar cell photovoltaic performance. Dark current due to carrier diffusion, recombination, and tunneling were identified through voltage, temperature, and device geometry dependencies. Recombination current was found to dominate at the maximum power-point voltage of the GaInP<sub>2</sub> solar cells, and was shown to limit the photovoltage. The magnitude of recombination current was reduced by a factor of 10~15 with increased doping density in diodes of similar structure. Recombination current occurred via defect centers at the perimeter and within the bulk of the junction, and perimeter recombination was dominant in devices with junction perimeter-to-area ratios larger than  $\approx 40$ . Two deep majority-hole trap centers were found at  $E_{a1} = E_t - E_v \approx 0.45$  eV and  $E_{a2} = E_t - E_v \approx 0.05$  eV. The center at  $E_{a1}$  exhibited Frenkel-Poole barrier lowering, and is believed to be the dominant recombination center. Dark current due to carrier tunneling was dominant in

"leaky" diodes and solar cells that contained line-like morphological defects. Excess tunneling current significantly degraded solar cell efficiency, and the line-defects are believed to be due to GaInP<sub>2</sub>-GaAs lattice mismatch.

The effects of 1 MeV electron irradiation on solar cell and diode dark current mechanisms and efficiency were studied. The AM0 conversion efficiency of GaInP<sub>2</sub> solar cells was shown to degrade less compared to Si and GaAs solar cells following exposure to  $10^{15}$  and  $10^{16}$  1 MeV electrons/cm<sup>2</sup>. A significant improvement in post-irradiated GaInP<sub>2</sub> solar cell efficiency was then shown via thermal annealing at 250 °C, demonstrating good potential for thermal annealing in space.

# **THE JUNCTION CHARACTERISTICS AND CURRENT CONDUCTION MECHANISMS OF GaInP<sub>2</sub> n<sup>+</sup>p DIODES AND SOLAR CELLS**

## **I. Introduction**

The solar photovoltaic cell, hereafter called the solar cell for brevity, was invented in 1954 at Bell Laboratories (Chapin *et al.*, 1954:676). The first solar cells to have wide application were Si cells utilized in the space program in the late 1950's. Today, thirty-five years later, Si cells continue to provide the main source of electrical power to practically all earth-bound satellites, mostly due to their high level of reliability. In the mid 1970's, a tremendous increase of interest in terrestrial photovoltaic power was sparked when oil supplies to the industrialized world were disrupted (Fahrenbruch and Bube, 1983:1-9). A strong emphasis was then placed on improving solar cell system efficiency, increasing reliability, and reducing costs. Good progress towards these goals has been steadily achieved over the last 20 years. However, today the high cost of photovoltaic systems still prevent their wide-spread terrestrial use. Currently, the average price of conventional electricity in the United States is 6-7 cents/kWhr, compared to a cost of 20 cents/kWhr for



solar photovoltaic electricity (Stone, 1993:28). Hence, a reduction in solar system cost by a factor of at least 3 is necessary before terrestrial photovoltaics will compete with conventional electricity. One method of reducing system costs is to increase solar module efficiency. The efficiency of solar cells utilized in currently available terrestrial systems is typically less than 15%. Attempts to substantially improve upon this efficiency have recently focused on the utilization of a manufacturable multijunction (MJ) solar cell having theoretical efficiencies in excess of 30% (Olson *et al.*, 1990:623; Chiang *et al.*, 1993:659).

Due to a reduction in complexity, lower-efficiency thin film and single junction solar cells are generally less costly to produce than higher-efficiency MJ solar cells.

However, lower-efficiency modules have to cost less (in dollars per square meter) than higher-efficiency modules to produce the same cost of electricity (cents/kWhr) (Stone, 1993:29). This is due to costs associated with the additional module substrate, wiring, and labor required for a larger area array. For example, it is projected that a 10% efficient module must cost ~10 times less than a 25% efficient module for it to achieve the same cost of electricity (Stone, 1993:29). Thus, the higher cost of high-efficiency solar cells is compensated by the cell's increased areal power density. Further, as industry begins to commit to larger, more cost-effective production facilities, the cost of higher efficiency solar cells will drop. Therefore, the development of higher efficiency MJ solar cells shows

good potential for use in future terrestrial systems that will compete with conventional sources of electricity.

As mentioned, solar cells also provide an extremely important source of electrical power to nearly all commercial and military satellites. Present day, space-qualified solar cells have air mass zero (AM0), beginning-of-life (BOL) solar energy conversion efficiencies, Eff, of ~13-19%, and can deliver between ~175 and 240 W/m<sup>2</sup> to the spacecraft user. Practically all space solar arrays currently utilize Si homojunction solar cells with AM0, BOL Eff ~13-14%. However, recent advances in higher efficiency InP (AM0 Eff  $\approx$  16-18%) and GaAs (AM0 Eff  $\approx$  18-19%) solar cells with enhanced radiation resistance have become important in applications where reduced solar array area and mass are paramount. High cell efficiency and radiation resistance are important because end-of-life (EOL)/BOL conversion efficiency ratios largely determine how much extra solar array area must be launched to meet the spacecraft's EOL mission requirement.

The impact of solar cell efficiency on the performance of a 1 kW rigid and flexible solar arrays designed for a 7 year mission in the space radiation environment is shown in Table I. Of special importance is the reduction in solar array mass and area that results through the utilization of higher efficiency solar cells. The table shows that a rigid solar array utilizing 26% efficient MJ cells will be 1.9 times lighter and 2.5 times smaller compared to the same array utilizing 15.5% efficient Si cells. The reduction in array area would significantly reduce

Table I. Trade study showing the effects of solar cell efficiency on solar array area, power density, and mass for a typical space mission

## 1 kW Solar Array Trade Study

Mission: 7 yrs in  $3 \times 10^{15}/\text{cm}^2$  1 MeV Electron Radiation

Solar Cell Design	Si	InP	GaAs	GaInP <sub>2</sub>
Cell AM0 Efficiency (production)	15.5	19	20	26
EOL Power at 25 K (W)	1000	1000	1000	1000
BOL Power at 25 K (W)	2316	1403	1760	1403
Array Area (m <sup>2</sup> )	12.65	6.25	7.45	4.95
EOL Power Density (W/m <sup>2</sup> )	79	160	134	202
Flexible Array:				
Mass (kg)	18.88	16.26	18.83	12.5
EOL Specific Power (w/kg)	53	62	53	80
Rigid Array:				
Mass (kg)	38	26	30	20
EOL Specific Power (w/kg)	26	39	33	50

both the array's radar cross section and aerodynamic drag. The reduction in array weight could significantly reduce the satellite launch weight and orbital delivery costs. Therefore, as is the case of the terrestrial photovoltaic power system, a substantial improvement in solar cell efficiency would greatly benefit the performance of the space solar array system. Currently, the best high efficiency candidate is the MJ solar cell.

The simplest and most desirable MJ solar cell is a monolithic, two-terminal, two-junction structure. In the monolithic two-junction design, a high bandgap p-n junction is vertically grown atop a bottom lower bandgap p-n junction. The top cell absorbs the high energy (blue) part of the solar spectrum, and the bottom cell absorbs the lower energy (red) part of the spectrum that passed through the top cell. In order to maximize the conversion efficiency for a given solar spectrum, the bandgaps of the top and bottom junctions must be optimized to achieve maximum solar absorption and current matching. Current matching is achieved when each cell generates equal currents during solar exposure. Lattice matching is important between the top and bottom cells because lattice-mismatched materials contain crystal defects that adversely affect the cell's photocurrent and photovoltage.

Progress towards developing a monolithic, two-junction solar cell has focused on the nominal bandgap combination of  $\sim 1.9$  eV/  $1.4$  eV (Olson *et al.*, 1990:623). This combination provides current matching and has a maximum theoretical AM0 and AM1.5 conversion efficiency of  $\sim 28$  and  $34\%$ , respectively (Cavicchi,

1991:215; Fan *et al.*, 1982:692). GaAs with an electronic bandgap,  $E_g$ , of 1.42 eV is ideal for the bottom cell. For the top cell, there exist only two known III-V alloys with bandgaps  $\sim 1.9$  eV that are lattice matched to GaAs, namely,  $\text{Al}_{0.4}\text{Ga}_{0.6}\text{As}$  and  $\text{Ga}_{0.5}\text{In}_{0.5}\text{P}$  (hereafter,  $\text{GaInP}_2$ ).

Although nearly perfect in its lattice match to GaAs, the growth of high quality  $\text{Al}_{0.4}\text{Ga}_{0.6}\text{As}$  has proven to be difficult due to its sensitivity to trace  $\text{O}_2$  and  $\text{H}_2\text{O}$  in the growth chamber (Olson *et al.*, 1990:623; Cavicchi *et al.*, 1991:63). This contamination results in material having low carrier lifetimes and diffusion lengths, causing a substantial reduction in the top  $\text{Al}_{0.4}\text{Ga}_{0.6}\text{As}$  solar cell photovoltage and photocurrent. Also, the formation of a low resistance tunnel junction between  $\text{Al}_{0.4}\text{Ga}_{0.6}\text{As}$  and GaAs is confounded by diffusion that results at high growth temperature ( $>780^\circ\text{C}$ ) required for low defect  $\text{Al}_{0.4}\text{Ga}_{0.6}\text{As}$  layers (Cavicchi *et al.*, 1991:63). As a consequence of these troubles, efforts to develop the  $\text{Al}_{0.4}\text{Ga}_{0.6}\text{As}/\text{GaAs}$  solar cell have been abandoned.

In contrast to  $\text{Al}_{0.4}\text{Ga}_{0.6}\text{As}$ , the growth of  $\text{GaInP}_2$  does not suffer from  $\text{O}_2$  and  $\text{H}_2\text{O}$  contamination problems (Cavicchi *et al.*, 1991:63; Olson *et al.*, 1990:623). Also, a lower allowable growth temperature of  $\sim 675^\circ\text{C}$  minimizes dopant diffusion at the  $\text{GaInP}_2/\text{GaAs}$  tunnel junction, resulting in a suitable low resistance interconnect. Thus, at present, the  $\text{GaInP}_2$  material system represents an excellent candidate for use as the top cell. However, to date the  $\text{GaInP}_2/\text{GaAs}$  solar cell has received very little attention.

### Research Motivation: The GaInP<sub>2</sub> Solar Cell

The GaInP<sub>2</sub>/GaAs solar cell shows good potential for achieving AM0 and AM1.5 conversion efficiencies in excess of 25% and 31%, respectively (~90% of theoretical). The highest efficiency reported for the GaInP<sub>2</sub>/GaAs solar cell measured under AM1.5 conditions is 27.3% (Olson *et al.*, 1990:623). The area of the cell was 0.25 cm<sup>2</sup>. A diagram of the GaInP<sub>2</sub>/GaAs solar cell structure is shown in Figure 1. In well developed Si, GaAs, and InP solar cells, ratios of demonstrated-to-theoretical conversion efficiency of greater than 90% are typical. Whereas, the reported efficiency of 27.3% for the GaInP<sub>2</sub>/GaAs cell is only 80% of the maximum theoretical efficiency of 34%. Thus, a significant improvement in the GaInP<sub>2</sub>/GaAs cell efficiency can still be expected. However, the factors that currently limit the cell efficiency are not well understood.

The factors that control conversion efficiency in the bottom GaAs solar cell of the MJ stack have been previously investigated, and are well understood. The conduction mechanisms, role of excess dark current on efficiency, identity of native and radiation induced deep levels responsible for enhancing dark current, degradation of cell parameters in the space radiation environment, radiation induced damage annealing properties, and temperature performance of GaAs solar cells are well established. (DeMoulin *et al.*, 1988:368; Li *et al.*, 1983:835; Li *et al.*, 1980:857; Fahrenbruch and Bube, 1983:304). A slow and steady development of GaAs solar cells has occurred over the last 20 years. An improvement in AM1.5

$t \text{ (Å)}$		
n - AlInP <sub>2</sub>	400	TOP GaInP <sub>2</sub> CELL
n - GaInP <sub>2</sub>	400	
p - GaInP <sub>2</sub>	8000	
p <sup>+</sup> - GaAs	200	TUNNEL DIODE
n <sup>+</sup> - GaAs	200	
n - AlGaAs	2000	BOTTOM GaAs CELL
n - GaAs	1000	
p - GaAs	35000	
p <sup>+</sup> - GaAs	substrate	

Figure 1. A schematic cross section of the GaInP<sub>2</sub>/GaAs tandem solar cell.

cell efficiency from 10% (Alferov *et al.*, 1971:2047) to over 25% (Stone, 1993:28) can be traced through the literature; there are over 300 papers alone on the GaAs solar cell development in the IEEE Photovoltaics Specialists Conference Proceedings from 1972 - 1993. However, in contrast to the bottom GaAs cell, the basic physics and electrical behavior of the top GaInP<sub>2</sub> p-n junction solar cell are relatively unknown. In fact, the basic electrical characteristics of the GaInP<sub>2</sub> p-n diode have yet to be studied.

In order to model and optimize the electrical performance of GaInP<sub>2</sub> solar cells operating in both the terrestrial and space environments, a basic understanding of the physics controlling current transport, light-generation, and radiation damage in the devices must be obtained. To do this, numerous basic fundamental questions must first be answered. For example, questions such as what current mechanisms are present in the junction, over what voltage range does each mechanism dominate, and how do these voltage ranges change with ambient temperature, junction doping, junction geometry, and device layer quality, must be addressed. Also, the influence of radiation damage on dark current transport, and the resulting effects on solar cell output parameters need to be established. Further, a knowledge of solar cell output parameter temperature coefficients is required to accurately model cells operating in earth's orbit due to large temperature excursions that are encountered by the solar array. In solar cells, excess junction dark currents play an important role in limiting cell efficiency. In many cases,



these currents are comprised of current due to carrier recombination and tunneling via defect centers within the junction. However, the dark current behavior in GaInP<sub>2</sub> n<sup>+</sup>p solar cells is unknown. The presence of deep levels in the GaInP<sub>2</sub> n<sup>+</sup>p junction, and their effects on current conduction have yet to be determined. Further, the effect of high energy electron irradiation on GaInP<sub>2</sub> solar cell dark current behavior and photovoltaic performance needs to be established.

Lastly, the annealing behavior of radiation induced electrical degradation in GaInP<sub>2</sub> solar cells has not yet been determined. The effects of ambient and accelerated thermal annealing on radiation induced defect centers, excess dark currents, and degradation of cell output parameters are of great interest. On-orbit solar array thermal annealing of radiation induced degradation has been successfully demonstrated with GaAs solar cells (Wolf *et al.*, 1992:88).

One further point is worth mentioning. The difference in electrical behavior between small GaInP<sub>2</sub> diagnostic test diodes used in device development and larger GaInP<sub>2</sub> solar cells are unknown. The current-voltage behavior of these structures can often be quite different, and understanding the sources of the differences is very important during device development (Demoulin *et al.*, 1988:368).

### **Problem Statement**

In order to help determine factors that limit the performance of GaInP<sub>2</sub> solar cells, a correct understanding of the mechanisms that control current transport, radiation damage, and radiation damage annealing is needed. In order to

understand these factors, basic research into the dynamics of the GaInP<sub>2</sub> junction is required. This effort consisted of basic research into the nature of GaInP<sub>2</sub> n<sup>+</sup>p diode and solar cell dark current mechanisms, of defect centers that influence these mechanisms, and of the response of dark current and solar cell photovoltaic parameters to electron irradiation and thermal annealing. The ultimate goal of this work is to establish an understanding of the basic current transport in the GaInP<sub>2</sub> p-n junction, and to correlate this behavior with the performance of the GaInP<sub>2</sub> solar cell.

### **Approach**

This research effort contained three main objectives. The first was to characterize the dark current mechanisms present in GaInP<sub>2</sub> n<sup>+</sup>p junction test diodes and solar cells. Small mesa diodes processed from identical n<sup>+</sup>p solar cell material were included for study because they were extremely useful in investigating the basic physics of the GaInP<sub>2</sub> n<sup>+</sup>p junction, and because only a limited number of solar cells were available for study. The current mechanisms were identified and studied through their forward-bias voltage, temperature, doping density, and device perimeter-to-area ratio dependencies. The identification of defect levels within the GaInP<sub>2</sub> bandgap responsible for enhancing recombination and tunneling current was achieved using reverse-bias current-voltage-temperature (I-V-T), deep level transient spectroscopy (DLTS), and capacitance-temperature-frequency (C-T-F) measurement techniques.

The second objective was to determine the electrical response of GaInP<sub>2</sub> diodes and solar cells exposed to 1 MeV electron radiation similar to that found in space. The behavior of device dark currents and solar cell output parameters were measured following 1 MeV electron irradiation to a fluence of  $10^{15}$  and  $10^{16}$  e<sup>-</sup>/cm<sup>2</sup>.

The third objective was to determine the annealing behavior of the electron-irradiated GaInP<sub>2</sub> diodes and solar cells. The primary goal was to determine the degree to which pre-irradiation electrical behavior could be recovered. Devices were carefully monitored following both room temperature (~25 °C) and pulsed hotplate thermal annealing at 250 °C.

## Outline

The present chapter provides a prospectus on the motivation for high efficiency multijunction solar cells, specifically the GaInP<sub>2</sub>/GaAs solar cell, a statement of the research problem, and the experimental approach used in this effort. Chapter 2 presents the physics and theory of p-n junction diodes and solar cells. In chapter 3, the techniques used to process and package GaInP<sub>2</sub> n<sup>+</sup>p diodes and solar cells are given. Chapters 4 and 5 discuss the characterization and analysis of pre-irradiated GaInP<sub>2</sub> solar cells and diodes, respectively, and in Chapter 6, an analysis of solar cell and diode electrical characteristics following 1 MeV electron irradiation is given. Finally, in Chapter 7, a summary of results, contributions, and recommendations for future work are given.

## **II. P-N Junction Diode and Solar Cell Device Physics**

### **Solar Cell Basics and the Photovoltaic (PV) Effect**

Photovoltaic conversion in a p-n junction device is a two step process where photocarriers (electron-hole pairs) are created within the semiconductor material and simultaneously collected across the junction. Consider the schematic of a typical single-junction p-n solar cell shown in Figure 2(a). The device structure consists of a shallow p-n junction formed very close to the top surface of the cell. The ohmic grid fingers allow solar energy to pass into the absorber layers of the cell, and the anti-reflection coating that covers the entire front surface minimizes reflective losses. The entire back surface is covered by a metal ohmic contact to complete the device structure.

When the solar cell is exposed to solar radiation, photons having energies greater than the cell's semiconductor bandgap,  $E_g$ , are absorbed in the n and p layers, and the generation of photocarriers results. Generated minority carrier electrons on the p-side, and holes on the n-side, diffuse towards the cell's junction due to a gradient of minority carriers that exists at the edge of each side of the junction. When the electrons and holes reach the junction, the space-charge layer's built-in potential (electric field) accelerates them to opposite sides of the junction, effectively separating them before they can recombine. This is shown in the p-n junction energy-band diagram of Figure 2(b).

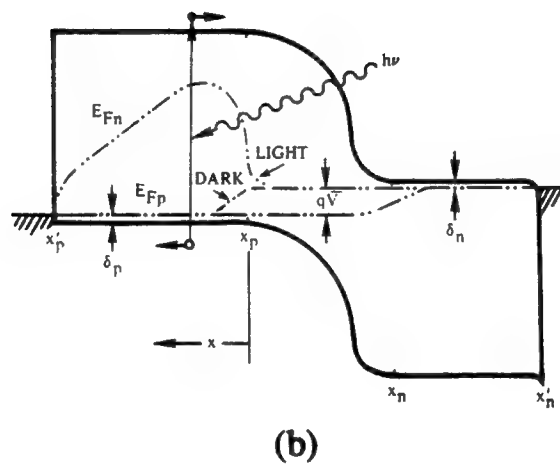
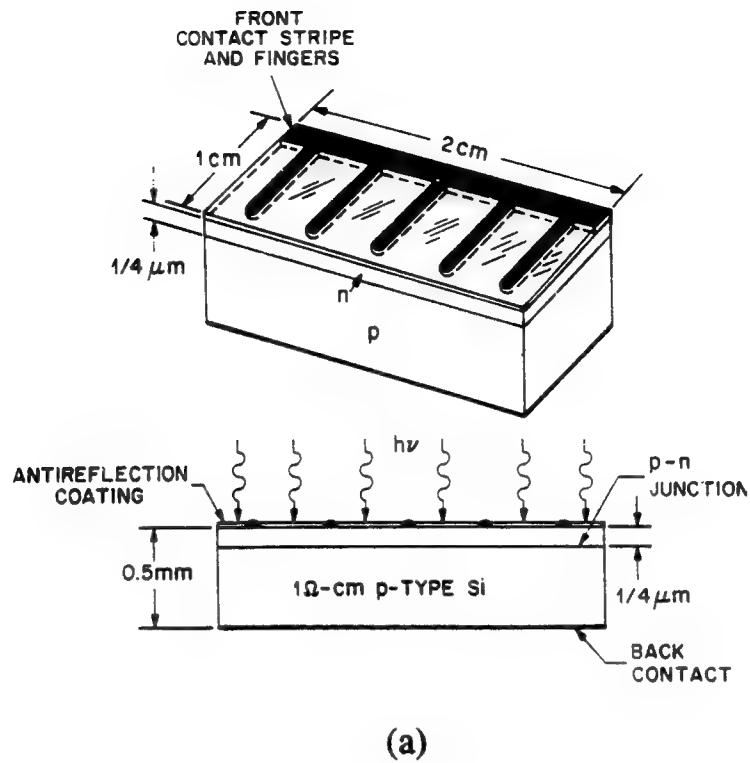


Figure 2. (a) Schematic of a typical shallow n<sup>+</sup>p junction solar cell, and (b) an energy -band diagram for the illuminated p-n junction solarcell shown in

The diffusion flux of optically generated carriers towards the junction constitutes the solar cell photocurrent. The direction of photocurrent is from the n-side to the p-side of the junction (the direction of hole transport, by convention). This current will flow through an external load (and also under short-circuit conditions) in order to restore equilibrium within the cell. The magnitude of the photocurrent is determined by the illumination flux, the optical absorption constant of the semiconductor (determined by  $E_g$ ), and the electron and hole minority carrier lifetimes. The maximum value of current is obtained under short-circuit conditions, and its value is called the short-circuit current,  $I_{sc}$ . Under open-circuit conditions, the photocarriers disturb the equilibrium carrier concentration resulting in a large split in the quasi-Fermi level of electrons and holes ( $E_{Fn}$  and  $E_{Fp}$ , respectively). A split in the quasi-Fermi levels due to carrier generation and build-up is shown in Figure 2(b). The difference between the quasi-Fermi levels under open-circuit conditions is equal to the open-circuit voltage,  $V_{oc}$ . The appearance of this photovoltage across the illuminated junction is called the photovoltaic effect. The maximum obtainable value of the photovoltage is equal to  $V_{oc}$ , and its value depends on  $E_g$ , the doping density on both sides of the p-n junction, and the electron and hole minority carrier lifetimes.

The photovoltage,  $V$ , developed across a solar cell can be used to drive current,  $I$ , through an external resistive load,  $R_L$ , in accordance with  $I = V/R_L$ . However, the polarity of the solar cell photovoltage is also in the forward-bias direction of

the cell's junction. As a result, the photovoltage also drives current through the solar cell from the p- to n-side of the junction. This detrimental current is opposite in direction to the photocurrent, and it is called the solar cell dark current. The dark current plays a very important role in controlling the maximum obtainable output power delivered by the cell. Under open-circuit conditions, the dark current resulting from  $V_{oc}$  across the junction equals the photocurrent, and the net junction current is zero.

The maximum power delivered by an illuminated solar cell to an external resistive load is the product of the cell's photocurrent and photovoltage when it is operating at its maximum power-point voltage. The maximum power-point voltage is the forward photovoltage across the cell (and the load) that maximizes the product of the cell's photocurrent and photovoltage output.

### **Solar Cell Conversion Efficiency and Dark Current**

The current-voltage characteristics for a typical p-n junction solar cell in the dark and under illumination are shown in Figure 3. The total solar cell current density,  $J_T$ , can be written as

$$J_T = J_{Dark} - J_L = J_D + J_R + J_{SH} - J_L, \quad (2.1)$$

where  $J_D$ ,  $J_R$ , and  $J_{SH}$  is junction dark current density due to diffusion, recombination, and shunting, respectively, and  $J_L$  is the photocurrent density. The photocurrent current displaces the dark forward-bias part of the I-V characteristics downward into the fourth quadrant of the plot in Figure 3. In the forth quadrant,

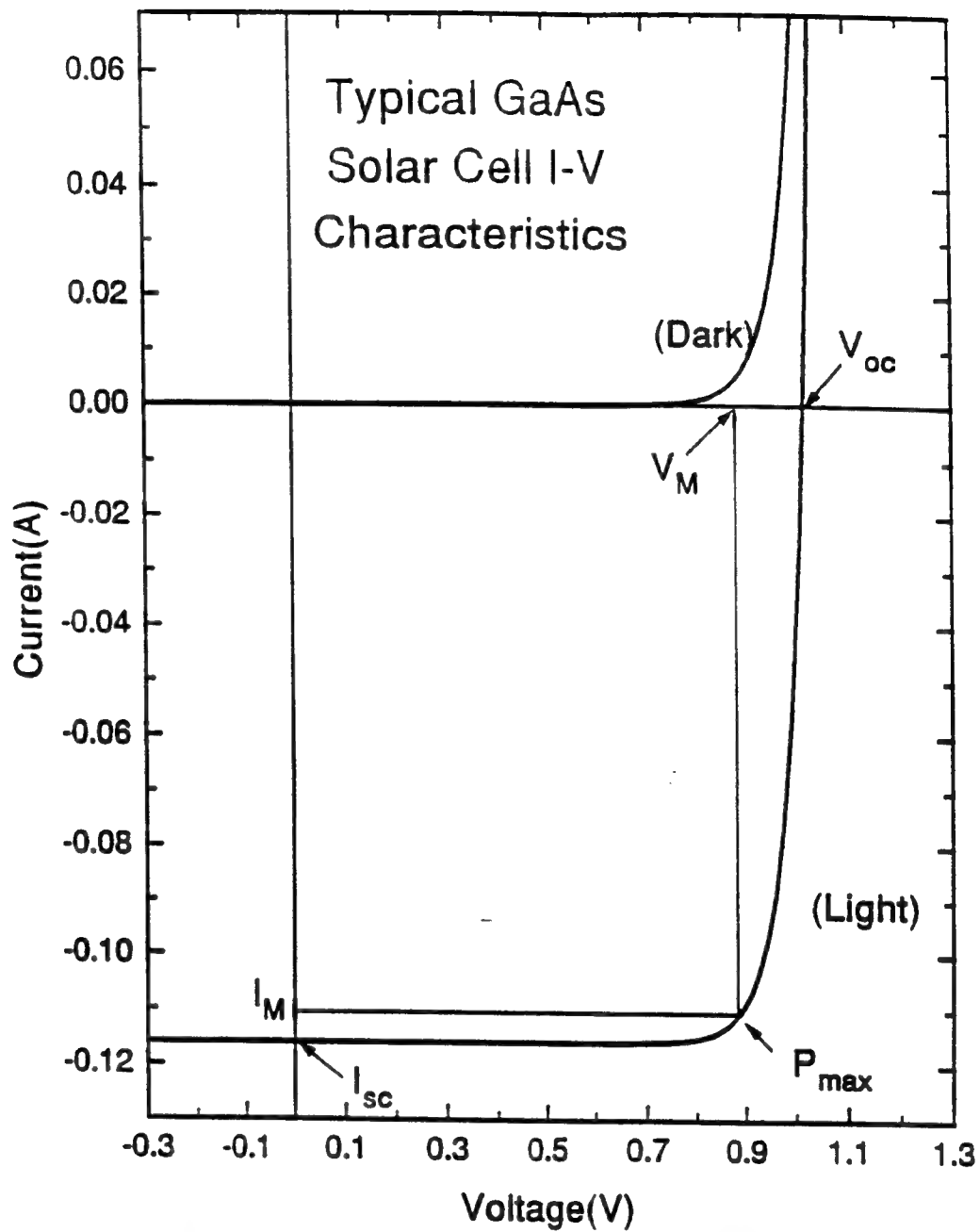


Figure 3. Typical light and dark I-V characteristics for a p-n solar cell.



the junction voltage,  $V$ , is positive and the current is negative. By convention, the direction of positive diode current is from the p- to n-side of the junction. Thus, the photocurrent current flows from the negative side of  $V$  to the positive side, as in a battery, and power is delivered from the junction to the external circuit.

The solar conversion efficiency for a solar cell can be evaluated in terms of its open-circuit voltage,  $V_{oc}$ , short-circuit current,  $I_{sc}$ , and fill-factor,  $ff$ , as shown in Figure 3. The ideal power output from the light I-V characteristics is equal to the product of  $I_{sc} \times V_{oc}$ . However, in practice only 75-90% of this power can be obtained in most cells due to internal device resistance and shunt losses. For practical purposes, a maximum power point  $P_m$  is defined such that

$$P_m = I_m \times V_m, \quad (2.2)$$

where  $I_m$  and  $V_m$  are the maximum power-point current and voltage, respectively. At the maximum power-point voltage, the product of the cell's photocurrent and photovoltage are a maximum. The curvature of the knee at the maximum power-point can be expressed by the fill-factor, where mathematically,

$$ff = \frac{I_m \times V_m}{I_{sc} \times V_{oc}}. \quad (2.3)$$

The solar cell conversion efficiency,  $Eff$ , is defined as

$$Eff = \frac{P_m}{P_{in}} \times 100\% \quad (2.4)$$

or

$$Eff = \frac{(I_{sc} \times V_{oc}) \times ff}{P_{in} \times S}, \quad (2.5)$$

where  $P_{in}$  is the input power in  $W/m^2$ , and  $S$  is the area of the device. For an AM0 solar spectrum,  $P_{in} \approx 135 W/m^2$ , and for the AM1.5 spectrum,  $P_{in} \approx 830 W/m^2$  (Fahrenbruch and Bube, 1983:26,541).

A useful analysis done by Wolf (Wolf, 1971:63) identified the major loss mechanisms in a typical Si solar cell. A chart of these loss mechanisms is shown in Figure 4. Each loss mechanism has been identified so it can be attacked separately in order to optimize the cell efficiency. The major contributions listed are:

- |      |                     |  |
|------|---------------------|--|
| (1)  | $h\nu > E_g$        | thermalization of hot carriers to near the band edge   |
| (2)  | $h\nu < E_g$        | low-energy photons pass through the cell without electron-hole generation  |
| (3)  | $qV_{oc} < E_g$     | determined by diode's parameters $A_1$ , $A_2$ , $I_{dif}$ , $I_{rec}$ - due to thermalization of carriers over junction potential barrier |
| (4)  | $ff$                | $I^2R$ losses due to internal series and shunt resistances, $R_s$ and $R_{sh}$ , respectively  |
| (5)) | $\eta_Q$            | collection efficiency of photo generated carriers - due to spectral response   |
| (6)  | Reflection          | reflection of photons at light-incident loss surfaces  |
| (7)  | Area factor         | grid coverage - usually $\sim 5\%$ of total area   |
| (8)  | Spurious absorption | Spurious absorption in anti-reflection coating, at absorption defects, etc.  |

Of the losses listed, the first two can be minimized only through the use of graded multi-bandgap solar cell structures. As discussed earlier, by splitting the solar spectrum into two or more broad bands that are routed to cells with different absorber bandgaps and connected in tandem, super- and sub-bandgap photons, relatively speaking, can be more efficiently collected. As described in the

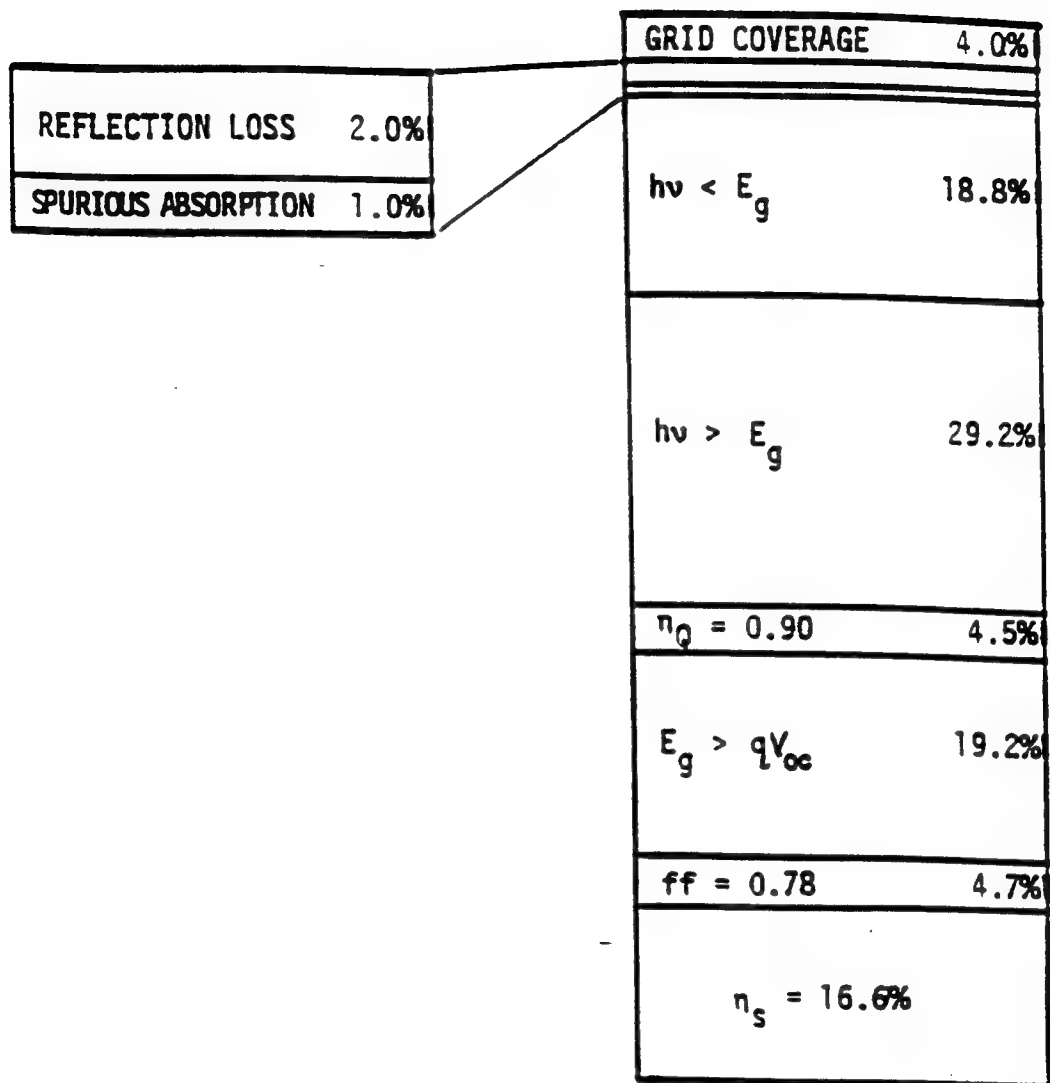


Figure 4. Power loss chart of a Si n<sup>+</sup>p solar cell operating at AM1.5. Percentage of each of the loss mechanisms is given (Fahrenbruch and Bube, 1983:242).

introduction, the two-junction, monolithic GaInP<sub>2</sub>/GaAs solar cell was specifically designed and optimized to minimize these losses.

The third loss mechanism listed,  $qV_{oc} < E_g$ , is a consequence of both the thermodynamic efficiency of the diode for separation of charge and the diode parameters themselves. For example, for the Shockley diode solar cell dominated by diffusion dark current, the open-circuit voltage,  $V_{oc1}$ , is given by (Stirn, 1972:73)

$$qV_{oc1} \approx kT \ln \left( \frac{J_L}{J_{dif}} \right), \quad (2.6)$$

where  $J_L$  and  $J_{dif}$  are the light-generated and diffusion reverse saturation current densities, respectively. For the case of the n<sup>+</sup>p diode, the Shockley expression derived for  $J_{dif}$  in the next section can be rearranged to give

$$qV_{oc1} \approx E_g - kT \ln \left\{ qN_c N_v \frac{\sqrt{D_n \tau_n^{-1}}}{N_A} \frac{1}{J_L} \right\}. \quad (2.7)$$

Eqs. (2.6) and (2.7) predict an increase in  $V_{oc1}$  with increasing  $E_g$ ,  $N_A$ ,  $\tau_n$ , and  $J_L$ , and a reduction in  $V_{oc1}$  with increasing  $J_{dif}$ . In practice,  $V_{oc}$  is typically very close to  $2/3 \times E_g$ . In the case of an n<sup>+</sup>p solar cell dominated by dark current due to recombination of carriers within the junction, the open-circuit voltage,  $V_{oc2}$ , becomes

$$qV_{oc2} \approx 2kT \ln \left( \frac{J_L}{J_{rec}} \right), \quad (2.8)$$

where  $J_{rec}$  is the dark recombination reverse saturation current density. Using the Shockley-Read-Hall formulation of  $J_{rec}$  derived in the next section, we get

$$qV_{oc2} \approx E_g - 2kT \ln \left[ kTf(b) \frac{N_c N_v 2\epsilon_0 \epsilon_s}{q\tau_n \tau_p (V_{bi} - V) N_A J_L} \right]. \quad (2.9)$$

Eqs. (2.8) and (2.9) also predict an increase in  $V_{oc2}$  with increasing  $E_g$ ,  $N_A$ ,  $J_L$ ,  $\tau_n$ , and  $\tau_p$ , and a reduction in  $V_{oc2}$  with increasing  $J_{rec}$ . Hence, the obtainable photovoltage is dependent upon the dominant dark current mechanism, as well as on how the dominant dark current mechanism is influenced by the junction parameters.

The relative influence of  $J_{rec}$  on solar cell  $V_{oc}$  can be demonstrated using a combination of Eqs. (2.6) and (2.8), which gives

$$V_{oc1} - \frac{V_{oc2}}{2} = \frac{kT}{q} \ln \left( \frac{J_{rec}}{J_{dif}} \right). \quad (2.10)$$

In general, the magnitude of  $J_{rec}$  will be many times greater than that of  $J_{dif}$ , i.e., the ratios of  $J_{rec}/J_{dif}$  for Si and GaAs p-n junction solar cells are reported to be  $10^3 - 10^6$  and  $10^8 - 10^{10}$ , respectively (Wolf *et al.*, 1977:419; Meulenber, 1991:39; Ringel *et al.*, 1989:1230). To show the influence of the ratio  $J_{rec}/J_{dif}$  on solar cell  $V_{oc}$ , a GaAs solar cell with  $V_{oc} \approx 1$  V will be used. First, it is noted that the solar cell will always exhibit the smaller of  $V_{oc1}$  or  $V_{oc2}$  calculated using Eqs. (2.6) or (2.8), respectively. Eq. (2.10) predicts that  $V_{oc1} = V_{oc2} = 1$  for the ratio  $J_{rec}/J_{dif} \approx 5 \times 10^8$ . Thus, for  $J_{rec}/J_{dif} > 5 \times 10^8$ ,  $V_{oc2} < V_{oc1}$ , and the open-circuit voltage of the cell will decrease. Further, for the ratios  $J_{rec}/J_{dif} = 10^9$ ,  $10^{10}$  and  $10^{11}$ , Eq. (2.10) predicts values for  $V_{oc2} = 0.96$ ,  $0.85$ , and  $0.73$  V, respectively. This shows that the

maximum obtainable  $V_{oc}$  will be severely reduced by the presence of excessive recombination dark current,  $J_{rec}$ .

As will be shown later, the predicted ratio of  $J_{rec}/J_{dif}$  is proportional to  $\exp(E_g/2kT)$ . Since the bandgap,  $E_g$ , of the  $GaInP_2$  material used in this study is 1.84 eV at room temperature, the ratio of  $J_{rec}/J_{dif}$  for the  $GaInP_2$  p-n junction is expected to be even larger than that for the Si and GaAs p-n junction, with  $E_g \approx 1.1$  and 1.4 eV, respectively. Therefore, dark recombination current is expected to play an even larger role in limiting the value of  $V_{oc}$  in the  $GaInP_2$  p-n junction, relative to Si and GaAs devices.

It is interesting to consider the theoretical AM0 conversion efficiency for solar cells dominated solely by dark diffusion current versus dark recombination current. Figure 5 shows theoretical efficiencies versus bandgap for an ideal p-n homojunction solar cell (Loferski, 1956:777). The top curve is for the case when the dark current is due solely to carrier diffusion, and the bottom curve represents the case when the dark current is comprised entirely of recombination current. As  $E_g$  of the material increases, both  $J_{dif}$  and  $J_{rec}$  decrease exponentially in accordance with the relations  $J_{dif} \propto \exp(-E_g/kT)$  and  $J_{rec} \propto \exp(-E_g/2kT)$  (derived in the next section), which in turn increases  $V_{oc}$  in accordance with Eqs. (2.6) and (2.8). An increase in  $E_g$ , however, results in a reduction in photocurrent since fewer and fewer photons are energetic enough to be absorbed. Therefore, a compromise in  $E_g$  must be made; the optimum value for  $E_g$  occurs at energies of 1.4 - 1.5 eV. A

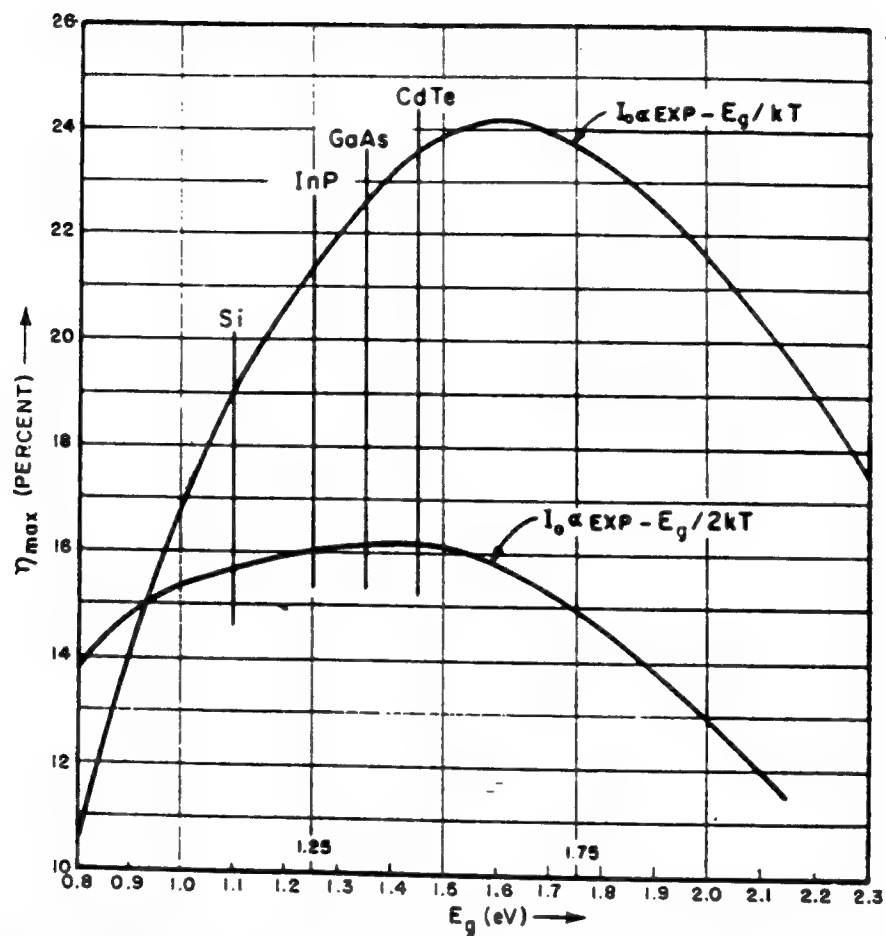


**Figure 5.** Theoretical solar efficiency versus semiconductor band gap for ideal homojunction cells with no surface recombination loss. Curves for two different diode mechanisms are shown: (top)  $A = 1$  for injection dominated current and (bottom)  $A = 2$  for recombination in the depletion layer. [After J. J. Loferski, *J. Appl. Phys.* 27, 777 (1956).]

maximum in the solar conversion efficiency results at these energies are shown in Figure 5. The effect of dark recombination current on conversion efficiency in Figure 5 is dramatic, demonstrating the importance of determining and understanding the factors that control dark recombination current in solar cells.

In general, a very important starting point in the optimization of solar cells is to determine the physical and electrical factors that influence and control junction dark current. As a consequence, a large volume of research has been devoted to the identification and reduction of dark current in various solar cell designs, notably in Si and GaAs solar cells (Wolf *et al.*, 1977:419; Rao *et al.*, 1985:817; DeMoulin *et al.*, 1988:368; DeMoulin *et al.*, 1987:93). However, to date the factors that control dark current conduction in GaInP<sub>2</sub> p-n junction diodes and solar cells have not been examined. In this work, for the first time, a study of the basic dark current mechanisms in both GaInP<sub>2</sub> n<sup>+</sup>p solar cells and test diodes has been undertaken.

### **Basic P-N Junction Current Conduction Models**

In p-n junction diodes, several current transport mechanisms (transport of electrons and holes across the junction) can be present at the same time. Ideally, dark current in p-n junctions is predicted by the diffusion mechanism described by Shockley (Shockley 1949:435). However, in practice a combination of several mechanisms are generally observed. A double exponential current mechanism in Si p-n junctions was first identified by Wolf (Wolf *et al.*, 1977:419) as due to



diffusion and junction space-charge recombination of the Shockley-Read-Hall (SRH) type (Sah *et al.* 1957:1228; Choo, 1968:1069). It was later reported that series and shunt resistances,  $R_s$  and  $R_{sh}$ , respectively, further modify the device current-voltage (I-V) characteristics (Stim 1972:72). An expression that includes these mechanisms is given by

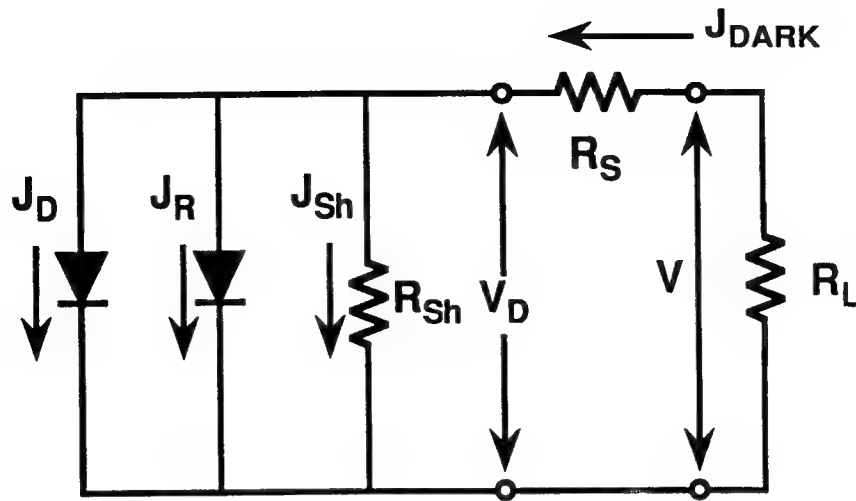
$$J_{Dark} = J_{dif} \left[ \exp\left(\frac{qV_D}{A_1 kT}\right) - 1 \right] + J_{rec} \left[ \exp\left(\frac{qV_D}{A_2 kT}\right) - 1 \right] + \frac{V_D}{R_{sh}}, \quad (2.11)$$

where  $J_{Dark}$  is the total dark current density,  $J_{dif}$  and  $J_{rec}$  are the saturation current densities for diffusion and space-charge layer recombination, respectively,  $A_1$  and  $A_2$  are the diode ideality factors;  $A_1 = 1$  for ideal diffusion and  $A_2 \approx 2$  for recombination via centers located near the center of the bandgap, and the third term accounts for current due to shunting. The diode junction voltage,  $V_D$ , is related to the terminal voltage  $V$ , by

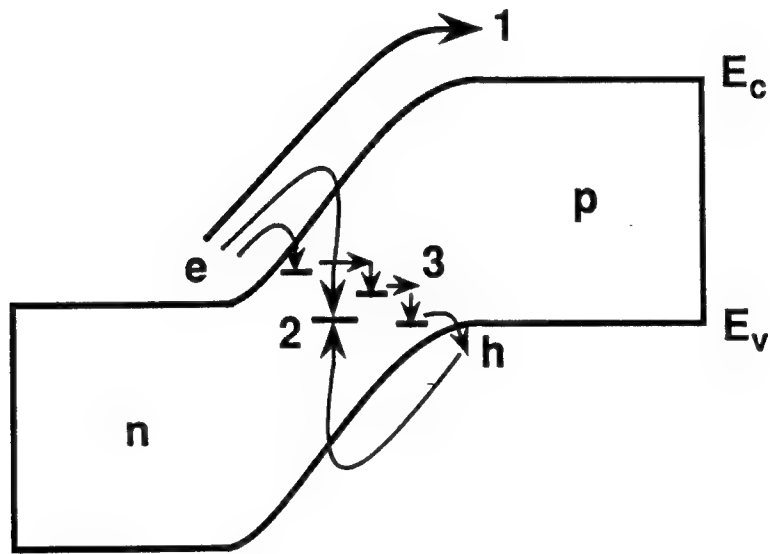
$$V_D = V - I_{Dark} \times R_s, \quad (2.12)$$

according to the equivalent circuit model shown in Figure 6(a). Ideally, the relative magnitude of each mechanism is determined by the semiconductor bandgap, and the doping density and minority carrier lifetimes on each side of the junction.

Investigation of p-n junction I-V curves under certain conditions often indicates the presence of an additional dark current mechanism; current due to tunneling. In fact, the shunting term in Eq. (2.11) can be explained in terms of carrier tunneling and trapping-detrapping (Banerjee and Anderson, 1986:38). Further, as will be



(a)



(b)

Figure 6. (a) Equivalent circuit model for a p-n solar cell, and (b) an energy-band diagram for a p-n junction showing three current transport mechanisms: (1) Carrier diffusion, (2) Carrier recombination via defects in the junction, and (3) Multistep carrier tunneling via defects in the junction.

shown in this work, the shunting current density,  $J_{sh}$ , can sometimes be better described using the expression  $J_{sh} = J_0 \exp(BV)$  in place of  $V_D/R_{sh}$ , where  $J_0$  is the reverse-saturation current density due to tunneling. Current shunting of the form  $J_0 \exp(BV)$  is predicted in p-n heterojunctions, where current is due to carrier tunneling through defect states in the junction (Ribben and Feucht, 1966:1055; Hovel, 1975:54). Dark junction current due to diffusion, recombination, and shunting/tunneling are shown in Figure 6(b) as currents 1, 2, and 3, respectively. These currents will be discussed in turn.

### Diffusion Dark Current - Shockley Diode Theory

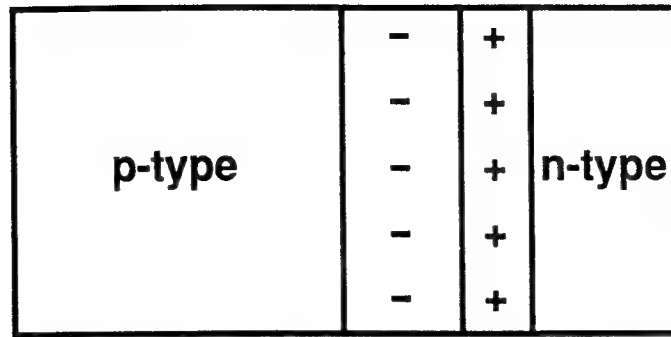
The dark I-V behavior of most solar cells is generally described by the simple Shockley diffusion current expression (Shockley 1949:435)

$$J_D = J_{dif} \left[ \exp\left(\frac{qV}{kT}\right) - 1 \right], \quad (2.13)$$

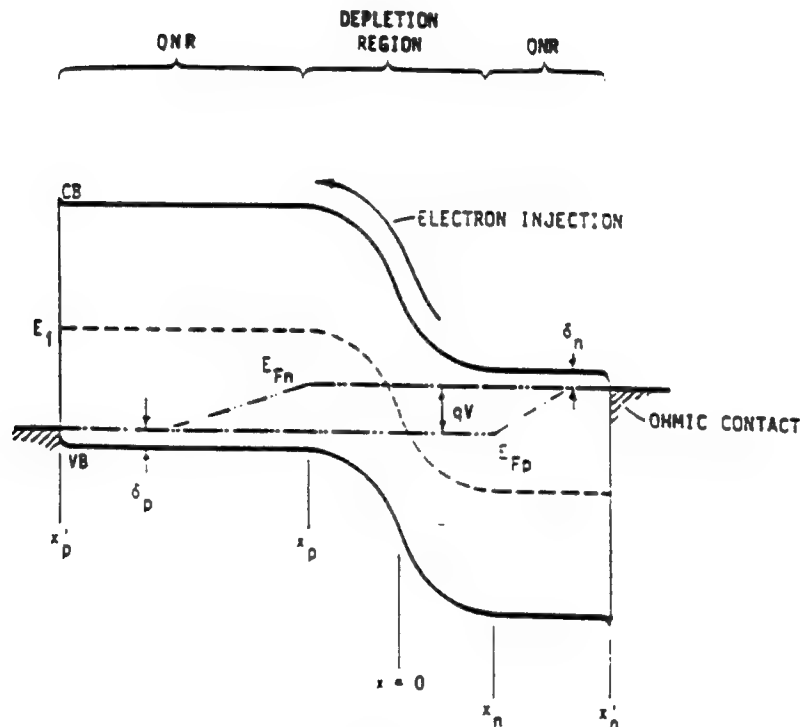
where

$$J_{dif} = q \left[ \frac{n_p D_n}{L_n} + \frac{n_n D_p}{L_p} \right]. \quad (2.14)$$

$J_{dif}$  is referred to as the reverse saturation diffusion current density. Eqs. (2.13) and (2.14) describe current transport via injection of carriers over a p-n homojunction barrier (A homojunction is a junction between n- and p-type layers of the same semiconductor material). This model is based on the forward-biased p-n junction energy-band diagram shown in Figure 7(b). The electrons are injected from the n-type region, where they are majority carriers, across the depletion



(a)



(b)

Figure 7. (a) Schematic of a semiconductor p-n junction, and (b) an energy-band diagram of a forward-biased p-n junction showing Fermi-level splitting.

region and into the p-type quasi-neutral region (QNR), where they become minority carriers. In the p-QNR, the injected electrons recombine with majority carrier holes. The holes required for recombination are supplied by the external circuit through the p-type ohmic contact.

A derivation of Eqs. (2.13) and (2.14) will be instructive. Only the charge carried by electrons is considered, the situation for holes is analogous. In the QNR (the region  $x'_p < x < x_p$ , in Figure 7(b)) the bands are assumed to be almost flat, i.e., a negligible electric field exists, and zero net charge density is assumed. Also, the usual assumptions are made concerning the junction (Sze, 1981:84): (1) the Boltzmann approximation holds; that is, throughout the depletion layer, the Boltzmann relations  $E_F - E_i = kT \ln(n_{no}/n_i)$  and  $E_i - E_F = kT \ln(p_{po}/n_i)$  are valid, where  $n_{no}$  and  $p_{po}$  are the majority equilibrium electron and hole carrier densities, respectively, and  $E_i$  is the intrinsic energy level; (2) the junction is abrupt with well-localized depletion layer edges; (3) there is complete thermal equilibrium across the depletion layer within each band, i.e., the carrier densities at  $x_n$  and  $x_p$  are in thermal equilibrium; and (4) no generation or recombination occurs within the depletion layers. In the case of this last assumption,  $E_{Fn}$  and  $E_{Fp}$  can be assumed to be constant across the depletion layer for forward-bias  $V$ , and  $qV = (E_{Fp} - E_{Fn})$ . The boundary condition at  $x_p$  can be obtained from the np product using the relation  $n_p p_p = n_i^2 \exp(E_{Fn} - E_{Fp})/kT$ . Then using  $p_p \approx p_{po} \approx N_A$ , we get

$$n_p = \left( \frac{n_i^2}{N_A} \right) \exp\left(\frac{qV}{kT}\right) = n_{po} \exp\left(\frac{qV}{kT}\right). \quad (2.15)$$

The electron transport is assumed to be controlled solely by diffusion into the p-type QNR followed by recombination there. The current-voltage relation for the p-n homojunction is calculated using the transport continuity equation (Hovel, 1975:50),

$$D_n \frac{d^2 n_p}{dx^2} + \mu_n E \frac{dn_p}{dx} - (n_p - n_{po}) \frac{1}{\tau_n} G(x) = 0. \quad (2.16)$$

This equation is solved in the p-QNR using the boundary condition given in Eq. (2.15). Considering Figure 7b and taking the boundary condition at  $x'_p$  as  $n_p \rightarrow n_{po}$  as  $x \rightarrow x'_p$ , which can occur if  $|x_p - x'_p| > L_n$ , Eq. (2.16) can be solved to obtain

$$(n_p - n_{po}) = n_{po} \left[ \exp\left(\frac{qV}{kT}\right) - 1 \right] \exp\left[\frac{-(x_p - x)}{\sqrt{D_n \tau_n}}\right] \quad (2.17)$$

( $x$  is taken as positive on the n-type side). Since the carrier transport is controlled by diffusion,

$$J_n(x) = qD_n \frac{dn_p}{dx}, \quad (2.18)$$

giving

$$J_n(x) = \left( qn_{po} \frac{D_n}{L_n} \right) \left[ \exp\left(\frac{qV}{kT}\right) - 1 \right] \exp\left[\frac{-(x_p - x)}{L_n}\right]. \quad (2.19)$$

Since all the current flowing into the n-QNR must pass  $x_p$ , we get

$$J_n = J_n(x_p) = \left( qn_{po} \frac{D_n}{L_n} \right) \left[ \exp\left(\frac{qV}{kT}\right) - 1 \right]. \quad (2.20)$$

A similar expression for  $J_p$  results for hole transport into the n-QNR by diffusion, and the total diffusion current density is given by

$$J_D = J_n + J_p = J_{dif} \left[ \exp\left(\frac{qV}{kT}\right) - 1 \right] \quad (2.21a)$$

$$\text{for } qV \gg kT, \quad J_D \approx J_{dif} \exp\left(\frac{qV}{kT}\right), \quad (2.21b)$$

where

$$J_{dif} = q \left[ \frac{n_p D_n}{L_n} + \frac{n_n D_p}{L_p} \right]. \quad (2.22)$$

Plots of  $n$ ,  $p$ ,  $J_n$ , and  $J_p$  for this model are illustrated in Figure 8 for an  $n^+p$  junction with a bandgap  $\sim 1$  eV. Eq. (2.21) predicts  $J_D \propto \exp(qV/kT) = \exp(qV/A_1 kT)$ , where  $A_1$  is called the diode "ideality" factor. In the case of ideal diffusion,  $A_1$  is equal to 1. Using the relations  $n_p = n_i^2/N_A$ ,  $p_n = n_i^2/N_D$ ,  $n_i^2 = N_c N_v \exp(-E_g/kT)$ , and  $N_c N_v \propto T^3$  (Sze, 1981:18-19), Eqs. (2.21) and (2.22) can be modified to give

$$J_{dif} \propto T^3 \exp\left(\frac{-E_g}{kT}\right), \quad (2.23)$$

and

$$J_D \propto T^3 \exp\left(\frac{-E_g}{kT}\right) \exp\left(\frac{qV}{kT}\right). \quad (2.24)$$

This shows the dependence of  $J_{dif}$  on temperature should be exponential with bandgap,  $E_g$ , and  $J_D$  should increase exponentially with  $V$ . In practice, these dependencies are used to identify current due to diffusion in p-n junctions.

### Recombination Dark Current

The dark I-V behavior of p-n diodes and solar cells can also be significantly affected by a second component of dark current; current due to the recombination

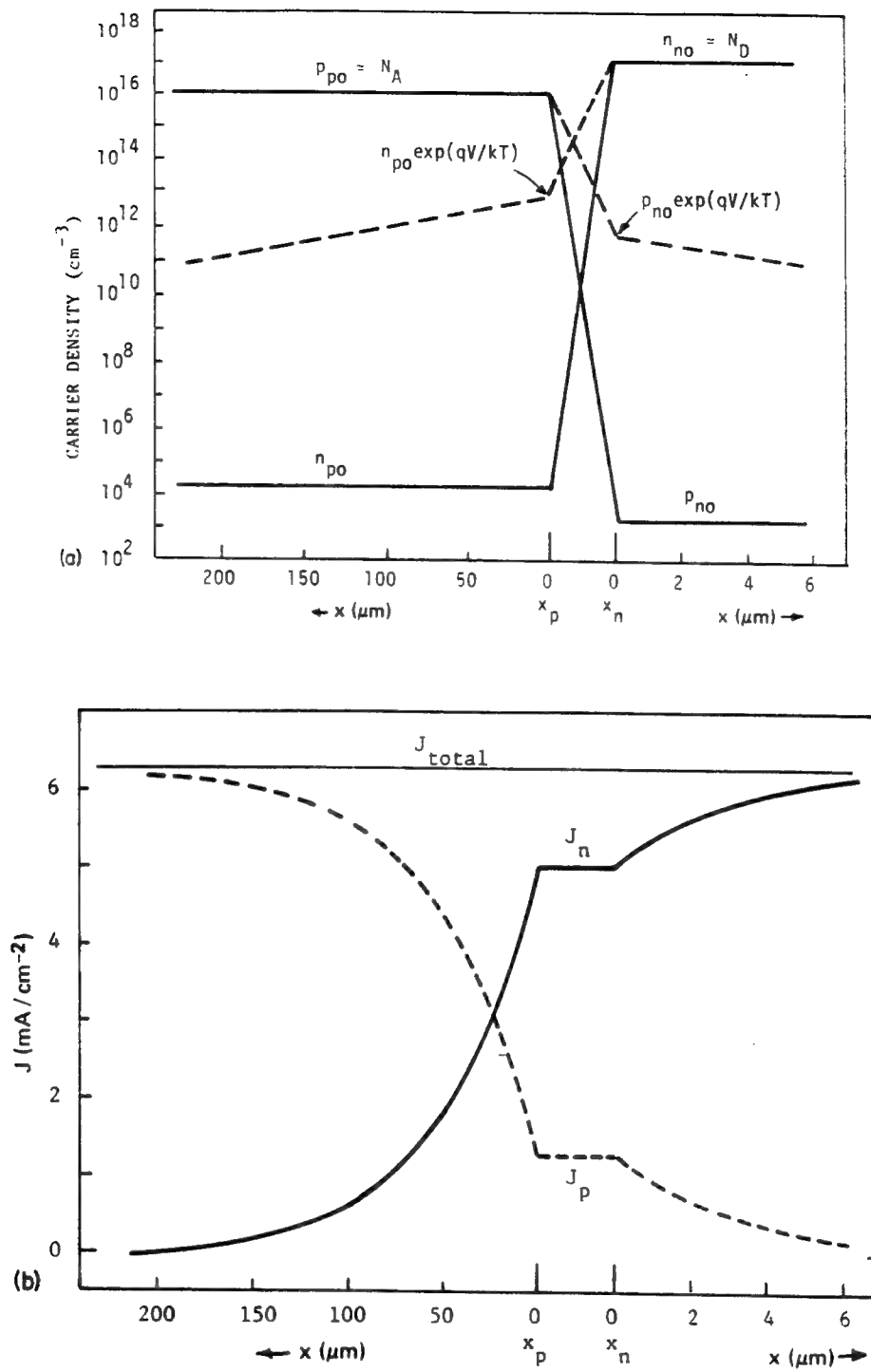


**Figure 8. (a) A plot of  $\log(n)$  and  $\log(p)$  versus distance for a Shockley p-n junction at forward biases of zero and 0.5 V, and (b) current density versus distance for a junction at a forward bias of 0.5 V.**



of carriers via defect centers in the junction. In many solar cells the recombination of carriers within the junction space-charge region cannot be neglected. This is especially true at low forward-bias and in materials with large bandgaps.

Various recombination processes occur in different regions of the solar cell. For example, bulk recombination is important in the base of the cell where nearly all solar absorption occurs. Base recombination limits the cell's photocarrier lifetime and diffusion length, resulting in the reduction of solar cell photocurrent. Recombination of carriers in the interior and at the perimeter of the junction space-charge region is responsible for enhancing the cell's dark current, resulting in the reduction of solar cell  $V_{oc}$ ,  $ff$ , and  $Eff$ .

In the next section, a review of basic concepts and terminology used to describe carrier recombination in semiconductors will be given. The theory of bulk recombination will then be presented, followed by the theory of p-n junction dark current transport due to carrier recombination within the junction space-charge region.

### **Basic Defect Level Terminology**

A defect level is defined as an electronic energy state located within the bandgap of a semiconductor resulting from a perturbation in the local potential of the host lattice (Huggins *et al.*, 1977:391-395). These perturbations are due to the presence of impurities and/or numerous types of structural defects within the crystal. A defect level can be classified as either a "shallow" or "deep" level. In

the case of a shallow level, the ionization energy can be approximately described using the hydrogenic model, where the defect is assumed to bind an extra charge in the same way that the nucleus of the hydrogen atom holds its single electron. These levels are typically related to substitutional impurities which have either a single excess (donor) or deficient (acceptor) valence electron structure relative to the atom replaced in the host material. Thus, a donor level can be defined as a level that becomes more positively charged when ionized (gives up an electron), and an acceptor level becomes more negatively charged when ionized (accepts an electron).

In the case of a deep level, the binding energies are greater than that described by the hydrogenic model. This definition also includes donors and acceptors that are near the valence and conduction band edges, respectively. It is interesting to note that the large ionization energy of deep levels suggests the presence of a strong potential that acts to localized the carrier wavefunction near the defect site.

Localization of the wavefunction in real space implies delocalization in k-space because more Fourier components are required to describe the smaller orbit (Huggins *et al.*, 1977:393). Consequently, deep levels tend to be nonradiative recombination centers because the wavefunction's large extent in k-space allows the defect to couple to a large variety of momentum vectors (or phonons) required to assist in nonradiative recombination.

The study of defects in semiconductors is sometimes confused by the many names used in their description. Common names for defect levels include traps, recombination centers, deep states, and deep impurities. Although these terms have precise meanings, a particular level can be a trap and/or a recombination center depending on variables such as the defect location, doping density, and temperature.

Traps and recombination centers can be expressed in terms of their carrier capture and thermal emission rates. The capture rate description is applicable to defects located in neutral (undepleted) material, and the emission rate description is applicable to defects located within the depleted space-charge region of a p-n junction.

The case of a neutral semiconductor is considered first. We can define a hole trap as a defect level in which the hole capture rate,  $c_p$ , is much larger than the electron capture rate,  $c_n$ , as shown in Figure 9(a). The opposite is true for an electron trap. A recombination center can be defined as a level in which both  $c_n$  and  $c_p$  are large, and  $c_n \sim c_p$ . This scenario is also shown in Figure 9(a). The electron and hole capture rates can be expressed by the respective expressions

$$c_n = \sigma_n v_{th} n \text{ and } c_p = \sigma_p v_{th} p, \quad (2.25)$$

where  $\sigma_n$  and  $\sigma_p$  are the capture cross sections for capturing electrons and holes, respectively, and  $v_{th}$  is the average thermal velocity of the carriers. From Eq.(2.25), it is clear that for a given defect level with fixed  $\sigma_n$  and  $\sigma_p$ , the defect

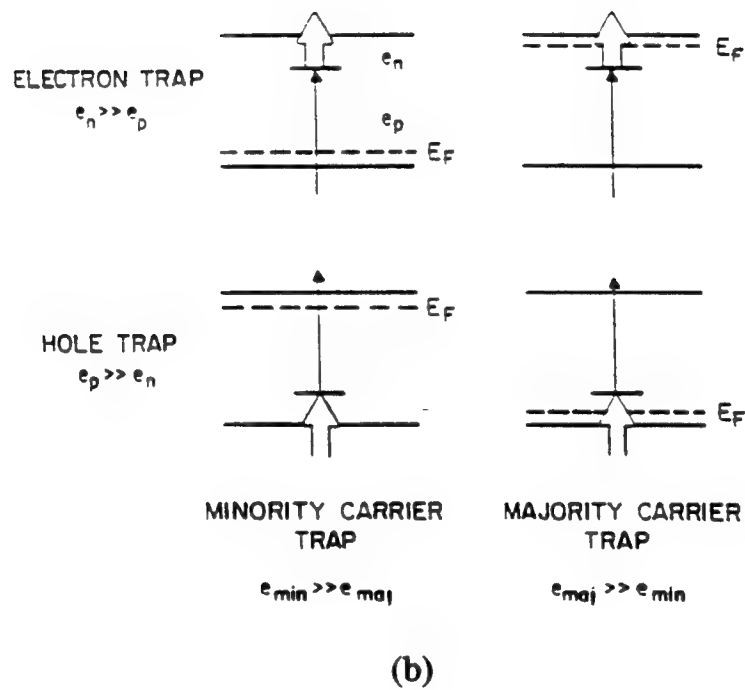
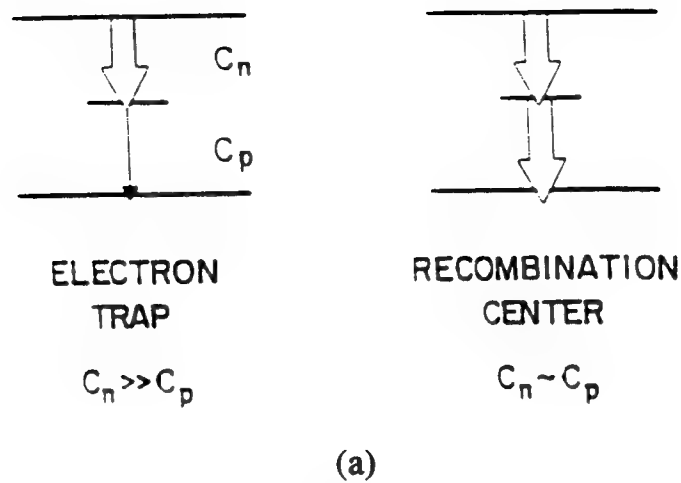


Figure 9. (a) Definition of the terms "electron trap" and "recombination center" by means of the relative magnitudes of the capture cross sections  $\sigma_n$  and  $\sigma_p$ , indicated by the widths of the arrows, and (b) the definition of the terms "majority carrier trap" and "minority carrier trap", and "electron trap" and "hole trap".

will be either a trap or recombination level (center) depending on the density of free carriers,  $n$  and  $p$ .

In the case of a defect level located within a p-n junction's space charge region,  $c_n$  and  $c_p$  are negligible because  $n$  and  $p \approx 0$ , and the traps and recombination centers must be considered in terms of their electron and hole emission lifetimes,  $e_n$  and  $e_p$ , respectively. Strictly speaking, defects within a p-n junction under zero or reverse-bias should be considered as traps because there are essentially no free carriers available for recombination. However, under forward-bias conditions, deep levels having  $c_n \sim c_p$  can capture electrons and holes injected across the junction. As will be discussed, this phenomena results in the transport of dark recombination current through the junction.

Further terminology found in the literature used to describe traps includes electron trap, hole trap, majority carrier trap, and minority carrier trap. Figure 9(b) illustrates the definition of an electron trap in terms of emission rates, where  $e_n \gg e_p$ , and a hole trap, where  $e_p \gg e_n$ . Further, a hole trap in p-material and an electron trap in n-material are defined as majority carrier traps, whereas a hole trap in n-material and an electron trap in p-material are minority carrier traps.

It will be instructive to review the basic theory of carrier emission rates for later use in understanding reverse-bias current transport in p-n junctions and deep level transient spectroscopy measurements. It is well known that carrier thermal emission rates are proportional to the Boltzmann factor  $\exp(-E_A/kT)$  (Huggins *et*

*al.*, 1977:395), where  $E_a$  is the energy difference between the deep level and the band edge to which the carrier is emitted. An expression for the hole emission rate is given by

$$e_p = A_p \exp\left(\frac{-E_a}{kT}\right), \quad (2.26)$$

where  $A_p$  is a factor related to the defect, and  $E_a = E_t - E_v$ . The principal of detailed balance is used to determine  $A_p$ , which states that the carrier capture and emission for each electron state must be equal at equilibrium (Huggins *et al.*, 1977:395). This gives

$$c_p(P) = e_p(1 - P), \quad (2.27)$$

where  $P$  is the probability that the level is occupied by an electron. The free hole density,  $p$ , in the valance band is given by

$$p = N_v \exp\left[\frac{-(E_F - E_v)}{kT}\right], \quad (2.28)$$

where  $N_v$  is the effective density of states at the valance band edge given by

$$N_v = 2M_v \left(\frac{2\pi m^* kT}{h^2}\right)^{\frac{3}{2}}. \quad (2.29)$$

Equations (2.25) - (2.28) can be combined to give an expression for the hole emission rate,

$$e_p = \sigma_p v_{th} N_v g^{-1} \exp\left(\frac{-E_a}{kT}\right), \quad (2.30)$$

where  $g$  is the degeneracy of the level. An analogous expression can be derived for the electron emission rate. Two important observations can be made considering Eq.(2.30) and the analogous expression for the electron emission rate.

First, efficient generation centers will tend to lie in the middle of the bandgap, where  $e_n \sim e_p$ , and secondly, hole traps will tend to lie in the lower half of the band gap and electron traps in the upper half.

As will be shown, efficient recombination centers also tend to lie in the middle of the bandgap. Eq.(2.30) will be used later in conjunction with deep level transient spectroscopy (DLTS) measurements to determine the energy level of dominant deep levels located within the  $\text{GaInP}_2$   $n^+p$  junction.

As eluded to, generation centers responsible for reverse-bias current transport in p-n junctions must be described in terms of emissions rates. Capture processes are not important because  $n$  and  $p$  are negligible within the space-charge region in accordance with Eq.(2.25). In this case, only electron and hole emission processes occur. When  $e_n \sim e_p$ , electrons and hole are continually emitted through defect centers, and a steady state reverse-current results across the junction. The rate of electron-hole pair generation under these conditions will be derived in a later section.

### **Bulk Recombination: Shockley-Read-Hall Theory**

A simple model to calculate the recombination rate was first proposed by Shockley and Read and independently by Hall, known as the Shockley-Read-Hall (SRH) recombination theory (Shockley and Read 1952:835; Hall, 1952:387). The basic assumption of this model is that the defect levels in the bandgap are generally populated by majority carriers, and recombination mainly depends on the capture

of minority carriers. A schematic diagram of recombination processes is shown in Figure 10. These processes include electron capture, electron emission, hole capture, and hole emission. The rate equations used to describe these processes are as follows (Muller and Kamis, 1977:152)

$$\text{electron capture rate: } c_n = nN_t \{1 - f(E_t)\} v_{th} \sigma_n \quad (2.31)$$

$$\text{electron emission rate: } e_n = N_t f(E_t) \alpha_n \quad (2.32)$$

$$\text{hole capture rate: } c_p = pN_t f(E_t) v_{th} \sigma_p \quad (2.33)$$

$$\text{hole emission rate: } e_p = N_t \{1 - f(E_t)\} \alpha_p \quad (2.34)$$

where  $N_t$  and  $E_t$  are the density and energy of the recombination level, respectively,  $f(E_t)$  is the Fermi-Dirac distribution function evaluated at  $E_t$ , which is equal to the probability that the level is occupied by an electron,  $\alpha_n$  and  $\alpha_p$  are the probability of electron and hole emission, respectively, and the other terms have their usual meanings. Under thermal equilibrium,

$$f(E_t) = \left[ 1 + \exp\left(\frac{E_t - E_f}{kT}\right) \right]^{-1} \quad (2.35)$$

$$\alpha_n = v_{th} \sigma_n n_i \exp\left(\frac{E_t - E_i}{kT}\right) \quad (2.36)$$

and

$$\alpha_p = v_{th} \sigma_p n_i \exp\left(\frac{E_t - E_i}{kT}\right), \quad (2.37)$$

where  $E_f$  and  $E_i$  are the Fermi- and intrinsic Fermi-levels, respectively. Equations (2.36) and (2.37) indicate that the probability of electron and hole emission is



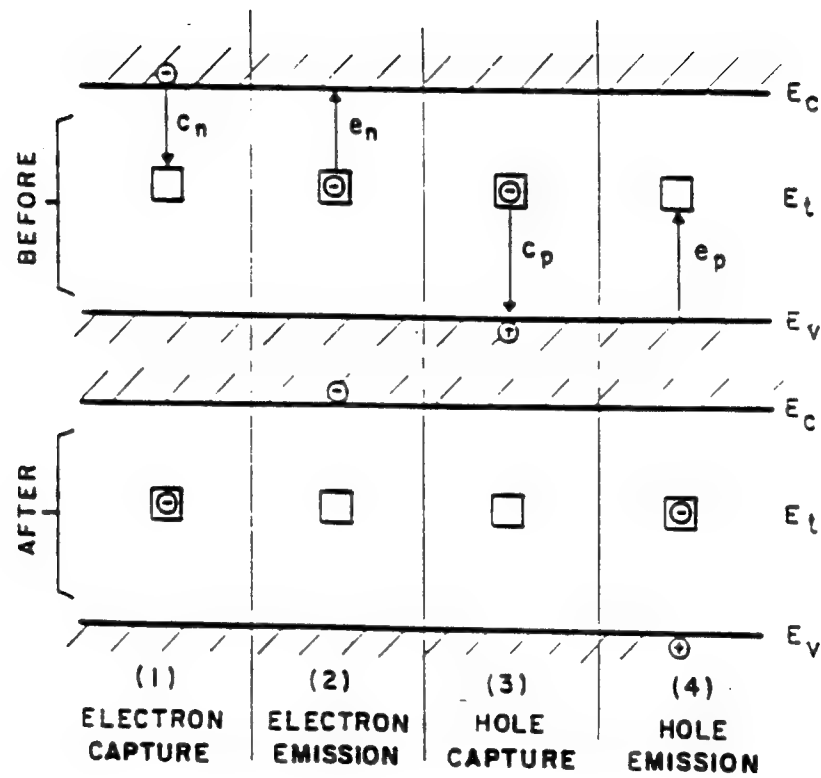


Figure 10. A schematic diagram of indirect generation-recombination processes at thermal equilibrium.

higher when the defect level is closer to the conduction and valence band edge, respectively.

The carrier recombination rate,  $U$ , can be expressed using the capture and emission rates in Eqs. (2.31) - (2.34), giving

$$U = -\frac{dn}{dt} = -\frac{dp}{dt} = c_n - e_n = c_p - e_p. \quad (2.38)$$

Substituting Eqs. (2.31) - (2.37) into Eq. (2.38) gives

$$U = \frac{(pn - n_i^2) N_t v_{th} \sigma_n \sigma_p}{\sigma_p \left[ p + n_i \exp\left(\frac{E_i - E_t}{kT}\right) \right] + \sigma_n \left[ n + n_i \exp\left(\frac{E_t - E_i}{kT}\right) \right]} \quad (2.39)$$

or

$$U = \frac{pn - n_i^2}{\tau_p \left[ p + n_i \exp\left(\frac{E_i - E_t}{kT}\right) \right] + \tau_n \left[ n + n_i \exp\left(\frac{E_t - E_i}{kT}\right) \right]}, \quad (2.40)$$

where

$$\tau_n = (N_t v_{th} \sigma_n)^{-1} \quad (2.41)$$

and

$$\tau_p = (N_t v_{th} \sigma_p)^{-1} \quad (2.42)$$

The terms  $\tau_n$  and  $\tau_p$  are the electron and hole recombination lifetime, respectively.

According to Eq. (2.40), the rate of maximum recombination will occur when  $E_t \sim E_i$ . The rate will drop rapidly as  $E_t$  differs appreciable from  $E_i$ .

It is clear from Eq. (2.40) that  $U$  will depend upon the location, density, and carrier capture cross sections of the levels within the junction. The influence of the

position of a single deep level on carrier lifetime,  $\tau$ , can be determined using an additional result of SRH statistics (Shockley and Read, 1952:835; Hall, 1952:600)

$$\tau = \frac{c_p(p + p_1) + c_n(n + n_1)}{c_n c_p N_t (n + p)}, \quad (2.43)$$

The terms  $n$  and  $p$  are the concentrations of conduction band electrons and valence band holes at equilibrium, respectively,  $n_1$  and  $p_1$  are the concentrations of conduction band electrons and valence band holes, respectively, when  $E_F$  is at  $E_t$ . Considering a p-type semiconductor ( $E_F < E_i$ ) with a defect level located below the Fermi-level ( $E_t < E_F$ ), it follows that  $p_1 \gg p \gg n \gg n_1$ , and Eq. (2.43) reduces to

$$\tau = \frac{p_1}{N_t c_n p}. \quad (2.44)$$

Then the influence of the defect level position,  $E_t$ , on  $\tau$  can be examined by considering two different defect levels at energies  $E_t(1)$  and  $E_t(2)$ , with  $E_t(1) > E_t(2)$ . For the case of constant doping density  $p$  and denoting  $\tau(1)$  and  $\tau(2)$  as the lifetime of the centers at  $E_t(1)$  and  $E_t(2)$ , respectively, Eq. (2.44) can be used to express the ratio of the lifetimes as

$$\frac{\tau(2)}{\tau(1)} = \frac{N_t(1)c_n(1)}{N_t(2)c_n(2)} \exp\left[\frac{E_t(1) - E_t(2)}{kT}\right]. \quad (2.45)$$

Then considering the case when  $c_n(1) \sim c_n(2)$ , i.e.,  $\sigma_n(1) \sim \sigma_n(2)$  in Eq.(2.25), the ratio of  $\tau(2)/\tau(1)$  will always be much larger than unity as long as  $p_1(2)N_t(1) \gg p_1(1)N_t(2)$ . Thus, from Eq.(2.45) we see that an energy difference of  $E_t(1) - E_t(2) = 0.40$  eV is sufficient for  $\tau$  of the free holes in the valance band to be determined by the deeper level, even if the concentration of the shallow level is 6 orders of

magnitude larger than the deeper level! The consequence of this result will be very important to the analysis of recombination current in GaInP<sub>2</sub> n<sup>+</sup>p junctions examined in this work, where two recombination centers with an energy difference of ~ 0.4 eV were found.

## **P-N Junction Bulk Recombination Current**

### **General Theory**

The principles of recombination discussed in the previous section also apply to the recombination of carriers in the space-charge-layer (SCL) of a p-n junction. The recombination of electrons and holes via defect centers within the SCL results in the flow of current from the p- to n-side of the p-n junction. This current is called the junction dark recombination current. An approximate treatment of the recombination/generation transport mechanism within the SCL is based on the assumption that the quasi-Fermi levels are constant there, an assumption which has been shown to be valid in the forward-bias case (Sah *et al.*, 1957:1228). Examination of the SRH recombination expression in Eq.(2.40) shows that the maximum recombination rate occurs when the intrinsic level,  $E_i$ , lies approximately halfway between the electron and hole level quasi-Fermi levels,  $E_{Fn}$  and  $E_{Fp}$ , respectively. This situation is shown at  $x = 0$  in Figure 7(b). The rate drops drastically as the intrinsic levels differ appreciably from  $(E_{Fn} + E_{Fp})/2$ , and thus the major recombination occurs for a small portion of the SCL width under forward-

bias. If we assume that the recombination center level lies at  $E_i$  and  $\tau_n = \tau_p$ , then from Eq.(2.40) and the relations  $n = n_i \exp[(E_{Fn} - E_i)/kT]$  and  $p = n_i \exp[(E_i - E_{Fp})/kT]$ , we get

$$U_{\max} \approx \frac{n_i}{2\tau_n} \left\{ \exp\left(\frac{qV}{2kT}\right) - 1 \right\}. \quad (2.46)$$

The recombination rate falls off exponentially on either side of the maximum with a characteristic length  $kT/qE$ , where  $E$  is the junction field given by  $E = 2(V_{bi} - V)W_d$ . Therefore, the effective thickness of the recombination region can be taken as approximately

$$\frac{2kT}{qE} = kT \frac{W_d}{q(V_{bi} - V)}. \quad (2.47)$$

This result predicts that the junction current density due to carrier recombination in the SCL can be approximately given by

$$J_R = q \int_{x_p}^{x_n} U_{\max} dx \cong \frac{n_i W_d kT}{2(V_{bi} - V) \tau_n} \left[ \exp\left(\frac{qV}{2kT}\right) - 1 \right]. \quad (2.48)$$

This model predicts that the forward current will increase with voltage as  $J_R \propto \exp(qV/A_2 kT)$ , where the diode ideality factor  $A_2$  equals 2. This approximation for  $J_R$  is fairly good for forward bias, although the more exact result that follows predicts that the value of  $A_2$  can deviate from 2 depending on the nature of the recombination centers.

Under reverse-bias, Eq. (2.40) predicts that the generation of carriers through the centers will occur with a maximum rate of

$$U_{\max} = \frac{-n_i}{\tau_n + \tau_p}. \quad (2.49)$$

In contrast to the forward-bias case, where the width of the region of maximum recombination in the junction is small compared to  $W_d$ , and changes little with bias, the width of the region responsible for carrier generation under reverse bias nearly equals  $W_d$ , and increases with increasing reverse-bias. The resulting current density is

$$J_G \approx \frac{-qW_d n_i}{\tau_n + \tau_p}. \quad (2.50)$$

Since  $W_d$  increases approximately as  $(V_{bi} + V)^{1/2}$ ,  $J_G$  increases slowly with increasing reverse-bias. Although the electron and hole quasi-Fermi levels are not constant across the depletion layer under appreciable reverse-bias (Fahrenbruch and Bube, 1983:120), this has little effect on the reverse current since  $U$  rapidly saturates to the value given by Eq. (2.49), for the condition  $E_{Fp} > E_i > E_{Fn}$ .

### Sah-Noyce-Shockley Theory

The problem of SCL recombination was attacked more carefully, first by Sah, Noyce, and Shockley (SNS) for the symmetrical homojunction (Sah *et al.*, 1957), and later by Choo for asymmetrical junctions (Choo, 1968). The treatment of Sah, Noyce and Shockley first determined that the positions of  $E_{Fn}$  and  $E_{Fp}$  are almost constant throughout the depletion layer of a symmetrical homojunction, and then used the SRH formulation to obtain an expression for  $U(x,V)$  within the depletion layer. They integrated  $U(x,V)$  across the junction to obtain the total current. The result cannot be obtained in closed form, but under moderate forward-bias, the recombination current density,  $J_R$ , is given by

$$J_R = J_{rec} 2 \sinh\left(\frac{qV}{2kT}\right), \quad (2.51)$$

where

$$J_{rec} = \frac{n_i W_d f(b)}{\sqrt{\tau_n \tau_p} \left( \frac{V_{bi} - V}{kT} \right)}, \quad (2.52)$$

and

$$f(b) = \int_{z_1}^{z_2} \frac{dz}{z^2 + 2bz + 1}, \quad (2.53)$$

$$b = \exp\left(-\frac{qV}{kT}\right) \cosh\left[\left(\frac{E_i - E_i}{kT}\right) + \frac{1}{2} \ln\left(\frac{\tau_p}{\tau_n}\right)\right], \quad (2.54)$$

$$z_1 = \sqrt{\frac{\tau_n}{\tau_p}} \exp\left[-\frac{qV_{bi} - E_{Fn} + E_{Fp}}{2kT}\right], \quad (2.55)$$

and

$$z_2 = \sqrt{\frac{\tau_n}{\tau_p}} \exp\left[\frac{qV_{bi} - E_{Fn} + E_{Fp}}{2kT}\right]. \quad (2.56)$$

Using  $n_i = (N_c N_v)^{1/2} \exp(-E_g/2kT)$ , Eqs. (2.51) and (2.52) give

$$J_{rec} \propto T^{\frac{5}{2}} \exp\left(-\frac{E_g}{2kT}\right), \quad (2.57)$$

and for  $qV \gg kT$

$$J_R \propto T^{\frac{5}{2}} \exp\left(-\frac{E_g}{2kT}\right) \exp\left(\frac{qV}{A_2 kT}\right). \quad (2.58)$$

Thus, the temperature dependence of  $J_{rec}$  due to recombination should be exponential with one-half the bandgap,  $E_g$ , and the voltage dependence of  $J_R$  should be exponential with  $V/A_2$ , where in the ideal case,  $A_2$  equals 2. In practice,

these dependences are used to identify current due to carrier recombination in p-n junctions.

For symmetrical junctions and  $V$  at least several  $kT$  less than  $V_{bi}$ , the integration limits  $z_1$  and  $z_2$  can be extended to zero and  $\infty$ , respectively, with a small error. The function  $f(b)$  is plotted in Figure 11(a), and approaches to  $\pi/2$  for small values of  $b$  (i.e., large  $V$ ). Thus, the function  $f(b)$  will increase slightly with increasing  $V$ , and the resulting recombination current will increase slightly faster than  $\exp(qV/2kT)$ . Hence, the apparent value of  $A_2$  will be less than 2. However, reported values for  $A_2$  in Si and GaAs junctions are occasionally greater than two (Wolf *et al.* 1977:419). One mechanism has been proposed that allows for  $2 < A_2 < 4$ , which involves carrier recombination through surface channels (Sah, 1962:94). Further, as will be shown in this work, a cause of unusually high  $A_2$  values can be due to the presence of ohmic shunting and carrier tunneling within the junction.

Under reverse-bias conditions, the concentration of free carriers  $n$  and  $p$  in the junction SCL is negligible, and Eq (2.40) becomes  $U = -n_i/\tau_g$ , where  $\tau_g$  is given by

$$\tau_g = \tau_p \exp\left(\frac{E_t - E_i}{kT}\right) + \tau_n \exp\left(-\frac{E_t - E_i}{kT}\right). \quad (2.59)$$

The reverse current density due to the generation of carriers within the SCL then becomes

$$J_R = q \int U dx = \frac{qn_i W_d}{\tau_g} \quad (2.60)$$



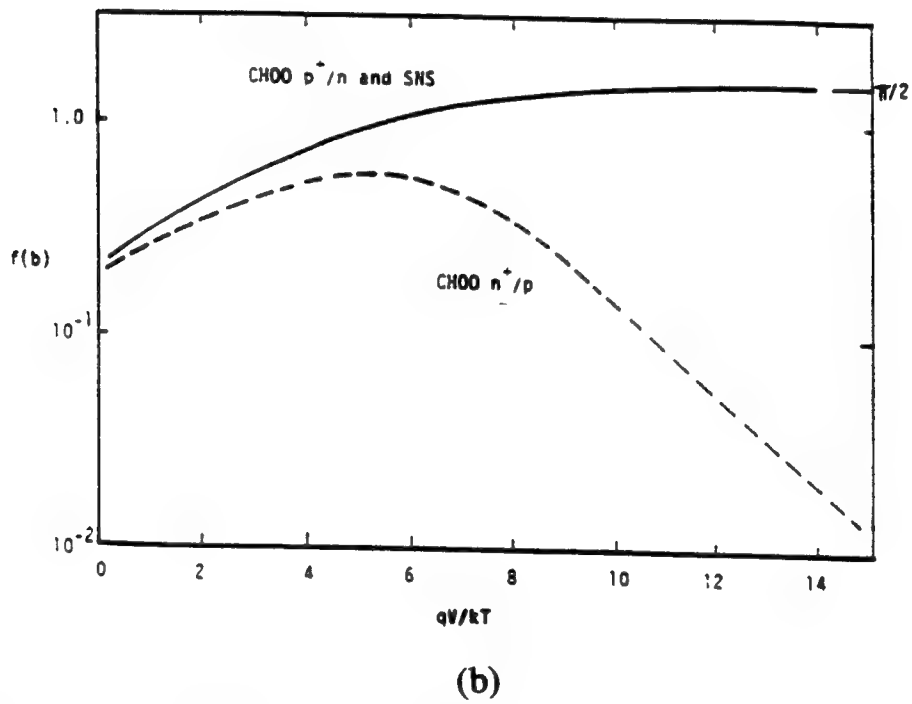
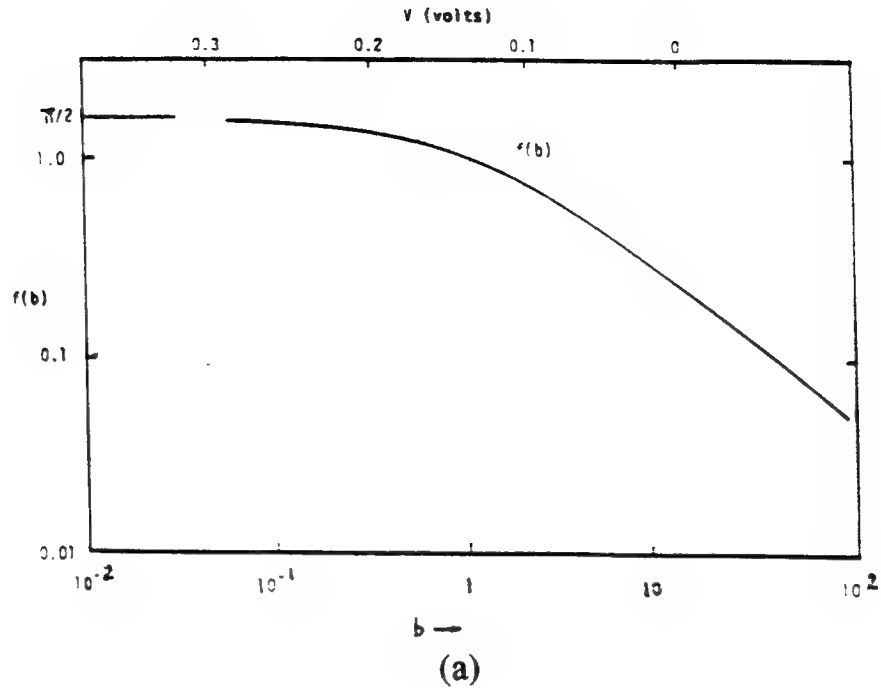


Figure 11. (a) The function  $f(b)$  versus  $b$  (Sah *et al.*, 1957). (b) The function  $f(b)$  versus normalized bias voltage according to Choo and Sah, Noyce, and Shockley (Sah *et al.*, 1957; Choo, 1968).

A combination of Eq.(2.59) and (2.60) results in

$$J_R \propto W_d \exp\left(-\frac{E_a}{kT}\right), \quad (2.61)$$

where

$$E_a = E_c - E_i \text{ for } E_i > E_t, \quad (2.62)$$

and

$$E_a = E_t - E_v \text{ for } E_i < E_t. \quad (2.63)$$

Thus, the temperature dependence of  $J_R$  should be exponential with  $E_a$ . In practice, Eq. (2.61) can be used to measure the energy level of dominant generation-recombination centers within the junction's SCL.

### Choo's Extension

Choo extended the SNS theory to junctions that are asymmetrically doped, and in which  $\tau_n$  and  $\tau_p$  are allowed to vary more widely. These junctions had a uniform distribution of recombination centers of a single energy throughout the depletion layer with properties similar to those in the bulk QNRs. In particular, Choo used a more accurate expression for the limits of the integrand determining  $f(b)$ , making  $f(b)$  a function of doping density  $N_A$  and  $N_D$  as well. Choo found that when donor-like centers were active in an  $n^+p$  junction, the asymmetry produced an increasingly large reduction in  $f(b)$  for high forward-bias, as shown in Figure 11(b). The amount of this reduction is greater when the ratio of  $\tau_p/\tau_n$  is large. For acceptor-like centers in an  $n^+p$  junction the effect is almost negligible. The opposite result holds for  $p^+n$  junctions. The result of the asymmetry dependence is to reduce

the generation/recombination currents for increasing forward-bias even to the point of causing saturation for the case of low bulk carrier concentration.

Although the SNS and Choo theories are successful in predicting the form of I-V characteristics in p-n junctions due to recombination, the recombination currents in real diodes are usually much larger, particularly for junctions involving materials with bandgaps larger than Si (Fahrenbruch and Bube, 1983:122). Although the Choo theory predicts currents that are even smaller than those predicted by SNS theory, the Choo model does provide a mechanism that predicts values of  $A_2$  equal to or larger than 2. The negative slope of  $f(b)$  with voltage shown in Figure 11(b) will result in a slower increase in current with voltage, and an apparent increase in  $A_2 > 2$  can result.

### **P-N Junction Perimeter Recombination Current**

It has been found that the " $A_2 = 2$ " current in many junctions, particularly those with small areas, is controlled by interface and surface recombination at the periphery of the junction plane. Stringfellow (1976) found that the recombination current in GaAsP and GaP heterojunction LEDs was directly related to the area-to-perimeter ratio, and that it could be reduced temporarily by  $CF_4$  plasma etching. Although Sah *et al.* (1957) found negligible perimeter current in Si p-n junctions used to substantiate their theory, later work by Sah (1962) showed that perimeter current in Si p-n diodes could be substantial unless the proper surface oxide was present. Henery *et al.* (1978) used luminescence techniques to show that the

$A_2 = 2$  current in AlGaAs p-n heterojunctions is due to surface recombination at the junction perimeter. He proposed a mechanism explaining the  $A_2 = 2$  perimeter current as due to a nearly constant ratio of electron,  $n$ , and hole,  $p$ , densities that is required to maintain charge neutrality at the p-n junction perimeter in the presence of Fermi-level pinning. This model predicts a recombination rate

$$U \propto \sqrt{np} = n_i \exp\left(\frac{qV}{2kT}\right), \quad (2.64)$$

showing the  $A_2 = 2$  current dependence on voltage. The result is that the magnitude of  $A \sim 2$  current density is found to increase with increasing junction perimeter-to-area ratio in the presence of perimeter recombination current.

### Tunneling Dark Current

A third type of dark current that can exist in p-n junctions is tunneling current due to electrons or holes tunneling from the conduction or valence band into energy states within the bandgap, followed by either tunneling the remainder of the way into the opposite band or by a tunneling-recombination mechanism (the current marked 3 in Figure 6(b)). Assuming a parabolic barrier and uniform electric field  $E$ , the direct band-to-band tunneling current is given by (Sze, 1982:98)

$$J_{tun} = \frac{\sqrt{2m^*} q^3 E V}{4\pi^2 \hbar^2 \sqrt{E_g}} \exp\left(\frac{-4\sqrt{2m^*} E_g^{\frac{3}{2}}}{3qE\hbar}\right). \quad (2.65)$$

It is clear from Eq. (2.65) that band-to-band tunneling is only slightly sensitive to temperature through the variation in bandgap,  $E_g$ . Also, this tunneling current is

expected to increase linearly with voltage. In most Si, GaAs, and AlGaAs/GaAs solar cells, only the injection and tunneling dark currents are usually important at room temperature under moderate forward-bias. However, tunneling dark current becomes increasingly important in heterojunctions, Schottky barriers, heavily doped p-n junctions, and in p-n junctions containing a high concentration of junction defects (Hovel, 1975:54). Also, because the tunneling of carriers is relatively insensitive to temperature, and current due to diffusion and recombination drop off exponentially with temperature, tunneling currents tend to dominate at low temperatures (Sze, 1982:98). Electron and hole tunneling can also explain the current shunting behavior of  $R_{sh}$  in Eq. (2.11). A mechanism responsible for  $R_{sh}$  in Si p-n junction solar cells has been identified as a combination of multistep tunneling and thermal trapping-detrapping of carriers through defect states in the space-charge region (Banerjee and Anderson, 1986:38). The origin of  $R_{sh}$  has previously been reported as due to local damage in the junction (Stirn, 1972:72), or leakage at the periphery (Hovel, 1975:53). The resulting shunt resistance is temperature dependent, and an expression for the finite SCL conductivity giving rise to  $R_{sh}$  is given as (Banerjee and Anderson, 1986:39)

$$\Delta\sigma(T) = q\mu n_0 \exp\left[-rv \exp\left(-\frac{E}{kT}\right)\right], \quad (2.66)$$

where  $\mu$  is the mobility of the carriers,  $n_0$  is the number of carriers initially present in a trap state,  $v$  is the attempt-to-escape frequency,  $E$  is the energy of the state,

and  $t$  is the time. It is obvious from Eq. (2.66) that  $R_{sh}$  becomes temperature dependent above some temperature threshold determined by  $E$ .

### Total P-N Junction Dark Current

To understand the relative influence of diffusion, recombination, and shunting dark currents on the total current in typical Si and GaAs p-n junction solar cells,  $J_{Dark}$  in Eq. (2.11) is plotted in Figures 12 - 16 for various combinations of  $J_{dif}$ ,  $J_{rec}$ , and  $R_{sh}$ . Values of  $J_{dif}$  reported for high-quality Si and GaAs p-n solar cells are typically  $\sim 10^{-12} - 10^{-8}$  and  $10^{-19} - 10^{-18}$  A/cm<sup>2</sup>, respectively (Wolf *et al.*, 1977; DeMoulin *et al.*, 1988). Values reported for  $J_{rec}$  are  $\sim 10^{-7} - 10^{-6}$  and  $10^{-11} - 10^{-10}$  A/cm<sup>2</sup> for Si and GaAs, respectively.

Figures 12 and 13 shows the influence of  $J_{rec}$  on  $J_{Dark}$  for constant  $J_{dif}$  in Si and GaAs p-n junctions, respectively. In all cases, recombination current becomes increasingly important relative to diffusion current at small bias voltages, where from Eqs. (2.24) and (2.58) the ratio of  $J_R/J_D \propto \exp(-qV/2kT)$ . The maximum power-point voltage of high-quality Si and GaAs solar cells under illumination is typically 0.55 - 0.60 and 0.75 - 0.80, respectively (Fahrenbruch and Bube, 1983). Thus, we see from Figure 12 that diffusion current will generally dominate at the maximum power-point voltage in Si cells, whereas from Figure 13, recombination current is seen to dominate in GaAs solar cells at the maximum power-point voltage.

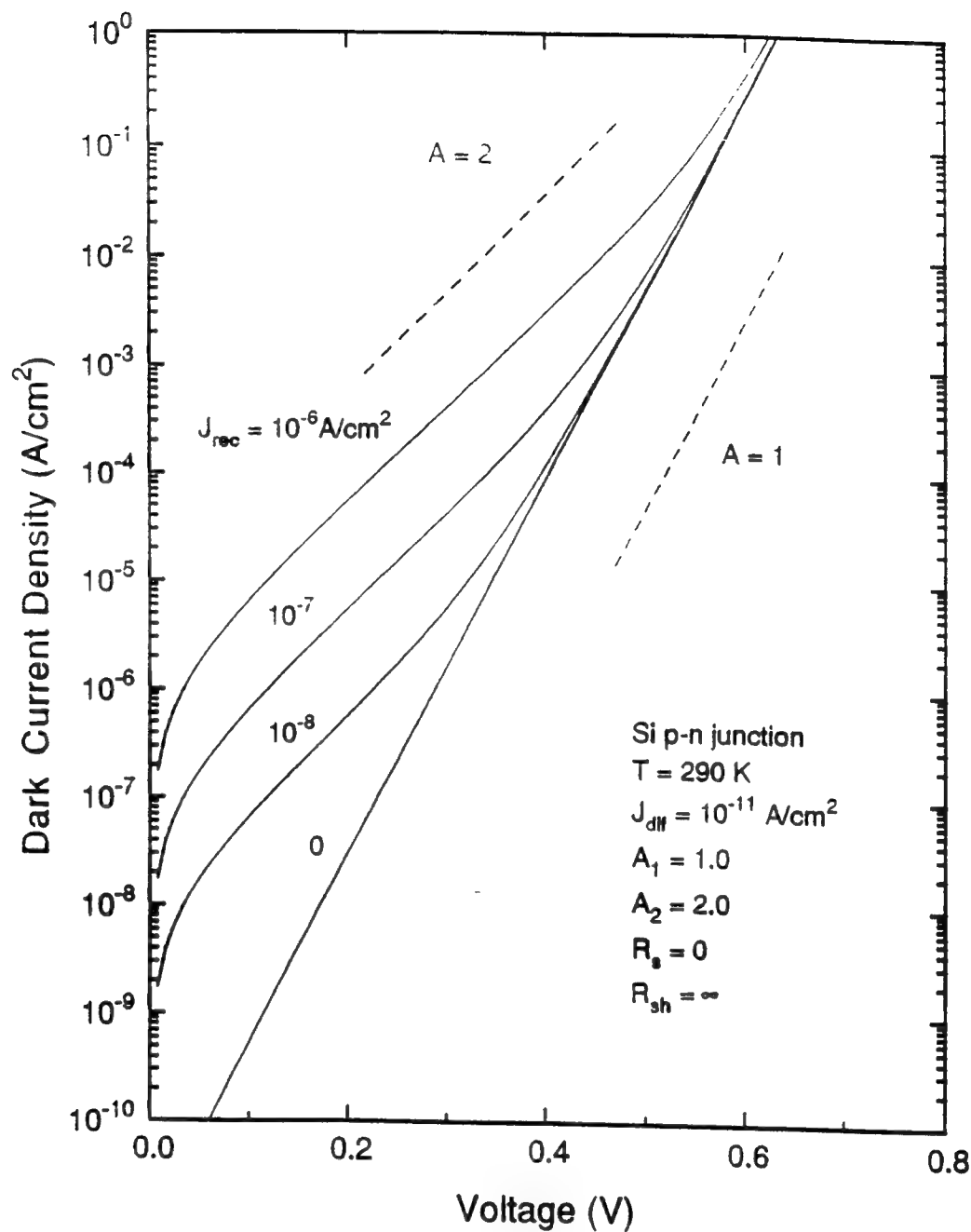


Figure 12. Ideal dark forward I-V characteristics for a Si p-n junction at room temperature showing the effects of recombination current.

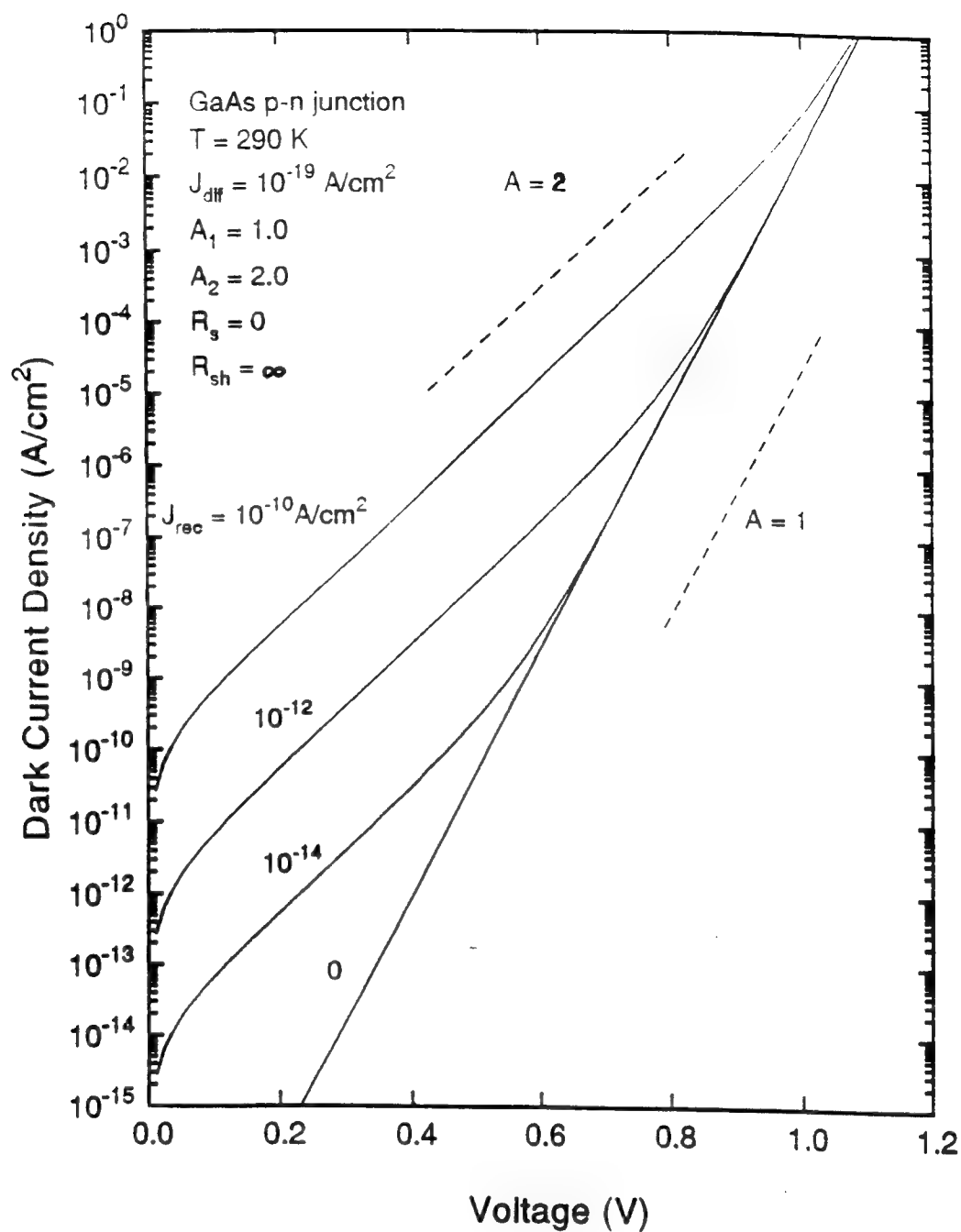


Figure 13. Ideal dark forward I-V characteristics for a GaAs p-n junction at room temperature showing the effects of recombination current.



The effects of current shunting are shown in Figures 14 and 15 for relatively low ( $10^{-14}$  A/cm<sup>2</sup>) and high ( $10^{-10}$  A/cm<sup>2</sup>)  $J_{rec}$ , respectively. In Figure 14 we see that shunting has a significant effect on the total dark current near the GaAs solar cell operating voltage when the recombination current is relatively small, while in Figure 15 shunting has very little effect when the recombination current is substantial. The presence of recombination current in the latter case affects the I-V characteristic over the entire voltage range of solar cell operation.

The resulting ratios of  $J_{rec}/J_{dif}$  for Si and GaAs solar cells are typically  $10^3 - 10^6$  and  $10^8 - 10^{10}$  respectively. This finding is consistent with the relation

$$\frac{J_{rec}}{J_{dif}} \propto \exp\left(\frac{E_g}{2kT}\right) \quad (2.67)$$

obtained from Eqs. (2.23) and (2.57), where  $E_g$  is the semiconductor bandgap equal to ~1.1 and 1.4 eV in Si and GaAs, respectively. Since the bandgap of the GaInP<sub>2</sub> material used in this study is 1.84 eV at 290 K, the ratio of  $J_{rec}/J_{dif}$  for the GaInP<sub>2</sub> p-n junction is expected to be even larger than that for GaAs. This, together with the fact that GaAs solar cells are often dominated by recombination dark current at their maximum power-point voltage, suggests that recombination current will also play a dominant role in GaInP<sub>2</sub> solar cells.

The effect of temperature on dark current in a typical GaAs p-n solar cell is shown in Figure 16, where the temperature dependences of diffusion and recombination current are given by Eq.(2.24) and (2.58), respectively. Figure 16 shows that shunting current becomes more important at lower temperatures. This

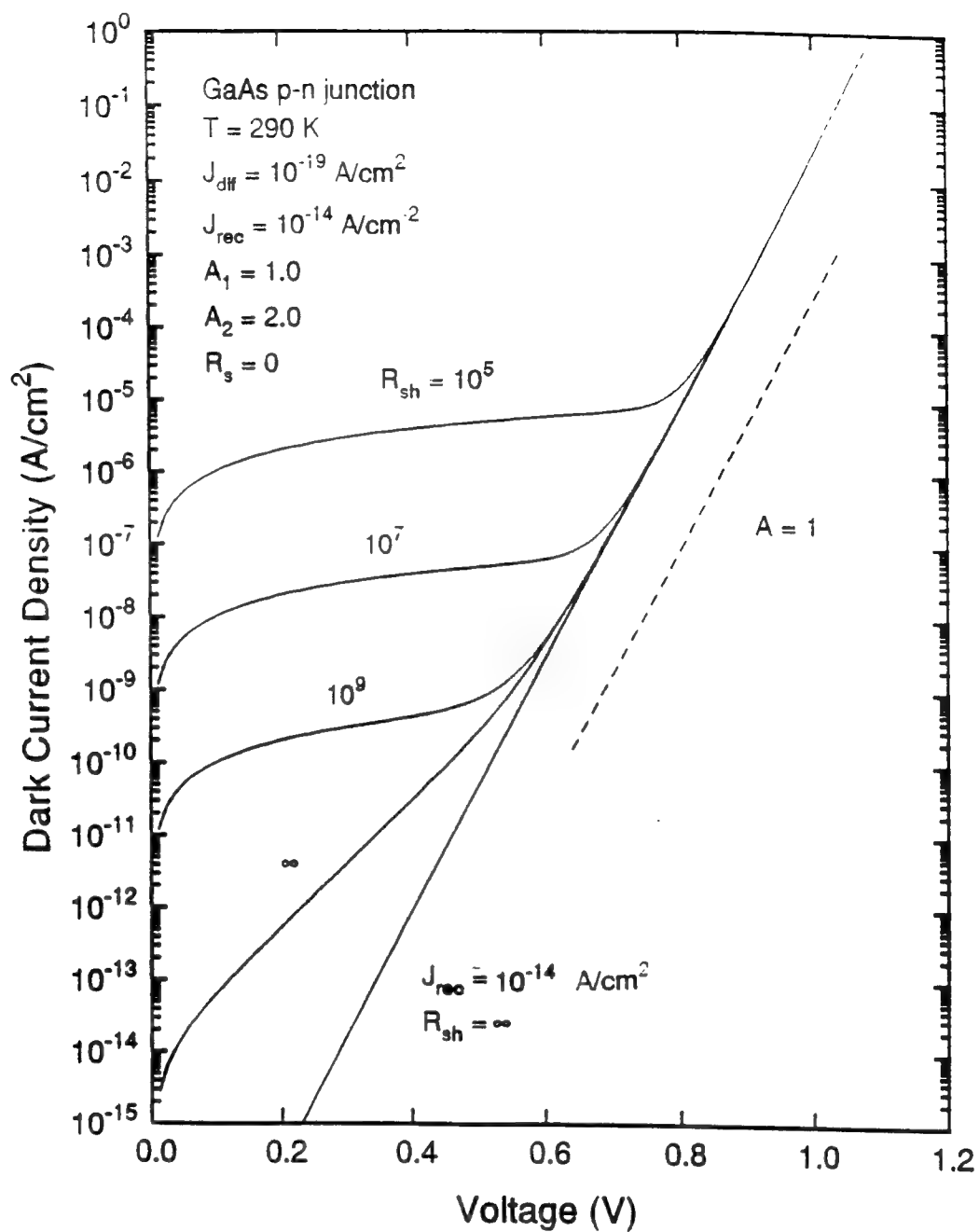


Figure 14. Ideal dark forward I-V characteristics for a GaAs p-n junction showing the effect of shunting resistance.

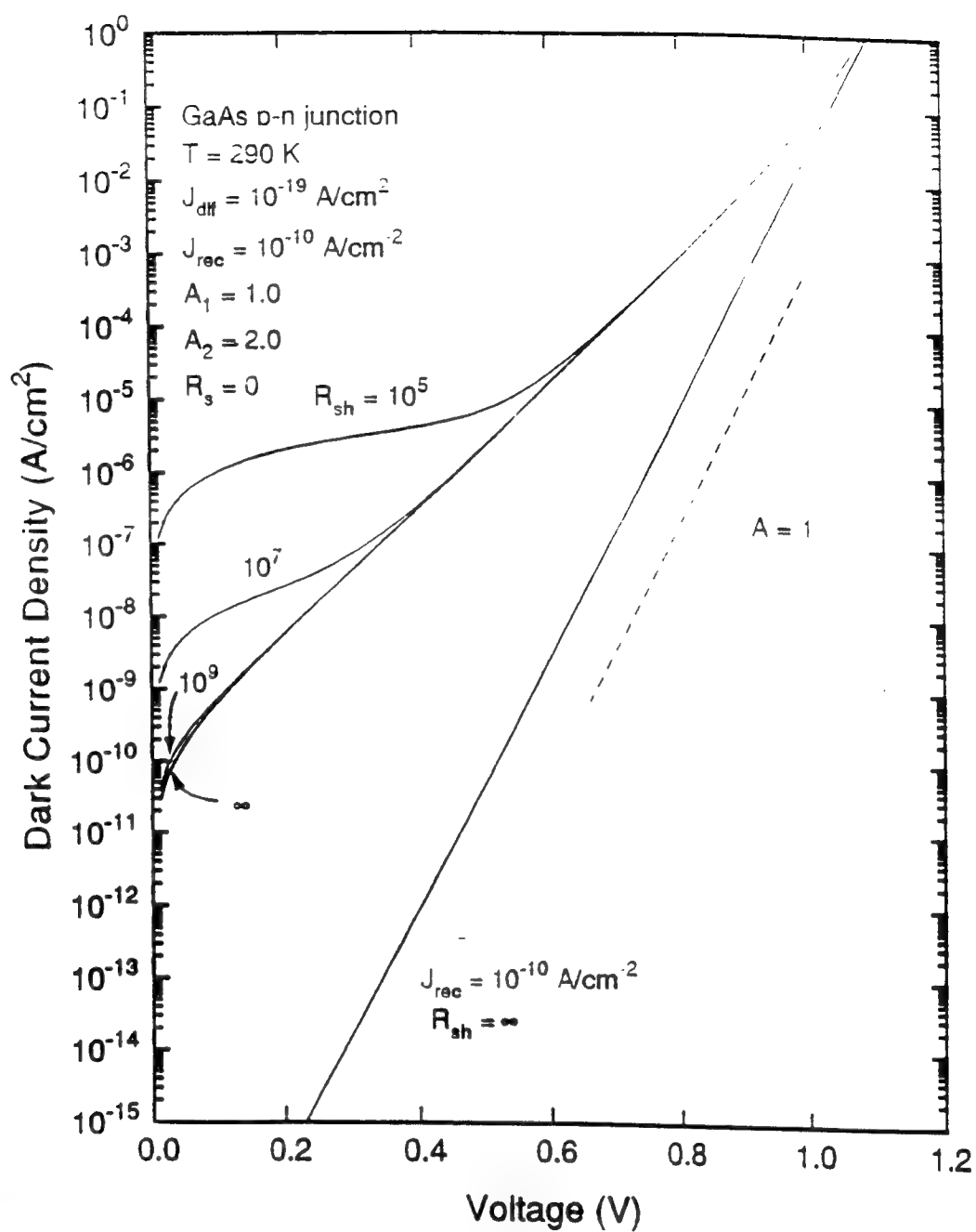


Figure 15. Ideal dark forward I-V characteristics for a GaAs p-n junction showing the effects of shunting resistance.

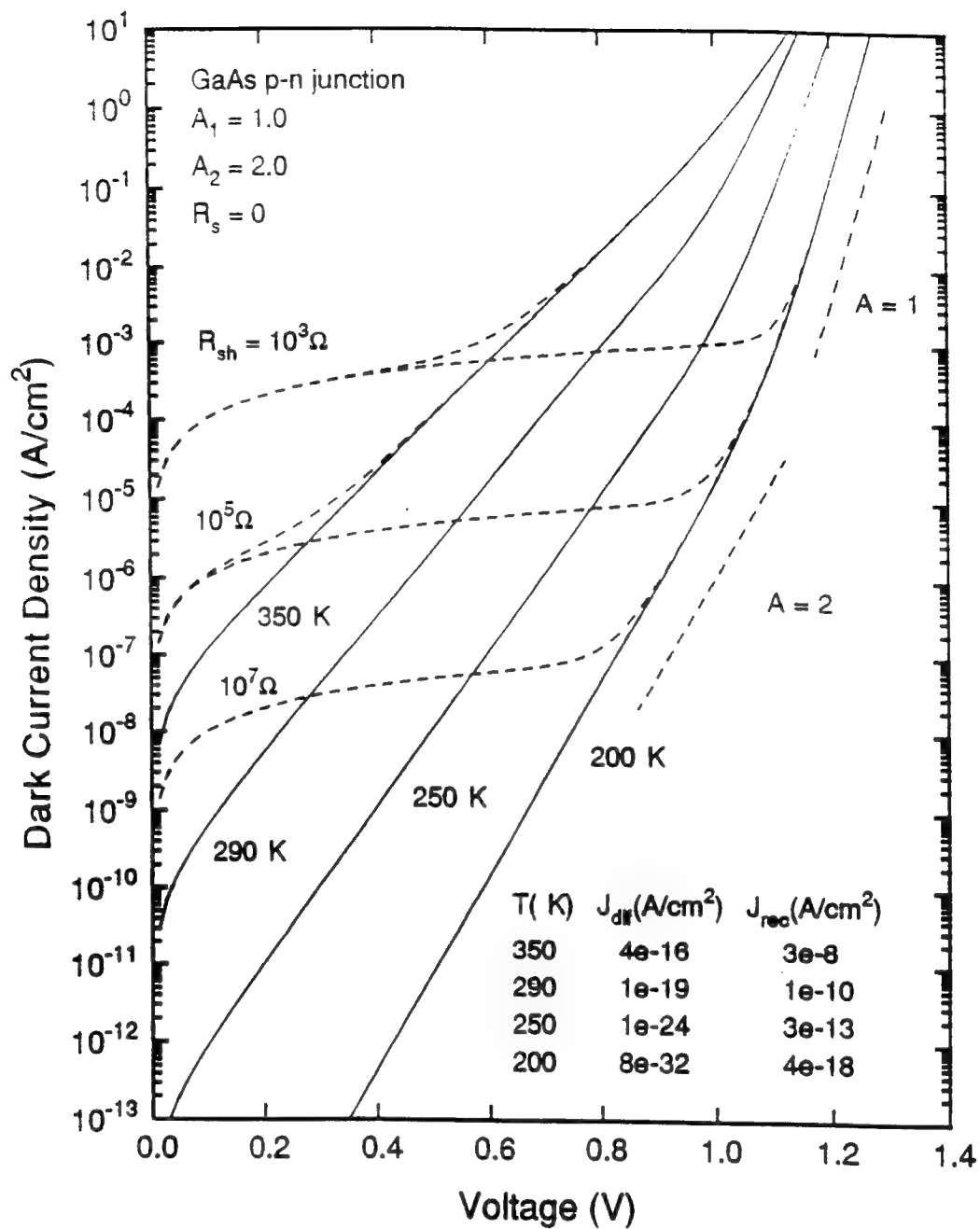


Figure 16. Ideal dark forward I-V characteristics as a function of temperature for a GaAs p-n junction showing the effects of shunting resistance.

occurs because the shunting current is essentially temperature independent, whereas  $J_D$  and  $J_R$  fall off exponentially with temperature. Also, since  $J_{dif}$  falls off faster than  $J_{rec}$  at lower temperature (as  $\propto \exp(-E_g/kT)$  compared to  $\propto \exp(-E_g/2kT)$ , respectively), the relative effect of recombination current becomes more pronounced at lower temperatures. Similarly, at fixed temperature, the larger the value of  $E_g$ , the smaller the role of diffusion current.

### **Space Radiation Damage in Solar Cells**

Solar cells provide a source of electrical power to nearly all earth-orbiting military and civilian satellites. The lifetime of solar cells orbiting in space is most limited by the presence of high energy particle radiation trapped in the space environment. The earth's natural radiation environment in outer space consists mainly of electrons and protons trapped in the earth's geomagnetic field (Tada *et al.*, 1982:3-1). The trapped particles form belts known as the van Allen belts.

An idea of the distribution of trapped particles is shown in Figure 17 as a function of distance in units of earth radius. (Hovel, 1975:150). In Figure 17(a), the regions around the inner van Allen belt are shown (shaded area), and are characterized by a particle density of about  $10^4$  protons/cm<sup>2</sup>sec, with very high energies from 20-200 MeV. The second van Allen belt is shown in Figure 17(b) and characterized by a high energy electron density of  $10^4$ - $10^5$ /cm<sup>2</sup>-sec with energies between 1 and 2 MeV. This belt also contains a high proton density of  $10^7$ - $10^8$ /cm<sup>2</sup>-sec with energies in the 1-5 MeV range (Figure 17(c)), while a high

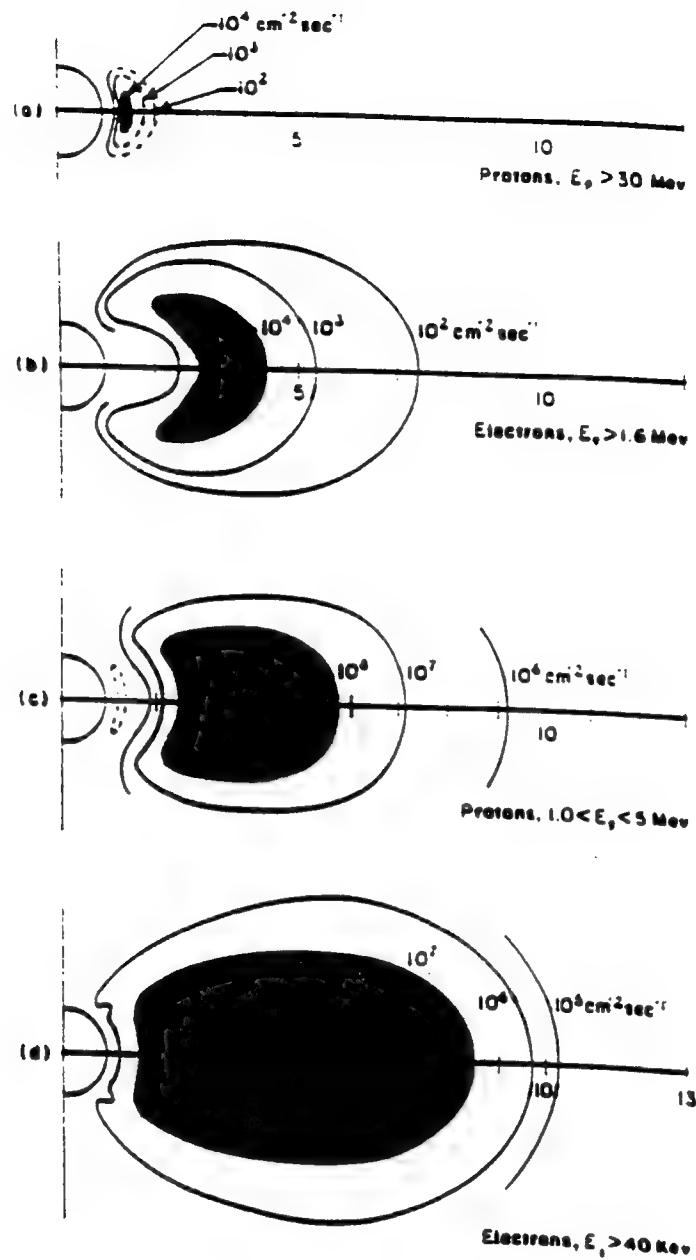


Figure 17. Diagram of the earth's radiation belts as a function of distance in units of the earth's radius.

density of  $10^6$ - $10^8/\text{cm}^2\text{-sec}$  of low energy electrons and protons (1-100 keV) occupy the space from the inner van Allen belt to about 10 earth radii (63,800 km) as shown in Figure 17(d). In practice, solar cells are exposed to actual fluence levels that exceed these numbers by a few orders of magnitude due to integrated exposure over long periods of time. A more elaborate description of the nature, origin, and variation in the density of this radiation has been compiled from actual flight experiments, and is presented elsewhere (Tada *et al.*, 1982).

### **Microscopic Effects of Radiation Damage in Solar Cells**

The primary effect of radiation damage in solar cells is to increase the concentration of defect energy levels present in the semiconductor bandgap. These defects enhance carrier recombination and reduce minority carrier lifetime which both reduce the solar cell  $V_{oc}$ ,  $J_{sc}$ , and Eff. Radiation damage in solar cells can be explained in terms of the microscopic interaction between the irradiating particles and the lattice of the solar cell material. The modes of radiation interaction are governed by the mass and energy of the interacting particle, along with the physical, chemical, and electrical properties of the crystal. Energy conservation takes place by elastic or inelastic collision processes as follows (Tada *et al.*, 1982:3):

- 1) the elastic collision between the incident particle and the positively charged nucleus of the lattice atom takes place by coulombic interaction. The large amount

of energy transferred to the nucleus results in a displacement of the atom from the lattice site, causing structural disorder in the parent lattice,

2) the inelastic interaction between heavy energetic particles and the atom forces the nucleus into a higher excited state. In the process of relaxation, the nucleus emits energetic nucleons and suffers a recoil. As a result of the recoil the atom is displaced from its lattice site. Due to its large size, the displaced nucleus caused more displacement damage along its track, and

3) the inelastic collision between the energetic particle and the bound electrons is the predominant mode of energy transfer. The large amount of energy transferred to the electrons causes ionization of the lattice atoms.

As a result of the above interactions, a large amount of structural damage is introduced into the lattice. The defects that result are called point defects, and they are extremely mobile and have a tendency to interact with other defects as well as with substitutional or interstitial impurities. Common defects include vacancies, interstitials, defect clusters, and vacancy-impurity complexes. The modification of the local structural order of the lattice causes a perturbation in the periodic potential of the crystal, which introduces localized energy states or deep-levels into the bandgap. The position and density of these states depend on the nature of the defect and the extent of the disorder, respectively. The defect levels alter the electrical properties of the semiconductor by several basic mechanisms.



The position and density of the levels generally determine which mechanism will dominate.

In solar cells, radiation damage affects electrical performance in the following ways.

1) Radiation induced defects introduce additional SRH-type recombination centers in the cell's SCL. This reduces the lifetimes  $\tau_n$  and  $\tau_p$  in Eq. (2.52) resulting in an increase in the dark recombination current density in accordance with Eq. (2.51). Since the minority carrier lifetimes are inversely proportional to the recombination rate (Eq. 2.40), the reciprocal lifetime contributions caused by various sets of recombination centers can be added to determine the inverse of lifetime as follows,

$$\tau^{-1} = \tau_0^{-1} + \sum_i \tau_i^{-1}, \quad (2.68)$$

where  $\tau$  is the new minority carrier lifetime,  $\tau_0$  is the lifetime before irradiation, and  $\tau_i$  is the lifetime of the  $i^{\text{th}}$  radiation induced recombination center. The lifetime of the radiation induced centers is given by the familiar  $\tau = (N_i v_m \sigma)^{-1}$ .

2) An increase in the number of SRH-type recombination centers in the cell's emitter and base regions results in the reduction of  $\tau_n$ ,  $\tau_p$ , and  $L$  (the respective carrier diffusion length), resulting in a reduction of the cells photocurrent,  $I_L$ . The effect of reduced  $L$  on  $I_L$  can be deduced from Eqs. (A10) and (A11) given in Appendix A, where  $L_{n,p} = (D_{n,p} \tau_{n,p})^{1/2}$ . In conventional  $n^+p$  Si solar cells, the

photocurrent is reported to follow the relation  $I_L \sim \ln(L_n)$ , where  $L_n$  in the cell's p-base controls  $I_L$  (Tada et al., 1982:2-15).

3) Defects introduced within the cell's SCL provide additional centers for multistep tunneling and thermal trapping-detrapping of carriers. An increase in the number of tunneling pathways through the junction will enhance the shunting dark current density,  $J_{sh}$ , resulting in a lowering of the cell's  $V_{oc}$ ,  $ff$ , and  $Eff$ .

### **Conventions for Characterizing Radiation Damage in Solar Cells**

The behavior of solar cells in a radiation environment can be described in three ways. The first and most common approach is to measure changes in solar cell electrical output parameters such as  $V_{oc}$ ,  $I_{sc}$ ,  $P_m$ , and  $Eff$  following radiation exposure. This approach is very practical and useful to the solar array designer who requires hard performance data to design for EOL requirements. The second approach involves measuring the degradation of solar cell minority carrier lifetime and diffusion length which provides damage coefficients used in the predicting solar cell degradation in the radiation environment. However, although this approach provides additional understanding of the electrical changes in the cell, it falls short of providing insight into microscopic physical changes that occur. In the third approach, the properties and behaviors of the defect centers directly responsible for the degradation are studied. Measuring how defect centers affect the cell's current conduction and collection mechanisms, and also, although very difficult, determining the precise structural configuration of the defect are included

in this approach. In this work, the first, and parts of the third approaches will be used to study the influence of electron radiation on GaInP<sub>2</sub> n<sup>+</sup>p diodes and solar cells.

Considering the first approach above, standards have been defined for testing the radiation resistance of solar cells for various kinds of radiation in a simulated environment. For testing and reporting radiation damage in solar cells under accelerated test conditions, 1 MeV electrons are commonly used (Tada *et al.*, 1982). The degradation in solar cell  $I_{sc}$ ,  $V_{oc}$ ,  $P_m$ ,  $I_m$ , and  $V_m$  are generally measured as a function of various 1 MeV electron fluences, typically from  $10^{12}$  to  $10^{16}$  cm<sup>-2</sup>. One MeV electrons of this fluence are conveniently produced in a laboratory environment using very simple machines. The earth's outer space radiation environment has been measured by various flight experiments and reduced to a damage equivalent 1 MeV electron fluence. The degrading effects of both electrons and protons found in the outer space environment are then described in terms of a 1 MeV equivalent electron fluence. Hence, the degradation of solar cell output parameters in the real outer space radiation environment can be accurately simulated using 1 MeV electrons generated in a laboratory.

For example, the reduction in output power of a spacecraft solar array designed for a 10 year mission in an orbit of 30 degrees inclination, at an altitude of 600 nmi, and using GaAs solar cells having a 3 mil coverglass can be determined. First, the tables in Appendix B give the annual equivalent 1 MeV electron fluences

resulting from trapped electrons and protons, respectively, in an orbit of 30 degree's inclination as a function of altitude and solar cell quartz coverglass thickness (Tada *et al.*, 1982). The tables show that solar cells placed in the desired orbit would be exposed to a total 1 MeV equivalent electron fluence of  $8.32 \times 10^{14}$  electrons/cm<sup>2</sup>. Second, GaAs solar cells can be irradiated in the laboratory with 1 MeV electrons of varying fluence, and changes in their output parameters measured. For example, Appendix C gives a plot of normalized maximum power as a function of 1 MeV electron fluence measured for GaAs single junction solar cells (Anspaugh, 1988:21). This data shows that for a 1 MeV equivalent electron fluence of  $\sim 8 \times 10^{14}$  e-/cm<sup>2</sup>, the output power of the GaAs solar cell can be expected to degrade by  $\sim 24\%$  at EOL. Therefore, from this data the solar array can be accordingly oversized at BOL to meet EOL power requirements.

In the next chapter, the processing techniques used to fabricate and package the GaInP<sub>2</sub> n<sup>+</sup>p test diodes and solar cells used in this study are presented.

### **III. Device Fabrication**

#### **GaInP<sub>2</sub> Solar Cell and Mesa Diode Structures**

This chapter describes the growth, fabrication, and packaging of GaInP<sub>2</sub> n<sup>+</sup>p mesa diodes and solar cells used in this study. The device structures examined were based on design and performance trade studies conducted in response to the Air Force Lightweight Low Cost, High-Efficiency Solar Cell for Space Planar Array development program PRDA 91-01-PKRN POC in 1991 (Cavicchi *et al.*, 1991; Timmons *et al.*, 1991; Linden *et al.*, 1991), and also on the high efficiency GaInP<sub>2</sub>/GaAs solar cell design of Olson (Olson *et al.*, 1990:623).

Layers of GaInP<sub>2</sub> were grown by the Research Triangle Institute, RTI, NC, on 12 mil, 1" x 1", (100) p<sup>+</sup> GaAs substrates at 675 K at one atmosphere. The wafer layer thicknesses and doping densities are shown in Figure 18. The Group III source gases were ethyldimethylindium, trimethylaluminum, and trimethylgallium, and the Group V source gases were 100% arsine and 100% phosphine. The source of dopants were diethylzinc and hydrogen selenide diluted in hydrogen. The n-type dopant was Se, and the p-type was Zn. The solar cell p-base doping density was  $\sim 1 \times 10^{16} \text{ cm}^{-3}$ , and the mesa diode p-base doping densities were  $\sim 1\text{-}2 \times 10^{16}$ ,  $1.2 \times 10^{17}$  and  $2 \times 10^{17} \text{ cm}^{-3}$  in low, mid, and high doped mesa diodes, respectively. The bandgap of GaInP<sub>2</sub> at 290 K was 1.84 eV, and the lattice mismatch of GaInP<sub>2</sub>-GaAs measured for similar samples was within 100 arcseconds. The n<sup>+</sup>p junction

$n^+$	GaAs Cap Layer	0.5 $\mu\text{m}$	$N_D \sim 10^{19} \text{ cm}^{-3}$
$n^+$	$\text{Al}_{0.5}\text{In}_{0.5}\text{P}$ Window Layer	0.04 $\mu\text{m}$	$N_D \sim 5 \times 10^{18} \text{ cm}^{-3}$
$n^+$	$\text{Ga}_{0.5}\text{In}_{0.5}\text{P}$ Emitter Layer	0.15 $\mu\text{m}$	$N_D \sim 10^{18} \text{ cm}^{-3}$
p	$\text{Ga}_{0.5}\text{In}_{0.5}\text{P}$ Base Layer	3.0 $\mu\text{m}$	$N_A \sim 1 \times 10^{16} \text{ cm}^{-3},$ $1 \times 10^{17} \text{ cm}^{-3},$ $2 \times 10^{17} \text{ cm}^{-3}$
p+	GaAs Substrate	$\sim 300 \mu\text{m}$	$N_A \sim 10^{19} \text{ cm}^{-3}$

Figure 18. Schematic diagram of  $\text{GaInP}_2$  mesa diode structure showing approximate layer thicknesses and doping densities. The  $\text{GaInP}_2$  solar cell has a similar structure except for 1  $\mu\text{m}$  thick top and bottom Au contacts. The p-base doping density of the solar cells is  $10^{16} \text{ cm}^{-3}$ .

structure of Figure 18 was chosen over the  $p^+n$  structure based on the fact that the lifetime of minority carrier electrons,  $\tau_n$ , in p-type semiconductors is generally longer than that for holes in n-type semiconductors. Since nearly all solar absorption occurs in the thick base region, the cell's junction collection efficiency will be greater when the minority carriers in cell's base are electrons rather than holes. Hence, the  $n^+p$  (p-base) structure was selected, where electrons are minority carriers in the base.

The cell's  $n^+$  emitter layer is generally doped at a level as high as possible, usually to the dopant solubility limit, to maximize both  $V_{oc}$  and the junction's built-in field for optimum carrier collection. The  $n^+$  emitter doping density,  $N_D$ , of the GaInP<sub>2</sub> wafers used in this study was  $\sim 10^{18} \text{ cm}^{-3}$ .

In contrast to the high n-emitter doping levels, an upper limit is placed on the p-base doping density,  $N_A$ , due to the fact that a reduction of  $\tau_n$  in the cell's p-base will occur for excessively large  $N_A$ . As discussed earlier, a reduction in  $\tau_n$  will reduce solar cell  $J_L$ ,  $V_{oc}$ , and ff. Hence, optimization of  $N_A$  is required to maximize the solar cell efficiency. In Si solar cells, the p-base doping density is generally  $10^{15} - 10^{16} \text{ cm}^{-3}$  (Tada *et al.*, 1982), in GaAs, it is mid  $10^{16}$  to  $10^{17} \text{ cm}^{-3}$  (Illes *et al.*, 1988; Weinberg *et al.*, 1989), and in InP, it is mid  $10^{16} \text{ cm}^{-3}$  (Weinberg *et al.*, 1989). In the case of the GaInP<sub>2</sub>  $n^+p$  solar cell, the optimum value of  $N_A$  in the p-base has not yet been established.

The group at RTI have grown their best cells with  $N_A = 1 - 5 \times 10^{16} \text{ cm}^{-3}$  (Timmons, 1993), whereas the groups at Spectrolab Inc. and the National Renewable Research Laboratory, NREL, report a value of  $N_A \sim 10^{17} \text{ cm}^{-3}$  in their best cells (Friedman *et al.*, 1991). Unfortunately, only GaInP<sub>2</sub> n<sup>+</sup>p solar cells with  $N_A \sim 10^{16} \text{ cm}^{-3}$  were available for examination in this work. The cells were supplied by RTI. Although cells with larger  $N_A$  were not available, the basic physics and dark electrical behavior of such cells can be obtained from analysis of smaller area GaInP<sub>2</sub> n<sup>+</sup>p diodes. A solar cell is basically a large area p-n junction diode. Therefore, the junction properties and dark I-V behavior of smaller area diodes will be extremely similar to that of larger area solar cells.

Based on values of  $N_A$  used in Si, GaAs, and InP solar cells, and values of  $N_A$  used by RTI, NREL, and Spectrolab in their GaInP<sub>2</sub> solar cells, values of  $N_A$  selected for the GaInP<sub>2</sub> n<sup>+</sup>p diodes in this study were  $\sim 10^{16}$ ,  $10^{17}$  and  $2 \times 10^{17} \text{ cm}^{-3}$ .

### Device Processing

All devices were processed under the same conditions except that a thicker top gold contact was used for the solar cell grid fingers to minimize series resistance. GaInP<sub>2</sub> mesa diodes were processed using facilities in Material and Aero Propulsion and Power Directorates, Wright Laboratory, and the solar cells were processed at RTI. The procedures used to fabricate the devices are outlined as follows:

- (1) Substrate inspection, preparation, and cleaning
- (2) Backside ohmic contact formation



- (3) Frontside ohmic contact formation
- (4) Mesa diode isolation

### **Substrate Inspection, Preparation, and Cleaning**

The GaInP<sub>2</sub> MOCVD wafers were first examined under 50 - 1000X optical magnification to observe any possible surface damage. Figures 19 and 20 show the presence of line-like defects found in localized regions randomly distributed over approximately 10% of the wafer's surface. Figure 19 shows an optical photograph taken under 200X magnification, and Figure 20 is a scanning electron microscope image (SEM) of a similar defect under a magnification of 1500X. The wafer grower, RTI, stated that these were believed to be line-dislocations resulting from lattice-mismatch related strain between the GaAs substrate and GaInP<sub>2</sub> layers. GaInP<sub>2</sub> is known to be lattice matched to GaAs over a very narrow compositional range (Cavicchi *et al.*, 1991:63; Olsen *et al.*, 1978). Slight non-uniformities in the gas phase during MOCVD growth can produce regions of non-stoichiometric GaInP<sub>2</sub> material. The GaInP<sub>2</sub> lattice constant in these regions can differ substantially from that of the GaAs substrate, and lattice mismatching between the materials can result. The mechanical strain associated with the mismatch can be relieved by layer shifting, resulting in the line-dislocations. The presence of these line-dislocations will be shown to adversely affect the dark current behavior of both the GaInP<sub>2</sub> diodes and solar cells.

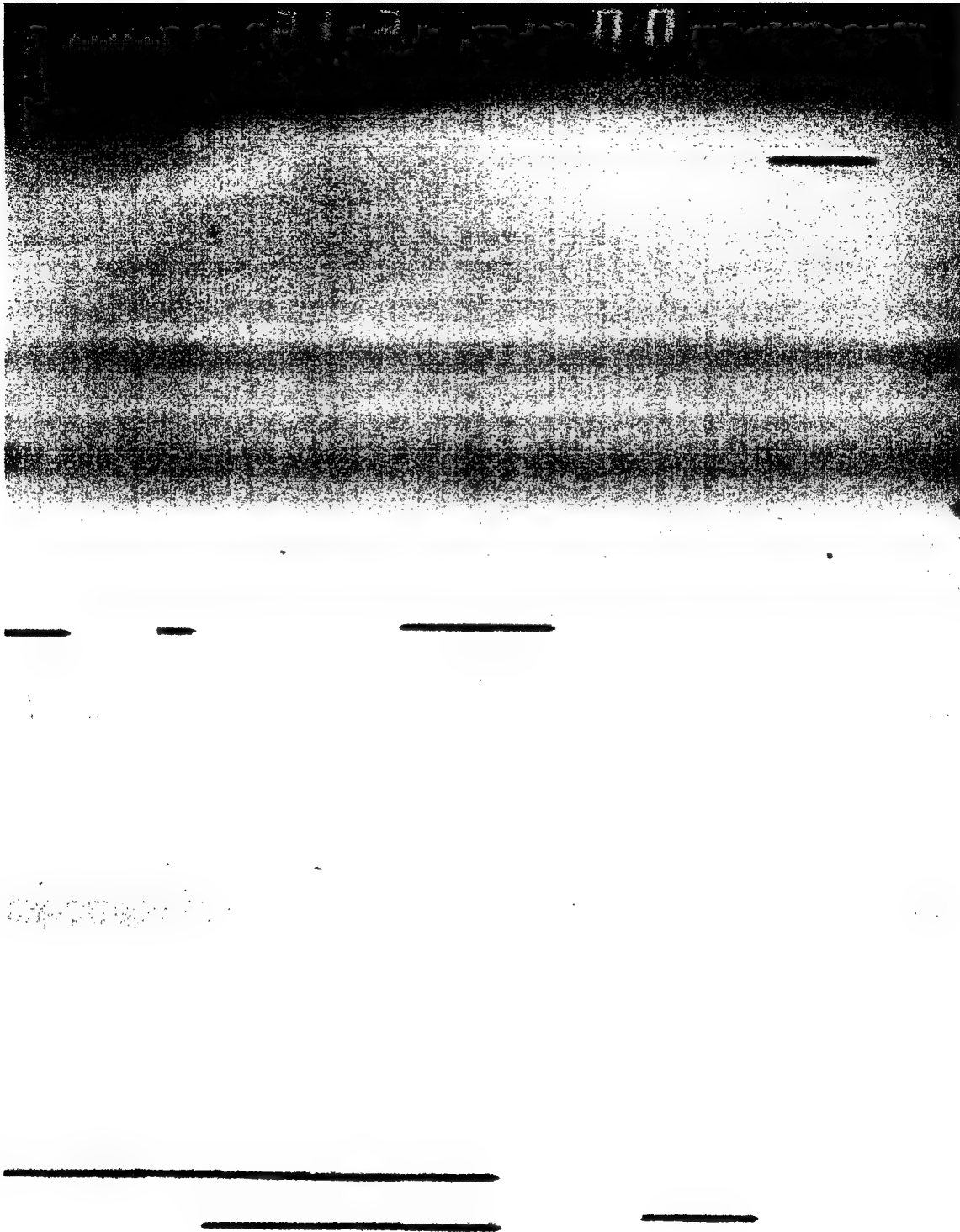


Figure 19. A photograph of GaInP<sub>2</sub>/GaAs line-defects taken under 200 x magnification.

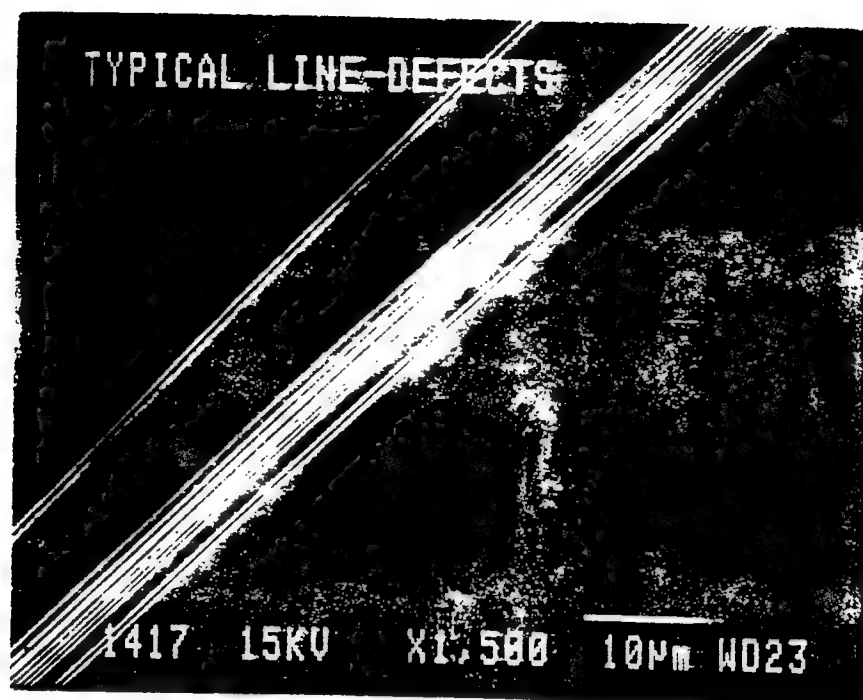


Figure 20. A scanning electron microscopy (SEM) image of a typical GaInP<sub>2</sub>/GaAs line-defect taken under 1500X magnification.

Several 1" x 1" GaInP<sub>2</sub> n<sup>+</sup>p wafers with N<sub>A</sub> ~ 10<sup>16</sup>, 10<sup>17</sup>, and 2 x 10<sup>17</sup> cm<sup>-3</sup> were cut into ~1/4" x 1/4" chips for diode processing using a diamond tip scribe. The chips were then cleaned prior to processing to remove any surface dirt or grease. The chips were mounted on a vacuum spindle, rotated at 500 RPM, sequentially sprayed with trichloroethylene, acetone, and methanol for 30 sec., followed by a 30 sec. rinse in deionized water, DI H<sub>2</sub>O and N<sub>2</sub> blow drying. The chips were then dipped in an etch bath of buffered hydrofluoric acid (HF):H<sub>2</sub>O (1:1) solution for 1 - 2 min. until dewetting of the chip surface occurred. The samples were thoroughly rinsed in DI H<sub>2</sub>O for 2 min., and blown dry with N<sub>2</sub>. The HF:H<sub>2</sub>O etch was used to remove the thin (~30 - 100 angstrom) native oxide that naturally grows on semiconductor surfaces exposed to ambient O<sub>2</sub>. The resulting semiconductor surface was clean and ready for device processing.

### **Backside Ohmic Contact Formation**

Ohmic contacts were formed on the backside of the p<sup>+</sup> GaAs substrate prior to frontside mesa diode processing. To protect the frontside layers during this process, the chips were mounted on the vacuum spindle, and a layer of Shipley 1400-27 photoresist was spin-deposited onto the front surface. Using a small eyedropper, several drops of photoresist were placed on the chip's surface. The chips were spun at 4000 RPMs for 30 seconds. The resulting photoresist thickness was ~ 4000 Å. The chips were then soft-baked on a hotplate at 100°C for 10 min. to remove solvent present in the photoresist. Then, immediately before loading the

samples into the metal deposition system, a final etch in HF:H<sub>2</sub>O was performed to remove any surface oxide that may have formed. The etch procedure was the same as that used during the initial cleaning. The chips were then quickly placed in the substrate holder of a Denton electron-beam metal deposition system where titanium, Ti, and gold, Au, ohmic contacts were sequentially deposited. The chips were mounted such that their backsides were fully exposed to the metal sources.

The deposition conditions used are as follows:

<u>Metal</u>	<u>Pressure</u> (Torr)	<u>Thickness</u> ( $\mu\text{m}$ )	<u>Rate</u> ( $\text{\AA}/\text{sec.}$ )	<u>Time</u> (sec)
Ti	$< 10^{-7}$	0.015	5	30
Au	$< 10^{-7}$	0.50	10	500

The chips were unloaded from the chamber, and the frontside photoresist was removed by sequential rinsing in acetone, methanol, and DI H<sub>2</sub>O, followed by N<sub>2</sub> blow drying. The resulting structure is shown in Figure 21(a).

### Frontside Ohmic Contact Formation

Frontside ohmic contacts were formed prior to mesa diode etching. These contacts connect to the diode's n<sup>+</sup> emitter. First, a layer of Shipley 1400-27 photoresist was spin-deposited onto the front surface of the chips at 1500 RPMs for 30 sec. The resulting photoresist thickness was  $\sim 0.8 \mu\text{m}$ . The chips were then soft-baked on a hotplate at 100°C for 10 min. A dark-field glass lithography mask containing an array of  $508 \mu\text{m}$  diameter circular dots (i.e., transparent openings)

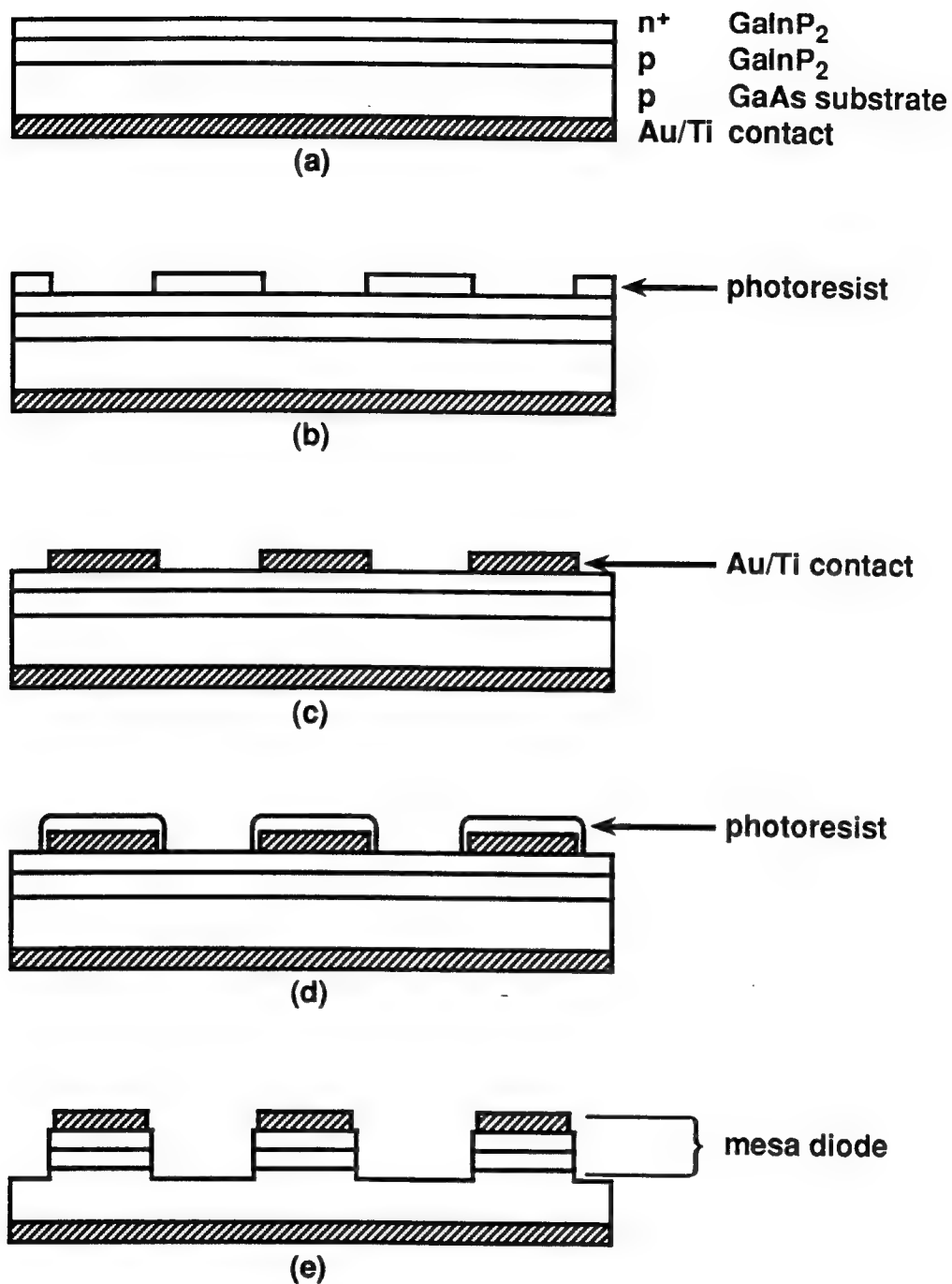


Figure 21. Sequence of the photolithography and metalization processes used to fabricate GaInP<sub>2</sub> mesa diodes.

was used to open windows in the photoresist. The separation between the dots on the mask was  $\sim 1000\text{ }\mu\text{m}$ . Windows in the photoresist define where metal contacts will be deposited. The chips were aligned with respect to the mask using a mask aligner tool. The radiation-sensitive photoresist was then exposed through the circular openings in the mask using an ultraviolet (UV) light source of wavelength  $\approx 0.2 - 0.4\text{ }\mu\text{m}$ . Since the Shipley 1400-27 resist is a positive photoresist, the regions of the resist exposed to UV become soluble in a developer solution. The chips were then sprayed with AZ-351:H<sub>2</sub>O (1:5) photoresist developer for  $\sim 1\text{ min.}$  until all exposed areas of the resist were dissolved. The chips were rinsed in DI H<sub>2</sub>O, dried with N<sub>2</sub>, and post-baked on a hotplate at 100°C for 10 min. to harden the resist. The resulting photoresist profile is shown in Figure 21(b). The patterned windows have a diameter of 508  $\mu\text{m}$  and extend down through the resist to the n<sup>+</sup> GaAs cap layer.

Metal was then deposited through the patterned windows to form the top ohmic contacts of the mesa diodes. The chips were first dipped in HF:H<sub>2</sub>O, rinsed, dried, and metalized utilizing the same procedures used above to form the back ohmic contacts. The photoresist and excess metal were then lifted from the chips by soaking the samples in a beaker of acetone placed in an ultrasonic cleaner for 10 min. This was followed by a rinse in acetone, methanol, and DI H<sub>2</sub>O, and N<sub>2</sub> drying. The resulting structure is shown in Figure 21(c). It is noted that ohmic

contact sintering was not required due to the high  $n^+$  substrate and cap doping densities.

### **Mesa Diode Isolation**

The formation of  $\text{GaInP}_2$   $n^+p$  mesa diodes was achieved via mesa etching. The top metal contacts were first protected with photoresist. Shipley 1400-27 photoresist was deposited on the chip's top surface and pre-baked using the procedures outlined previously. A second light-field mask containing  $540\text{ }\mu\text{m}$  circular opaque dots was aligned with the circular metal contacts formed in the previous section. The opaque dots prevent the photoresist that covers the contacts from being exposed by UV radiation. The chips were then exposed with UV light, and the photoresist was developed, rinsed, and dried as before. The resulting photoresist profile is shown in Figure 21(d). Before mesa etching, the back ohmic contact was coated with photoresist for protection.

The  $n^+p$  mesa diode structures were formed using  $\text{Br}_2:\text{HBr}:\text{H}_2\text{O}$  in the ratio of 1:17:34. The chips were dipped in the etchant for  $\sim 30$  sec., followed by DI water rinsing and  $\text{N}_2$  blow drying. The resulting mesa step height measured with a Dektak profilometer was  $\sim 6\text{ }\mu\text{m}$ . Since the thickness of the  $n^+p$   $\text{GaInP}_2$  layers above the GaAs substrate was less than  $4\text{ }\mu\text{m}$ , complete device isolation was achieved. The backside photoresist was then removed by sequential rinsing in acetone, methanol, and DI  $\text{H}_2\text{O}$ , followed by  $\text{N}_2$  blow drying. The resulting  $n^+p$  mesa diode structure is shown in Figure 21(e).



GaInP<sub>2</sub> solar cells were fabricated at RTI, Inc. using the same procedures outlined above. Nine GaInP<sub>2</sub> n<sup>+</sup>p solar cells were processed on a 1" x 1" wafer having  $N_A \approx 10^{16} \text{ cm}^{-3}$ . The solar cell epitaxial structure is the same as that shown in Figure 18. However, a Au metal thickness of  $\sim 1\mu\text{m}$  was used to reduce series resistance. The active and total solar cell areas are 0.14 and 0.16 cm<sup>2</sup>, respectively. Also, each solar cell chip contains 12 mesa diodes of junction area of 0.0001, 0.0009, and 0.0025 cm<sup>2</sup>.

### Device Packaging

All device packaging was performed at the Electronics Directorate of Wright Laboratory, WPAFB, OH. Each 1/4" x 1/4" chip contained 50 ~ 60 GaInP<sub>2</sub> mesa diodes. Each chip was diced into small die ( $\sim 0.062 \times 0.062$  in.) containing 4 diodes each (2 x 2 dots). Each die was mounted in a 10 pin T05 header with EPO-TEK E-3081 thermally and electrically conductive adhesive. The top contact of each diode (connected to the n-emitter) was ultrasonic-wedge wire bonded to one pin of the T05 header with 0.7 mil Au wire. The planar ohmic contact on the back of the die (connected to the diode p-base) was connected to the base of the T05 header via the EPO-TEK electrically conductive adhesive. This adhesive was also used to connect the header base to one of the header pins. A picture of a completed mesa diode package is shown in Figure 22.

Nine solar cell die were cut from the 1" x 1" GaInP<sub>2</sub> wafer processed by RTI, and each cell was separately mounted in a 36 pin T100 flat package using EPO-

TEK adhesive. The cell's top contact grid busbar and the top contacts of 12 adjacent test diodes were each ultrasonic-wedge wire bonded to a pin of the flat package. These contacts are connected to the  $n^+$  layer of the junctions. The planar ohmic contact on the back of the die was electrically connected to one pin of the package via the electrically conductive EPO-TEK adhesive. This contact is connected to the p-base layer of the junctions. A picture of a completed solar cell package is shown in Figure 23.

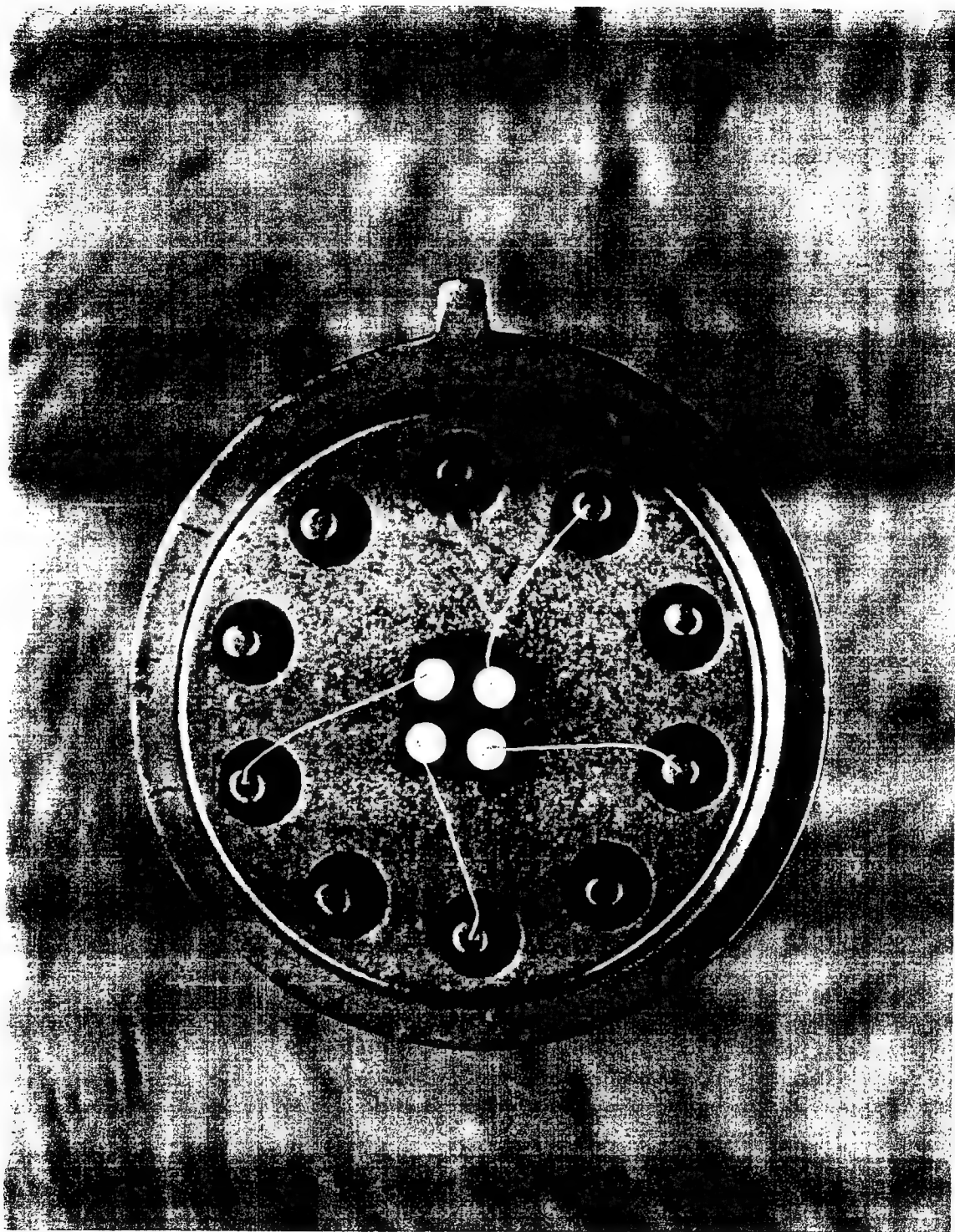


Figure 22. A photograph of a completed mesa diode die mounted and wire-bonded in a 10 pin T05 can.

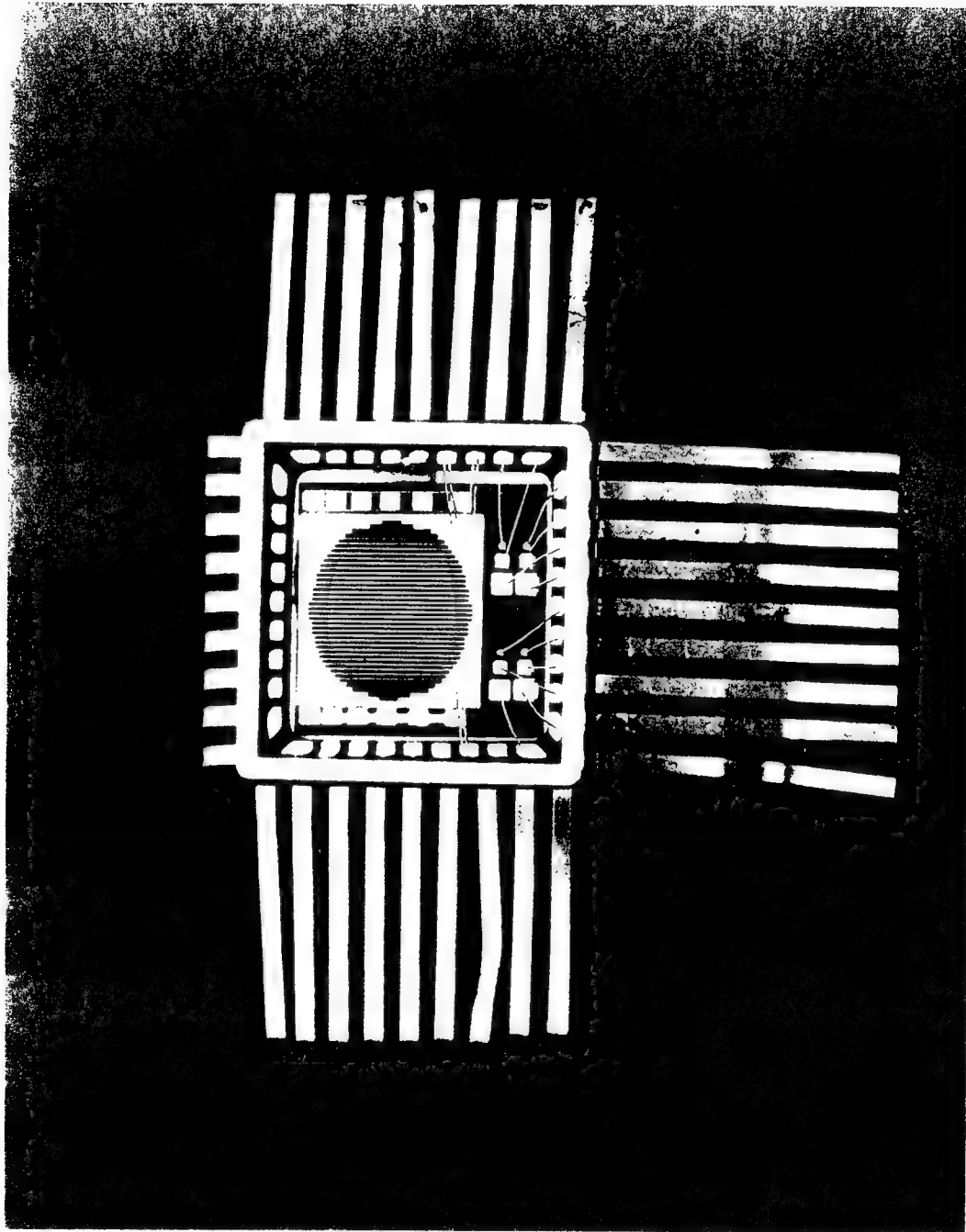


Figure 23. A photograph of a solar cell/diode die mounted and wire-bonded in a 36 pin flat electronics package.

#### **IV. Pre-Radiation GaInP<sub>2</sub> Solar Cell Characterization and Analysis**

##### **GaInP<sub>2</sub> Solar Cell Measurements**

An important goal of this work is to determine the factors that control dark current conduction in GaInP<sub>2</sub> solar cells. As a consequence, the photovoltaic performance of n<sup>+</sup>p junction GaInP<sub>2</sub> solar cells was measured and correlated with dark current behavior. The epitaxial structure of the GaInP<sub>2</sub> solar cells is shown in Figure 18, and the p-base doping density of the cells is  $\sim 10^{16} \text{ cm}^{-3}$ . The solar cell efficiencies were measured under AM0 conditions using a model 81173 1 kW xenon lamp Oriel solar simulator and a model 81011 Oriel air mass 0 filter. A schematic of the simulator is shown in Figure 24. The intensity of the simulator was calibrated using a single n<sup>+</sup>p junction GaInP<sub>2</sub> solar cell calibrated at RTI, Inc. A discussion of the solar spectrum is given in Appendix D. A precise measurement of solar cell parameters was achieved using a Keithley 238 Source Measure Unit (SMU). A voltage-bias was repetitively switched across the solar cells by the SMU, and the resulting current was measured. The voltage range was typically 0 - 1.5 V, in increments of 0.05 V. The test circuit used is shown in Figure 25.

A set of dark and light I-V curves for nine n<sup>+</sup>p GaInP<sub>2</sub> solar cells is shown in Figure 26. The dark I-V curves have been displaced by the photocurrent as described earlier. Values of  $J_{sc}$ ,  $V_{oc}$ , ff, Eff for these cells were obtained from the

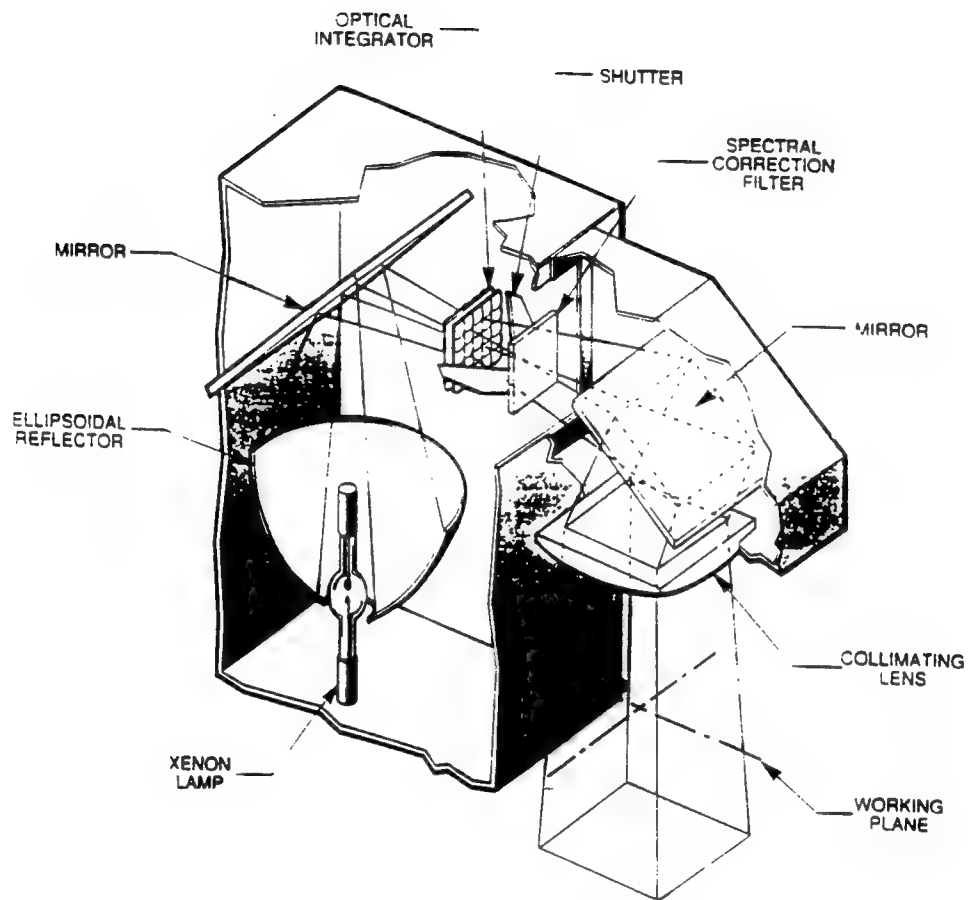


Figure 24. A schematic of the 1kW xenon lamp Oriel solar simulator.

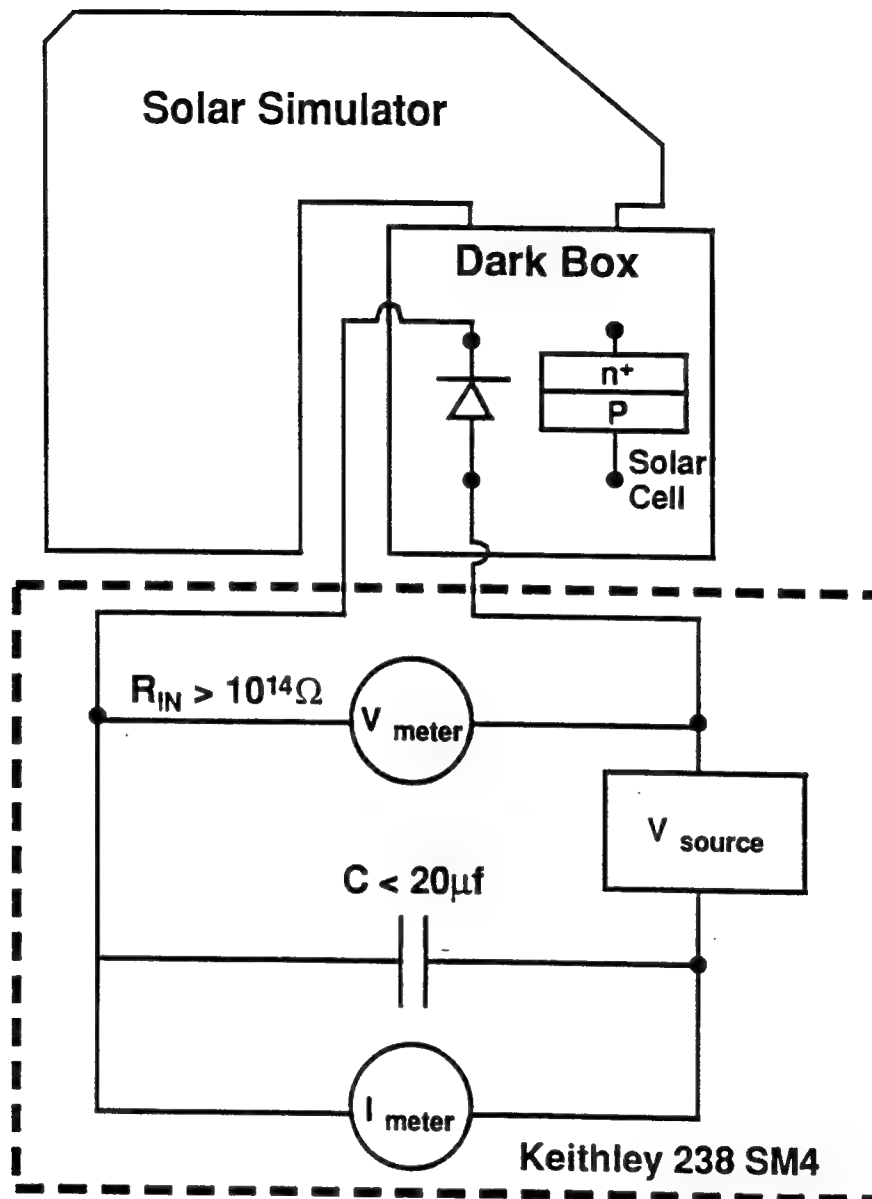


Figure 25. A schematic of the GaInP<sub>2</sub> diode and solar cell test circuit.

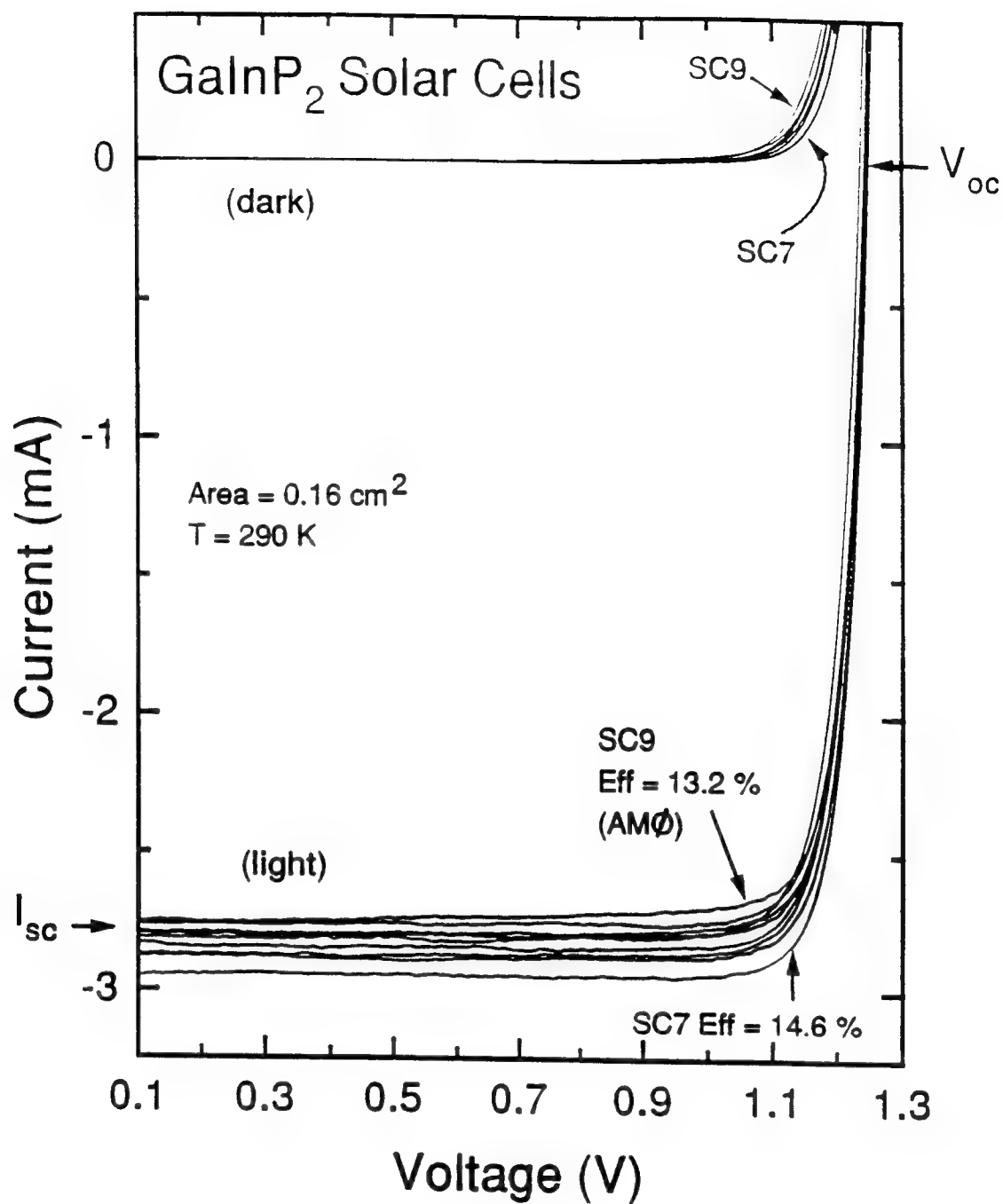


Figure 26. Forward-bias dark and AM0-light I-V curves for n<sup>+</sup>p GaInP<sub>2</sub> solar cells.



curves using Eq.s (2.3) - (2.5). The highest AM0 conversion efficiency measured for our single junction GaInP<sub>2</sub> cells was 14.6%, compared to the best reported cell efficiency of 15.3% (Chiang *et al.*, 1993:659). The solar cell parameters are given in Table II. The lower measured efficiency of our cells is due to a lower p-base doping density and a larger device perimeter-to-area (P/A) ratio, both of which are related to recombination current effects, and also, our cells had no back surface field layer which can significantly improve the cell's photovoltage. These issues will be discussed in turn.

### **Solar Cell Dark Current and Open-Circuit Voltage**

To understand the effect of dark current on GaInP<sub>2</sub> solar cell efficiency, the dominant dark current mechanisms were identified at the solar cell maximum power-point (MPP) voltage. The dark current that dominates at this voltage limits solar cell  $I_m$ ,  $V_m$ , and  $V_{oc}$ . The MPP voltage in these cells was measured to be  $\sim 1.1$  V. For the three highest efficiency cells (Eff = 14.2 - 14.6%), the current measured near the MPP can be well described by the second term in Eq. (2.11) between voltages of 0.8 and 1.2 V. As discussed in the theory, this term describes current due to carrier recombination via defect states within the junction. Values for the recombination current parameters  $J_{rec}$  and  $A_2$  were obtained from fits of Eq. (2.11) with the data. Values for  $J_{rec}$  varied between  $1.06 \times 10^{-14}$  and  $4.7 \times 10^{-14}$  A/cm<sup>2</sup> for the "well-behaved cells", and corresponding values of  $A_2$  varied between 1.77 - 1.87. These values of  $A_2$  are consistent with recombination theory

Table II. Summary of GaInP<sub>2</sub> solar cell photovoltaic parameters measured at ~290 K

Device	$J_{sc}$ (mA/cm <sup>2</sup> )	$V_{oc}$ (V)	ff(%)	Eff(%)*	$J_{rec}$ (A/cm <sup>2</sup> )	$A_2$	$J_{dark}^{**}$ (A/cm <sup>2</sup> )
SC1	17.56	1.240	0.849	13.69	2.81E-14	1.87	4.6E-4
SC2	17.19	1.236	0.848	13.35	--	--	6.2E-4
SC3	17.94	1.244	0.858	14.18	1.17E-14	1.83	3.1E-4
SC4	18.00	1.246	0.860	14.28	5.21E-15	1.78	2.8E-4
SC5	17.44	1.239	0.851	13.62	--	--	4.7E-4
SC6	17.75	1.241	0.850	13.87	1.86E-14	1.86	3.5E-4
SC7	18.38	1.248	0.859	14.60	3.20E-15	1.77	2.0E-4
SC8	17.44	1.235	0.842	13.43	--	--	5.8E-4
SC9	17.25	1.232	0.841	13.23	--	--	7.9E-4

\* AM0,  $P_{IN} = 1350 \text{ W/m}^2$

\*\* Measured at 1.1 V forward-bias

which predicts  $A_2 \approx 2$  through Eqs. (2.11) and (2.58), compared with the predicted value of  $A \approx 1$  for current due to diffusion.

The temperature dependence of  $J_{\text{rec}}$  was also used to identify the recombination current. Recombination theory predicts that the temperature dependence of current should be exponential with one-half the bandgap,  $E_g$ , in accordance with Eqs. (2.57) and (2.58). Forward-bias I-V measurements were taken as a function of temperature for the "well-behaved" GaInP<sub>2</sub> solar cells. A set of I-V-T curves for the 14.6% cell is shown in Figure 27. The constant positive sloped portion of the curves is due to carrier recombination. As before, values for  $J_{\text{rec}}$  and  $A_2$  were obtained using Eq. (2.11). The positive slope of the curves is seen to increase with decreasing temperature,  $T$ , in accordance with the recombination current factor  $\exp(qV/A_2kT)$  in Eq. (2.58). The values of  $A_2$  for this cell varied between 1.77 at 299 K and 1.96 at 100 K, and were relatively insensitive to temperature as predicted by recombination theory. The activation energy,  $E_A$ , for the  $A_2 \approx 2$  current mechanism was obtained from an Arrhenius plot of  $\ln(I_{\text{rec}})$  versus  $1000/T$ , which from Eq. (2.57),  $E_A = E_{g0}/2$  for ideal recombination. The term  $E_{g0}$  is the bandgap of GaInP<sub>2</sub> at  $T = 0$  K. Figure 28 shows an Arrhenius plot for the I-V-T data of Figure 27, and the resulting value of  $E_A$  for this cell is 1.02 eV. Values of  $E_A = 0.99$  and 1.02 eV were measured for the 14.2 and 14.3% efficiency solar cells, respectively. The corresponding value of  $E_{g0}$  for the above cell is  $2 \times E_A = 2.04$  eV. This value is within 3% of the measured value of  $E_{g0} \approx 1.98$  eV for the

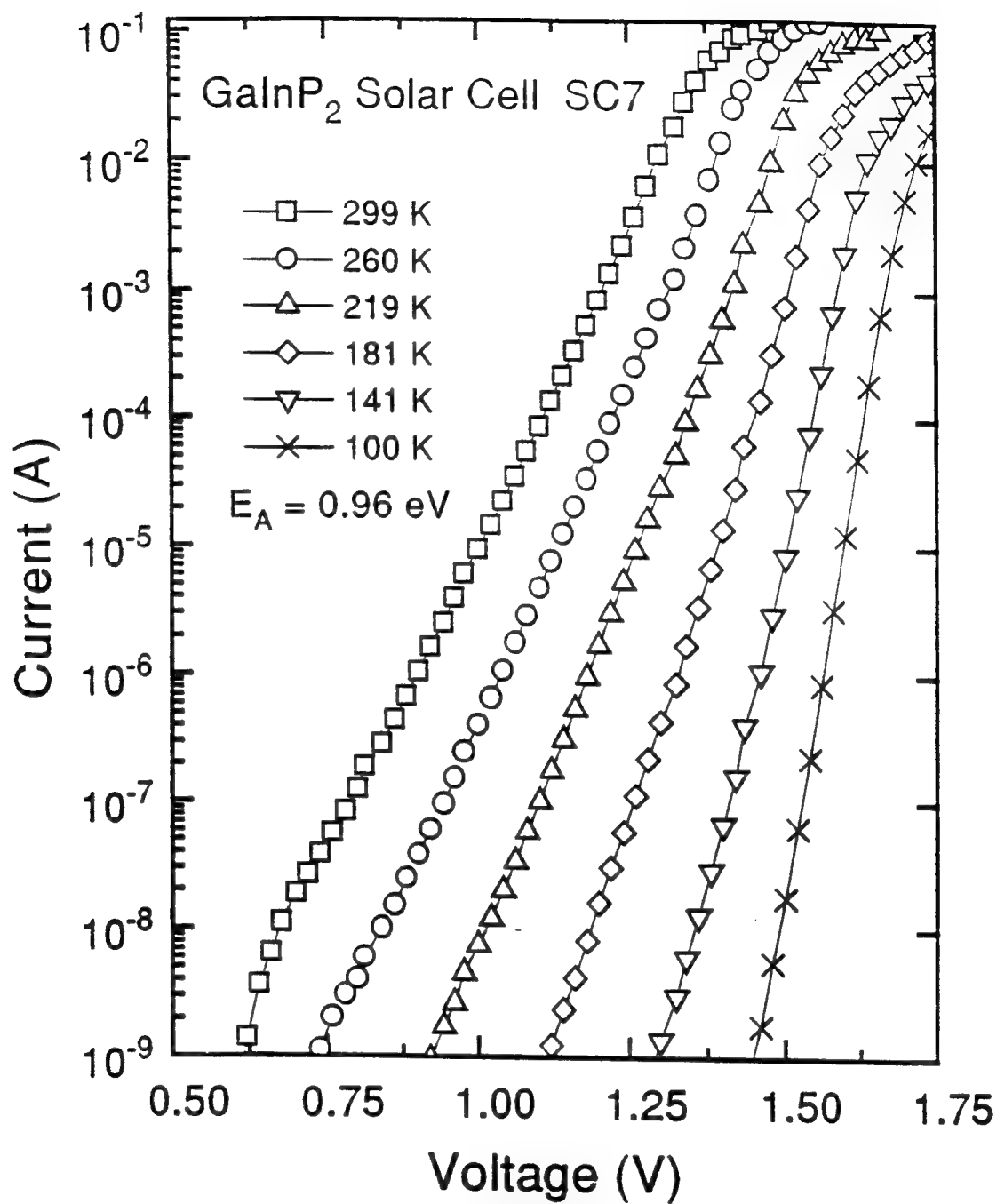


Figure 27. Forward-bias dark I-V curves as a function of temperature for a "well-behaved" GaInP<sub>2</sub> solar cell.

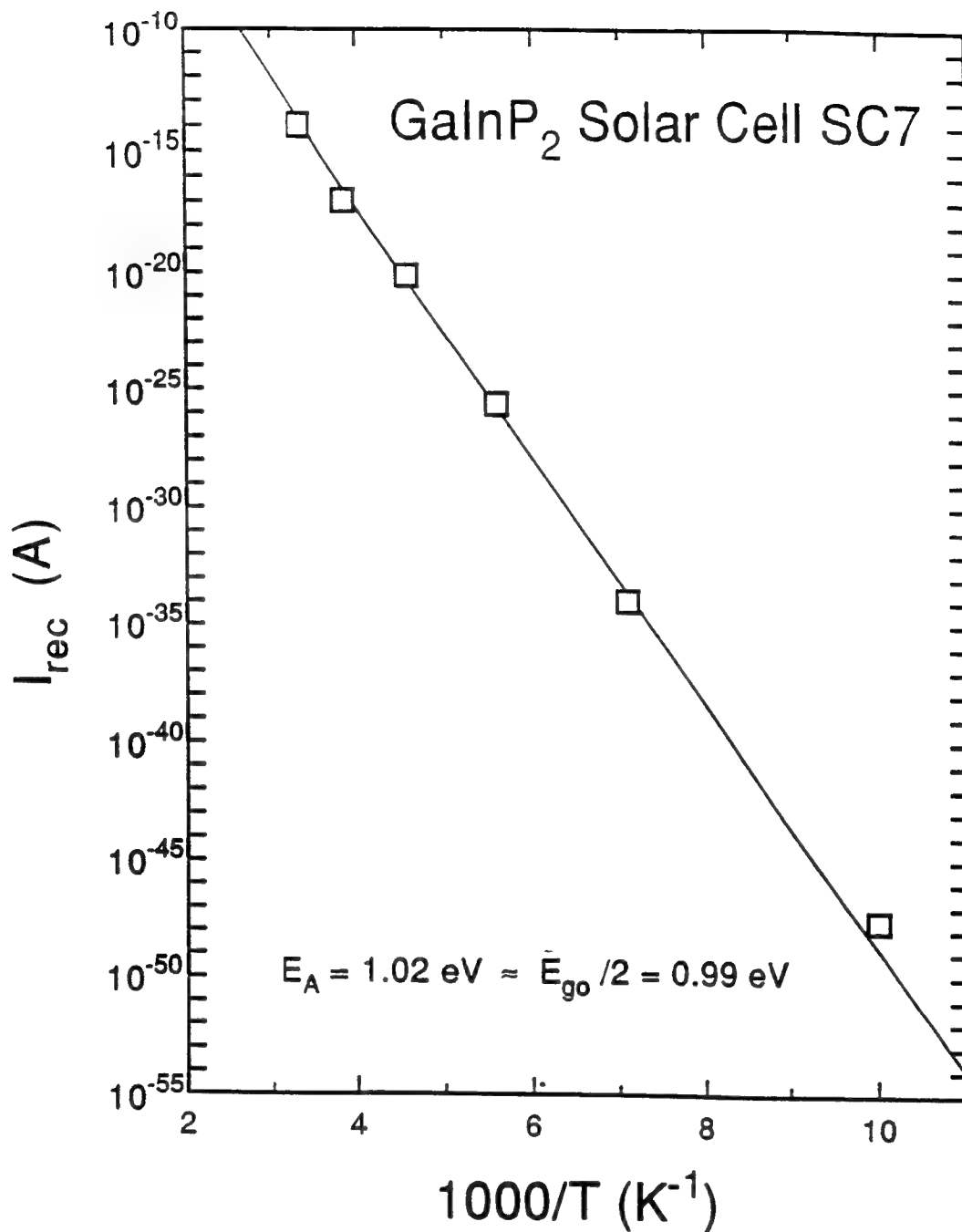


Figure 28. A plot of recombination coefficient  $I_{rec}$  vs.  $1000/T$  for the GaInP<sub>2</sub> solar cell of Figure 27.

GaInP<sub>2</sub> as determined from low temperature photoluminescence measurements at RTI, Inc. Therefore, both the voltage (i.e.,  $A_2 \approx 2$ ) and temperature dependences of dark current found at the solar cell MPP are in good agreement with SNS recombination theory, and hence, recombination current will play a very important role in determining GaInP<sub>2</sub> solar cell efficiency.

The influence of dark current on the GaInP<sub>2</sub> solar cell PV parameters will be further examined. An important correlation between  $J_{\text{dark}}$  and cell efficiency is shown in Figure 29. An increase in  $J_{\text{dark}}$  measured at 1.1 V from  $2.0 \times 10^{-4}$  A/cm<sup>2</sup> to  $7.9 \times 10^{-4}$  A/cm<sup>2</sup> corresponds with the decrease in cell efficiency from 14.6 to 13.2%.  $J_{\text{dark}}$  is noted at  $V = 1.1$  V because this is the solar cell MPP voltage. The reduction in cell efficiency with increasing dark current occurs primarily through the reduction in  $V_{\text{oc}}$  and  $I_{\text{sc}}$  in Eq. (2.5), where the  $ff$  was found to remain nearly constant in the "well-behaved" cells.

The reduction in  $V_{\text{oc}}$  results from an increase in  $J_{\text{rec}}$  and  $J_{\text{dark}}$  in accordance with Eqs. (2.8) and (2.11). From Eq. (2.11),  $J_{\text{dark}}$  is shown to be linearly proportional to  $J_{\text{rec}}$  when the current is dominated by recombination. Hence, the observed increase in  $J_{\text{dark}}$  shown in Figure 29 for the "well-behaved" cells results from an increase in  $J_{\text{rec}}$ . This trend is shown in Figure 30, where the influence of  $J_{\text{rec}}$  on both  $J_{\text{dark}}(1.1 \text{ V})$  and  $V_{\text{oc}}$  for the "well behaved" GaInP<sub>2</sub> cells is seen. Least squares fits through the data are shown as solid lines. Values of  $J_{\text{dark}}$  are shown to increase in a linear fashion with increasing  $J_{\text{rec}}$ , and as expected, values of  $V_{\text{oc}}$  decrease.

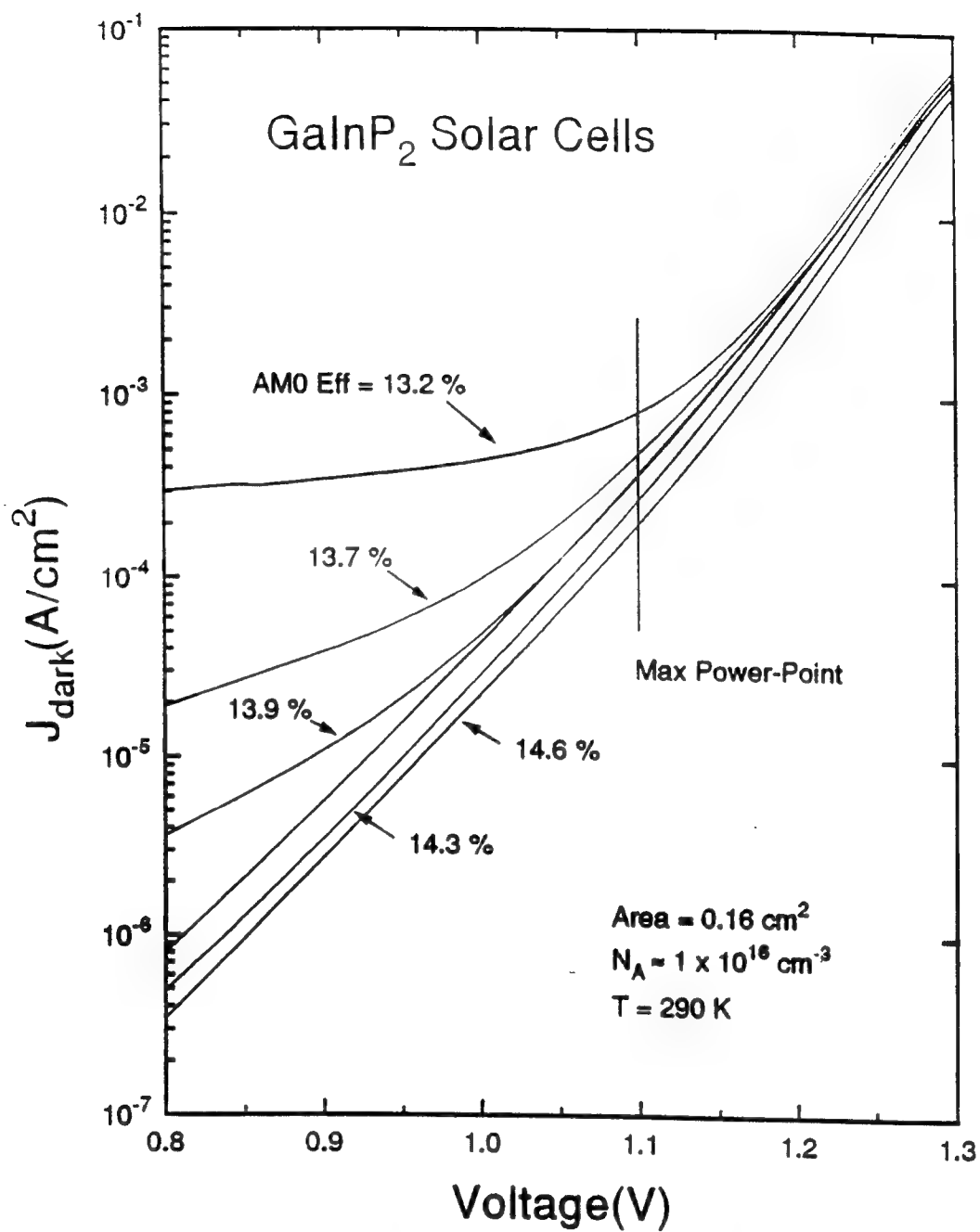


Figure 29. Forward-bias dark I-V curves for single junction n<sup>+</sup>p GaInP<sub>2</sub> solar cells showing a correlation between the magnitude of dark current and AM0 conversion efficiency.

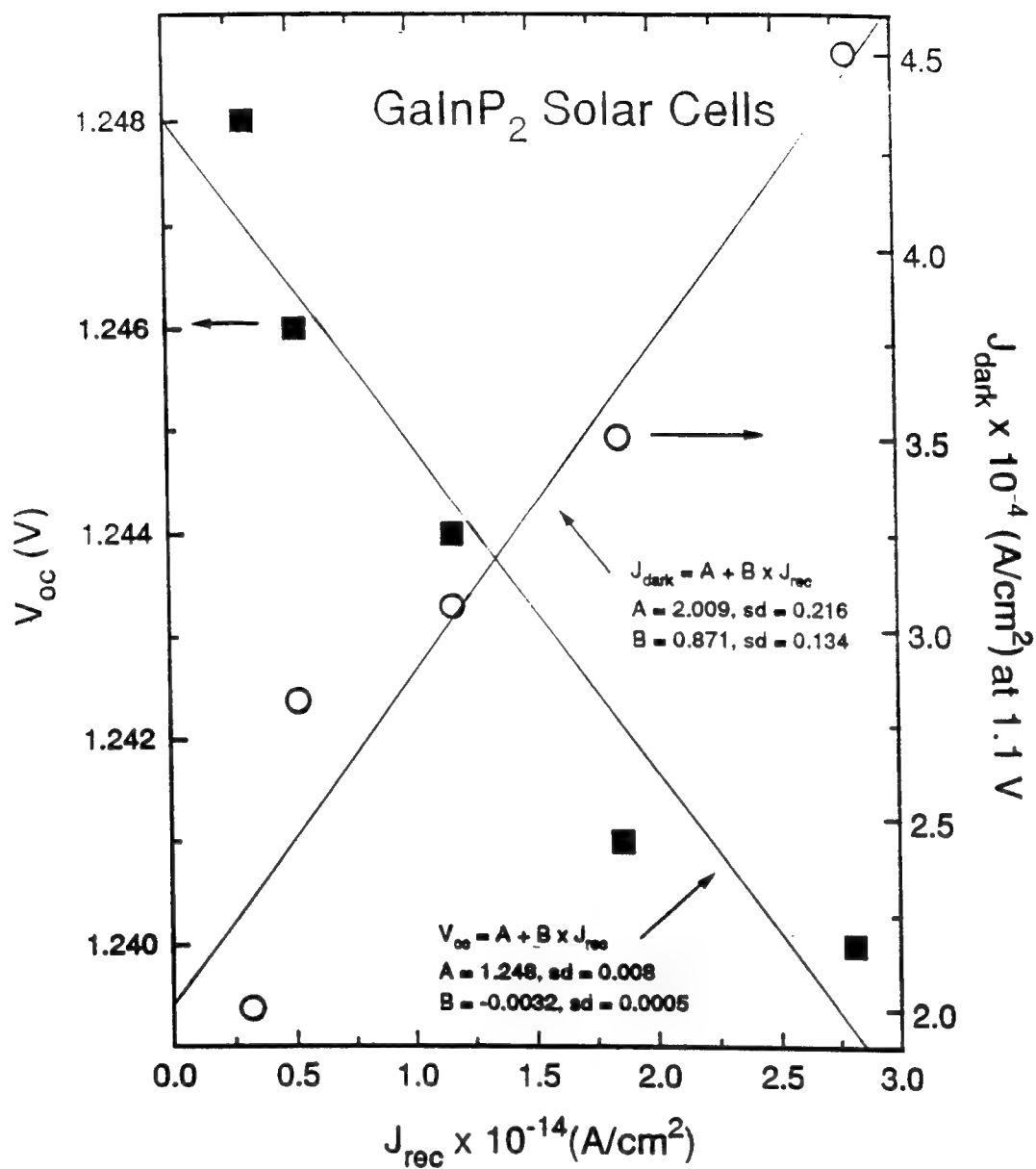


Figure 30. GaInP<sub>2</sub> solar cell open-circuit voltage,  $V_{oc}$ , and dark current density,  $J_{dark}$ , versus dark current recombination coefficient,  $J_{rec}$ .



Measured values of  $V_{oc}$  are within 6-8 % of values calculated using Eq. (2.8) when the value of 2 resulting from ideal recombination was replaced with the measured values of  $A_2$  given in Table II. This result indicates that  $V_{oc}$  is indeed limited by recombination dark current. As was discussed in the theory, the observed increase in  $J_{rec}$  shown in Table II and Figure 30 can be explained by an increase in SRH-type recombination within the junction. Variations in doping density,  $N_A$ , and/or the minority carrier lifetimes,  $\tau_n$  and  $\tau_p$ , will directly affect  $J_{rec}$  through Eq. (2.52), where  $W_d \propto N_A^{-1/2}$ , yielding  $J_{rec} \propto [\tau_n \tau_p N_A (V_{bi} - V)]^{-1/2}$ . The effect of  $N_A$  on  $J_{rec}$  and  $A_2$  will be discussed in the next chapter.

It is interesting to note that excessive junction current with  $A_2 \geq 2$  was also found to limit the efficiency of NREL's GaInP<sub>2</sub> solar cells. "Well-behaved" and "leaky" dark I-V curves for GaInP<sub>2</sub> top cells utilized in NREL's world-record GaInP<sub>2</sub>/GaAs cell design are shown in Figures 31 and 32, respectively. The MPP voltage of NREL's best GaInP<sub>2</sub> cells is reported to be ~1.25 V (Friedman *et al.*, 1991:358). For the "leaky" I-V curves of Figure 31, current with  $A_2 > 2$  is found near the MPP voltage, whereas for the "well-behaved" cell in Figure 32, dark current at the MPP exhibits  $A_2 \approx 2$  behavior. These I-V curves are similar to those shown in Figure 29. Thus, recombination dark current, as well as leaky shunt-current, also appears to play an important role in the NREL cells. The 0.25 M $\Omega$  shunting-current that dominates at voltages of less than 1 V in Figure 32 is due to a parasitic shunt resistance that is part of NREL's solar simulator set-up. The

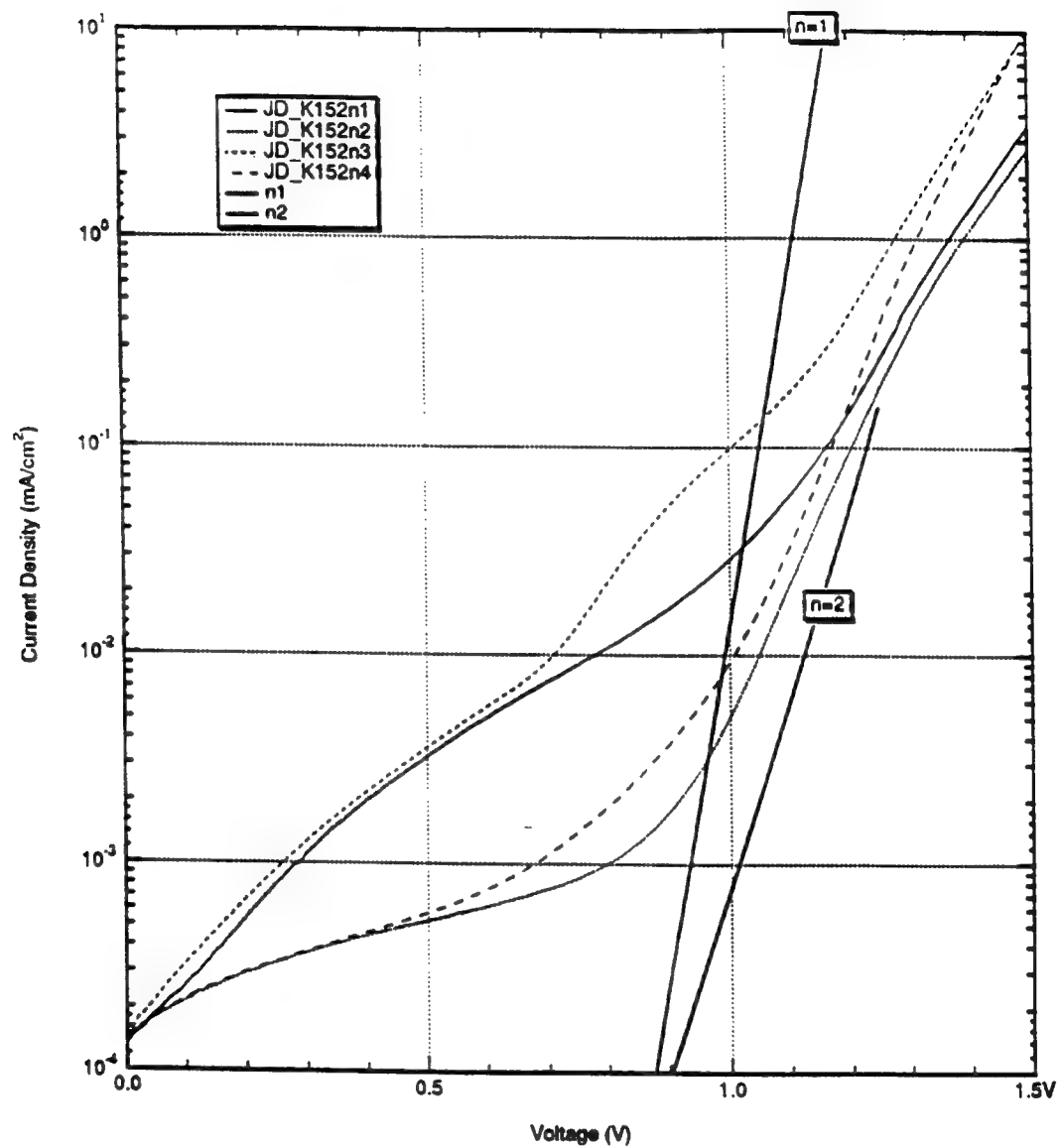


Figure 31. Forward-bias dark I-V curves for "leaky" NREL  $n^+p$  GaInP<sub>2</sub> solar cells.

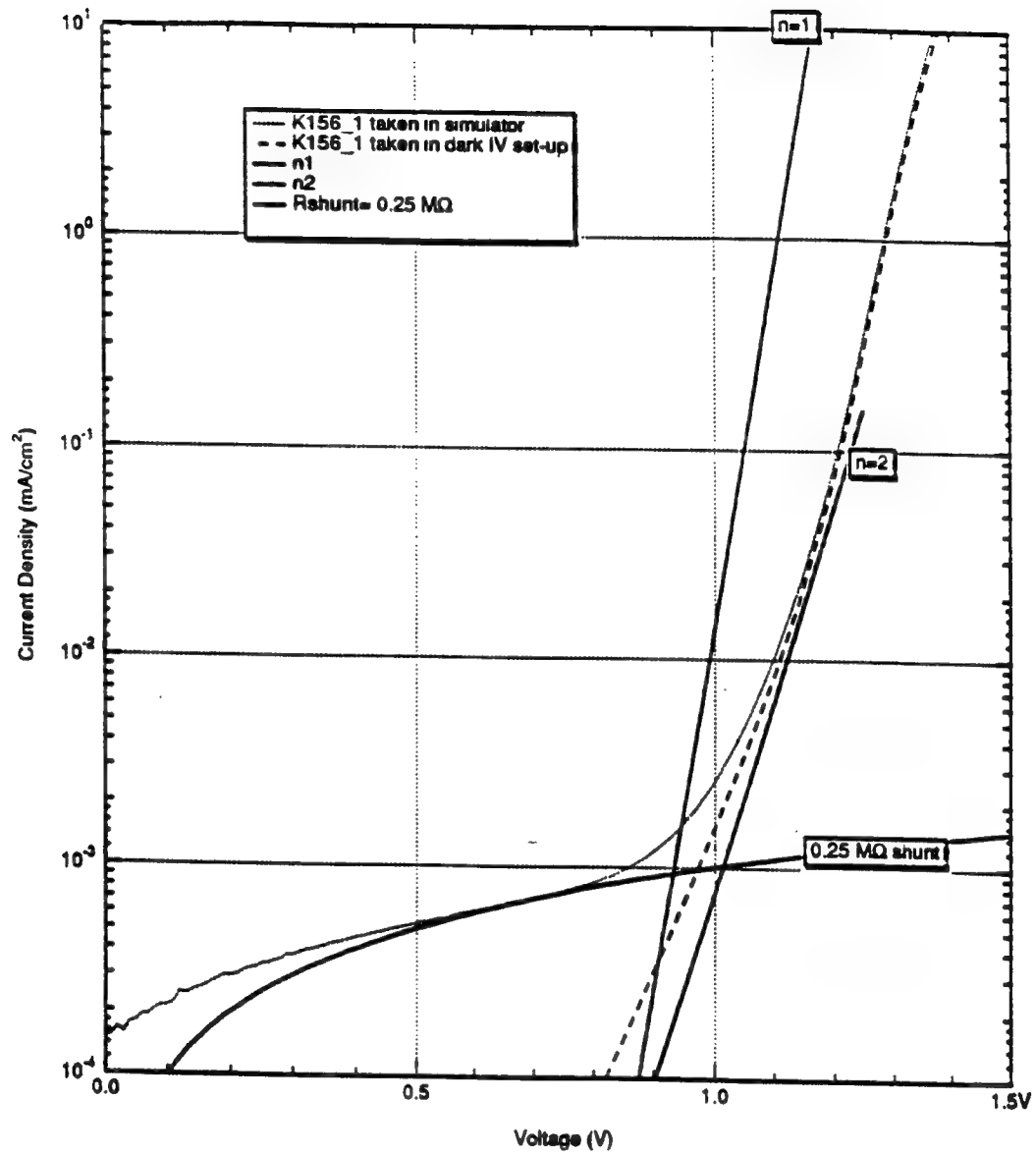


Figure 32. Forward-bias dark I-V curves for a "well-behaved" NREL n<sup>+</sup>p GaInP<sub>2</sub> solar cell.

source of the  $A_2 > 2$  shunting-current at the MPP voltage of the "leaky" cells was not known by NREL, but they suspected physical wafer damage due to possible scratches, morphological defects grown into the crystal, or spurious doping spikes might be responsible. The initial motivation for conducting this research was actually sparked by the anomalous I-V behavior reported in the NREL cells. In the sections ahead, similar  $A > 2$  shunting-current will be shown to be due to carrier tunneling, and the source of such current is found to be related to crystal defects resulting from GaInP<sub>2</sub>-GaAs lattice mismatch.

### **Solar Cell Photocurrent**

The factors that contribute to enhancing junction dark current in solar cells can also affect the cell's photocurrent. The value of solar cell  $J_{sc}$  can be significantly influenced by carrier recombination. Also, the maximum value of  $V_{oc}$  will be affected by  $J_{sc}$ . Figure 33 shows how  $J_{sc}$  decreases with increasing  $J_{rec}$  for the "well-behaved" GaInP<sub>2</sub> solar cells. The reduction in  $J_{sc}$  can be explained in terms of a reduction in carrier lifetime,  $\tau$ , and carrier diffusion length,  $L$ , in the bulk of the solar cell. A reduction in  $\tau$  and  $L$  result from an increase in SRH-type recombination. An expression for  $\tau$  resulting from SRH recombination theory was derived in the theory section, where  $\tau = (N_t v_{th} \sigma)^{-1}$ , and  $L = (\tau D)^{1/2}$ . Besides bandgap,  $L$  is most important parameter affecting  $J_{sc}$ . A derivation of the photocurrent density,  $J_{ph}$  ( $J_{ph} = I_{sc}/S$  under short-circuit conditions), showing the dependence of  $J_{ph}$  on  $L$ , is given in Appendix A. As stated previously, in

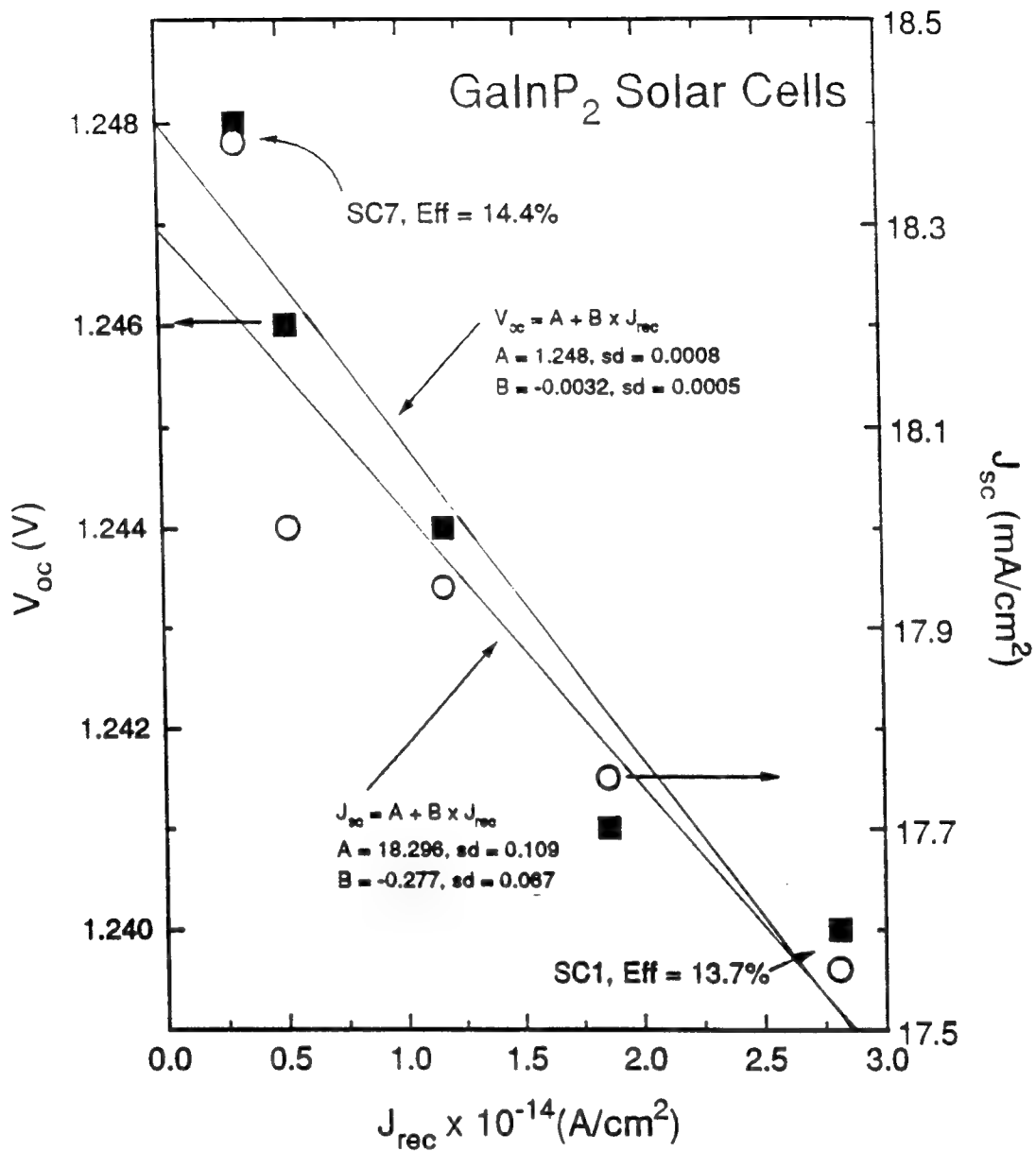


Figure 33. GaInP<sub>2</sub> solar cell open-circuit voltage,  $V_{oc}$ , and short-circuit current density,  $J_{sc}$ , versus dark current density recombination coefficient,  $J_{rec}$ .

conventional Si solar cells,  $J_{sc}$  is generally found to be proportional to  $\ln(L)$ . Thus, SRH recombination is not only responsible for the  $A \approx 2$  dark current that reduces  $V_{oc}$ , but it also explains the reduction of  $J_{sc}$  with increasing  $J_{rec}$  shown in Figure 33. Determining the factors that control carrier recombination in the GaInP<sub>2</sub> solar cell is, therefore, very important.

### **Dark Shunting-Current and "Leaky" Solar Cells**

Dark current due to a combination of transport mechanisms in "well-behaved", "leaky", and "very leaky" GaInP<sub>2</sub> solar cells is shown in Figure 34. As mentioned, the recombination term in Eq. (2.11) describes the I-V curves of the "well-behaved" cells between voltages of 0.8 - 1.2 V. For the "leaky" and "very-leaky" cells of Figure 34, the dark current was found to vary as  $I_0 \exp(BV)$  between voltages of 0.6 and 1.0 V, where B is a constant and V is the junction voltage. The parameters  $I_0$  and B are empirical, but have a theoretical basis related to tunneling effects in heterojunctions (Hovel, 1975:54). The origin of this tunneling current is due to local damage in the junction (Stirn, 1972:72), or leakage at the periphery (Hovel, 1975:53). At room temperature, values of B ranged from ~3.8 in the 13.2 % efficiency cell to 9.6 in the 13.9% efficiency cell. Corresponding values of  $I_0$  ranged from  $\sim 10^{-5}$  to  $10^{-8}$  A. It is interesting to note that values of B between 3.8 - 9.6 at room temperature correspond to an ideality factor of  $A_3 = 4.2 - 10.5$  when considering the equivalent expression of  $I_0 \exp(BV) = I_0 \exp(qV/A_3 kT)$ . A mechanism for dark current with  $A > 4$  has been proposed as due to excessive

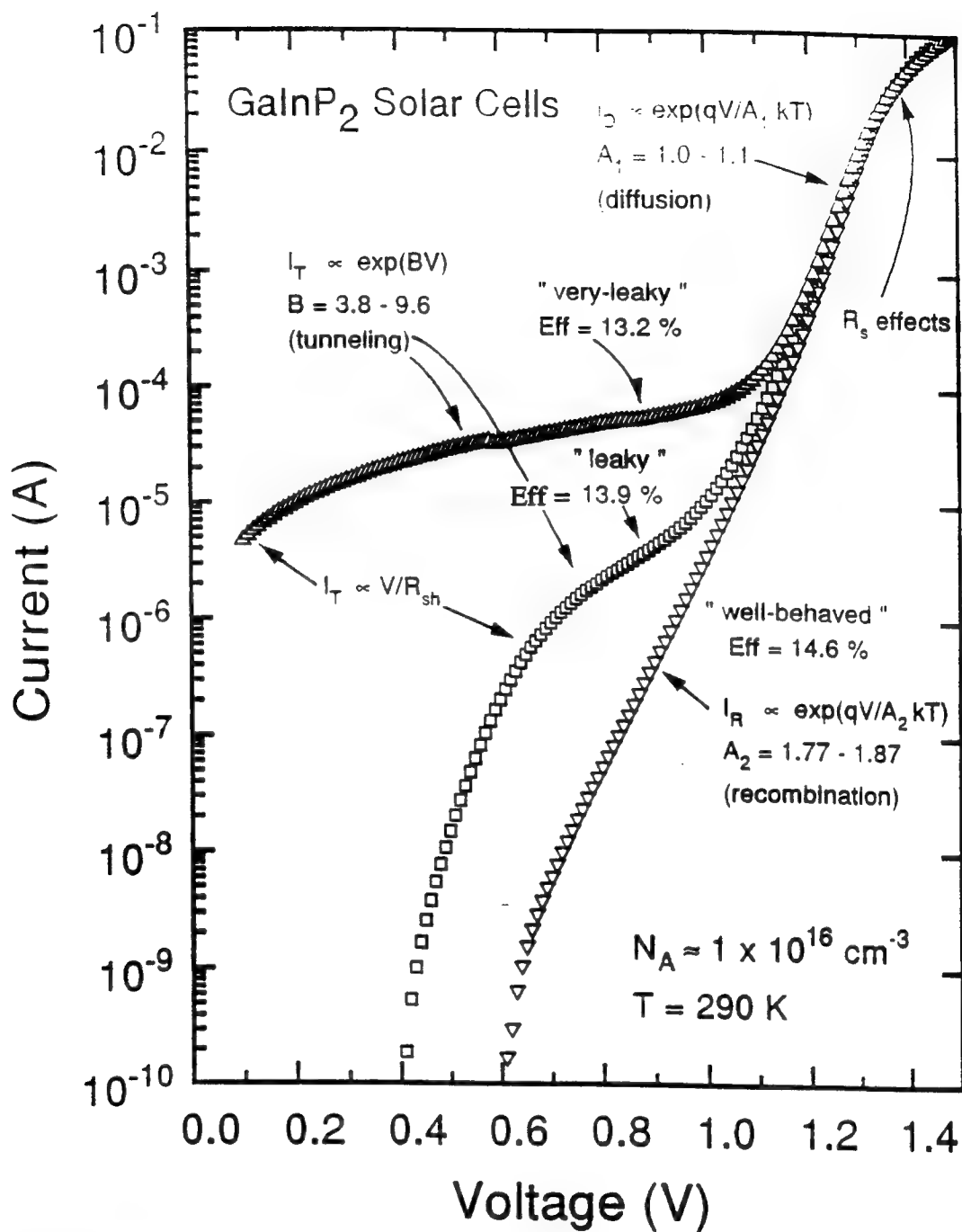


Figure 34. Forward-bias dark I-V curves for GaInP<sub>2</sub> solar cell showing behavior due to carrier diffusion, recombination, and tunneling.

surface leakage current at the perimeter of the p-n junction (Sah, 1962:94). However, in our "leaky" cells, excess shunting-current will be shown to be related to the presence of surface defects.

In Figure 34, the behavior of the I-V curves for voltages greater than  $\sim 1.2$  V can be explained in terms of carrier diffusion and series resistance effects. Although obscured by a series resistance effect, the onset of dark current due to carrier diffusion of the form described by Eqs. (2.13) and (2.14) occurs between voltages of 1.2 - 1.35 V. It is noted that it was difficult to obtain accurate values for  $J_{\text{dif}}$  and  $A_1$  from fits of Eq. (2.13) to the data, where  $qV/kT$  was replaced by  $qV/A_1kT$ . However, approximate fits to the I-V data between 1.2 - 1.35 V yielded values of  $J_{\text{dif}} \approx 10^{-25}$  A/cm<sup>2</sup> and  $A_1 \approx 1.1$ .

The presence of diffusion current will not influence the performance of the GaInP<sub>2</sub> solar cells because its magnitude is very small at the cell MPP voltage ( $\sim 1.1$  V). Further, the measured value of solar cell  $V_{\text{oc}}$  ( $\sim 1.24$  V) was consistent with  $V_{\text{oc}}$  predicted by recombination theory. Hence, the recombination current is dominant up to voltages of at least  $\sim 1.24$  V, which is well in excess of the cell's MPP voltage. The rolling off of the I-V curves seen in Figure 34 at voltages greater than  $\sim 1.35$  V is due to series resistance effects in accordance with Eqs. (2.11) and (2.12). The effect of series resistance is generally not important in small area devices having low currents, and hence low voltage drops. However, series resistance can significantly reduce the ff in larger area solar cells.



The measured values of  $J_{\text{dif}}$  and  $J_{\text{sc}}$  can be used to predict the effect of recombination current on GaInP<sub>2</sub> solar cell efficiency. In Figure 35, several theoretical light I-V curves and resulting power output densities versus  $J_{\text{rec}}$  are shown. The data was obtained using Eqs. (2.1) and (2.11) where  $J_L = J_{\text{sc}}$ , and series resistance and shunting-current effects have been neglected. The value of  $J_{\text{dif}} \approx 1 \times 10^{-25} \text{ A/cm}^2$  found above was used. Also, in Figure 33, the relationship between measured  $J_{\text{sc}}$  and  $J_{\text{rec}}$  was found using a least squares fit, giving  $J_{\text{sc}} \approx 0.0183 \text{ A/cm}^2 + 2.77 \times 10^{10} \times J_{\text{rec}} (\text{A/cm}^2)$ . The power density of the solar cell is represented by the downward dashed lines. The resulting solar cell PV parameters are summarized in Table III. As expected, values for  $V_{\text{oc}}$ ,  $V_m$ ,  $J_m$ ,  $\text{ff}$ , and  $\text{Eff}$  all decrease with increasing  $J_{\text{rec}}$ . The calculated efficiencies in Table III are very consistent with the measured efficiencies given in Table II. This is not surprising, however, considering that experimental values for  $J_{\text{dif}}$  and  $J_{\text{sc}}$  were used. However, the data does show that the value of  $J_{\text{rec}}$  plays a significant role in determining cell efficiency.

### **GaInP<sub>2</sub>/GaAs Lattice Mismatch versus Solar Cell Performance**

When examining the top surface of the nine solar cells under magnification, a number of line-like defects were observed. A photograph of several line-defects found atop the "leaky" 13.2% efficient GaInP<sub>2</sub> cell is shown in Figure 36. The width of defects were found to be  $\sim 5 - 15 \mu\text{m}$  from SEM photos, and in some cases the length of the line-defects crossed the entire solar cell. The orientation of

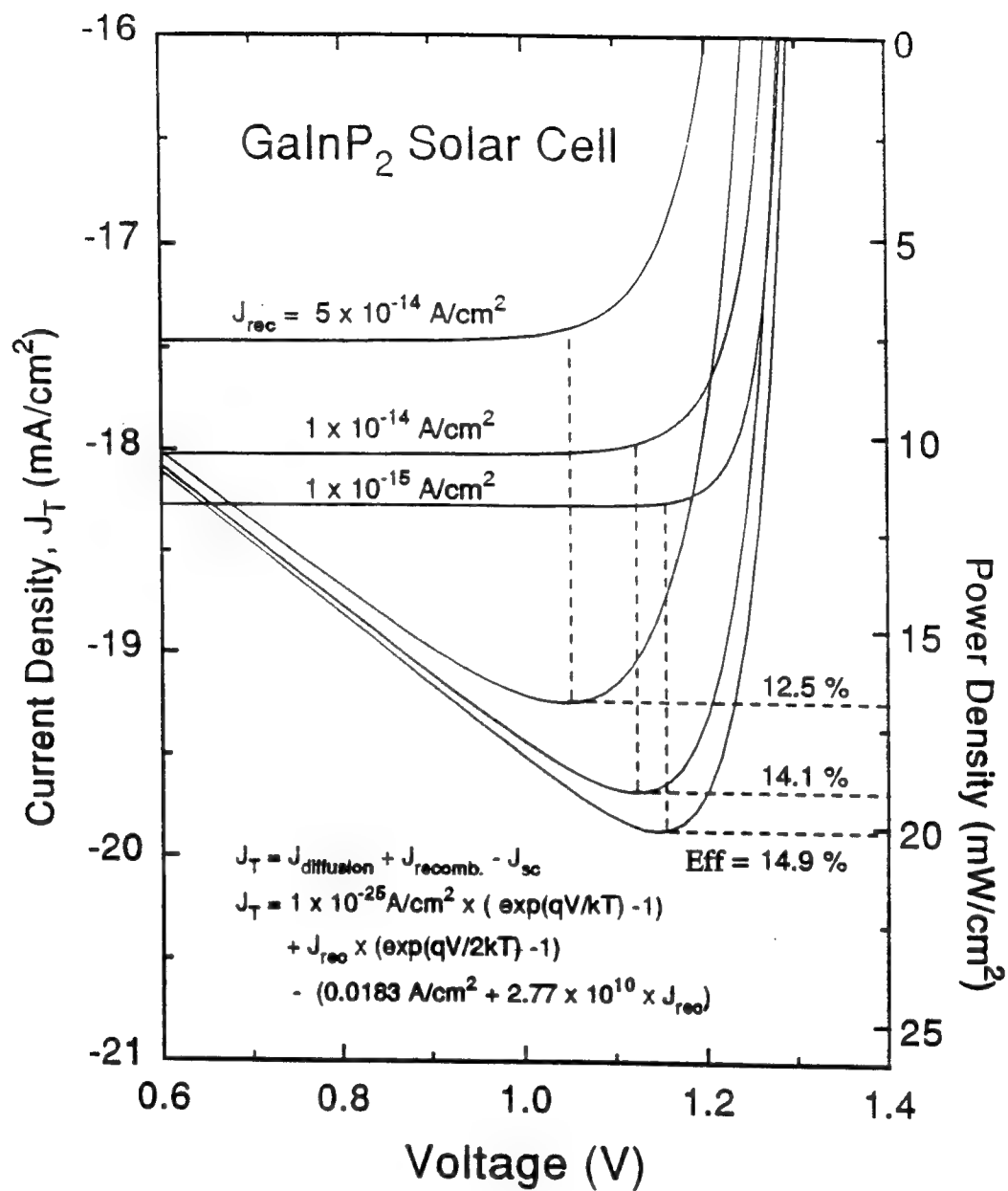


Figure 35. Theoretical AM0 light I-V curves for a GaInP<sub>2</sub> solar cell for various recombination current density coefficient,  $J_{rec}$ . The maximum power density is represented by the minimums of the pointed curves.

**Table III. GaInP<sub>2</sub> n<sup>+</sup>p solar cell photovoltaic parameters versus dark recombination current density, J<sub>rec</sub>**

<u>J<sub>rec</sub></u> <u>(A/cm<sup>2</sup>)</u>	<u>J<sub>sc</sub></u> <u>(mA/cm<sup>2</sup>)</u>	<u>V<sub>oc</sub></u> (V)	<u>J<sub>m</sub></u> <u>(A/cm<sup>2</sup>)</u>	<u>V<sub>m</sub></u> (V)	<u>ff</u> (%)	<u>P<sub>m</sub></u> (W)	<u>Eff</u> (%)
5x10 <sup>-14</sup>	17.47	1.241	16.13	1.052	0.76	0.0169	12.5
1x10 <sup>-14</sup>	18.02	1.282	17.46	1.122	0.85	0.0191	14.1
1x10 <sup>-15</sup>	18.27	1.296	17.57	1.153	0.86	0.0201	14.9



Figure 36. A photograph showing a portion of the 13.6% GaInP<sub>2</sub> solar cell die containing line-defects. The line-defects extend across the solar cell and mesa diodes.

a majority of the line-defects was parallel to the [100] crystal axis. The nine solar cells forming a 3 x 3 matrix were originally cut from one 1" x 1" wafer. A correlation between the number of line-defects on each cell, the location of the cell on the original wafer, and the resulting cell dark currents and conversion efficiencies were found. The efficiency distribution across the 1" x 1" wafer is shown in Figure 37. The cells labeled 1 - 4 in the top-left quadrant of the wafer contained a relatively few number of line-defects that propagated across a portion of the cells, typically 2 - 3, and consequently the cells exhibited the highest relative efficiencies. The 14.6 % cell had two very short line defects near the edge of the device. The lower efficiency cells cut from the right sides of the wafer had 5 - 8 partial line-defects per cell, and the lowest efficiency cells cut from the bottom of the wafer in Figure 37 had 7 - 10 line-defects per cell, many of which that crossed the entire cell. A definite correlation between the line-defect density, the amount of cell shunting-current, and the value of  $J_{sc}$  is found in the data in Table II and Figures 29 and 37. The cells exhibiting the "leaky" I-V curves and lowest  $V_{oc}$ ,  $J_{sc}$ , and Eff contained the highest density of line-defects.

The size and number of line-defects propagating down through the p-n junction will determine the magnitude of resulting shunting-current. Deep level defects resulting from line-defect induced by crystalline damage will increase the number of recombination and tunneling centers within the solar cell junction. An increase in the number of tunneling centers will increase current shunting of the form

<b>14.3 %</b> <b>(1)</b>	<b>14.2 %</b> <b>(2)</b>	<b>13.7 %</b> <b>(5)</b>
<b>13.9 %</b> <b>(3)</b>	<b>14.6 %</b> <b>(4)</b>	<b>13.6 %</b> <b>(6)</b>
<b>13.4 %</b> <b>(7)</b>	<b>13.4 %</b> <b>(8)</b>	<b>13.2 %</b> <b>(9)</b>

**Figure 37.** Solar cell efficiency distribution across the 1" x 1" GaInP<sub>2</sub>/GaAs wafer.

$I_{0exp}(BV)$  (Ribben and Feucht, 1966:1055). Tunneling in the junction can also be responsible for current shunting of the form  $V/R_{sh}$  (Banerjee and Anderson, 1986:38), where the source of  $R_{sh}$  is due to a combination of tunneling and trapping-detrapping of carriers through defects states in the junction. Evidence of  $V/R_{sh}$  current in the solar cells is shown in Figure 34, and current of this form will be shown to be important in smaller GaInP<sub>2</sub> test diodes. Therefore, the observed increase in shunting-current that corresponds with the increased number of solar cell line-defects can be explained by increased carrier tunneling through defects in the GaInP<sub>2</sub> junction.

The reduction of  $J_{sc}$  in the lower efficiency "leaky" cells shown in Figure 26 and Table II can also be explained by considering the effects of the line-like defects. These defects can also introduce bulk SRH recombination centers in the emitter and base regions of the cell that reduce  $\tau$  and  $L$ , and consequently  $J_{sc}$ . Since GaInP<sub>2</sub> is a direct bandgap material, the solar absorption coefficient is relatively large, and a majority of super-bandgap photons will be absorbed less than 1  $\mu m$  from the top surface (Cavicchi *et al*, 1991:2-18). The line-defect induced bulk recombination centers located within this 1  $\mu m$  layer will trap photocarriers in the vicinity, and prevent them from reaching the junction where they can contribute to  $J_{sc}$ . SEM observation of the GaInP<sub>2</sub> solar cell mesa edges reveal line-defects that appear to originate down below the GaInP<sub>2</sub> top surface. In fact, one would expect that such defects may also extend down to the GaAs substrate, considering that the

width of the defects are  $\sim 5 - 15 \mu\text{m}$ , and the thickness of the  $\text{GaInP}_2$  layer is only  $\sim 3.5 \mu\text{m}$ . In any case, the observed localized regions or patches of line-defect-recombination centers will act as photocarrier sinks, and a significant reduction in carrier lifetime in this region can be expected. Thus, a reduction in cell  $J_{sc}$  would result with increased line-defects density, which is consistent with the experimental data of Table II and Figure 26.

It is also important to mention that the line-defects were found to exhibit nonradiative carrier recombination and/or tunneling through electroluminescence measurements. When the  $\text{GaInP}_2$  p-n junction solar cells were forward-biased at 1.5 V into the light-emitting diode (LED) mode, red light of wavelength,  $\lambda \approx 0.67 \mu\text{m}$ , (i.e.,  $E_g = 1.84 \text{ eV}$ ) was emitted. This electroluminescence results from radiative recombination of diffusion current within and near the junction. The onset of  $\text{GaInP}_2$  cell diffusion current was seen to be  $\sim 1.25 \text{ V}$  in Figures 29 and 34. However, the cell area containing the line-defects was observed under magnification to remain totally dark. This suggests that nonradiative carrier recombination and/or tunneling defect centers are located within and/or near the junction directly below the line-defects. This behavior is consistent with increased degradation of solar cell PV parameters with increasing line-defect density.

Problems with  $\text{GaInP}_2/\text{GaAs}$  surface morphology have been reported in the literature (Olsen *et al.*, 1978:5523; Takeda *et al.*, 1991:351; Schmitz *et al.*, 1991:471), and the presence of line-like defects on the surface of the  $\text{GaInP}_2/\text{GaAs}$



chips (GaAs is the substrate) is not surprising. The source of the defects are most probably caused by local strain due to lattice mismatch between GaInP<sub>2</sub> and GaAs.

As mentioned, GaInP<sub>2</sub> is lattice matched to GaAs over a very narrow compositional range, and very slight nonuniformities in the gas phase during MOCVD growth can result in nonstoichiometric strained material (Timmons, 1994). Considering the line-defect vs. cell efficiency data, it is clear that a tight tolerance on lattice mismatch will be required over large area GaInP<sub>2</sub>/GaAs wafers to assure high solar cell yields. High production yields are essential to the practical utilization of GaInP<sub>2</sub> solar cells, where a significant reduction in production cost needs to be achieved before the cells can become economically viable.

#### **Localization of Defects and Small Area Test Diodes**

The localized nature of current-shunting can be seen in the I-V curves of the GaInP<sub>2</sub> solar cells and adjacent mesa diodes. Dark I-V curves for both "well-behaved" and "leaky" GaInP<sub>2</sub> solar cells and adjacent diodes from one die are shown in Figure 38. Each solar cell die contains 12 adjacent test diodes as shown in Figure 23. The diode I-V curves shown in Figure 38 are for the largest diodes of area 0.0025 cm<sup>2</sup>. The relative uniformity of the diode I-V curves is shown here, where only one of the four diodes is shown to exhibit shunting behavior similar to that found in the "leaky" solar cell shown in this figure. It was found that 19 of 108 diodes examined on the solar cell die exhibited similar current-shunting, i.e., less than 1 in 4. In contrast, 6 of the 9 GaInP<sub>2</sub> solar cells exhibited appreciable

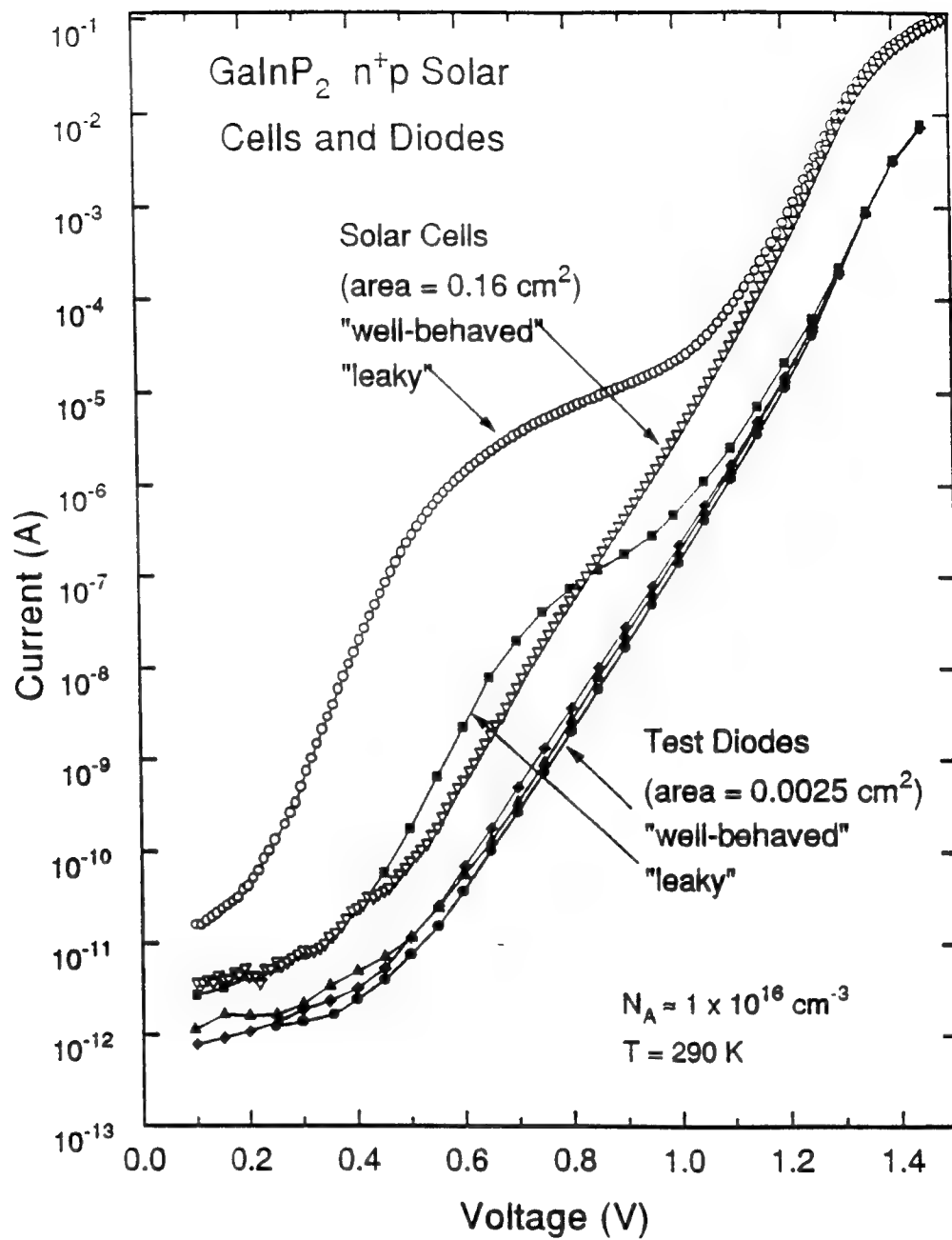


Figure 38. Forward-bias dark I-V curves for both "well-behaved" and "leaky" low doped GaInP<sub>2</sub> solar cells and mesa diodes.

shunting behavior. Thus, the mesa diodes were found to behave more consistently compared to the solar cells.

Although in some cases it was difficult to detect defects below the Au ohmic contacts on several of the diodes, many of the "leaky" diodes contained discernable line-like defect structures running through them. Two diodes with line-defects are shown in Figure 36. This indicates that although the shunting-current paths may be spread out and localized, and occasionally a diode happens to fall on such a line-defect path that results in "leaky" behavior, the shunting paths act in parallel and contribute to "leaky" behavior in a majority of the solar cells. This result is very important, because it shows the utility of the small mesa diodes in the study of "well-behaved" GaInP<sub>2</sub> solar cells. A very large number of mesa diodes can be processed on a small piece of wafer, i.e. approximately 30 diodes on the same wafer area used by the solar cells above, and a very large number of them could be well-behaved. The diodes can be used to study the basic behavior of recombination current in the larger cells, to identify the defect centers responsible for such current, and to study the effects of space radiation damage and thermal annealing. One important issue must first be addressed. How does the electrical behavior of the smaller diode differ from that in larger area solar cells? In Figure 38, the ratio of "well-behaved" solar cell-to-diode dark current measured at 1.1 V is ~40. On the other hand, the ratio of the solar cell-to-diode area is 64. Thus, the solar cell dark current does not scale linearly with device p-n junction area as

was expected. To examine the cause of this discrepancy, diodes of differing junction area adjacent to the solar cells, as shown in Figure 23, were examined.

### **Dark Current vs P-N Junction P/A Ratio in GaInP<sub>2</sub> Devices**

A set of I-V curves for 12 diodes adjacent to a "well-behaved" cell (SC3, Eff = 14.2%) is shown in Figure 39. The area of the diodes are 0.0001, 0.0009, and 0.0025 cm<sup>2</sup>. Values of ideality factor,  $A_2$ , for the diodes were measured to be 1.84 - 1.90 between voltages of 0.6 - 1.3 V. The similarity in slope of the diode and solar cell I-V curves can be seen in Figures 38 and 39. This result shows that the dominant current transport mechanism in the diodes is also due to recombination. To compare the relative magnitude of dark current density in the devices, it was convenient to consider the device current density,  $J_{\text{dark}}$ , versus device junction perimeter-to-area (P/A) ratio. A plot of  $J_{\text{dark}}$  versus P/A ratio for the solar cells and diodes is shown in Figure 40. The solar cells have a P/A ratio of 9, and the diodes of area 0.0025, 0.0009, and 0.0001 cm<sup>2</sup> have a P/A ratio of 80, 130, and 400, respectively. Values of  $J_{\text{dark}}$  were measured at 1.1 V because this is the approximate solar cell MPP voltage. The value of  $J_{\text{dark}}$  will remain constant when the dark current scales linearly with device area. However, the  $A_2 \approx 2$  dark current density is shown to be proportional to the device P/A ratio as seen in Figure 40. The increase in  $J_{\text{dark}}$  with increasing P/A ratio indicates that a contribution of dark recombination current must be present at the perimeter of the p-n junction. Similar behavior has been reported in Si, GaAs, AlGaAs, and GaP

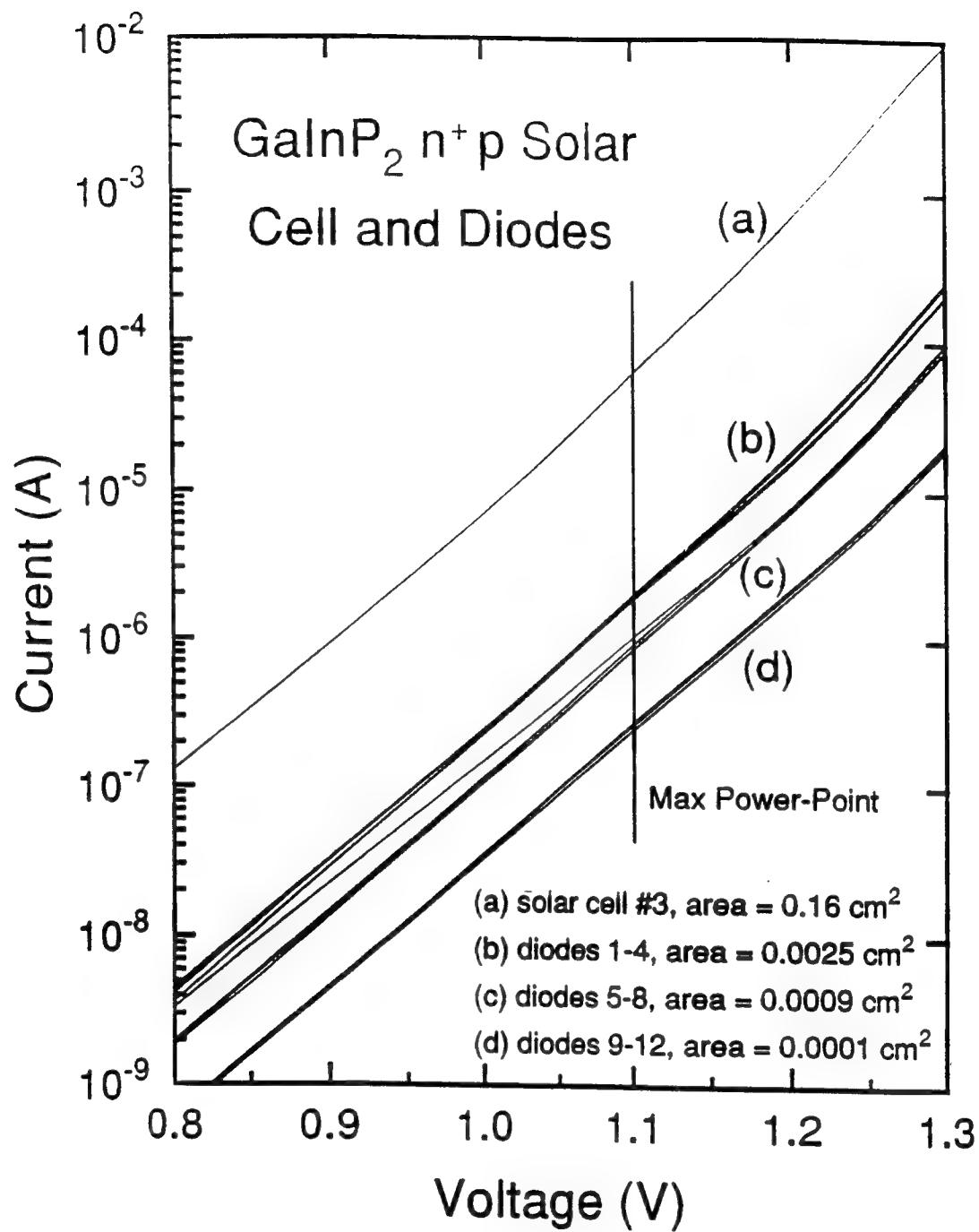


Figure 39. Forward-bias dark I-V curves for GaInP<sub>2</sub> n<sup>+</sup>p junctions of different area.

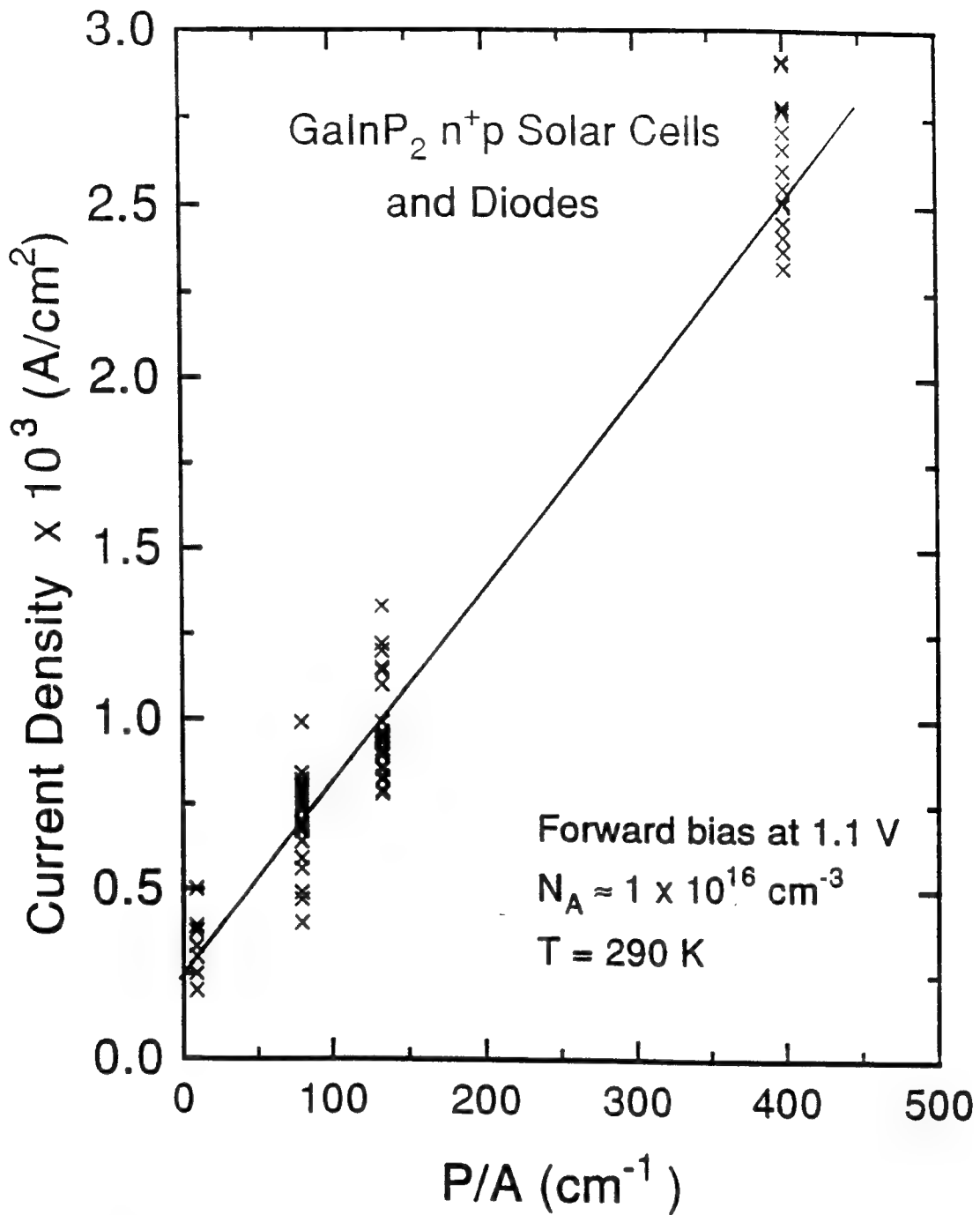


Figure 40. A plot of total current density vs. perimeter-to-area ratio ( $P/A$ ) for  $\text{GaInP}_2$   $n^+p$  junctions of different area at a forward-bias voltage of 1.1 V.

diodes (DeMoulin *et al.*, 1988:368; Sah, 1962:94; Henry *et al.*, 1978:3530; Henry and Logan, 1978:1471).

As discussed in the theory section, a mechanism explaining  $A \approx 2$  recombination current at the perimeter of the p-n junction was proposed by Henry and Logan. In this model, a nearly constant ratio of electron,  $n$ , and hole,  $p$ , densities is required to maintain charge neutrality at the junction perimeter in the presence of Fermi level pinning. It is reminded that the perimeter of the devices was formed via mesa etching, and that the resulting p-n junction was exposed to air at the mesa perimeter interface. Electrons and holes present at the interface recombine through surface states at the junction interface. Surface states result from unsatisfied electronic "dangling" bonds at the semiconductor surface. Logan's model predicts a carrier recombination rate,  $U$ , proportional to  $(np)^{1/2} = n_i \exp(qV/2kT)$ , showing the  $A \approx 2$  current dependence on voltage. The observed increase in  $J_{\text{dark}}$  with increasing device  $P/A$  ratio shown in Figure 40 is consistent with this model, and perimeter recombination in the  $\text{GaInP}_2$   $n^+p$  junction is reported here for the first time.

The value of  $J_{\text{dark}}$  at the  $P/A = 0$  intercept includes current due to diffusion ( $A \approx 1$ ) and current due to recombination in the interior (bulk) of the junction. However, the magnitude of diffusion current at 1.1 V was estimated using the measured values of  $A_1$  and  $J_{\text{dif}}$  from higher voltage extrapolation, and was determined to be many orders of magnitude smaller than the total current from the

interior of the junction. Although it was difficult to accurately determine the contribution of the perimeter current to the total current in the larger solar cells, it was estimated to be about 15% for  $P/A = 9$ . However, it is evident that the perimeter current dominates in the smaller area diodes, and on the average, it is as high as 60, 75, and 90% of the total current in the diodes with  $P/A = 80, 130$ , and 400, respectively. Also, it is noted that the magnitude of perimeter current would become negligible in practical larger area solar cells, for example, having areas of 2 cm x 2 cm ( $P/A = 2$ ) or 4 cm x 4 cm ( $P/A = 1$ ).

An estimate for the perimeter surface recombination rate,  $s_0 L_s$  (cm<sup>2</sup>/sec) for the GaInP<sub>2</sub> n<sup>+</sup>p junction can be made, where  $s_0$  is the intrinsic surface recombination velocity and  $L_s$  is the surface diffusion length. This follows from the theory of Henry and Logan (Henry and Logan, 1978:1471), where the surface recombination current per unit length,  $I_s$ , at the perimeter of the p-n junction is expressed as

$$I_s = q s_0 L_s n_i \exp\left(\frac{qV}{2kT}\right) \quad (4.1)$$

where

$$I_{recp} = q s_0 L_s n_i . \quad (4.2)$$

Considering the largest diodes in Figure 40 ( $P/A \approx 80$ ), the contribution of perimeter current at 1.1 V in the "well-behaved" devices is estimated to be ~ 50%. Since the value of recombination current at 1.1 V scales with  $I_{rec}$  in accordance with Eq. (2.51), approximately 50% of  $I_{rec}$  will be due to perimeter recombination.



The average measured value of  $I_{rec}$  in these diodes was  $5 \times 10^{-16}$  A, therefore, the contribution of  $I_{rec}$  due to perimeter current,  $I_{recp}$ , is estimated to be  $\sim 2.5 \times 10^{-16}$  A. Using Eq. (4.2), a measured value for  $n_i$  of  $2400 \text{ cm}^{-3}$  for GaInP<sub>2</sub> (measured in the next chapter), and the diode perimeter length of 0.2 cm, a value for  $s_0 L_n \sim 3.3 \text{ cm}^2/\text{sec}$  was obtained. This value is consistent in magnitude with values of  $s_0 L_n \sim 1.0 - 15 \text{ cm}^2/\text{sec}$  reported for AlGaAs p-n junctions (Henry and Logan, 1978:1471; Henry *et al.*, 1978:3530).

In the next chapter, the source of bulk recombination current that dominates in larger area devices is explored. However, before proceeding, a brief set of temperature coefficient data will be presented for the GaInP<sub>2</sub> solar cells. This data is important to the modeling of solar cells operating in the fluctuating hot and cold space environment.

### **GaInP<sub>2</sub> Solar Cell Temperature Coefficients**

Temperature coefficients were measured for several "well-behaved" GaInP<sub>2</sub> solar cells between temperatures of 250 - 400 K. AM0 light I-V curves were measured at temperatures of 250, 300, 350, and 400 K, and values of the short circuit current density,  $J_{sc}$ , open-circuit-voltage,  $V_{oc}$ , fill factor,  $ff$ , and conversion efficiency,  $Eff$ , were obtained. A set of light I-V-T curves for a typical GaInP<sub>2</sub> solar cell is shown in Figure 41. For each cell measured, each parameter was fit to the data with a straight line over the temperature range. The coefficients that resulted were then averaged over 4 "well-behaved" cells, and the final values are

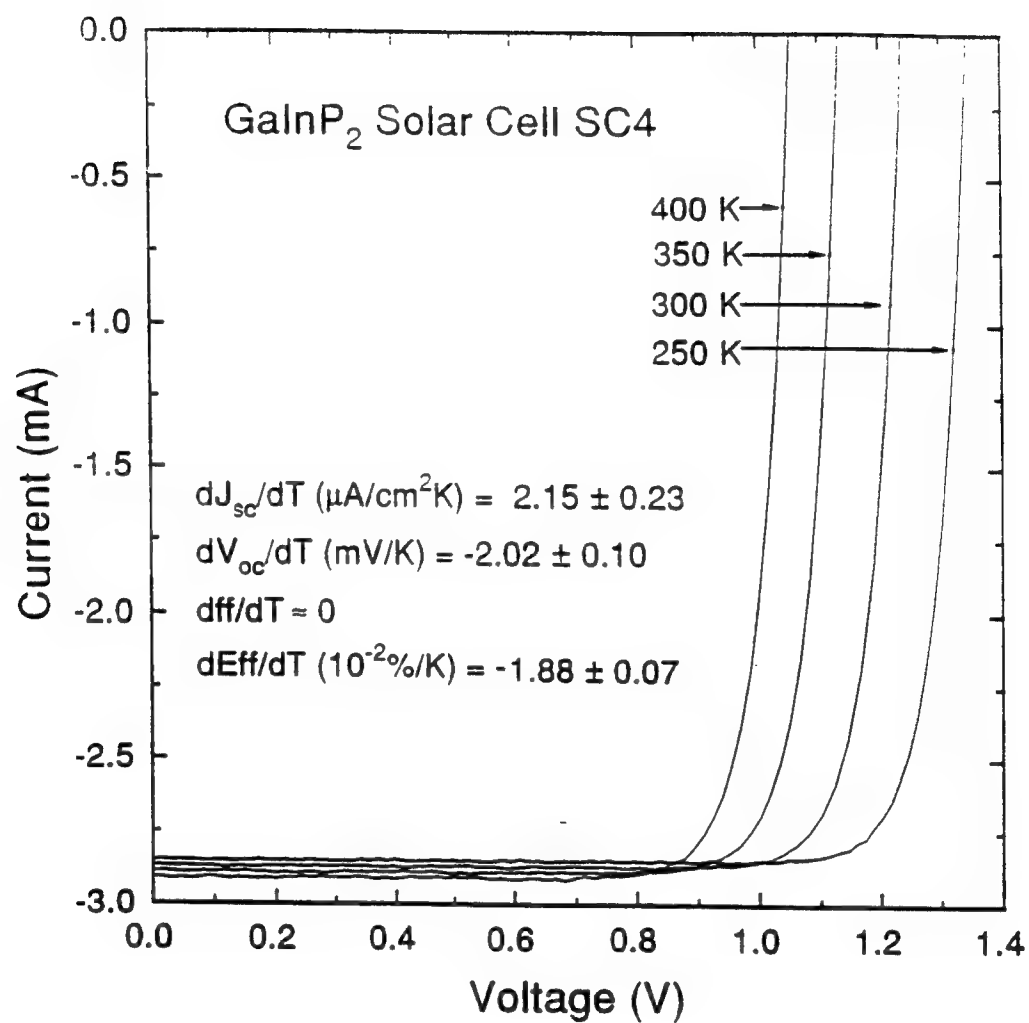


**Figure 41. Forward-bias light-I-V curves as a function of temperature for an n<sup>+</sup>p GaInP<sub>2</sub> solar cell.**

listed in the inset of Figure 41. The individual values for the solar cell parameters are given in Table IV. From Figure 41 and Table IV, values of  $J_{sc}$  and  $V_{oc}$  are seen to increase and decrease, respectively, with increasing temperature. This behavior is consistent with theory. The average value for AM0 conversion efficiency temperature coefficient,  $d\text{Eff}/dT$ , was  $-1.88 \times 10^{-2}\%/K$ , which is less (better) than that reported for GaAs and InP solar cells (Ansbaugh, 1988:6; Walters *et al.*, 1991:42).

The value of  $J_{sc}$  is affected primarily through the terms involved in the minority carrier diffusion length,  $L$ , where  $L = (\mu k T \tau / q)^{1/2}$ . Depending on the type of recombination center that controls the process,  $\tau$  has been observed to vary in Si as  $\propto T^{3/2}$  in some cases, and  $\tau \propto \exp(T)$  in others (Fahrenbruch and Bube, 1983:236). The dominant scattering mechanism determines the temperature dependence of mobility,  $\mu$ . In the case of acoustic scattering,  $\mu \propto T^{-m}$ , where  $m = 1.5$  in the simplest case (Sze, 1981:28). Also, a small shift in the absorption edge energy with temperature will tend to increase  $J_{sc}$  slightly with increasing temperature, and a small increase in  $J_{sc}$  with increasing temperature also occurs due to a change in the absorption coefficient itself. The end result in most solar cells is a slow increase in  $J_{sc}$  with increasing temperature. The value of  $V_{oc}$  decreases with increasing temperature through changes in  $J_{dif}$  or  $J_{rec}$  in accordance with Eqs. (2.6) and (2.23), or (2.8) and (2.57), respectively. In either case,  $V_{oc}$  is predicted to decrease almost linearly with increasing temperature. The solar cell  $ff$  is also

Table IV. Summary of GaInP<sub>2</sub> solar cell photovoltaic parameters measured as a function of temperature

<u>T(K)</u>	<u>Device</u>	<u>I<sub>sc</sub>(mA)</u>	<u>V<sub>oc</sub>(V)</u>	<u>ff(%)</u>	<u>Eff(%)</u>
250	1	2.80	1.34	0.84	14.6
	4	2.86	1.35	0.84	15.0
	6	2.83	1.33	0.85	14.8
	7	2.94	1.35	0.85	15.6
300	1	2.81	1.23	0.85	13.2
	4	2.88	1.24	0.86	14.2
	6	2.85	1.23	0.85	13.8
	7	2.95	1.25	0.86	14.7
350	1	2.83	1.13	0.85	12.6
	4	2.90	1.13	0.87	13.2
	6	2.86	1.14	0.86	13.0
	7	2.96	1.17	0.87	13.9
400	1	2.84	1.00	0.86	11.3
	4	2.91	1.05	0.87	12.3
	6	2.89	1.03	0.86	11.9
	7	2.98	1.07	0.87	12.8

expected to decrease with increasing temperature due to a similar decrease in  $V_m$  with increasing temperature through Eq. (2.3). In the case of the GaInP<sub>2</sub> solar cells, however, Table IV shows that there was almost no change in  $ff$  with temperature. From the inset of Figure 41, it can be seen that a larger decrease in  $V_{oc}$  occurred than did an increase in  $J_{sc}$  with increasing temperature, and the result was an overall decrease in cell conversion efficiency with increasing temperature.

In this chapter, dark I-V behavior for GaInP<sub>2</sub> n<sup>+</sup>p solar cells was measured and correlated with solar cell PV performance. Dark current due to carrier diffusion and recombination was identified through voltage and temperature dependences. Recombination current was found to be dominant at the MPP voltage of "well-behaved" GaInP<sub>2</sub> solar cells, and was shown to limit the solar cell  $V_{oc}$ . In "leaky" solar cells, the density of line-like surface defects were correlated with excessive shunting-currents that reduced solar cell  $V_{oc}$ . A significant reduction in solar cell  $J_{sc}$  in these cells was also explained by the effects of enhanced photocarrier recombination and tunneling through line-defect related centers. Small area mesa diodes were used to confirm the localized nature of the line-defects. The small mesa diodes were further used to show the presence of junction perimeter recombination current, and this current was shown to be negligible in the larger area solar cells. In the next chapter, a detailed study into the factors that control bulk recombination current will be examined utilizing the mesa diodes, with the goal of understanding the source of such current.

## V. GaInP<sub>2</sub> Mesa Diode Characterization and Analysis

### Capacitance-voltage (C-V) Measurements

In this section C-V measurements were performed to determine the doping density of the p-GaInP<sub>2</sub> layer in the GaInP<sub>2</sub> n<sup>+</sup>p mesa diode structures before electron irradiation. The C-V measurements were also used to determine the junction depletion width,  $W_d$ , and the intrinsic carrier concentration,  $n_i$ , in the GaInP<sub>2</sub> diodes. This data will be useful in the analysis of junction recombination current conducted in the next section. The capacitance for a one-sided n<sup>+</sup>p abrupt junction is given by (Sze, 1981:79),

$$C = \frac{\epsilon_s \epsilon_o S}{W_d} = S \sqrt{\frac{q \epsilon_s \epsilon_o N_A}{2 \left( V_{bi} - V - 2 \frac{kT}{q} \right)}}, \quad (5.1)$$

and

$$N_A = \frac{-2}{S^2 q \epsilon_s \epsilon_o} \frac{dV}{d(C^{-2})}, \quad (5.2)$$

where  $C$  is the junction capacitance,  $S$  is the diode junction area,  $q$  is the electronic charge,  $\epsilon_s$  is the dielectric constant ( $\sim 11.75$  for GaInP<sub>2</sub>) (Brennan and Chiang, 1992:1055),  $\epsilon_o$  is the permittivity of free space,  $V_{bi}$  is the built-in junction potential,  $k$  is the Boltzmann's constant, and  $T$  is the temperature. A large number (12 or more) of diodes of each doping level was examined, and a typical plot of  $1/C^2$  vs.  $V$  at 290 K is shown in Figure 42. The straight line slopes yielded values of  $N_A = (1.22 \pm 0.06) \times 10^{17}$  and  $(2.06 \pm 0.04) \times 10^{17} \text{ cm}^{-3}$  for the mid and high doped

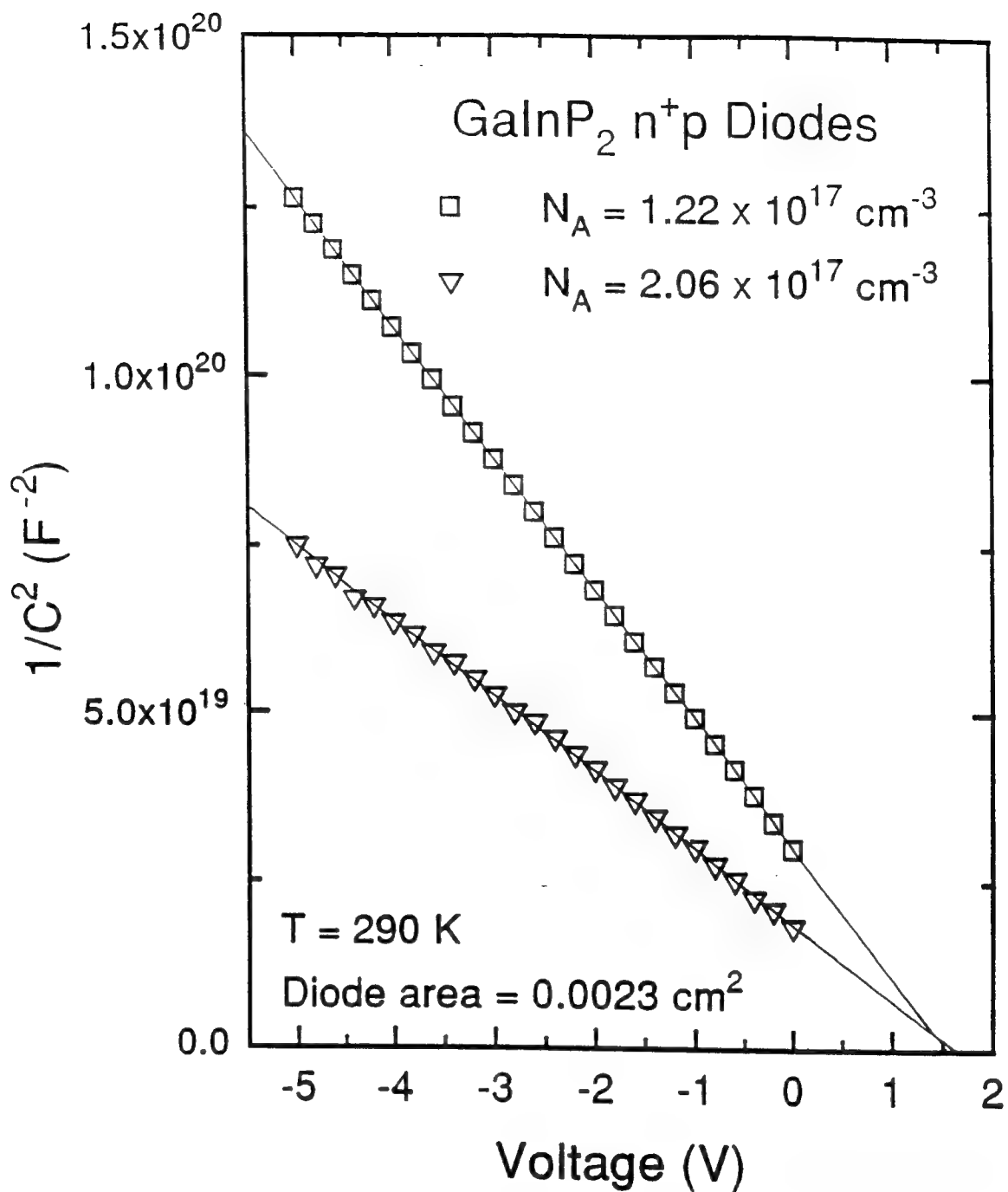


Figure 42.  $1/C^2$  vs. reverse-bias voltage for mid and high doped GaInP<sub>2</sub> diodes, where  $C$  is the junction capacitance.

diodes, respectively. In Figure 43, a nonconstant slope is shown for the case of the low doped diodes indicating a slightly graded doping profile. This is believed to be due to compensation by diffusion of Se into the p-base during growth of the  $n^+$  emitter at relatively high growth temperatures. Nonetheless, values for  $N_A$  in the base of the low doped solar cells and diodes were estimated to be  $1\sim 2 \times 10^{16} \text{ cm}^{-3}$ .

It is noted that the values for  $N_A$  in the solar cells were obtained using the smaller adjacent test diodes because the capacitance of the solar cells was beyond the range of the capacitance meter. Eq. (5.1) also provides the value of  $(V_{bi} - 2kT/q)$  at the  $1/C^2$  intercept as shown in Figure 42. The measured values of  $V_{bi}$  at 290 K were  $1.55 \pm 0.06$ ,  $1.68 \pm 0.02$ , and  $1.74 \pm 0.02$  eV for the low, mid, and high doped devices, respectively.

Values obtained for  $W_d$  at zero bias were about 4100, 1300, and 1050 angstroms in the low, mid, and high doped devices, respectively. Using the abrupt junction relation of  $V_{bi} = (kT/q)\ln(N_A N_D / n_i^2)$  and the donor density,  $N_D$ , in the n-type emitter ( $\sim 10^{18} \text{ cm}^{-3}$ ),  $n_i$  was calculated to be  $\sim 2400 \text{ cm}^{-3}$  at 290 K for both the mid and high doped devices. This value is consistent in magnitude with the measured bandgap of 1.84 eV at 290 K for this material, and with the calculated value of  $n_i \approx 775 \text{ cm}^{-3}$  for  $\text{GaInP}_2$  having a bandgap of 1.92 eV at 300 K (Brennan and Chiang, 1992:1055) in accordance with the relation  $n_i \propto \exp(-E_g/2kT)$ , where  $E_g$  is the bandgap energy. Measured values for  $N_A$ ,  $V_{bi}$ , and  $W_d$  are given in Table



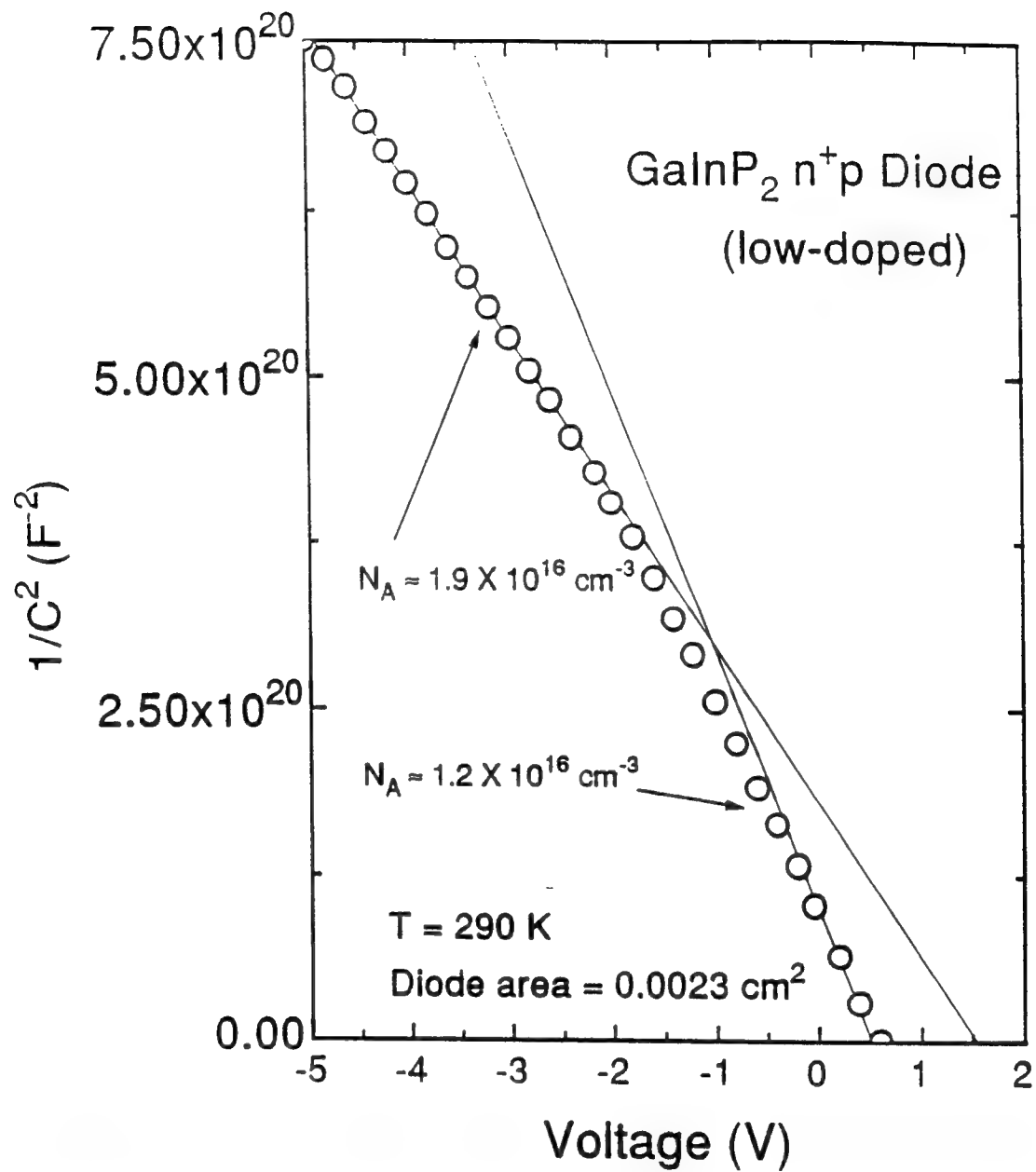


Figure 43.  $1/C^2$  vs. reverse-bias voltage for a low doped GaInP<sub>2</sub> diode, where C is the junction capacitance.

V. The device labeling GL, GM, and GH indicates the low, mid, and high doped diodes, respectively.

### Forward-bias Current-Voltage (I-V) Measurements

Typical forward-bias dark I-V curves for "well-behaved" GaInP<sub>2</sub> mesa diodes with a p-base doping density of  $N_A \approx 1.6 \times 10^{16}$ ,  $1.2 \times 10^{17}$ , and  $2.1 \times 10^{17} \text{ cm}^{-3}$  are shown in Figure 44. These are representative of a large number (20 or more) of diodes for each doping density. This figure also includes one "leaky" diode ( $\Delta$ ) for comparison. The solid lines are fits to the equation

$$I = I_{diff} \exp\left(\frac{qV}{A_1 kT}\right) + I_{rec} \exp\left(\frac{qV}{A_2 kT}\right) + I_o \exp(BV), \quad (5.3)$$

which is a modified form of Eq. (2.11), where  $I$  is the total forward-bias dark current, and  $V$  is the applied junction voltage. As discussed, the first term in Eq. (5.3) accounts for carrier diffusion, the second term accounts for SRH recombination current, and the last term describes current due to tunneling (Hovel, 1975:50; Riben and Feucht, 1966:1055).

The major difference between the three dark current terms in Eq. (5.3) resides in their dependence on voltage, temperature, and bandgap. As discussed, the value of  $A_1$  equals 1 for ideal diffusion current, the value of  $A_2$  is approximately 2 for ideal recombination current, and the parameters  $I_o$  and  $B$  are empirical, but are related to tunneling effects in the junction. Expressions for the first two coefficients in Eq. (5.3) are given as

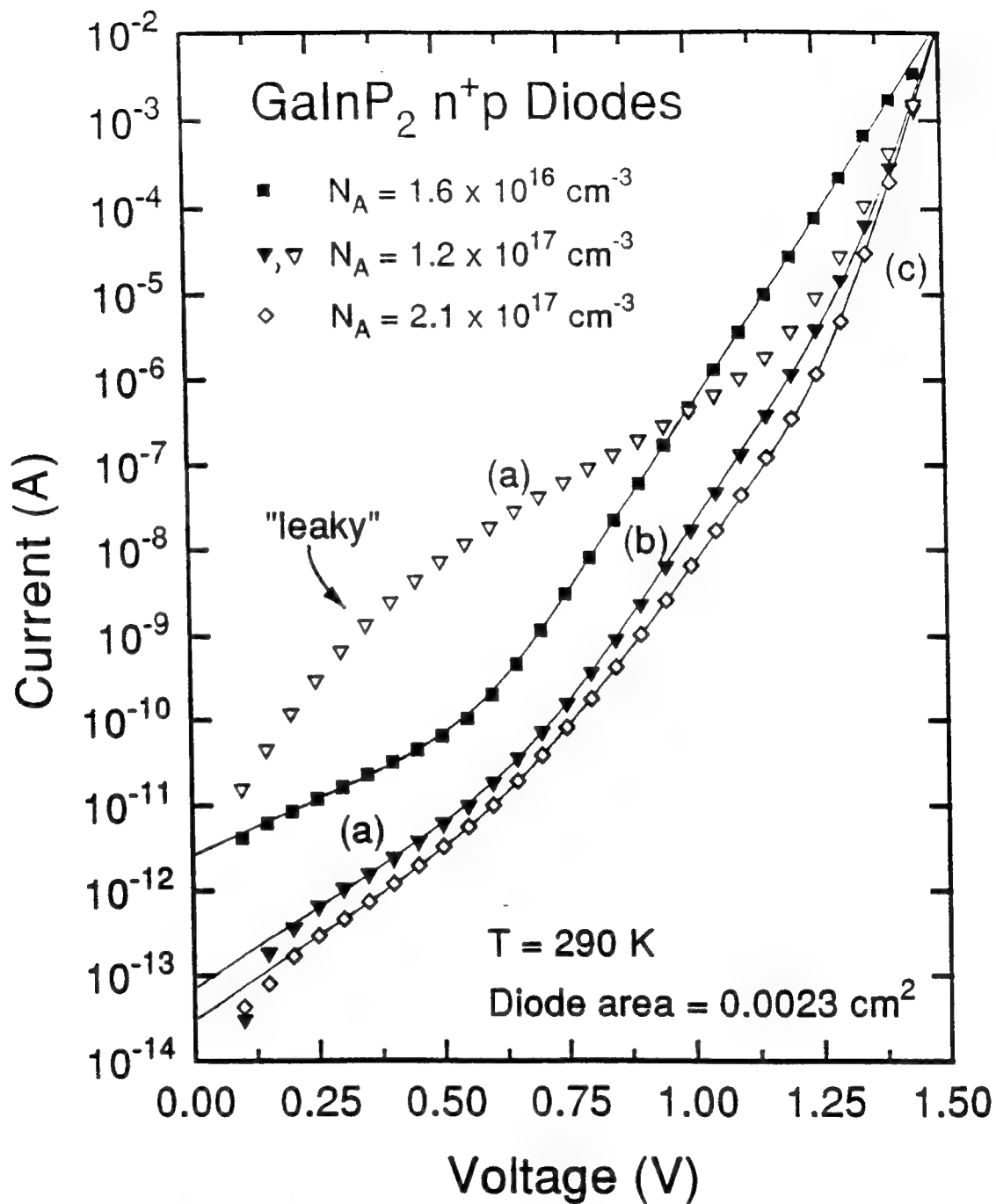


Figure 44: Forward-bias dark I-V curves for low, mid, and high doped GaInP<sub>2</sub> diodes. (a) Tunneling current region, (b) recombination current region, (c) diffusion current region. The solid lines are fits to Eq.(2.11).

**Table V.** Summary of GaInP<sub>2</sub> n<sup>+</sup>p junction parameters for low, mid, and high doped diodes

<u>Device</u>	<u>N<sub>A</sub>(cm<sup>-3</sup>)</u>	<u>V<sub>bi</sub>(V)</u>	<u>W<sub>d</sub>(Å)</u>	<u>J<sub>rec</sub> (A/cm<sup>2</sup>)</u>	<u>A<sub>2</sub></u>	<u>E<sub>a</sub>(eV)</u>
GL3-2	1.4E16	1.57	4052	1.8E-13	1.90	0.97
GL4-2	1.6E16	1.53	4087	1.5E-13	1.91	0.98
GL7-2	1.1E16	1.50	4103	2.7E-13	1.87	0.98
GL7-3	1.1E16	1.52	4121	2.3E-13	1.87	1.02
GL12-1	1.4E16	1.58	4081	1.9E-13	1.90	0.99
GL12-2	1.5E16	1.61	4106	2.0E-13	1.91	1.01
GM31-2	1.26E17	1.67	1305	1.7E-14	1.93	0.99
GM33-1	1.20E17	1.69	1276	2.2E-14	1.91	1.02
GM33-4	1.22E17	1.69	1290	1.3E-14	1.92	1.00
GM34-1	1.25E17	1.68	1298	1.6E-14	1.93	0.98
GM34-2	1.25E17	1.68	1309	1.9E-14	1.92	1.01
GM35-3	1.19E17	1.67	1285	2.2E-14	1.90	0.97
GH51-1	2.10E17	1.73	1037	2.2E-14	2.09	1.02
GH51-2	2.08E17	1.75	1044	2.3E-14	2.09	1.00
GH52-1	2.03E17	1.72	1040	1.9E-14	2.03	0.98
GH52-2	2.04E17	1.70	1061	1.7E-14	2.04	0.99
GH57-1	2.05E17	1.75	1058	2.0E-14	2.07	1.01
GH57-4	2.06E17	1.74	1071	2.1E-14	2.06	1.03

Values for N<sub>A</sub>, V<sub>bi</sub>, W<sub>d</sub>, and A<sub>2</sub> were measured at 290 K.

$$I_{dif} = qS \left( \frac{D_n n_p}{L_n} + \frac{D_p p_n}{L_p} \right) = J_{dif} S, \quad (5.4)$$

and

$$I_{rec} = \frac{qS n_i W_d f(b)}{\frac{q(V_{bi} - V)}{kT} \sqrt{\tau_p \tau_n}} = J_{rec} S. \quad (5.5)$$

As discussed,  $f(b)$  is a complicated factor involving the recombination trap center energy level,  $E_t$ , and electron and hole minority carrier lifetimes,  $\tau_n$  and  $\tau_p$ , respectively. It's value can be calculated by numerical integration, and it has a maximum value of  $\pi/2$ . For the  $n^+p$  junction,  $p_n \ll n_p$ , and thus,

$$I_{dif} = qS \frac{D_n n_p}{L_n} = qS \frac{D_n}{L_n} \frac{n_i^2}{N_A} \propto T^3 \exp\left(-\frac{E_g}{kT}\right). \quad (5.6)$$

Also,

$$I_{rec} \propto T^{\frac{5}{2}} \exp\left(-\frac{E_g}{kT}\right). \quad (5.7)$$

In Figure 44, three distinct slopes in the I-V curves for the mid and high doped diodes are seen, whereas only two obvious slopes are seen in the low doped diode.

Also, as seen earlier, the "leaky" diode exhibits very different I-V characteristics compared to the "well-behaved" diodes. The dark current in region (c) for the mid and high doped diodes at voltages greater than  $\sim 1.25$  V can be well described by the first diffusion term in Eq. (5.3). The I-V characteristics in region (b) between voltages of  $\sim 0.5$  to  $1.5$  V for the low doped diode and  $\sim 0.9$  to  $1.2$  V for the mid and high doped diodes are fitted well by the second recombination term in Eq. (5.3). Dark current in region (a) at voltages less than  $\sim 0.5$  V for "well-behaved"

diodes and less than  $\sim 1.25$  V for "leaky" diodes can be explained by the third tunneling/shunting term in Eq. (5.3).

Values for  $J_{\text{dif}}$  obtained for both the mid and high doped devices ranged from  $1.2$  to  $3.5 \times 10^{-15}$  A/cm<sup>2</sup>. Although Eq. (5.6) predicts  $I_{\text{dif}} \propto 1/N_A$ , no significant difference in  $I_{\text{dif}}$  was observed between mid and high doped diodes. It was also noted that for some diodes, it was difficult to obtain accurate values for  $I_{\text{dif}}$  due to series resistance effects appearing at  $V > 1.5$  V. Values of  $A_1$  for both the mid and high doped diodes were estimated to be  $1.06 \pm 0.04$ . However, values for  $J_{\text{dif}}$  and  $A_1$  could not be measured for the low doped diodes because no significant diffusion current was observed for voltages up to  $1.5$  V as shown in Figure 44.

Values for  $J_{\text{rec}}$  obtained for the low, mid, and high doped diodes were  $(2.3 \pm 0.5) \times 10^{-13}$ ,  $(1.8 \pm 0.4) \times 10^{-14}$ , and  $(1.9 \pm 0.5) \times 10^{-14}$  A/cm<sup>2</sup>, respectively. These data agree well with the theoretical value of  $J_{\text{rec}} \approx 5 \times 10^{-14}$  A/cm<sup>2</sup> for  $N_A = 2 \times 10^{17}$  cm<sup>-3</sup> given by Cavicchi *et al.* (Cavicchi *et al.*, 1991:63). It is noted that the magnitude of dark current in the high doped diode is generally smaller than that of the mid doped diode at a given voltage, as shown in Figure 44, although the values of the coefficient  $J_{\text{rec}}$  are nearly identical for both diodes. This is due to a slight difference in the values of  $A_2$  where the average value of  $A_2$  for the high doped diodes ( $\sim 2.05$ ) exceeds that for the mid doped diodes ( $\sim 1.91$ ).

It can be shown that the ratio of the total recombination-to-diffusion current is proportional to  $\exp(E_g/2kT)\exp(-qV/2kT)$  from Eqs. (5.3), (5.6), and (5.7). The

magnitude of the recombination current, therefore, becomes increasingly important relative to diffusion current for large bandgap materials and/or small bias voltages.

Since the bandgap of the GaInP<sub>2</sub> material used in this study is 1.84 eV at 290 K, the ratio of  $J_{\text{rec}}/J_{\text{dif}}$  for the present diodes is expected to be larger than those for Si and GaAs p-n junctions, which have  $E_g \approx 1.1$  and 1.4 eV, respectively. Indeed, this is the case, i.e., as previously discussed, the ratios of  $J_{\text{rec}}/J_{\text{dif}}$  for Si and GaAs p-n junctions are reported to be  $10^3 - 10^6$  and  $10^8 - 10^{10}$ , respectively, while the same measured ratios for the present mid and high doped GaInP<sub>2</sub> devices were as high as  $2 \times 10^{11}$ . It was shown in Figure 40 that approximately 50 % of the recombination current for these diodes may be due to perimeter current. Therefore, in larger area GaInP<sub>2</sub> devices, presumably solar cells, the ratio is still expected to be on the order of  $10^{11}$ . In fact, the average value of the ratio  $J_{\text{rec}}/J_{\text{dif}}$  for the 5 "well-behaved" GaInP<sub>2</sub> solar cells in Table II is  $1.3 \times 10^{11}$ . Considering the larger values of  $J_{\text{rec}}/J_{\text{dif}}$  ratios for a large number of GaInP<sub>2</sub> mesa diodes, and the fact that GaAs solar cells are often dominated by recombination dark current at their MPP voltage (DeMoulin *et al.*, 1988:368; Hovel, 1975:56), it is not surprising that recombination current also dominates at the MPP voltage in the GaInP<sub>2</sub> solar cells.

Values for  $J_{\text{rec}}$  in the mid and high doped devices are typically 10 - 15 times smaller than those for the low doped diodes. Some of this difference can be explained using Eq. (5.5), which can be rewritten as

$$J_{rec} \propto [\tau_n \tau_p N_A (V_{bi} - V)]^{-1/2} f(b). \quad (5.8)$$

The factor  $[N_A(V_{bi} - V)]^{-1/2}$  predicts a reduction of  $J_{rec}$  by a factor of 3~5 for the mid and high doped diodes relative to the low doped devices. A possible explanation for the additional reduction in  $J_{rec}$  could be related to the reduction in the factor  $f(b)$ , which may also depend on doping levels of the base layer. Measured values of  $A_2$  at 290 K are  $1.88 \pm 0.03$ ,  $1.91 \pm 0.03$ , and  $2.05 \pm 0.04$  for the low, mid, and high doped diodes, respectively, and in nearly all devices examined, values of  $A_2$  increase with doping density. Values for both  $J_{rec}$  and  $A_2$  are given in Table V. The recombination theory of Choo showed that  $A_2$  is dependent on  $\tau_n$ ,  $\tau_p$ ,  $E_t$ ,  $T$ , and  $V$  through the factor  $f(b)$ , and thus, the dependence of  $A_2$  on  $N_A$  suggests that the factor  $f(b)$  may be affected by  $N_A$  as well. However, at present, the details of how  $N_A$  affects the factor  $f(b)$  in these samples are unknown.

The observed reduction of  $J_{rec}$  in diodes with increasing  $N_A$  suggests that the efficiency of the GaInP<sub>2</sub> solar cells can be improved by increasing  $N_A$  in the p-base. However, it is noted that there is an upper limit on  $N_A$  imposed by the reduction in minority carrier lifetime that generally occurs in semiconductors with excessively large  $N_A$ . The reduction in carrier lifetime degrades solar cell efficiency primarily through a reduction in light-generated current. Thus, an optimization of  $N_A$  is necessary to realize optimum cell performance. The value of  $N_A$  used by Cavecchi



*et al.* (Cacicchi *et al.*, 1993:659) in a 15.3% efficient GaInP<sub>2</sub> solar cell design was  $1-2 \times 10^{17} \text{ cm}^{-3}$ .

Values of  $I_0 = J_0 S$  obtained from fits to Eq. (5.3) are not as consistent as values for  $I_{\text{dif}}$  and  $I_{\text{rec}}$ . Typical values for  $J_0$  in the low doped diodes ranged from  $10^{-10}$  -  $10^{-18} \text{ A/cm}^2$  with  $B = 6 - 7$ , and those for the mid and high doped diodes yielded  $5 \times 10^{-12}$  -  $10^{-10} \text{ A/cm}^2$  with  $B = 7 - 9.5$ . It can be seen that values of  $B$  between 6 - 9.5 at room temperature correspond to an ideality factor of  $A_3 = 4.2 - 5.7$  when considering the equivalent expression of  $I_0 \exp(BV) = I_0 \exp(qV/A_3 kT)$ . As noted earlier, a mechanism for current with  $A > 4$  has been proposed as due to excessive leakage current at the perimeter of the p-n junction. On the other hand, it is also noted that for several "well-behaved" diodes, the low voltage portion of the I-V curves is better fit by a linear current dependence of  $R_{\text{sh}}/V$  as the third term in Eq. (5.3) instead of  $I_0 \exp(BV)$ , where  $R_{\text{sh}}$  is a shunting resistance associated with the junction. As previously noted, the origin of  $R_{\text{sh}}$  is reported to be due to a combination of tunneling and trapping-detrapping of carriers through defects states in the junction.

It is also worthwhile to mention that when several diodes were exposed to water vapor for several minutes, values of  $J_0$  increased by almost an order of magnitude as shown in Figure 45. Values of  $J_0$  then recovered to nearly their pre-exposure value following approximately 24 hours of room temperature exposure. However, as shown in Figure 45, the magnitude of  $J_{\text{dif}}$  and  $J_{\text{rec}}$  were not affected by

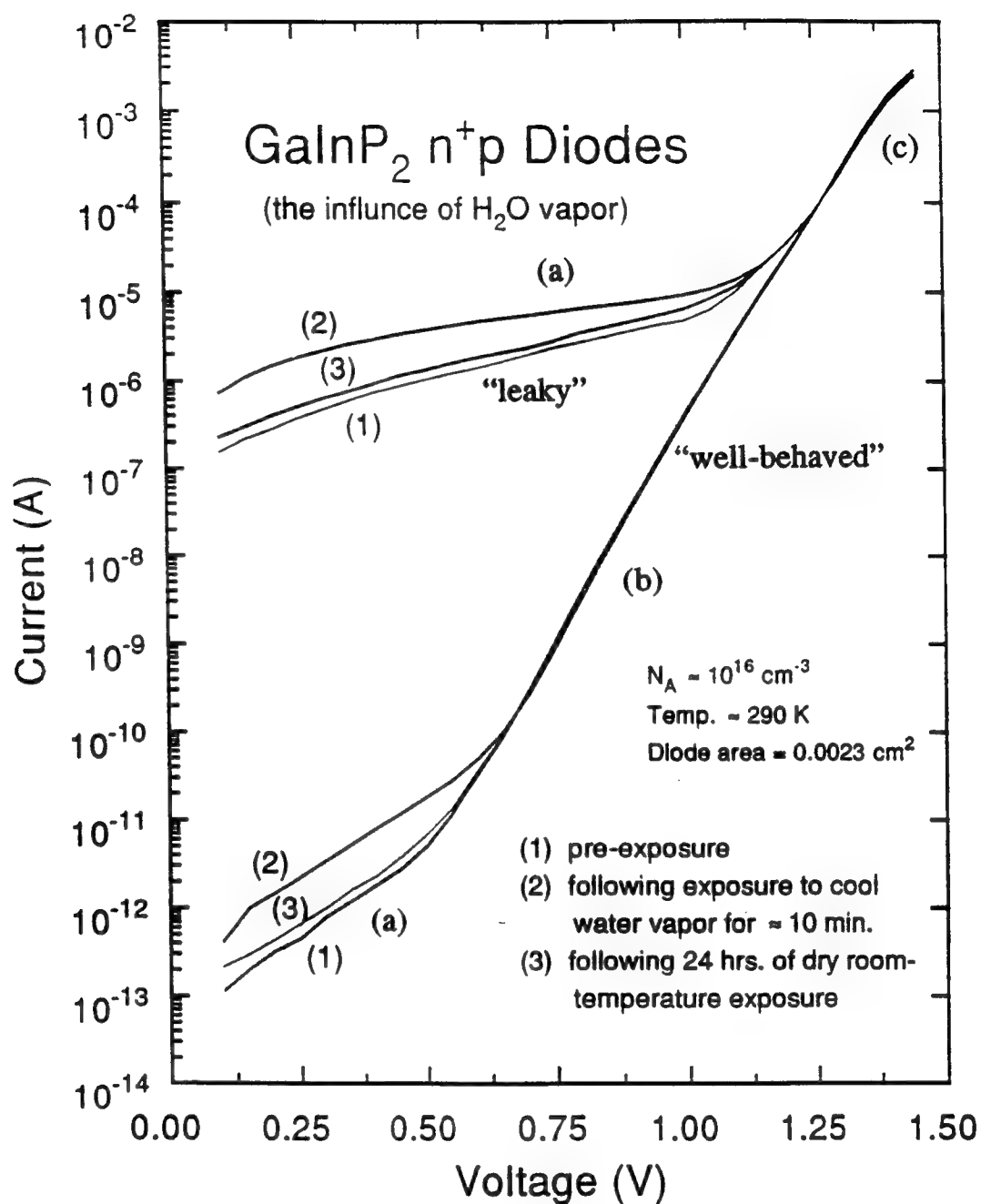


Figure 45. Forward-bias dark I-V curves for low doped GaInP<sub>2</sub> diodes exposed to H<sub>2</sub>O vapor.

exposure to the water vapor. For these mesa diodes, since only the perimeter of the junction was exposed to the water vapor, the origin of increased  $J_0$  appears to be related to perimeter effects. Similar behavior following exposure to water vapor has also been reported in Si and Ge diodes, where excessive surface currents resulted with exponential behavior (Statz *et al.*, 1957:133).

### **Forward-bias Current-Voltage-Temperature (I-V-T) Measurements**

As in the case of the GaInP<sub>2</sub> solar cells, forward-bias I-V data for the GaInP<sub>2</sub> n<sup>+</sup>p diodes were taken as a function of temperature to identify dark current due to tunneling, diffusion, and recombination. A set of typical I-V-T curves for "well-behaved" and "leaky" diodes with  $N_A \approx 1.2 \times 10^{17} \text{ cm}^{-3}$  are shown in Figures 46 and 47, respectively. As seen earlier, there exists several distinct trends in the I-V curves. In these diodes, dark currents in the region indicated by (b) and diffusion in the region (c) fall off with temperature,  $T$ , as  $\exp(-E_g/2kT)$  and  $\exp(-E_g/kT)$ , respectively, at a given voltage. However, dark current due to shunting in region (a<sub>1</sub>) and (a<sub>2</sub>) for "well-behaved" diodes exhibit little change as a function of temperature, and remains about the same at low temperatures as the forward-bias changes.

The nearly horizontal ln I-V curves at the bottom on Figures 46 and 47 in the region (a<sub>1</sub>) are due to finite conductivity in the junction space-charge region, and result in  $R_{sh}/V$  behavior, where  $R_{sh}$  is found to decrease with increasing temperature. Similar behavior has been reported for Ga<sub>0.51</sub>In<sub>0.49</sub>P/GaAs

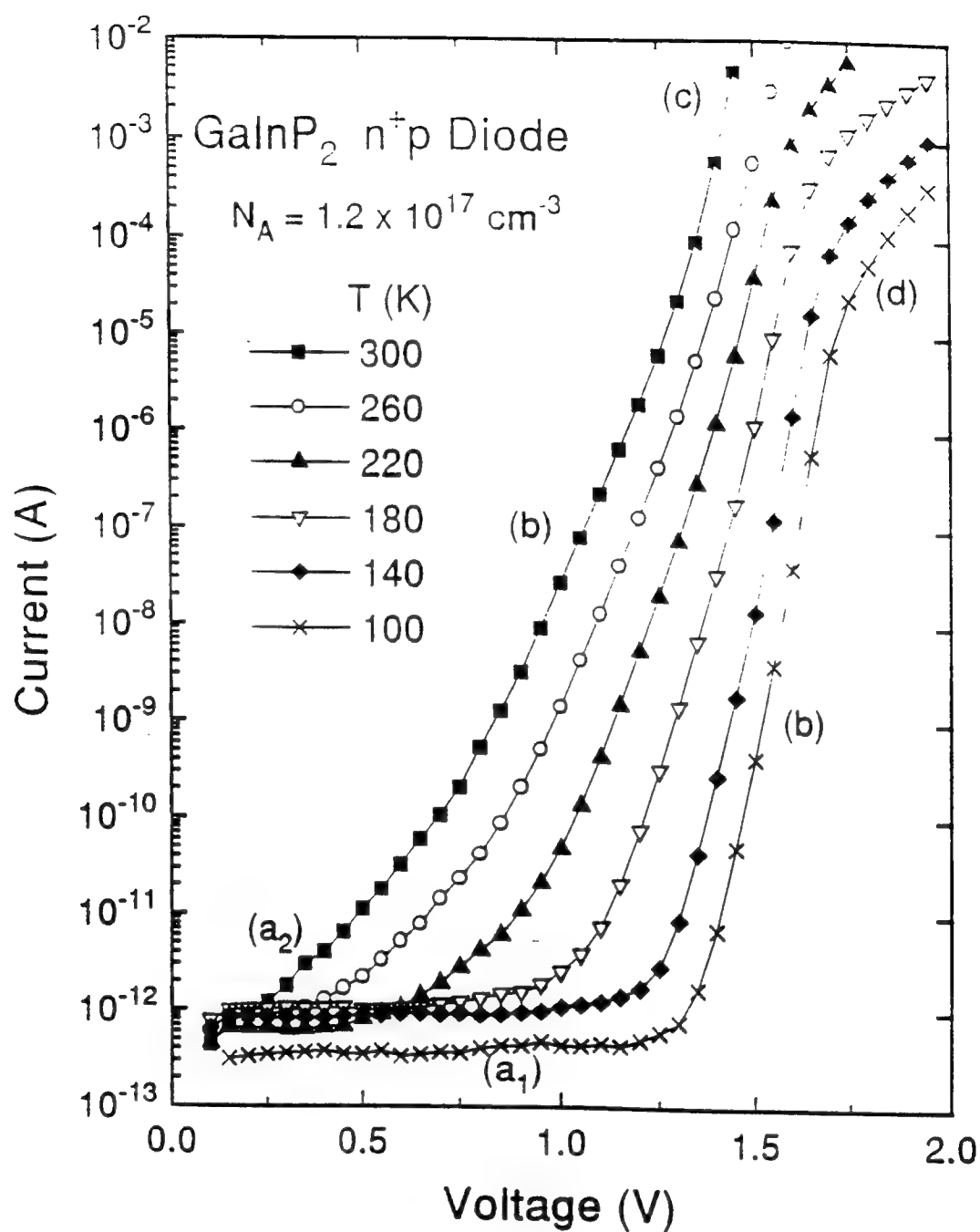


**Figure 46.** Forward-bias dark I-V curves plotted as a function of temperature for a typical "well-behaved" mid doped GaInP<sub>2</sub> diode. (a<sub>1</sub>) Linear tunneling current region of the form  $V/R_{sh}$ . (a<sub>2</sub>) Exponential tunneling current region of the form  $I_0 \exp(BV)$ . (b) Recombination current region. (c) Diffusion current region. (d) Series resistance effect at low temperatures.

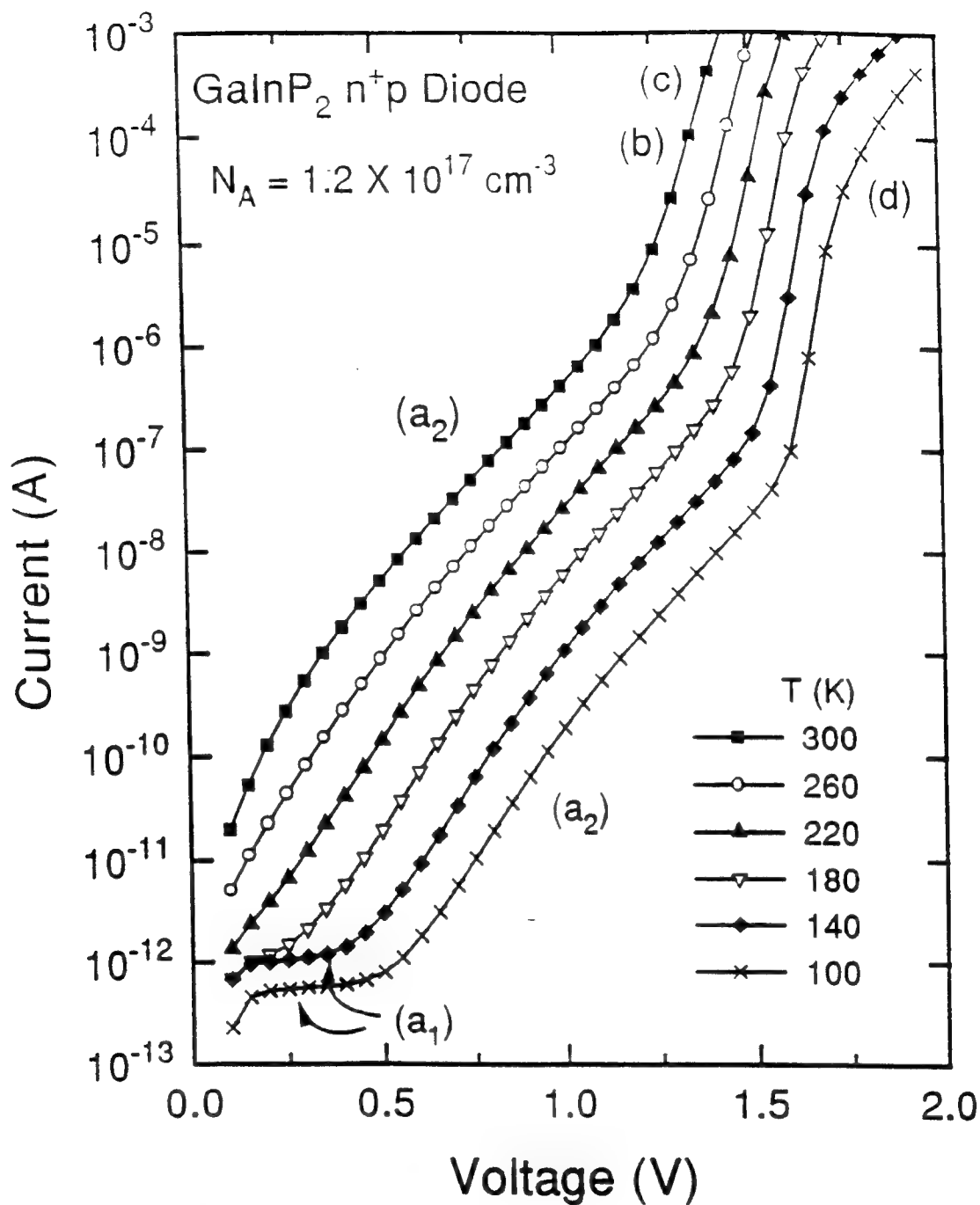


Figure 47. Forward-bias dark I-V curves plotted as a function of temperature for a typical "leaky" mid doped GaInP<sub>2</sub> diode. (a<sub>1</sub>) Linear tunneling current region of the form  $V/R_{sh}$ . (a<sub>2</sub>) Exponential tunneling current region of the form  $I_0 \exp(BV)$ . (b) Recombination current region. (c) Diffusion current region. (d) Series resistance effect at low temperatures.

heterojunction devices at low temperatures (Paloura *et al.*, 1992:2749). On the other hand, the shunting current in the region ( $a_2$ ) of the "leaky" diode shown in Figure 46 increases exponentially as  $I_0 \exp(BV)$ . The slope  $B$  is nearly constant, and is only slightly dependent on temperature. This behavior is predicted in the tunneling-recombination heterojunction model yielding the third term in Eq. (5.3) (Ribben and Feucht, 1966:1055). Furthermore, the values for  $J_0$  in the region ( $a_2$ ) in Figure 47 obtained from fitting data taken at 300 K between 0.5 and 1.0 V, and data taken at 100 K between 0.5 and 1.5 V are seen to decrease exponentially with decreasing temperature, which is also predicted in this model.

In Figure 46, the constant slope region (b) of the I-V-T curves is due to carrier recombination, and the rolling-off of the curves in the region (d) of Figures 46 and 47 at the high current levels is due to series resistance effects that occur at low temperatures. The slope of the I-V curves dominated by recombination increases with decreasing temperature  $T$  in accordance with the factor  $\exp(qV/A_2 kT)$  in Eq. (5.3). Values of  $A_2$  obtained from I-V-T data for typical well-behaved low, mid, and high doped diodes are shown in Figure 48. As can be seen,  $A_2$  is relatively insensitive to temperature as predicted by recombination theory. The larger value of  $A_2$  observed for the high doped diodes, relative to the low and mid doped samples, was briefly discussed in the previous section. A more detailed discussion on this will be given in the section on post-radiation behavior.

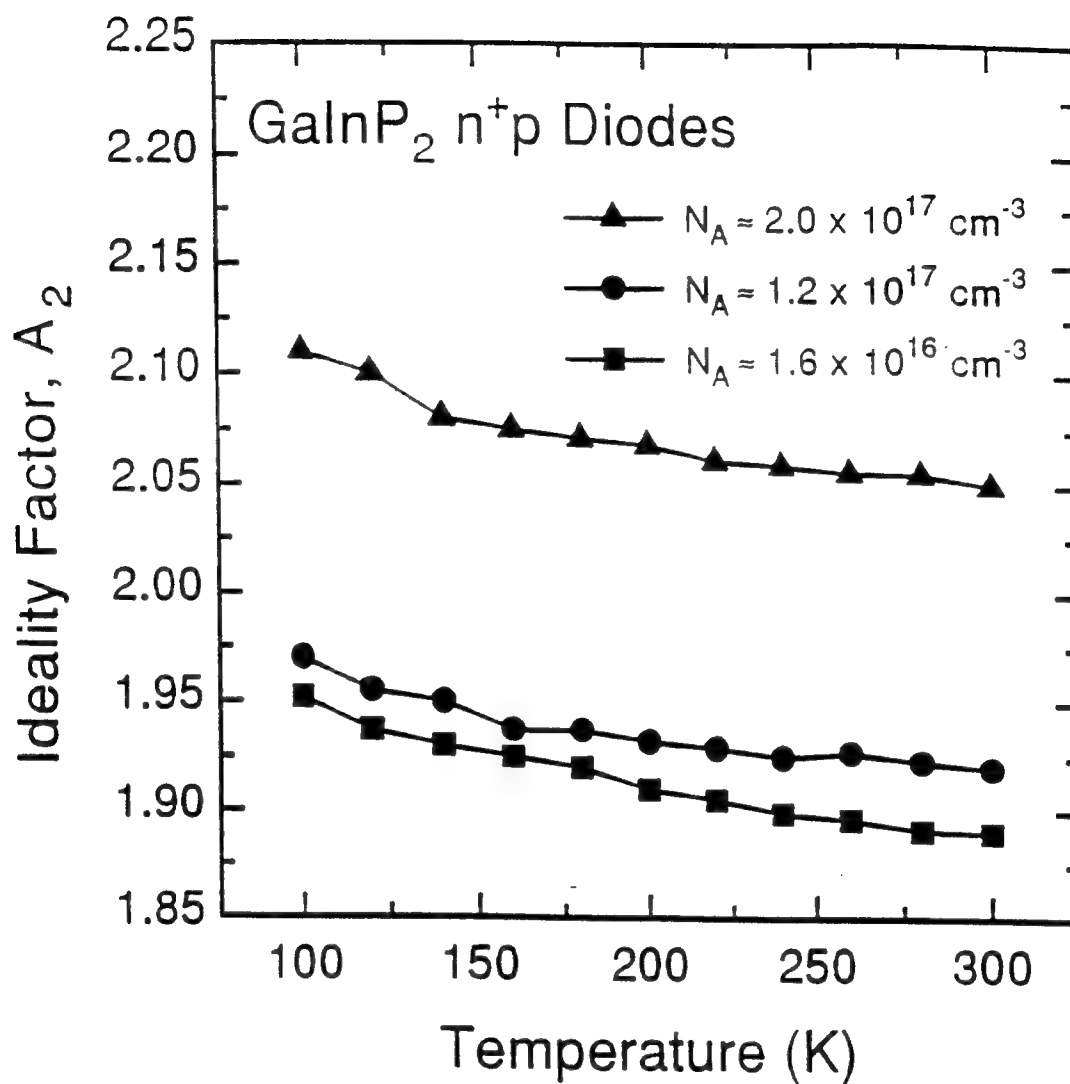


Figure 48. A plot of dark current ideality factor ( $A_2$ ) vs. temperature for typical low, mid, and high doped GaInP<sub>2</sub> diodes.

The activation energy,  $E_A$ , for the  $A_2 \approx 2$  current mechanism in the diodes was obtained from Arrhenius plots of  $\ln(I_{\text{rec}})$  versus  $1000/T$ , where  $E_A = E_{\text{go}}/2$  for ideal recombination. This comes from the relation  $I_{\text{rec}} \propto T^{5/2} \exp(-E_{\text{go}}/2kT)$ , where  $E_{\text{go}}$  is the bandgap of GaInP<sub>2</sub> at  $T = 0$  K. The perimeter recombination current,  $I_{\text{recp}}$ , is also expected to vary as  $\exp(-E_{\text{go}}/2kT)$  as well, in accordance with Eq. (4.2), where  $n_i \propto \exp(-E_{\text{go}}/2kT)$ . In Figure 49, Arrhenius plots are shown for "well-behaved" low, mid, and high doped diodes. The measured values for  $E_A$  in nearly all "well-behaved" diodes were  $0.99 \pm 0.04$  eV over the temperature range 100-300 K, with no obvious observed dependence on  $N_A$ . Values of diode  $E_A$  are also given in Table V. As in the case of the GaInP<sub>2</sub> solar cells, values obtained for  $E_{\text{go}} \approx 2$  eV (where  $E_{\text{go}} = 2 \times E_A$ ) agrees very well with the value of  $E_{\text{go}} \approx 1.98$  eV measured by PL. Therefore, the temperature dependence of the  $A_2$  current in the GaInP<sub>2</sub> diodes is also in good agreement with SNS recombination theory.

It is noted that in several of the slightly "leaky" diodes, values of  $I_{\text{rec}}$  at very low temperatures, i.e.,  $T < 150$  K, decreased slower with temperature than was predicted by  $I_{\text{rec}} \propto T^{5/2} \exp(-E_g/2kT)$  alone. This indicated the presence of tunneling currents, which are known to be relatively insensitive to temperature. Also, in these slightly "leaky" devices, values of  $A_2$  for  $T < 150$  K were found to increase slowly with decreasing temperature, indicating that the dominant current mechanism was changing from "pure" recombination to more of a recombination-tunneling-like mechanism. This behavior was also observed in GaInP<sub>2</sub> diodes



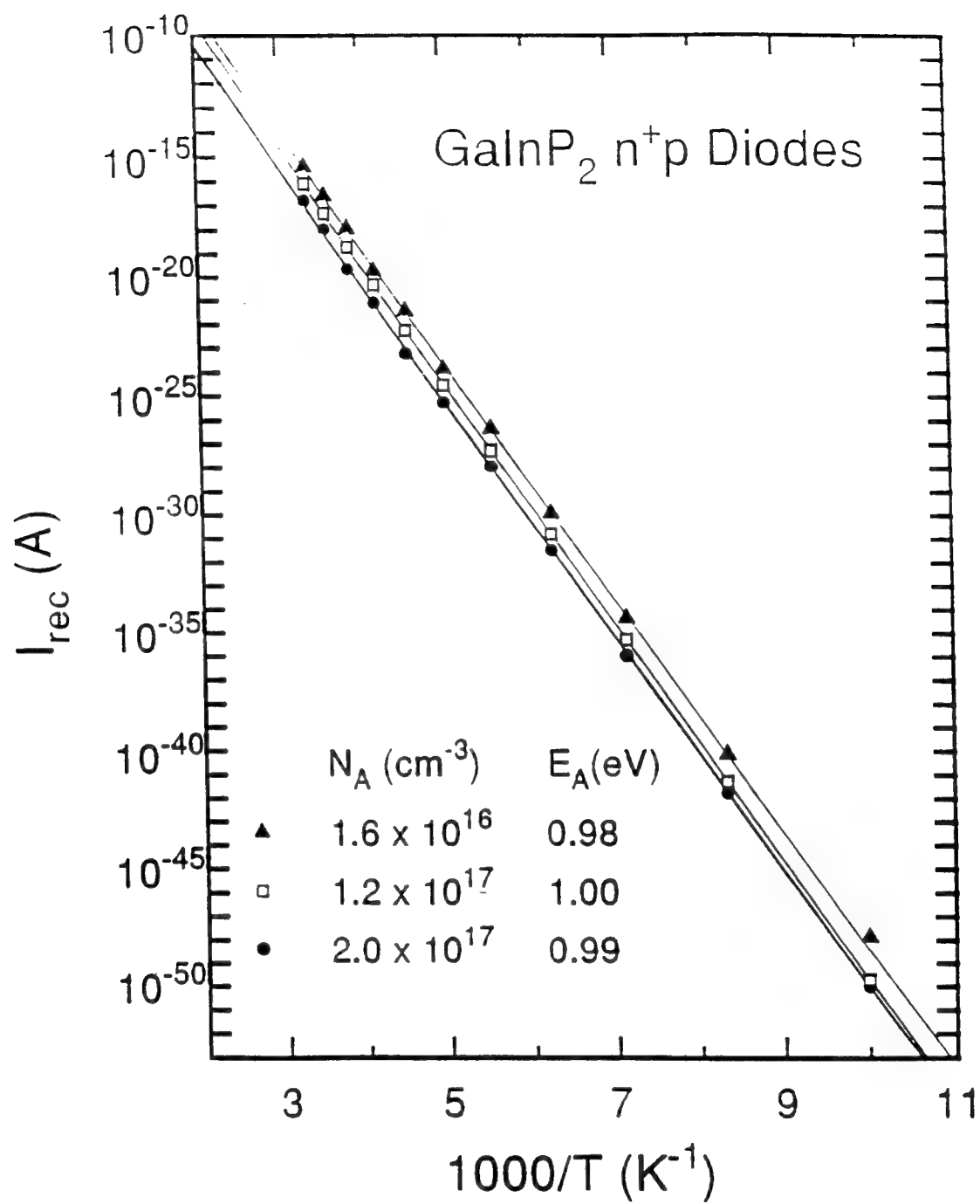


Figure 49. Recombination current coefficient  $I_{\text{rec}}$  vs.  $(1000/T)$  for typical low, mid, and high doped  $\text{GaInP}_2$  diodes.

irradiated with 1 MeV electrons discussed in the next chapter, but in that case, the discrepancy in  $J_{\text{rec}}$  and the increase in  $A_2$  were much more significant.

Up to now, dark junction current due to bulk and perimeter recombination has been found to dominate in the GaInP<sub>2</sub> solar cells and diodes between forward-bias voltages of  $\sim 0.75$  and  $1.25$  V. In the next three sections, measurements of the energy levels responsible for carrier recombination in the junction made using reverse-bias I-V-T, deep level transient spectroscopy (DLTS), and capacitance-frequency-temperature (C-F-T) measurement techniques will be discussed.

### Reverse-bias I-V-T Measurements

Reverse-bias I-V-T measurements can be used to identify the activation energy of deep SRH-type levels responsible for the forward-bias recombination current. The total reverse current,  $I_{\text{rev}}$ , generally includes a thermally generated space-charge component,  $I_{\text{gen}}$ , a voltage-independent bulk diffusion component,  $I_{\text{bulk}}$ , and a surface perimeter component,  $I_{\text{sur}}$  (Sze, 1981:91). Since,  $I_{\text{bulk}} \approx qS(D_n/\tau_n)^{1/2}n_i^2/N_A \propto \exp(-E_g/kT)$  for an n<sup>+</sup>p junction, and  $I_{\text{gen}} \approx qSn_iW_d/\tau_g \propto \exp(-E_g/2kT)$ , where  $\tau_g$  is the effective generation lifetime,  $I_{\text{gen}}$  will dominate in semiconductors with a large bandgap  $E_g$ . Furthermore, since it is well known that the  $I_{\text{rev}}$  is generally dominated by  $I_{\text{gen}}$  in GaAs diodes with  $E_g = 1.42$  (Ringel *et al.*, 1989:1230), it is reasonable to assume that  $I_{\text{rev}}$  will also be dominated by  $I_{\text{gen}}$  for GaInP<sub>2</sub> diodes having a larger  $E_g \approx 1.84$  eV. Thus, for the present diodes, it is assumed that the reverse current is dominated by  $I_{\text{gen}}$ , and  $I_{\text{bulk}}$  and  $I_{\text{sur}}$  are neglected.

The reverse current, after neglecting  $I_{\text{bulk}}$  and  $I_{\text{sur}}$ , can be obtained using the SRH recombination rate expression of Eq. (2.40) and the relation  $I_{\text{rev}} = qS \int U dx$ , which gives

$$I_{\text{rev}} = qS \frac{n_i W_d}{\tau_g}, \quad (5.9)$$

where

$$\tau_g = \tau_p \exp\left[\frac{(E_t - E_i)}{kT}\right] + \tau_n \exp\left[\frac{-(E_t - E_i)}{kT}\right]. \quad (5.10)$$

A combination of Eqs.(5.9) and (5.10) results in

$$I_{\text{rev}} \propto W_d \exp\left(\frac{-E_a}{kT}\right), \quad (5.11)$$

where

$$E_a = E_c - E_t \quad \text{for} \quad E_t > E_i \quad (5.12)$$

and

$$E_a = E_t - E_v \quad \text{for} \quad E_t < E_i. \quad (5.13)$$

$E_a$  is the activation energy of the generation/recombination center,  $E_i$  is the intrinsic Fermi level,  $E_c$  and  $E_v$  are the conduction and valence band minimum energy levels, respectively, and the other terms have their usual meanings.

A typical set of reverse-bias I-V-T curves for "well-behaved" low and mid doped GaInP<sub>2</sub> diodes are shown in Figures 50 and 51. In general,  $I_{\text{rev}}$  is expected to vary as  $\propto V^{1/3}$  for a linear-graded doping profile, and as  $V^{1/2}$  for an abrupt doping profile (Sze, 1981:90). From C-V measurements, the doping profile for the low doped diodes was shown to be graded, and the mid and high doped diode profiles were shown to be abrupt. However, the reverse I-V curves shown for the diodes in Figures 50 and 51 exhibit more exponential-like behavior at temperatures

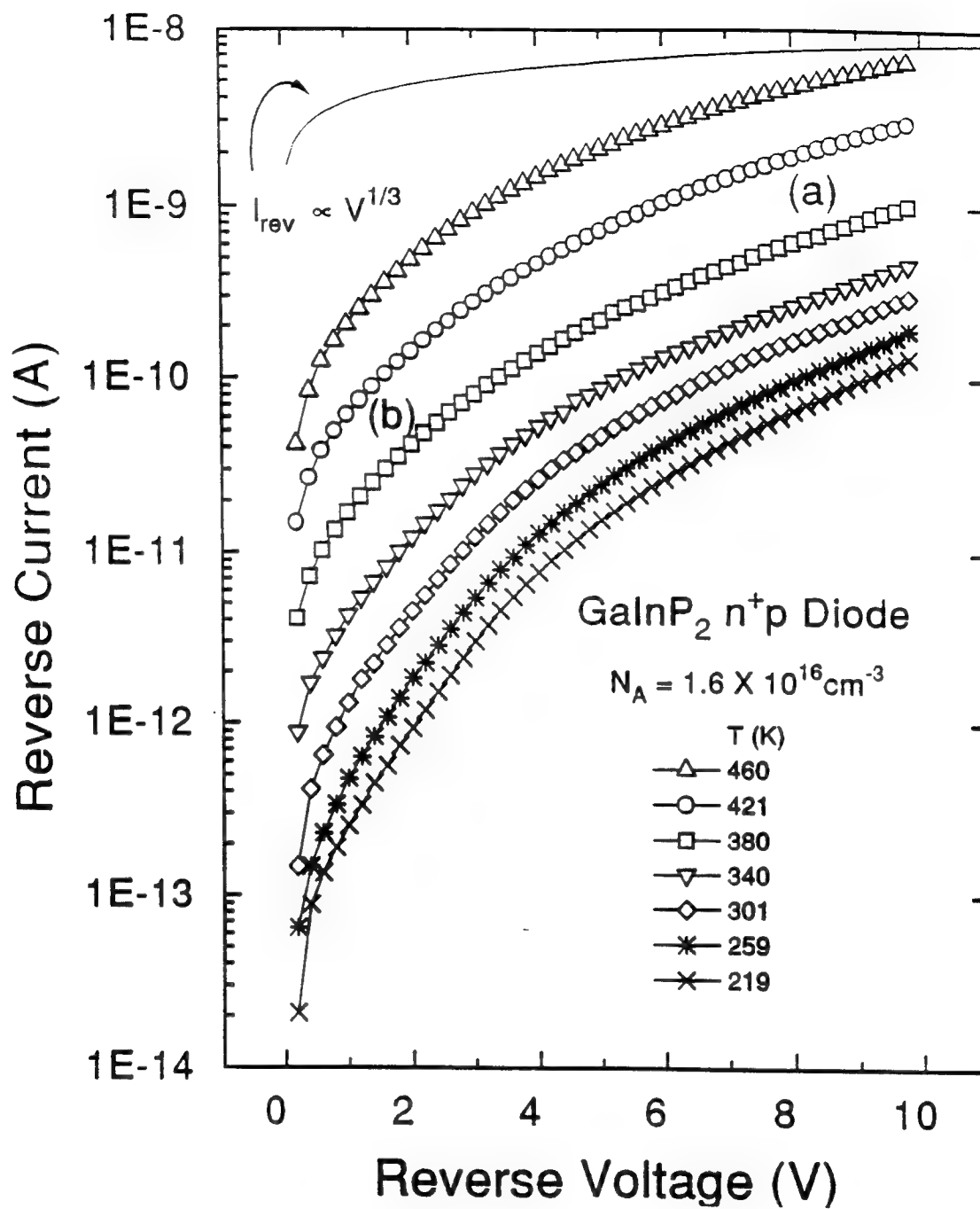


Figure 50. Reverse-bias dark I-V curves as a function of temperature for a typical low doped GaInP<sub>2</sub> diode. (a) Exponential-like behavior, (b) Shunting-like behavior.

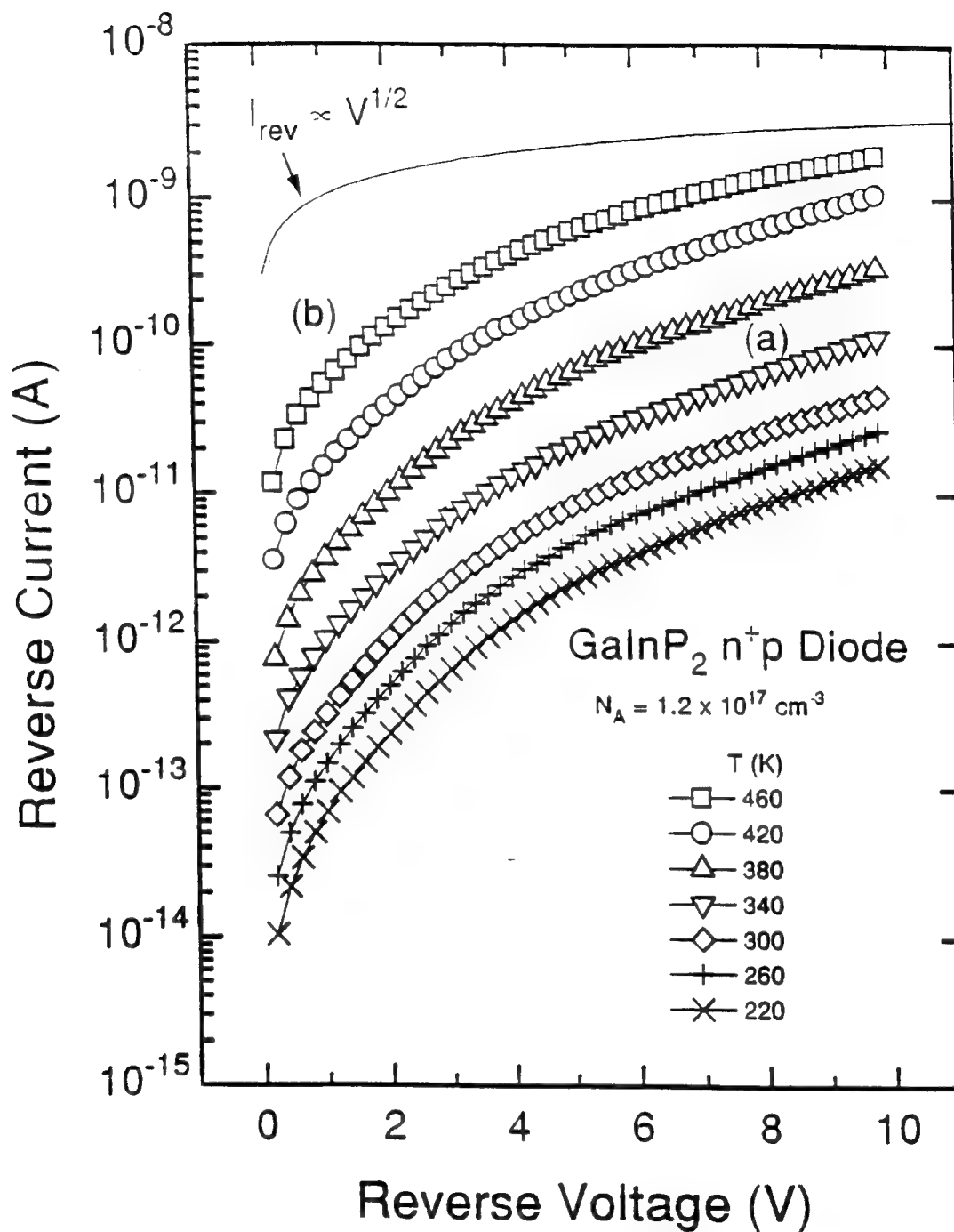


Figure 51. Reverse-bias dark I-V curves as a function of temperature for a typical mid doped GaInP<sub>2</sub> diode. (a) Exponential-like behavior. (b) Shunting-like behavior.

between ~220 and 460 K in the region (a) for bias greater than 5 V instead of  $V^{1/3}$  or  $V^{1/2}$  behavior. The deviation from  $I_{rev} \propto V^{1/3}$  or  $V^{1/2}$  may be partly due to the junction perimeter component that was neglected. Also, similar shunting-like behavior can be seen more prominently at high temperatures in the region (b) for reverse bias less than 5 V. Similar exponential and shunting-like behavior has also been reported in InGaAs<sub>2</sub> photodiodes (Shaw *et al.*, 1993:7244).

In Table VI, a good correlation between values for  $J_{rev}$  measured at -5 V and  $J_{rec}$  in the "well-behaved" diodes is shown, i.e., values of  $J_{rev}$  increase with increasing values of  $J_{rec}$ . This trend can be explained through the dependence of  $J_{rev}$  and  $J_{rec}$  on the lifetimes  $\tau_g$ , and  $\tau_n$  and  $\tau_p$ , respectively, through Eqs. (2.52) and (5.9), where in the case of  $\tau_n = \tau_p = \tau_r$ , it can be shown from Eq. (2.40) that  $\tau_g = 2\tau_r(\sigma_n/\sigma_p)^{1/2} \cosh[(E_t - E_i)/kT]$  (Schroder, 1982:1336). This predicts that the lifetimes will be directly proportional to each other, which would explain the observed increase in  $J_{rev}$  with  $J_{rec}$  shown in Table VI.

In Figure 52, a plot of  $\ln(I_{rev})$  vs.  $1000/T$  for the low and mid doped diodes of Figures 50 and 51, and for a typical high doped diode are shown at a reverse-bias voltage of -5 V. The reverse current is shown to decrease with decreasing temperature as predicted by  $I_{rev} \propto \exp(-E_a/kT)$  in Eq. (5.9). Also, values for  $I_{rev}$  decrease with increasing p-base doping density  $N_A$  at a given temperature as shown in Figure 52. For example, values for  $I_{rev}$  measured for high and mid doped diodes are 5-7 times smaller than  $I_{rev}$  in low doped diodes between  $T \approx 300$ -450 K,

Table VI. Summary of forward- and reverse-bias measured current densities and generation/recombination center activation energies,  $E_a$ , for the low, mid, and high doped GaInP<sub>2</sub> diodes

<u>Device</u>	$J_{\text{rec}}$ (A/cm <sup>2</sup> )	$J_{\text{rev}}^*$ (A/cm <sup>2</sup> )	$E_{a1}$ (eV) **	$E_{a2}$ (eV) **
<u>low</u>				
GL4-2	1.5E-13	2.1E-8	0.42	0.07
GL7-2	2.7E-13	5.1E-8	0.47	0.06
GL7-3	2.3E-13	4.6E-8	0.44	0.05
GL12-1	1.9E-13	3.9E-8	0.43	0.05
<u>mid</u>				
GM31-2	1.7E-14	4.1E-9	0.46	0.07
GM33-1	2.2E-14	7.1E-9	0.43	0.06
GM33-3	1.3E-14	3.7E-9	0.45	0.07
GM34-1	1.6E-14	4.3E-9	0.47	0.06
GM35-3	2.4E-14	6.5E-9	0.44	--
<u>high</u>				
GH51-2	2.3E-14	3.0E-9	0.45	0.06
GH52-2	1.7E-14	8.0E-10	0.41	--
GH57-1	2.0E-14	1.1E-9	0.43	0.08
GH57-4	2.1E-14	9.7E-10	0.43	0.06

\* Measured at -5V at 300 K.

\*\* Measured at -5V.

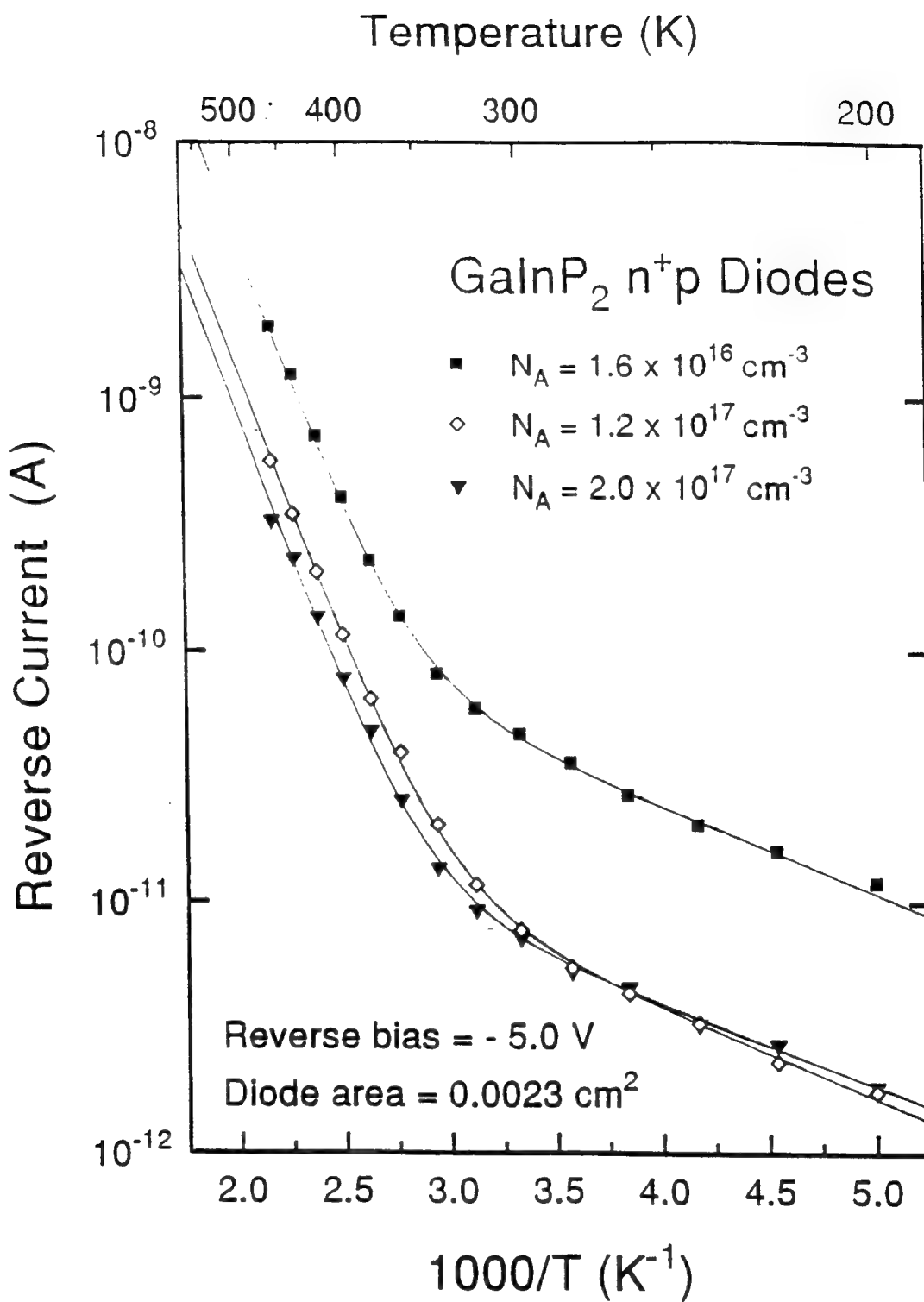


Figure 52. A plot of reverse-bias current vs.  $(1000/T)$  for low, mid, and high doped GaInP<sub>2</sub> diodes measured at a reverse-bias voltage of -5.0 V.



and almost 10 times smaller for  $T < 300$  K. For  $T > 300$  K,  $I_{rev}$  in the mid doped diodes is on average slightly larger than  $I_{rev}$  in high doped samples, whereas for  $T < 300$  K, values of  $I_{rev}$  are nearly identical for both diodes. The reduction in  $I_{rev}$  with increasing  $N_A$  is predicted from Eq. (5.9), where  $W_d$  varies as  $\sim (V/N_A)^{1/2}$  for reverse voltage  $V \gg V_{bi}$ . An increase in  $N_A$  of 10 and 20 times would reduce  $W_d$  by a factor of  $\sim 3$  and  $\sim 4.5$ , respectively. Slightly larger than expected values of  $I_{rev}$  in the high doped diodes at low  $T$  relative to those in the mid doped devices may be related to a reduction of  $\tau_n$  in the p-base with larger  $N_A$  in accordance with Eq. (5.9).

The activation energies  $E_a$  of the dominant deep levels were determined from the slope of  $\ln(I_{rev})$  versus  $1000/T$  data under constant reverse-bias shown in Figure 52 using a modified form of Eq. (5.11) for the presence of two generation centers. The solid lines in Figure 52 are fits to the equation

$$I_{rev} = C_1 \exp\left(\frac{-E_{a1}}{kT}\right) + C_2 \exp\left(\frac{-E_{a2}}{kT}\right). \quad (5.14)$$

Values for  $C_1$  and  $C_2$  decrease with increasing  $N_A$  through the dependence of  $W_d$  in Eq. (5.11). However, a larger decrease in  $C_1$  and  $C_2$  with increasing  $N_A$  has been observed at  $V = -5$  and  $-10$  V than is predicted by changes in  $W_d$  alone.

The activation energies obtained were  $E_{a1} = 0.44 \pm 0.03$  eV for all reverse-bias voltages between  $-0.2$  and  $-10$  V, and  $E_{a2} = 0.06 \pm 0.01$  eV at  $-0.2$  V. These activation energies are either from the valence band or conduction band as described in Eqs. (5.9) - (5.11). The center at  $E_{a1}$  dominates the reverse current

between  $T \approx 300 - 450$  K, and the center at  $E_{a2}$  appears to dominate for  $T < 300$  K. A dependence of activation energy on doping density is not apparent. A summary of values for  $E_{a1}$  and  $E_{a2}$  values for a number of "well-behaved" diodes is given in Table VI.

Assume for the time being that  $E_{a1}$  and  $E_{a2}$  are located relative to the valance band. In the theory section on Bulk Recombination, Eq. (2.45) predicts that a difference in energy between two centers of  $\sim 0.40$  eV is sufficient for the lifetime  $\tau$  of the free holes in the valance band to be determined by the deeper level, even if the concentration of the shallower level is 6 orders of magnitude larger than the deeper level. The average difference between measured  $E_{a1}$  and  $E_{a2}$  in the GaInP<sub>2</sub> diodes is 0.37 eV. This, together with Eq. (2.40) which shows the maximum recombination rate occurs when  $E_i$  is at the center of the bandgap, and the fact that  $E_{a2}$  is  $< 0.10$  eV from the band edge, strongly suggests that  $E_{a1} \approx 0.44$  eV is the dominant recombination center responsible for  $I_{rec}$ . In the next sections, DLTS and C-F-T measurements are used to confirm the positions of  $E_{a1}$  and  $E_{a2}$  relative to the valance band edge.

### **Deep Level Transient Spectroscopy (DLTS) Measurements**

DLTS provides a fast thermal scan of deep centers that are electrically active within the p-n junction (Lang, 1974:3023). DLTS involves a measurement of junction capacitance transients that result from the filling and emptying of energy levels with free carriers. This action is induced by applying a series of appropriate

voltage pulses across the junction. The time constant associated with the capacitance transient is measured as a function of temperature, and used in conjunction with the emission rate equation (2.28) derived in the theory to give the activation energy,  $E_a$ .

In Figure 53(a), an  $n^+p$  junction is shown under a steady reverse-bias, called the measure-bias (MB). The junction capacitance is given by  $C_1 = \epsilon_0 \epsilon_s A / W_{d1}$  in accordance with Eq. (5.1), and is shown in Figure 53(e). The junction capacitance arises from the charged ionized donor and acceptor atoms. An energy band diagram for the reverse-biased  $n^+p$  junction is shown in Figure 53b. In the following example, the transient response of a hole trap located at  $E_t < E_i$  will be discussed, where  $E_i$  is the intrinsic Fermi energy level. The energy levels at  $E_t$  located below  $E_{Fp}$  in Figure 53(b) will be occupied by electrons, in accordance with Fermi statistics, while levels above  $E_{Fp}$  will be empty. An empty state is represented by  $\_$ , and a filled states is shown as  $\bullet$ .

When the junction is biased with a fill-pulse, i.e.,  $V = -1$  V in Figure 53(c), the filled states that fall below  $E_{Fp}$  rapidly lose their electrons to the valence band, i.e., they capture holes. The voltage-bias is called a fill-pulse or fill-bias (FB) because it fills the levels with majority carriers, i.e., holes in this case. The capture process occurs rapidly because of the large number of holes in the valence band,  $p$ , in accordance with Eq. (2.25). The junction width shrinks to  $W_{d2}$  in accordance with

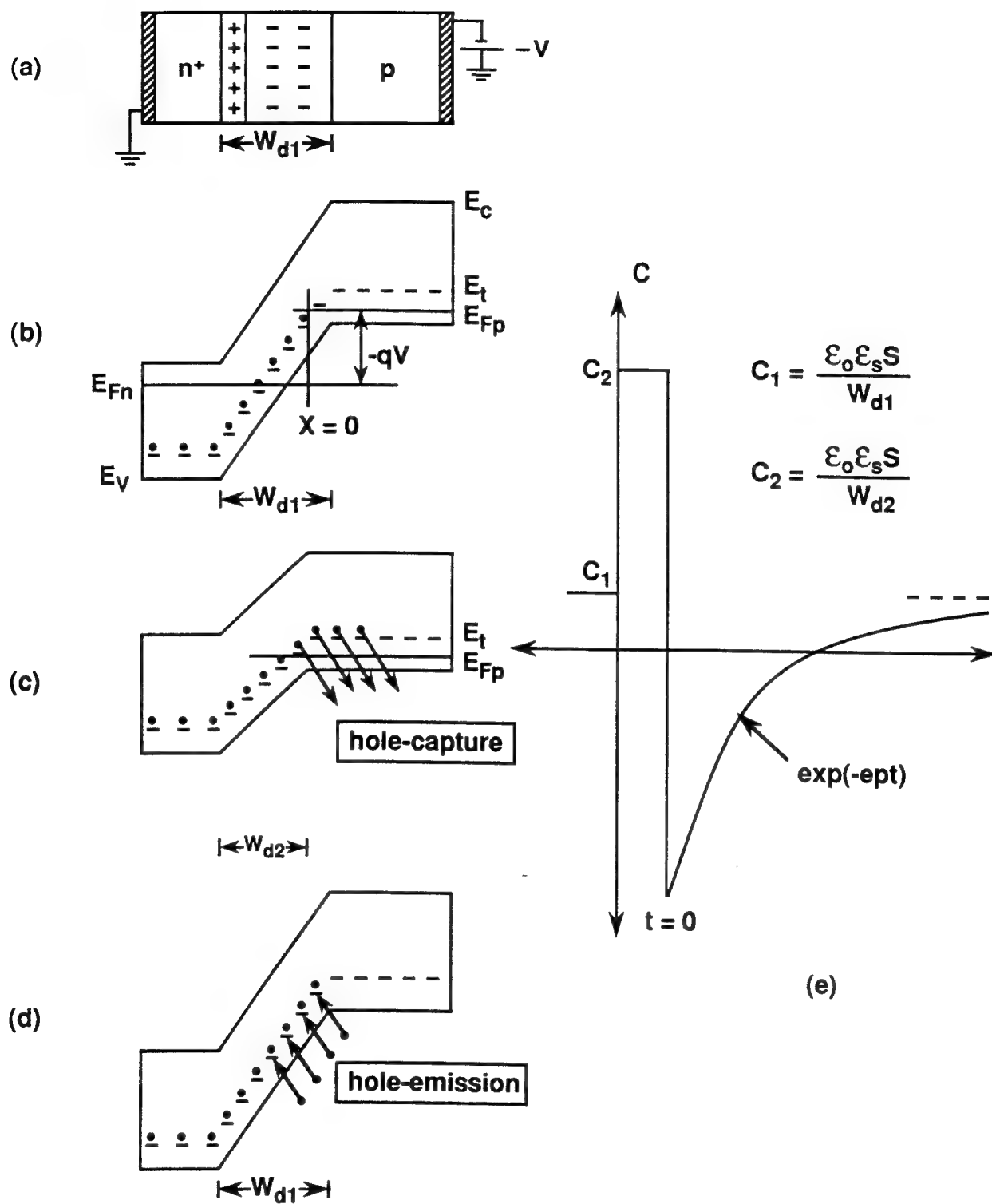


Figure 53. A schematic showing the detection of a deep level at  $E_t$  using DLTS.

Eq. (5.1), where  $W_{d2}$  is shown in Figure 53(c), and an increase in junction capacitance results, shown as  $C_2$  Figure 53(e).

As shown in Figure 53(e), the beginning of a capacitance transient occurs at  $t = 0^+$  when the fill-pulse is removed. The junction width immediately returns to  $W_{d1}$ . However, the presence of the extra holes in the p-space-charge region captured in the previous process reduces the amount of negative charge associated with the ionized acceptors, and the capacitance drops below  $C_1$  to the value  $C_3$  shown in Figure 53(e). The situation is restored to equilibrium by the emission of holes from the states, and the junction capacitance increases for  $t > 0$  as shown in the transient. This transient is an exponential function of time with a rate constant equal to  $e_p$  (Lang, 1974:3023), where  $e_p$  is the hole emission rate derived in the theory section resulting in Eq. (2.28). The case just considered is for a majority carrier level (trap), i.e., a hole trap in p-type material (see the section on Defect Level Terminology). In the case of a minority carrier trap, an increase in junction capacitance will occur at  $t = 0^+$ , and a negative transient will result for  $t > 0$  (Lang, 1974:3023).

DLTS measurements were taken for a number of low and mid doped GaInP<sub>2</sub> diodes to verify the energy levels measured using reverse-bias I-V-T. A typical plot of junction capacitance vs. time for a mid doped diode is shown in Figure 54. The transient begins at  $t = 0^+$ , and is seen to increase with time indicating the presence of a majority carrier trap. Since this data is for an asymmetrical n<sup>+</sup>p

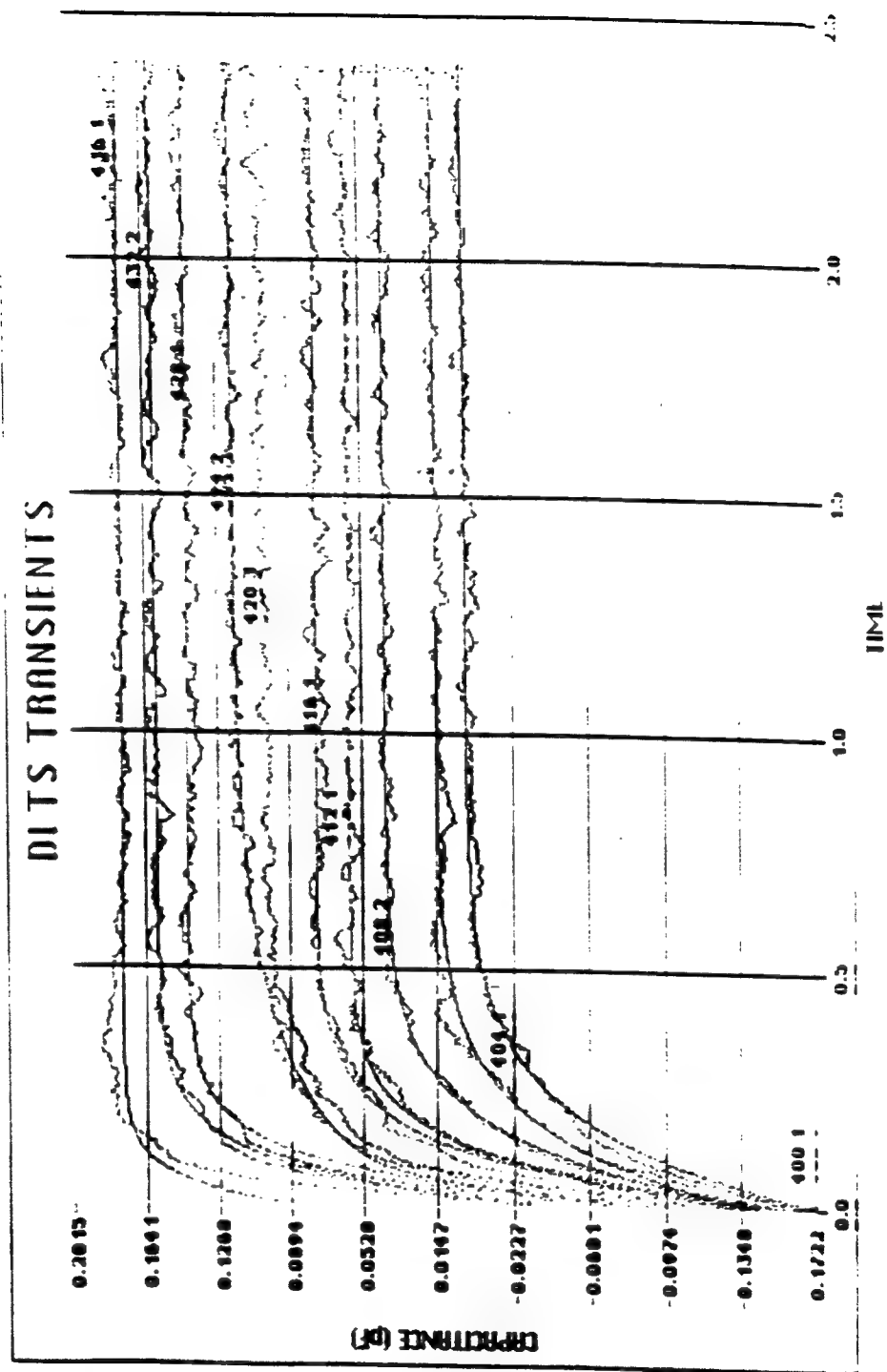


Figure 54. Junction capacitance transients due to a majority carrier trap in the p-base of a  $\text{GaInP}_2$  n-p diode.

diode, the depletion is primarily in the low-doped side of the junction, and the transients will be much more sensitive to traps on the p-side (Lang, 1974:3023). Thus, the measured transient indicates a majority carrier trap in the p-material, which by convention is called a hole trap. The energy level of the trap was obtained by fitting the capacitance transients to a function of the form  $\exp(-e_p t)$ , where  $e_p$  is the rate constant for the Arrhenius process given by  $e_p = \sigma_p v_{th} N_v g^{-1} \exp(-E_a/kT)$  in Eq. (2.30), and  $E_a = E_t - E_v$ . Substituting for the temperature dependence of  $v_{th} N_v$  gives

$$\frac{e_p}{T^2} = \sigma(\infty) \exp\left(\frac{-E_a}{kT}\right), \quad (5.15)$$

where the parameter  $\sigma(\infty)$  contains all the unmeasured constants. Thus a plot of  $\ln(T^2/e_p)$  vs  $1/KT$  will yield a straight of slope  $E_a$ . In Figure 55, a typical set of Arrhenius data is shown for a low and mid doped GaInP<sub>2</sub> diode, and a straight line fit through the data yields values of  $E_a = E_t - E_v \approx 0.40$  and  $0.48$  eV, respectively. The MB = -5 V, and the FB was -1 V. As discussed, the energy levels were measured relative to the valance band because the sign of the transient was positive in the p-type material. In Table VII, the  $E_a$  values measured using DLTS are compared with values of  $E_{a1}$  obtained from I-V-T measurements. These values are in good agreement with each other, and their average difference is less than 2% of the bandgap of GaInP<sub>2</sub>,  $E_g \sim 1.84$  eV. In the next section the values of  $E_a$  will be shown to be dependent on the electric field in the junction, and therefore dependent on the MB and PB. In some cases, differences in  $E_a$  measured by

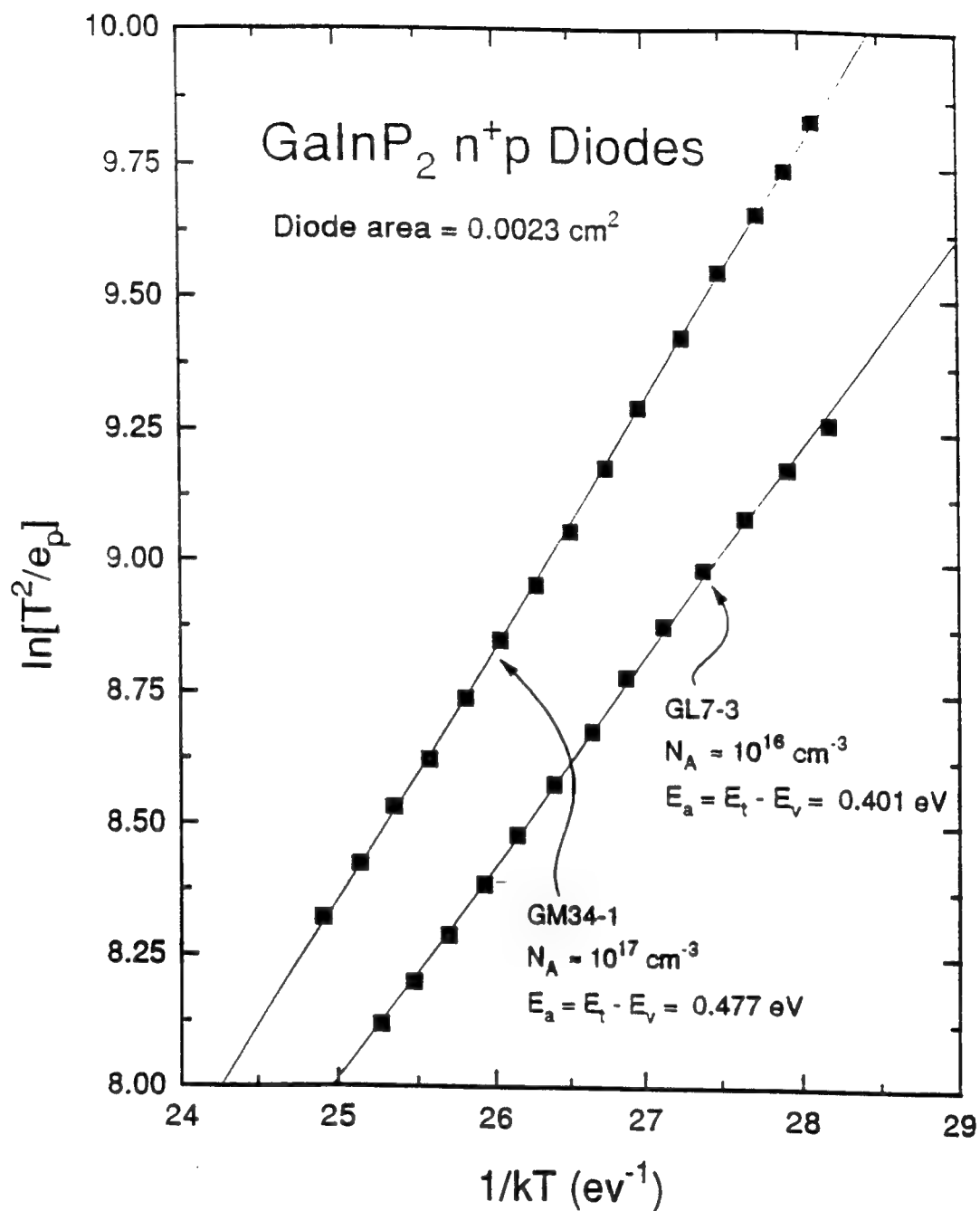


Figure 55. A plot of  $\ln[T^2/e_p]$  vs  $1/T$  for low and mid doped GaInP<sub>2</sub> diodes determined from DLTS spectra, where  $e_p$  is the majority hole emission rate in the p-GaInP<sub>2</sub>. The slope gives the energy of the deep level at  $E_a = E_t - E_v$ .



Table VII. Summary of deep energy levels measured in GaInP<sub>2</sub> using reverse-bias I-V-T and DLTS measurements

<u>Device</u>	<u>E<sub>al</sub> (eV) *</u>	<u>E<sub>t</sub> - E<sub>v</sub> (eV)**</u>	<u>PB(V)</u>	<u>MB(V)</u>
GL4-2	0.42	0.44	-1	-5
GL7-3	0.44	0.40	-1	-5
GL12-1	0.43	0.48	-1	-5
GM31-2	0.46	0.52	-1	-5
GM33-3	0.43	0.56	-0.2	-3
GM34-1	0.47	0.48	-1	-5
GM35-3	0.44	0.43	-1	-5

\* Measured by reverse-bias I-V-T

\*\* Measured by DLTS

PB - Pulse bias

MB - Measure bias

DLTS and I-V-T were as large as 12% of the bandgap. The DLTS measured values of  $E_a$  are important not only because they confirm the values of  $E_{a1}$  obtained from I-V-T, but because they locate the levels relative to the valance band, in the bottom half of the bandgap. To date, these are the first reported deep levels in p-type GaInP<sub>2</sub>.

It is noted that DLTS was not able to conclusively confirm the  $E_{a2}$  level detected by I-V-T. In several diodes there was evidence of some minority carrier trap behavior (negative transients) at low temperatures,  $T < 200$  K, however, these signals were very weak and could not be consistently repeated. The  $E_{a2}$  level will be confirmed later using capacitance-frequency-temperature (C-F-T) measurements.

### **Frenkel-Poole Barrier Lowering**

Of particular interest in the GaInP<sub>2</sub> diodes is also the observed decrease in  $E_a$  with increasing junction electric field. This behavior can be explained in terms of the Frenkel-Poole emission effect (Frenkel, 1938:657). As discussed in the theory, impurities and/or lattice defects are responsible for the energy states at  $E_a$  in the bandgap. The Frenkel-Poole effect predicts that the presence of an electric field,  $F$ , in the region of the impurities/defects will lower the energy barrier associated with the center in the direction of the field by the amount  $\Delta E_a$ . The decrease in  $E_a$  is given as  $\Delta E_a = q (qF/\pi\epsilon)^{1/2}$ , where  $\epsilon$  is the dielectric constant. This effect is due to a lowering of the center's emission barrier by the field  $F$ , which increases the

carrier emission probability, and hence, the measured value of  $E_a$ . This behavior is shown in the data of Figure 56, where the decrease in  $E_a$  for two "well-behaved" GaInP<sub>2</sub> diodes goes as approximately  $\Delta E_a \propto F_{ave}^{1/2}$ , where  $F_{ave}$  is the average field seen by the centers. The field strength in the junction was varied with the PB, and an average value for  $F$  in the region of hole emission was calculated using the measured values of doping density,  $N_A$ , and the field strength equations given by Sze (Sze, 1981:81) for an abrupt p-n junction.

The effect of Frenkel-Poole energy lowering can be seen in Figure 57(a), which shows an energy diagram for a defect and/or impurity center occupied by a hole. The diagram has been inverted relative to the standard energy band diagram for convenience, where  $E_v$  is the valance band edge,  $E_a$  is the zero-field trap energy level, and  $\Delta E_a$  is the Frenkel-Poole energy lowering due to the electric field. The electric field can be increased by simply increasing the reverse-bias. The barrier lowering in Figure 57(a) can be explained by the effects of a distribution of localized positive charge associated with the defect/impurity center as shown in Figure 57(b). In this figure, a hole (open circle) has been trapped by a state localized near the center of the charge distribution. The resulting barrier formed by the charge contributes to the hole emission barrier. In the presence of an applied electric field, the barrier is lowered as shown on the right side of Figure 57(c), and the emission rate will increase. Current samples are Zn-doped p-type. Similar Frenkel-Poole effects have been reported in Zn-doped p-InP material,

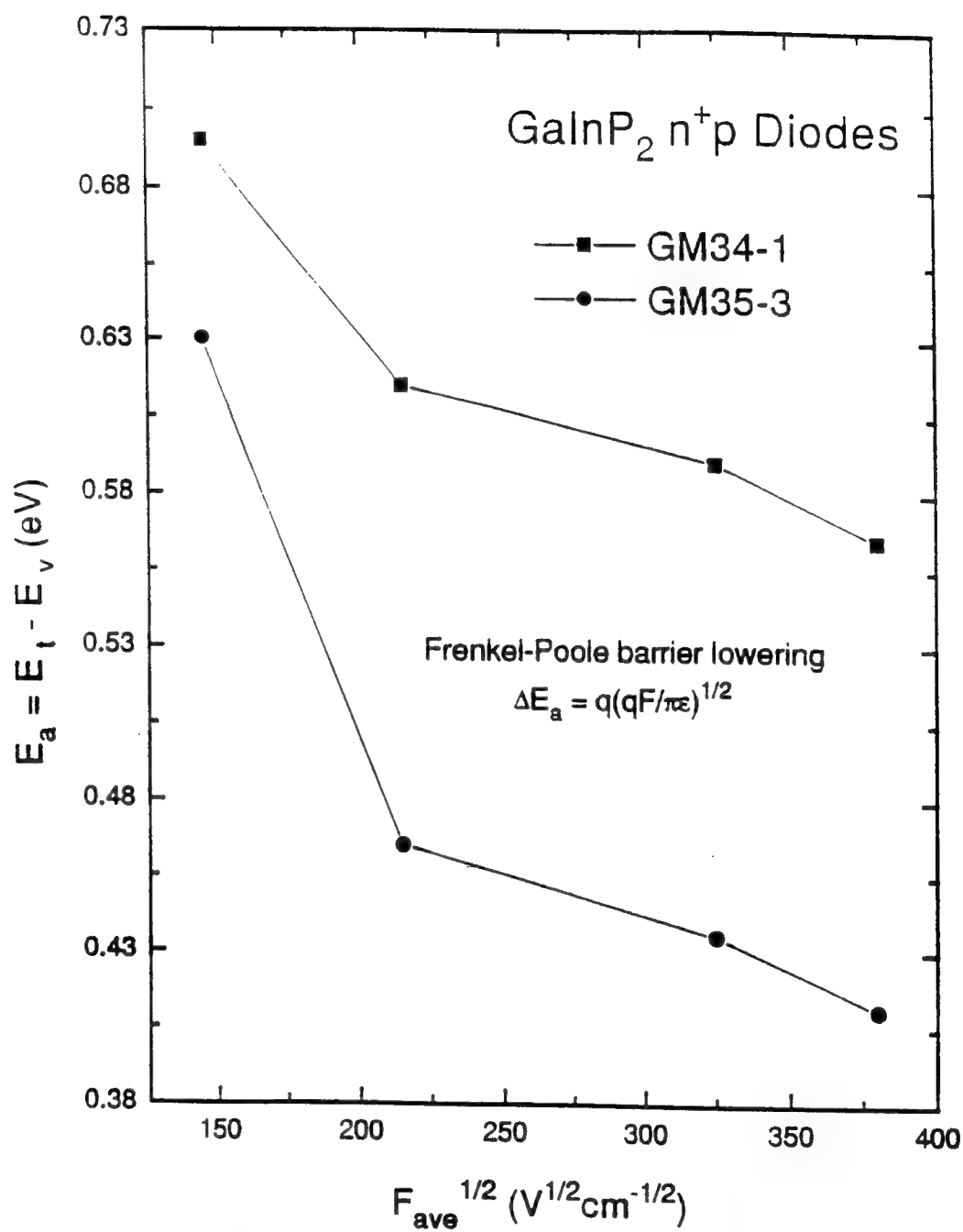


Figure 56. The effect at Frenkel-Poole barrier lowering on the measured energy,  $E_a$ , of deep levels in GaInP<sub>2</sub> n<sup>+</sup>p diodes.

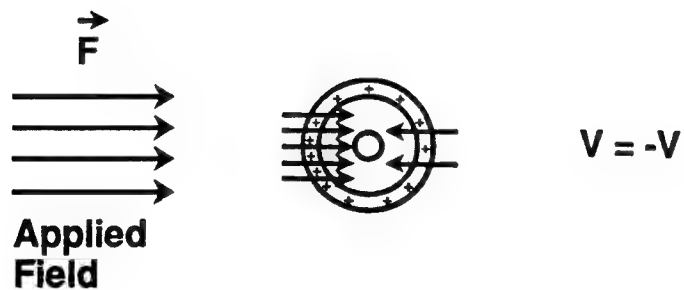
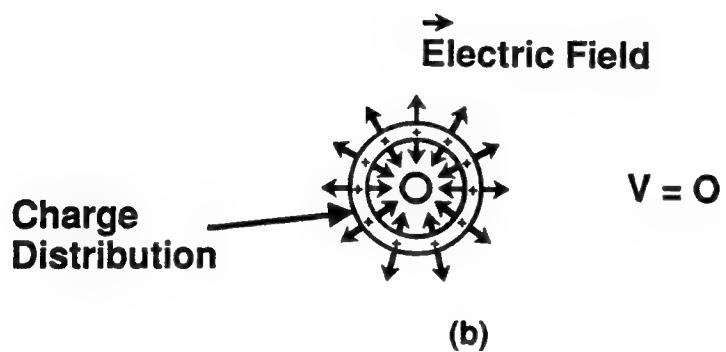
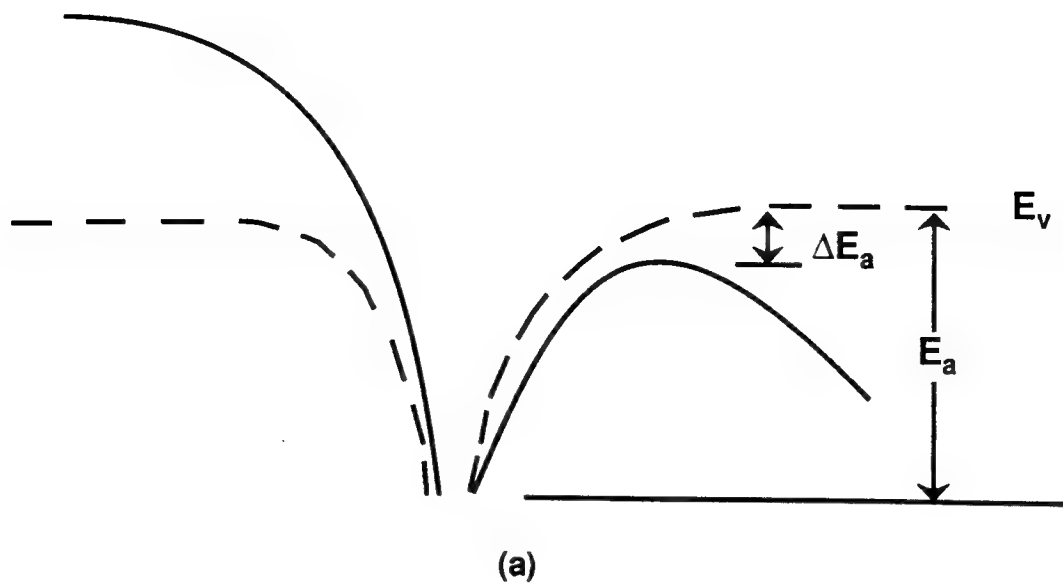


Figure 57. (a) Frenkel-Poole emission barrier lowering,  $\Delta E_a$ . (b) Electric field emanating from localized charge distribution associated with defect/impurity center. (c) Electric field is shown lowered on right-side of charge distribution by applied field,  $F$ , and the resulting emission barrier is lowered by  $\Delta E_a$ .

where several dominant majority-hole traps were found between energies of  $\sim 0.30 - 0.60$  eV (Messenger *et al.*, 1992:4201). Although no information was given into the nature of Zn related defect centers in InP, the concentration of Zn was shown to play an important role in determining the introduction and annealing rates of 1 MeV electron induced defect centers. This fact suggests that Zn related defect complexes may be involved in p-GaInP<sub>2</sub> as well. Similar observations of Frenkel-Poole effects in both GaInP<sub>2</sub> and InP are due to the chemical similarity between the two materials, where GaInP<sub>2</sub> is essentially an alloy of InP with exactly 1/2 of the In atoms replaced with Ga. In the next section, the shallow generation/recombination center  $E_{a2}$  measured by I-V-T will also be examined with capacitance-frequency-temperature (C-T-F) measurements.

### Capacitance-Frequency-Temperature (C-F-T) Measurements

The frequency-dependent temperature derivative,  $dC/dT$ , of p-n junction capacitance can also be used to determine  $E_a$  of deep levels (Tan and Xu, 1989:25). The technique is based on changes in junction capacitance resulting from the dependency of deep level emission rates on junction temperature and test signal frequency. The capacitance,  $C$ , of a p-n junction is determined by applying a small oscillating voltage,  $\Delta V_{osc}$ , across the junction. The depletion width remains approximately constant, and the junction capacitance,  $C = \Delta Q/\Delta V$ , is determined by measuring the induced current by the oscillating voltage. The  $\Delta V_{osc}$  will sweep  $E_t$  above and below  $E_{Fp}$  near  $x = 0$  in Figure 53(b), and holes will be repeatedly

captured and emitted, respectively. If the capture and emission rates,  $c_p$  and  $e_p$ , respectively, are both larger than  $\omega(\Delta V_{\text{osc}})$ , where  $\omega$  is the angular signal frequency, then the equilibrium value for capacitance  $C_1$  shown in Figure 53(e) will result. However, if either  $c_p$  or  $e_p$  are less than  $\omega(\Delta V_{\text{osc}})$ , the traps cannot follow the oscillating voltage, and the measured value of capacitance will be less than  $C_1$ . As previously discussed,  $c_p$  will be very large because of the large hole density,  $p$ , in Eq. (2.25). Therefore, the emission rate will be the limiting process.

Since the emission rate increases with temperature as  $e_p \propto \exp(-E_a/kT)$  (Lang, 1974:3023), the temperature at which  $e_p = \omega(\Delta V_{\text{osc}})$  occurs can be obtained from C-V vs  $\omega$  data. Then the activation energy,  $E_a$ , of the level can be found by measuring the temperatures  $T_1$  and  $T_2$  that satisfy  $e_p = \omega(\Delta V_{\text{osc}})$  for  $\omega = \omega_1$  and  $\omega_2$ , respectively. For  $T_2 - T_1 \ll T_2$  or  $T_1$ , the ratio of  $\exp(-E_a/kT_1) = \omega_1(\Delta V_{\text{osc}})$  to  $\exp(-E_a/kT_2) = \omega_2(\Delta V_{\text{osc}})$  can be rearranged to give (Tan and Xu, 1989:28),

$$E_a = E_t - E_v = \frac{kT_1T_2}{T_2 - T_1} \left[ \exp\left(\frac{f_1}{f_2}\right) - 2 \ln\left(\frac{T_2}{T_1}\right) \right], \quad (5.16)$$

where  $\omega = 2\pi f$ . This equation was used to obtain values of  $E_a$  in "leaky" and "well-behaved" mid doped GaInP<sub>2</sub> diodes.

In Figure 58, a set of typical  $\ln(I)$  vs.  $V$  curves for a "leaky" and a "well-behaved" mid doped diode is shown. The "leaky" diode contained a visible line-like defect on its surface. In Figure 59, a set of  $C$  vs.  $T$  data taken at 100 kHz and 1 MHz between 20 and 300 K for the same diode is also shown. Large steps in  $C$

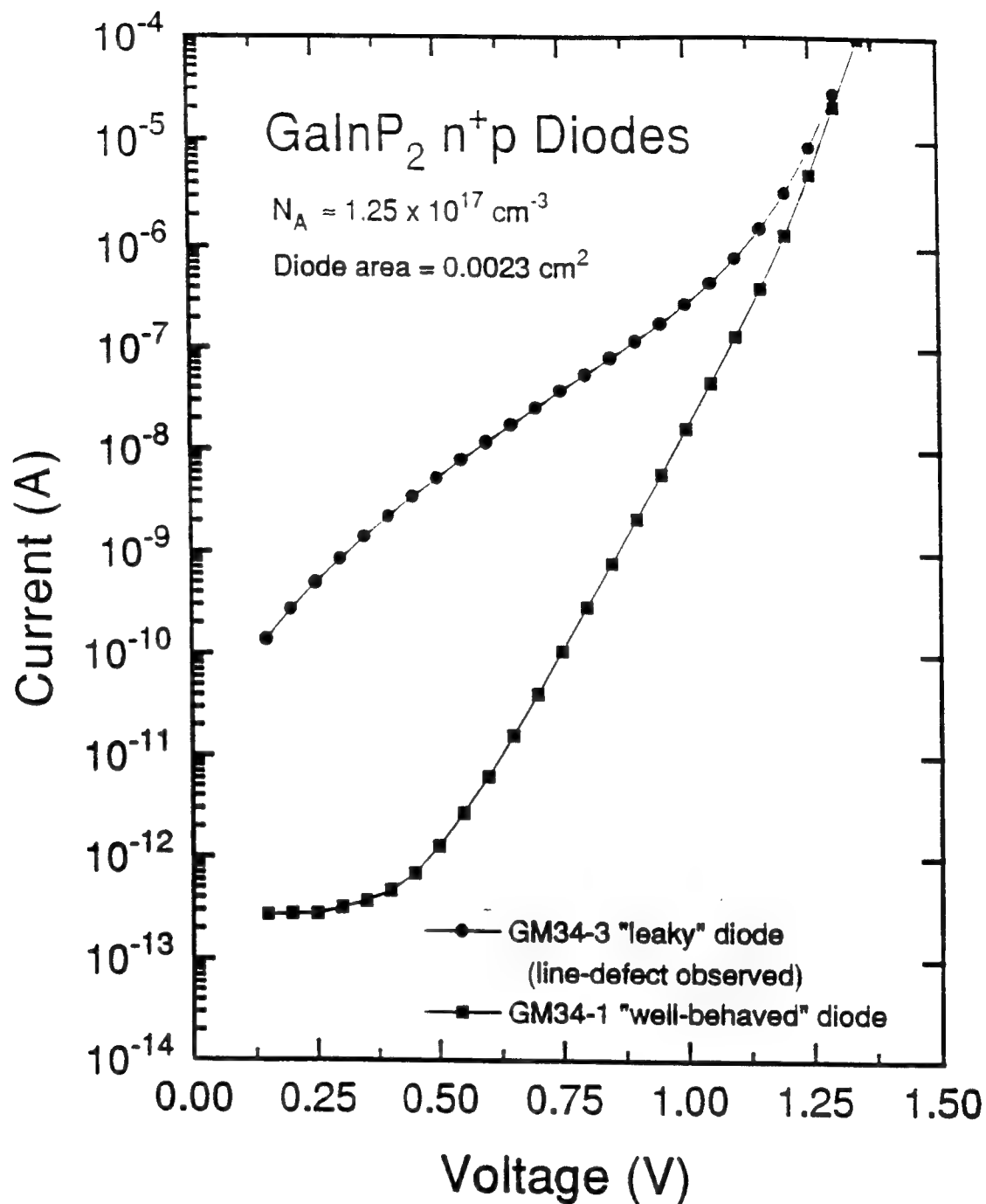


Figure 58. Forward-bias I-V curves for the mid doped "leaky" and "well-behaved" GaInP<sub>2</sub> diodes used for C-F-T measurements.



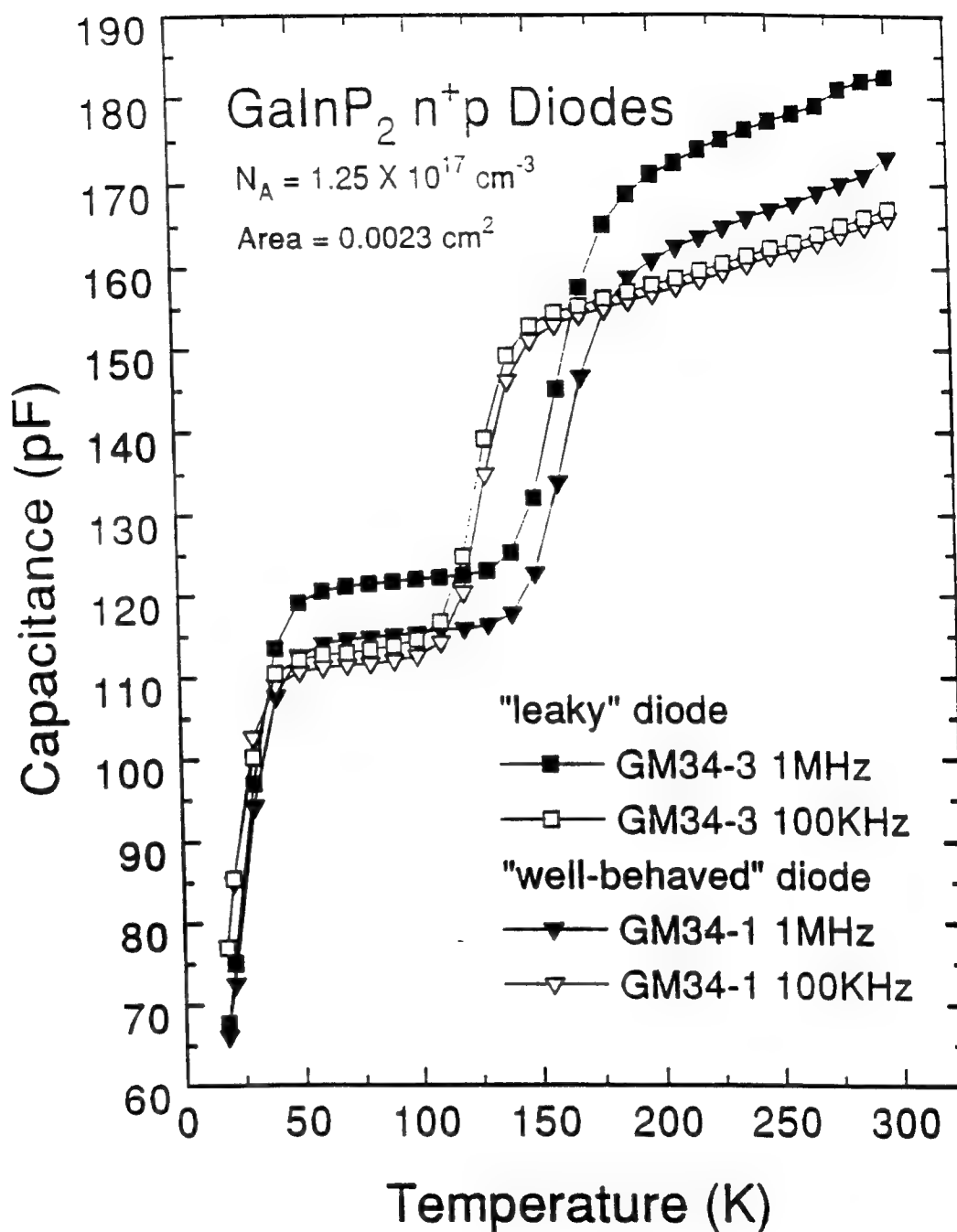


Figure 59. Typical capacitance-frequency-temperature data for GaInP<sub>2</sub> n<sup>+</sup>p diodes.

with increasing  $T$  are seen to occur at  $\sim 25$  and  $130$  K for  $f_1 = 100$  KHz, and at  $\sim 25$  and  $160$  K for  $f_2 = 1$  MHz. These steps indicate the presence of the emission limited trapping discussed above. To determine the approximate temperature for which  $e_p = \omega(\Delta V_{osc})$ , a maximum rate of change in temperature,  $T_m$ , was obtained from the plot of  $dC/dT$  shown in Figure 60. At  $T_m$ , the trap begins to follow  $\Delta V_{osc}$ , and its value corresponds to the peaks in Figure 60. The shift in  $T_m$  towards higher temperatures as the test signal frequency increases is due to the required larger  $e_p$  to follow the faster test signal (higher  $\omega$ ). Values of  $E_a$  for the deep levels were obtained using Eq. (5.16), and  $T_{m1}$  and  $T_{m2}$  in Figure 60, giving  $E_a \approx 0.10$  eV for both diodes. The  $E_a$  values obtained using this technique are compared with values of  $E_{a2}$  obtained using I-V-T in Table VIII. These values are in excellent agreement with each other with an average activation energy difference in energy of  $\sim 1\%$  of the bandgap.

In nearly all diodes examined, values of  $E_{a2}$  obtained for the "leaky" diodes were consistent with  $E_{a2}$  obtained for the "well-behaved" diodes. However, an interesting difference in values for  $\Delta C$  with  $\Delta f$  was observed at a given temperature between the "leaky" and "well-behaved" devices. At  $100$  kHz, the C-T curves were found to be nearly identical between "leaky" and "well-behaved" diodes. However, at  $1$  MHz,  $\Delta C$  at a given temperature for the "leaky" diodes was much larger than that for the "well-behaved" diodes. For example, in Figure 59,  $\Delta C$  for the "well-behaved" device is  $\sim 5$  pF at temperatures of  $75$  and  $250$  K, whereas

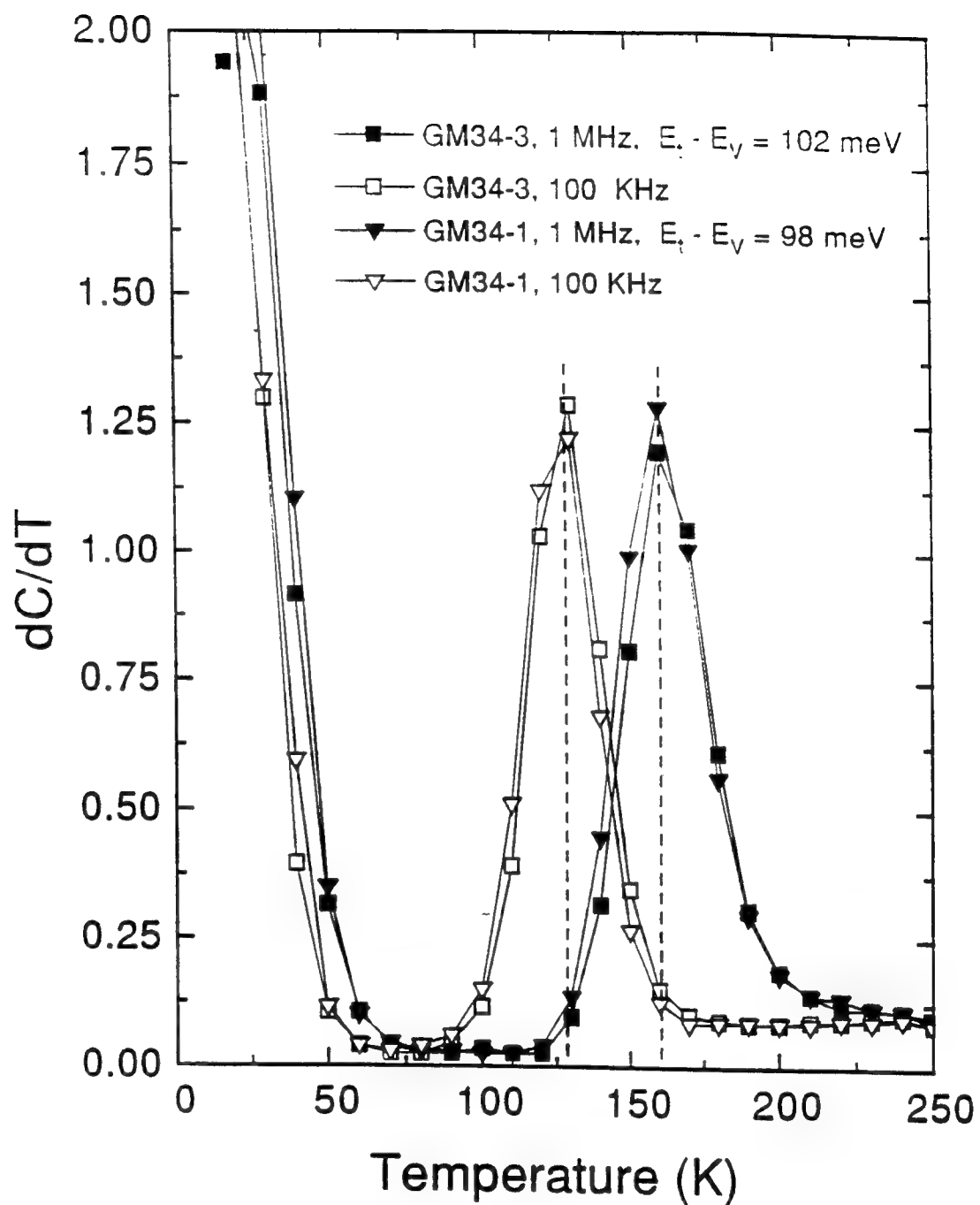


Figure 60. A plot of  $dC/dT$  for the  $\text{GaInP}_2$  diodes of Figure 59, used for determining activation energy  $E_a = E_t - E_v$ .

Table VIII. Summary of activation energies obtained using reverse-bias I-V-T and C-F-T measurements

<u>Device</u>	<u><math>N_A</math> (cm<sup>-3</sup>)</u>	<u><math>E_{a2}</math> (ev) *</u>	<u><math>E_{a2}</math>(ev) **</u>
GL12-1	1.4E16	0.06	0.07
GL12-2	1.5E16	0.05	0.06
GM31-1	1.24E17	0.07	0.06
GM31-2	1.26E17	0.07	0.05
GM33-1	1.20E17	0.06	0.09
GM33-2	1.20E17	--	0.07
GM33-3	1.22E17	--	0.08
GM34-1	1.25E17	0.06	0.10
GM34-3	1.25E17	0.08	0.10

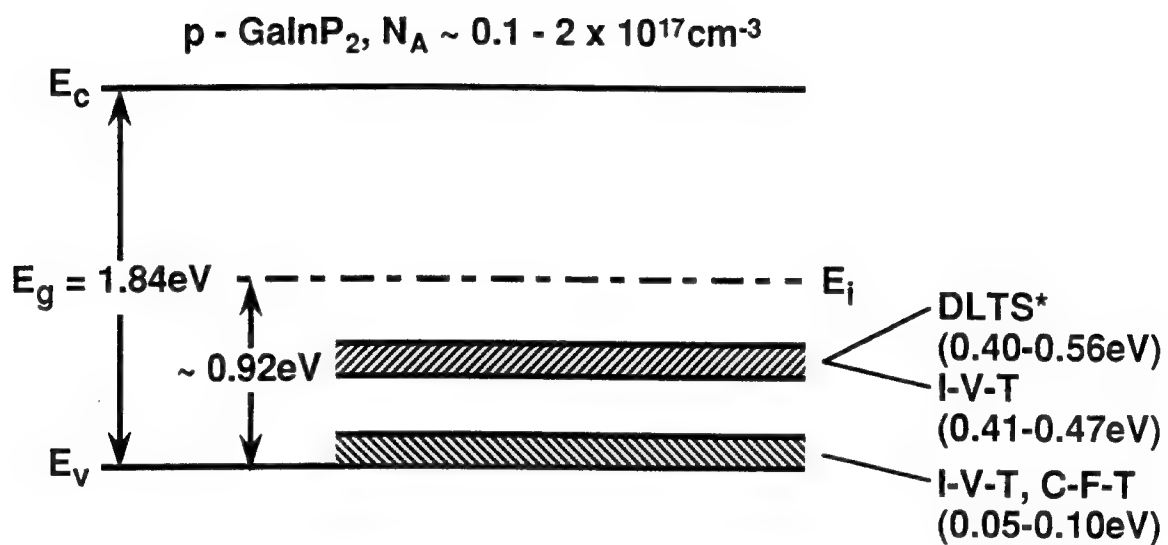
\* Obtained from reverse-bias I-V-T

\*\* Obtained from C-F-T

those for the "leaky" diode are  $\sim 10$  and  $15$  pF, respectively. A similar trend was found in nearly all "leaky" diodes examined. It is believed that this behavior may be related to carrier tunneling that was found in these devices, or possibly due to the nature of the visible line-defects. However, at this time the exact reason for the discrepancy in  $\Delta C$  is unknown. The slope of the C-T curve for  $T > 200$  K is predicted through the temperature dependence of  $V_{bi}$  in Eq. (5.1). The slopes are the same for the "leaky" and "well-behaved" diodes in agreement with the equivalent values of  $N_A$  measured in the devices. It is interesting to note that there was no apparent  $dC/dT$  observed in the diodes for  $T > 300$  K, where  $E_{a1}$  was expected to be. The reason for this is also not understood at this time, however, the presence of  $E_{a1}$  was firmly established from I-V-T and DLTS data.

### Summary of Deep Levels in GaInP<sub>2</sub>

In Figure 61, an energy band diagram for the GaInP<sub>2</sub> is shown, which summarizes the energies of deep levels found using I-V-T, DLTS, and C-F-T measurements. Levels are shown in the p-GaInP<sub>2</sub>, because dark current due to recombination in the  $n^+p$  diodes and solar cells is controlled by these centers, i.e.,  $\sim 80$ ,  $90$ , and  $98\%$  of the depletion region is located on the p-side of the junction in the high, mid, and low doped diodes, respectively. Figure 61 shows two bands of energy levels centered around  $E_{a1} \approx 0.45$  eV and  $E_{a2} \approx 0.07$  eV. These levels are responsible for the dominant recombination current found in the diodes and solar cells. However, as previously discussed, a difference in energy of  $\sim 0.40$  eV between  $E_{a1}$  and  $E_{a2}$



\* measurements taken with PB = -1V, mB = -5V

Figure 61. A summary of deep levels found in GaInP<sub>2</sub> n<sup>+</sup>p diodes using reverse-bias I-V-T, DLTS, and C-F-T measurements.

predicts that the lifetime for holes,  $\tau_p$ , will be dominated by  $E_{a1}$  even if the concentration of  $E_{a2}$  was 6 orders of magnitude larger than that of  $E_{a1}$ . Also, the maximum rate of recombination occurs for  $E_a = E_i$ , where  $\tau_p$  drops off exponentially with  $E_i - E_a$ . Therefore, levels at  $E_{a2}$  should not play an important role in affecting recombination current in these devices.

## **VI. Characterization of Electron Irradiated GaInP<sub>2</sub> Solar Cells and Diodes**

A series of radiation tests for GaInP<sub>2</sub> solar cells and mesa diodes were performed using 1 MeV electrons to a fluence of  $10^{15}$  and  $10^{16}$  e<sup>-</sup>/cm<sup>2</sup>. The goal was to study the behavior of the top GaInP<sub>2</sub> solar cell of the GaInP<sub>2</sub>/GaAs tandem operating in the space environment. The response of the bottom GaAs cell in the radiation environment can be easily extrapolated from the literature (Fan, 1980; Yamaguchi and Amano, 1985:537; Markvart, 1990:12). The solar cells were measured under AM0 conditions before and after each irradiation, and changes in the solar cell PV parameters were monitored following thermal annealing at 250°C. The response of solar cell and diode dark currents to electron irradiation were also examined following thermal annealing.

### **The Response of GaInP<sub>2</sub> Solar Cells to 1 MeV Electron Irradiation and Thermal Annealing**

The GaInP<sub>2</sub> solar cells and diodes studied in Chapters 4 and 5, respectively, were irradiated with electrons at the Air Force Geophysics Directorate, Phillips Laboratory, MA. The solar cells were irradiated with 1 MeV electrons to a fluence of  $10^{15}$  and  $10^{16}$  e<sup>-</sup>/cm<sup>2</sup> using a Dynamitron accelerator. A fluence of about  $5 \times 10^{15}$  e<sup>-</sup>/cm<sup>2</sup> is representative of a fluence encountered in many typical space



missions in geosynchronous- and low-earth-orbits that last 10 to 15 years (Wolff *et al.*, 1992:96). The Dynamitron sample holder provided four positions for the solar cells and eight positions for the T05 diode cans. Consequently, four solar cells were irradiated with  $10^{15}$  electrons/cm<sup>2</sup>, and four cells with  $10^{16}$  electrons/cm<sup>2</sup>. An average electron beam current of 60  $\mu$ A was used, and a device temperature of  $\sim 30^{\circ}\text{C}$  was maintained during the irradiation using a water cooled cold plate. Immediately following irradiation, the solar cells were stored on dry ice to prevent ambient annealing prior to measurement. The solar cells were removed from the dry ice 1 hr prior to initial post-irradiation measurement and allowed to reach ambient room temperature ( $\sim 25^{\circ}\text{C}$ ). Solar cell dark and light I-V parameters were obtained using measurement procedures outlined in Chapter 4. Also, since high energy electron radiation is known to produce a significant amount of semiconductor lattice damage through atomic displacement (Tada *et al.*, 1982:3-6), the GaInP<sub>2</sub> cells were heated at  $250^{\circ}\text{C}$  in an attempt to anneal out such damage. On-orbit thermal induced annealing of 1 MeV electron degradation was recently reported for Si and GaAs solar cells (Wolff *et al.*, 1992:88). Periodic pulse thermal heating at  $250^{\circ}\text{C}$  resulted in solar cell strings that provided 4 to 11% more power than control cells that were not heated. In this experiment, the GaInP<sub>2</sub> solar cells were annealed at  $250^{\circ}\text{C}$  for 10 mins. several times, and data were taken after each annealing.

Typical light-I-V curves for GaInP<sub>2</sub> solar cells before and after electron irradiation to a fluence of  $10^{15}$  and  $10^{16}$  e<sup>-</sup>/cm<sup>2</sup> are shown in Figures 62 and 63, respectively. The average reduction in solar cell  $V_{oc}$ ,  $I_{sc}$ , ff, and Eff immediately following exposure to  $10^{15}$  electrons/cm<sup>2</sup> was about 3, 8, 1, and 10%, compared to a reduction of 11, 18, 8, and 33% for cells exposed to  $10^{16}$  electrons/cm<sup>2</sup>. A summary of resulting solar cell PV parameters is given in Tables IX and X for a number of cells. In Figure 64, the amount of degradation in these cells is compared to 1 MeV electron irradiation degradation in Si, GaAs, and InP solar cells (Yamaguchi and Ando, 1988:5555). These data appear to indicate that the radiation resistance of these GaInP<sub>2</sub> solar cells lies between that of GaAs and InP solar cells. This is not surprising considering the similarity in chemistry between GaInP<sub>2</sub> and InP, i.e., one-half of the atoms in InP are replaced by Ga atoms, and the fact that InP solar cells are found to be more radiation resistant than GaAs solar cells.

The reduction of solar cell  $V_{oc}$  and  $I_{sc}$  following electron irradiation can be explained through the effects of reduced minority carrier lifetime, as discussed in Chapters 3, 4 and 5. Lattice damage induced by electron irradiation results in the formation of recombination centers that reduce carrier lifetime and diffusion length. For example, in InP, the main hole trap induced by 1 MeV electrons, H4, is thought to be due to a phosphorus vacancy and interstitial complex (Yamaguchi and Ando, 1988:5555). This trap was shown to be an efficient recombination

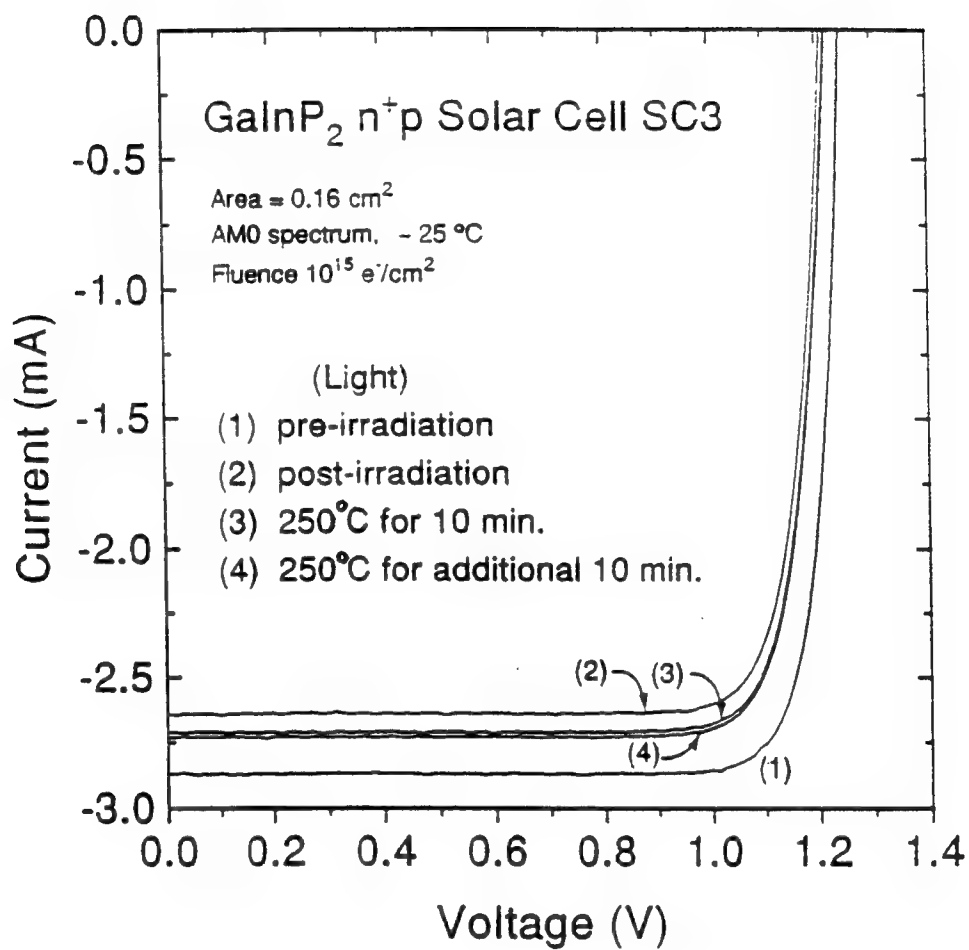


Figure 62. Light I-V curves for a GaInP<sub>2</sub> solar cell before and after 1 MeV electron irradiation of fluence 10<sup>15</sup> e<sup>-</sup>/cm<sup>2</sup>, and subsequent thermal annealing at 250 °C.

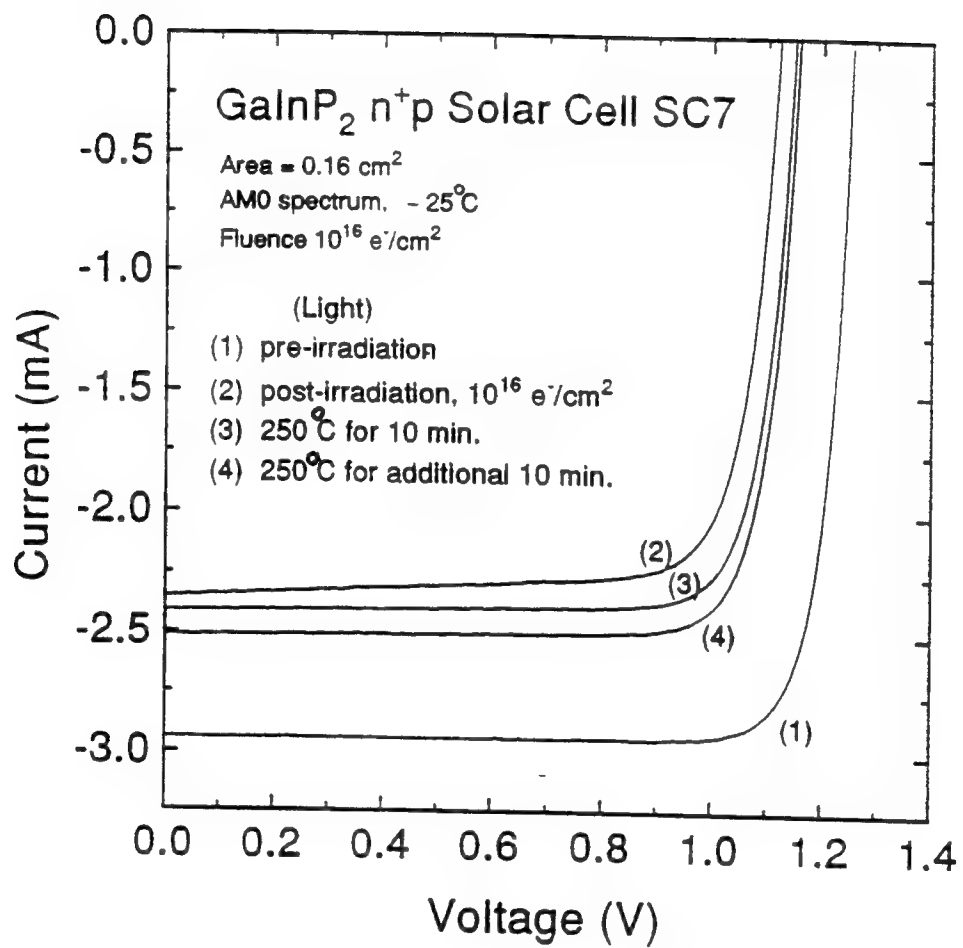


Figure 63. Light I-V curves for a GaInP<sub>2</sub> solar cell before and after 1 MeV electron irradiation of fluence 10<sup>16</sup> e<sup>-</sup>/cm<sup>2</sup>, and subsequent thermal annealing at 250°C.

**Table IX. Summary of GaInP<sub>2</sub> solar cell photovoltaic parameters before and after exposure to 1 MeV electrons of fluence  $10^{15}$  e<sup>-</sup>/cm<sup>2</sup>, and subsequent multiple thermal annealing at 250°C for 10 min.**

**1 MeV Electron Fluence =  $10^{15}$  e<sup>-</sup>/cm<sup>2</sup>**

Cell #	Condition	V <sub>oc</sub> (V)	I <sub>sc</sub> (mA)	ff (%)	Eff (%)
SC3	Pre-rad	1.24	2.87	0.86	14.2
	Post-rad	1.21	2.04	0.84	12.4
	+10 min at 250°C	1.22	2.71	0.84	12.8
	+10 min at 250°C	1.22	2.73	0.84	12.9
	+10 min at 250°C	1.21	2.72	0.83	12.7
SC5	Pre- rad	1.24	2.79	0.85	13.6
	Post-rad	1.20	2.53	0.84	11.8
	+10 min at 250°C	1.21	2.62	0.84	12.3
	+10 min at 250°C	1.22	2.59	0.85	12.4
	+10 min at 250°C	1.21	2.59	0.84	12.2
	+10 min at 250°C	1.21	2.59	0.83	12.1
SC6	Pre-rad	1.24	2.84	0.85	13.9
	Post-rad	1.21	2.59	0.84	12.2
	+10 min at 250°C	1.22	2.64	0.84	12.5
	+10 min at 250°C	1.22	2.70	0.84	12.7
	+10 min at 250°C	1.21	2.70	0.83	12.6
	+10 min at 250°C	1.21	2.69	0.83	12.5
SC8	Pre-rad	1.24	2.79	0.84	13.4
	Post-rad	1.19	2.56	0.83	11.7
	+10 min at 250°C	1.20	2.63	0.83	12.1
	+10 min at 250°C	1.21	2.64	0.83	12.2
	+10 min at 250°C	1.21	2.64	0.82	12.1
	+10 min at 250°C	1.21	2.63	0.81	12.0

Table X. Summary of GaInP<sub>2</sub> solar cell photovoltaic parameters before and after exposure to 1 MeV electrons of fluence  $10^{16} \text{ e}^-/\text{cm}^2$ , and subsequent multiple thermal annealing at 250°C for 10 min.

1 MeV Electron Fluence =  $10^{16} \text{ e}^-/\text{cm}^2$

Cell #	Condition	V <sub>oc</sub> (V)	I <sub>sc</sub> (mA)	ff (%)	Eff (%)
SC1	Pre-rad	1.24	2.81	0.85	13.7
	Post-rad	1.11	2.27	0.79	9.2
	+10 min at 250°C	1.14	2.37	0.81	10.1
	+10 min at 250°C	1.16	2.41	0.81	10.5
	+10 min at 250°C	1.15	2.42	0.80	10.3
	+10 min at 250°C	1.14	2.42	0.79	10.1
SC2	Pre-rad	1.24	2.75	0.85	13.4
	Post-rad	1.09	2.27	0.78	8.9
	+10 min at 250°C	1.12	2.37	0.80	9.9
	+10 min at 250°C	1.14	2.39	0.82	10.3
	+10 min at 250°C	1.13	2.37	0.81	10.1
	+10 min at 250°C	1.13	2.37	0.80	9.9
SC4	Pre-rad	1.25	2.88	0.86	14.3
	Post-rad	1.11	2.40	0.79	9.7
	+10 min at 250°C	1.14	2.46	0.82	10.6
	+10 min at 250°C	1.15	2.52	0.83	11.1
	+10 min at 250°C	1.15	2.50	0.82	10.9
	+10 min at 250°C	1.14	2.50	0.81	10.7
SC7	Pre-rad	1.25	2.94	0.86	14.6
	Post-rad	1.13	2.35	0.79	9.8
	+10 min at 250°C	1.15	2.40	0.81	10.3
	+10 min at 250°C	1.16	2.51	0.83	11.2
	+10 min at 250°C	1.16	2.52	0.81	11.1
	+10 min at 250°C	1.16	2.52	0.80	10.8

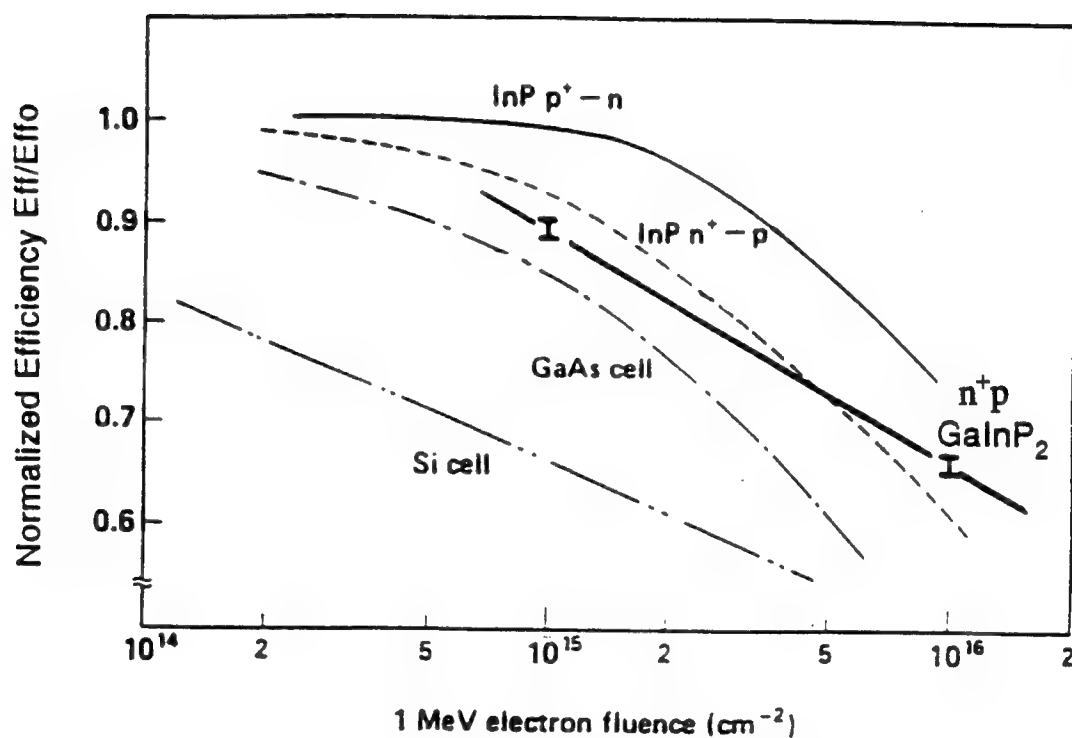


Figure 64. A comparison of normalized solar conversion efficiency for various solar cells as a function of 1 MeV electron fluence, where  $Eff_0$  and  $Eff$  are the pre- and post-irradiation efficiencies, respectively.

center responsible for reducing carrier lifetime and diffusion length in InP solar cells (Ando *et al.*, 1986:3041).

The reduction of minority carrier lifetime in the GaInP<sub>2</sub> solar cells following 1 MeV electron irradiation are shown through the increase in junction dark current. In Figure 65, dark current data is shown for GaInP<sub>2</sub> solar cells before and after electron irradiation. The initial increase in solar cell dark current following irradiation is compared for cells irradiated to a fluence of  $10^{15}$  and  $10^{16}$  e<sup>-</sup>/cm<sup>2</sup>. The enhancement in dark current can be explained through reductions in carrier lifetime,  $\tau_n$  and  $\tau_p$ , in accordance with Eq. (5.8), where  $J_{rec} \propto (\tau_n \tau_p)^{-1/2}$ . Values of dark current increased by a factor of about 4 and 40 at the MPP voltage for the cells irradiated with  $10^{15}$  and  $10^{16}$  electrons/cm<sup>2</sup>, respectively. Assuming that the other factors in Eq.(5.5) are not appreciably affected by electron irradiation, the increase in dark currents can be explained through a reduction in the product  $(\tau_n \tau_p)$  by a factor of 16 and 1600, respectively. If it is further assumed that  $\tau_n \approx \tau_p = \tau$ , then the increase in dark current can be explained by a reduction in  $\tau$  by a factor of 4 and 40, respectively. However, a slight decrease in GaInP<sub>2</sub> diode p-base carrier density will be shown to result after 1 Mev electron irradiation, which in turn will slightly increase the junction depletion width,  $W_d$ . The reduction in  $(\tau_n \tau_p)$  will then be slightly smaller than predicted above, in accordance with Eq.(5.5).



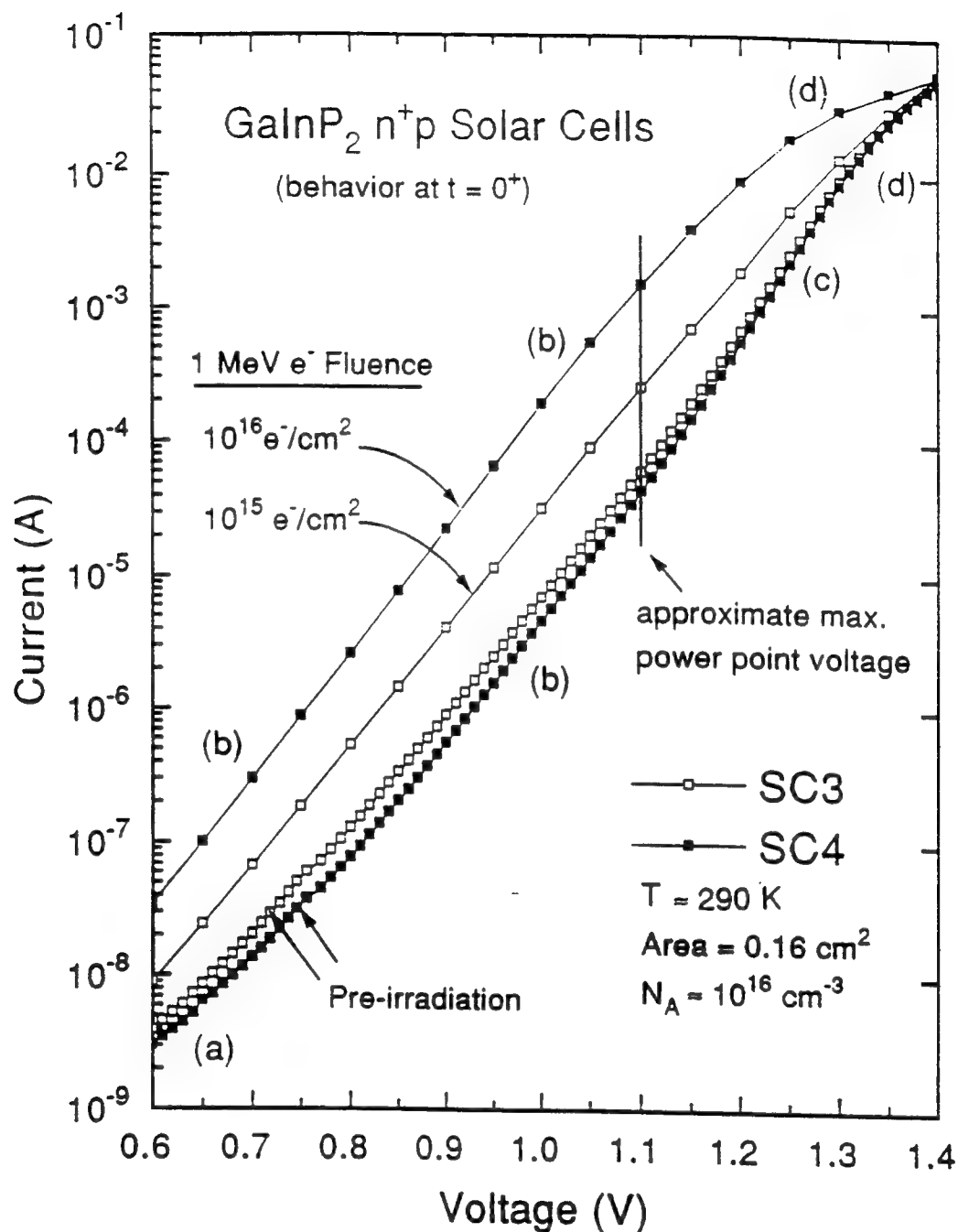


Figure 65. A comparison of forward-bias dark I-V curves for GaInP<sub>2</sub> n<sup>+</sup>p solar cells before and after 1 MeV electron irradiation of fluence  $10^{15}$  and  $10^{16} \text{ e}^-/\text{cm}^2$ . The (a), (b), (c), and (d) regions indicate the main dark current contributions due to tunneling, recombination, diffusion, and series resistance effects, respectively.

A recovery in minority carrier lifetime can be achieved through thermal annealing. For example, in InP, a significant amount of 1 MeV electron-defect annealing occurs at room temperature (Yamaguchi *et al.*, 1984:1207). Also, the main 1 MeV electron-induced hole trap, H4, in InP is completely annealed out at about 100°C (Yamaguchi *et al.*, 1984:1429). In the case of the GaInP<sub>2</sub> diodes, it will be shown that thermal annealing at 250°C results in significantly greater dark current recovery (reduction) than room temperature annealing at ~25°C. Consequently, the GaInP<sub>2</sub> solar cells were hotplate annealed at 250°C.

In Figures 62 and 63, the effects of multiple annealing the GaInP<sub>2</sub> solar cells at 250°C for 10 mins. are shown. A significant recovery of solar cell  $V_{oc}$ ,  $I_{sc}$ ,  $ff$ , and  $Eff$  can be seen in the figures and in Tables IX and X following 2-3 hotplate thermal pulse anneals at 250°C for 10 min. A plot of resulting normalized values of solar cell  $V_{oc}$ ,  $I_{sc}$ ,  $ff$ , and  $Eff$  versus thermal annealing is shown in Figure 66 for the GaInP<sub>2</sub> cells irradiated to a fluence of  $10^{16}$  e<sup>-</sup>/cm<sup>2</sup>. This figure shows a significant recovery in cell performance following the first and second 10 min. pulse anneals, followed by a slight reduction in cell  $Eff$  after subsequent anneals. The reduction in solar cell  $Eff$  can be traced mostly to the reduction in cell  $ff$ , because the cell  $V_{oc}$  decreases very little and  $I_{sc}$  remains nearly constant following the third and fourth anneals. The reduction in  $ff$  is generally to an increase and/or decrease in device series and shunt resistance, respectively. As discussed in Chapters 4 and 5, an increase in carrier shunting (i.e., a reduction in cell shunt

resistance) will increase the cell's dark current. However, as shown in Figure 66, the dark current measured at the cell's MPP voltage remains nearly constant following the third and fourth anneals. This indicates that the reduction in  $\eta$  during the third and fourth 250°C anneals may be due to an increase in device series resistance. Similar behavior was also observed for the GaInP<sub>2</sub> solar cells subjected to a fluence  $10^{15}$  e<sup>-</sup>/cm<sup>2</sup>, as shown in Table IX. These annealing results are important because they demonstrate the feasibility of on-orbit, thermal recovery of GaInP<sub>2</sub> solar cell efficiency. On-orbit annealing will enable a longer spacecraft mission lifetime and/or a reduction in solar array size.

Changes in GaInP<sub>2</sub> solar cell dark current before and after exposure to  $10^{16}$  electrons/cm<sup>2</sup>, and following thermal annealing are shown in Figure 67. A substantial increase in dark current resulted following irradiation, followed by a significant recovery (reduction) in current after thermal annealing at 250°C. The I-V curves of the recombination dominant region are parallel, and have values of ideality factor  $A_2 \approx 1.8$ . The reduction (recovery) in dark current,  $I_{\text{dark}}$ , can be explained in terms of changes in  $I_{\text{rec}}$ , where from Eqs. (2.11) and (5.8),  $I_{\text{dark}} = I_{\text{rec}} \exp(qV/A_2 kT)$  and  $I_{\text{rec}} \propto [\tau_n \tau_p N_A (V_{\text{bi}} - V)]^{-1/2}$ . In this analysis, it is again assumed that  $\tau_n \sim \tau_p = \tau_o$ , where  $\tau_o$  is the pre-irradiated value of minority carrier lifetime. In Figure 67, the initial increase in dark current following electron irradiation corresponds to a reduction in  $\tau_o$  by a factor of  $\sim 40$ , or likewise,  $\tau = 0.025\tau_o$ . A reduction in dark current by 80% resulted following the first 10 min.

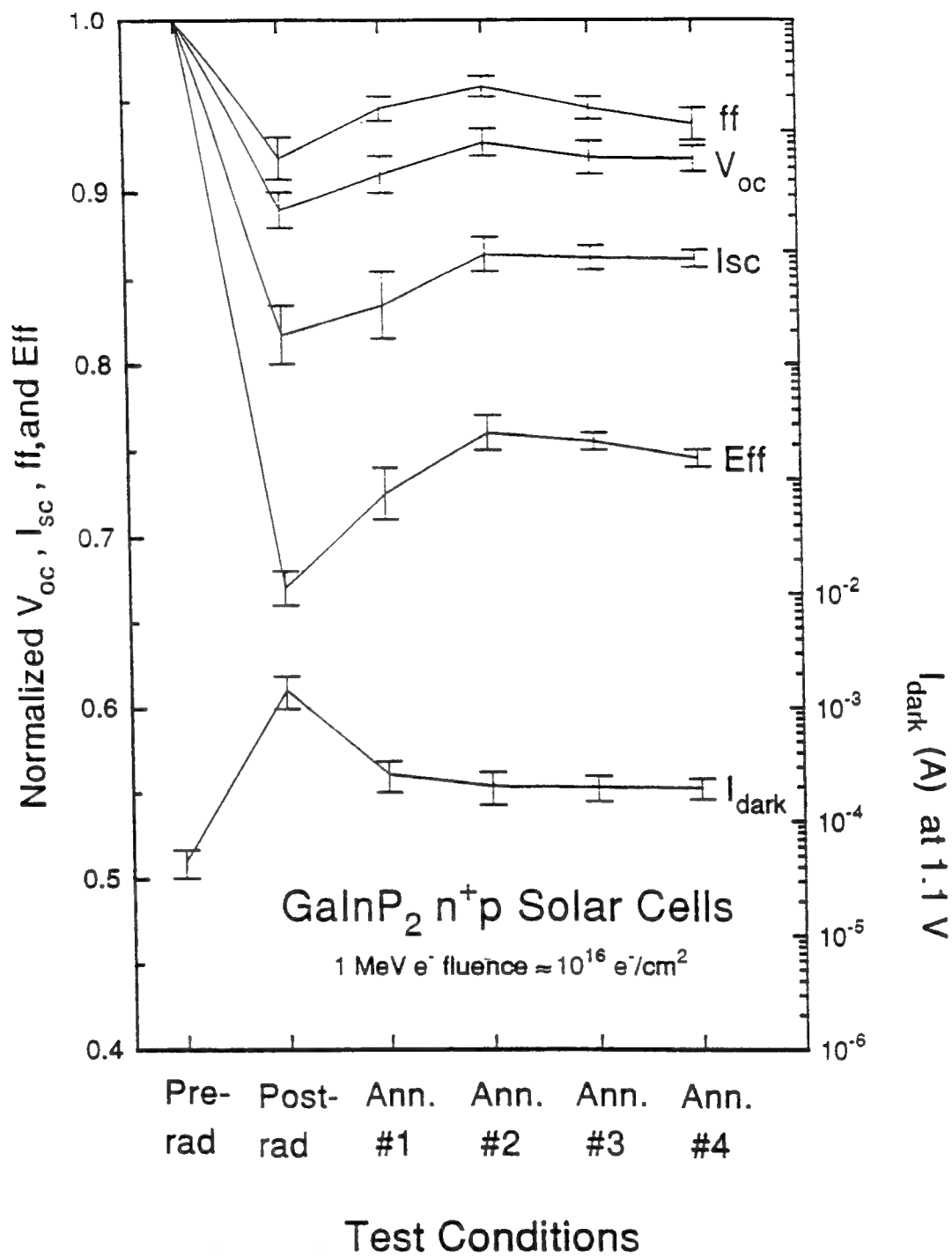


Figure 66. A plot of normalized values of GaInP<sub>2</sub> solar cell  $V_{oc}$ ,  $I_{sc}$ , FF, and Eff following 1 MeV electron irradiation of fluence  $10^{16}$  e<sup>-</sup>/cm<sup>2</sup> and multiple hotplate thermal annealing at 250°C for 10 min.

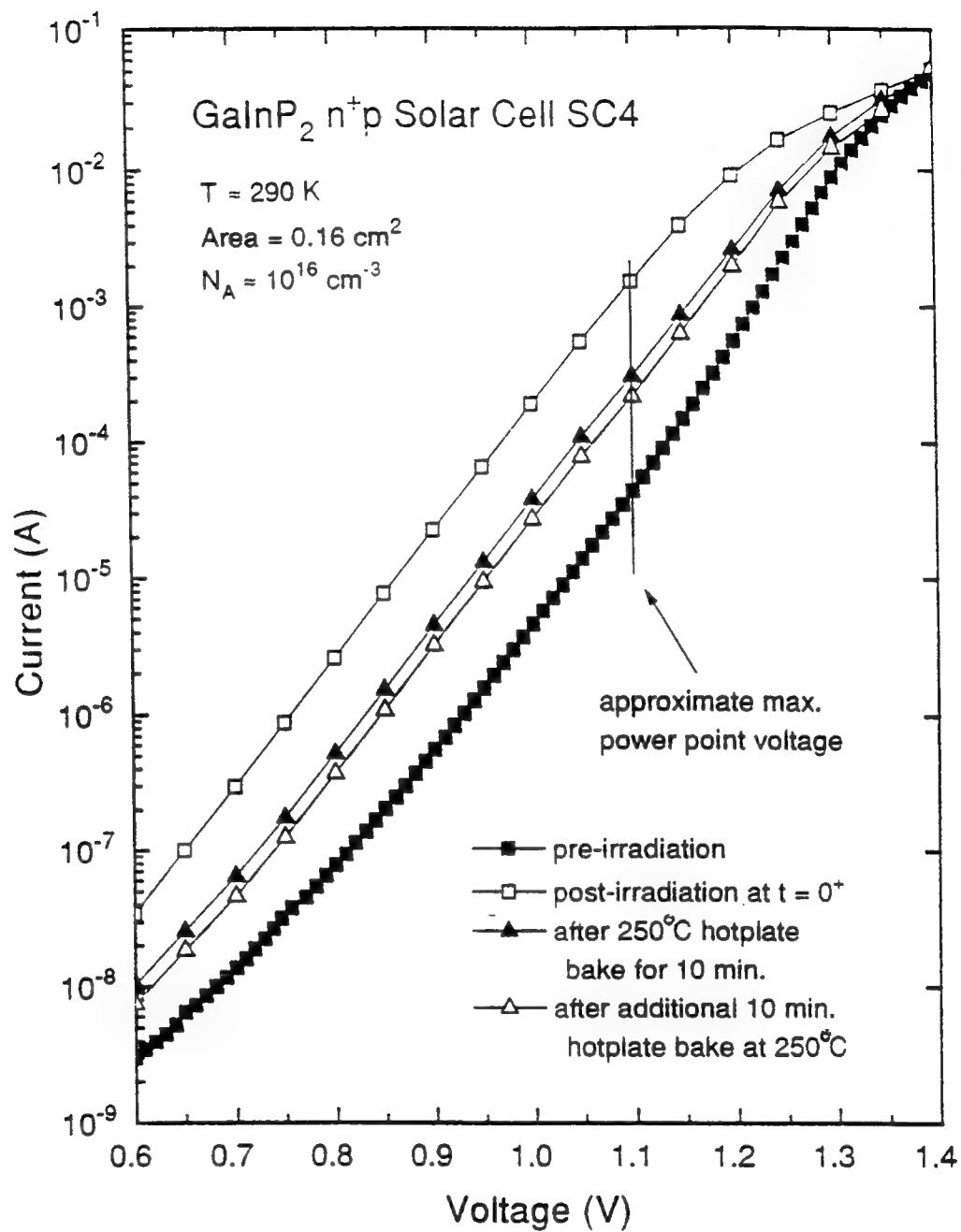


Figure 67. Forward-bias dark I-V curves for a  $\text{GaInP}_2$  n<sup>+</sup>p solar cell before and after 1 MeV electron irradiation and thermal annealing at 250°C.

anneal, corresponding to a recovery in minority carrier lifetime to a value of  $\tau = 0.125\tau_0$ . Following a second 10 min. anneal, a minimal reduction in dark current resulted corresponding to a recovery in lifetime to a value of  $\tau = 0.181\tau_0$ . A third and fourth anneal was conducted, however, no further appreciable reduction in dark current was observed. As mentioned earlier, no further improvement in solar cell  $V_{oc}$ ,  $I_{sc}$ ,  $ff$ , or  $Eff$  was also observed following the third and fourth anneals. A very small change in carrier density was observed in the  $GaInP_2$  diodes following the first thermal anneal, but these changes were too small to influence the observed recovery of the dark current.

The apparent increase in minority carrier lifetime following annealing can be explained in terms of defect annihilation. As mentioned, a significant amount of room temperature annealing has been reported in 1 MeV electron irradiated InP solar cells, where the behavior of the relatively light and mobile phosphorus atom is believed to be responsible. The two major 1 MeV electron-defects in InP are believed to be due to a pair of phosphorous vacancy and interstitial complexes, which give rise to the hole trap H4, and a phosphorous-zinc impurity complex, which gives rise to the hole trap H5 (Yamaguchi and Ando, 1988:5559). Zinc was the dopant in the InP solar cell. The defect centers H4 and H5 are located at 0.37 eV and 0.52 eV above the valance band, respectively, and have been confirmed to be recombination centers (Ando *et al.*, 1986:3041). The defect H4 has been shown to be completely annealed out at about 100°C by the thermal

migration of displaced indium and phosphorous atoms (Yamaguchi and Ando, 1988:5562; Yamaguchi *et al.*, 1984:1429). In the case of GaInP<sub>2</sub>, since there are essentially as many phosphorous atoms per cm<sup>3</sup> as there are in InP, it is conceivable that similar phosphorous and zinc related defects may also play an important role in determining the annealing behavior. It is noted that the p-base dopant in the GaInP<sub>2</sub> solar cells is also zinc. The apparent recovery of the minority carrier lifetime following the 250°C hotplate anneals could be related to migration of displaced indium and phosphorus atoms. This migration would annihilate irradiation induced defect interstitials and vacancies. A reduction in the density of these defects would reduce the amount of carrier recombination, and result in the increase in minority carrier lifetime observed in the GaInP<sub>2</sub> solar cells. In the next section, the influence of 1 MeV electron irradiation on GaInP<sub>2</sub> diode dark current will be examined.

### **The Response of GaInP<sub>2</sub> Diodes to 1 MeV Electron Irradiation and Thermal Annealing**

In this section, the response of GaInP n<sup>+</sup>p diodes to 1 MeV electron irradiation is examined. Good agreement in the response between the diodes and solar cells was found. In Figure 68, typical dark I-V curves for low doped ( $N_A \approx 10^{16} \text{ cm}^{-3}$ ) GaInP<sub>2</sub> diodes are shown before and after 1 MeV electron irradiation of fluence  $10^{15}$  and  $10^{16} \text{ e}^-/\text{cm}^2$ . As expected, a larger increase in dark current occurred at the higher fluences in agreement with the solar cells. However, the values of dark

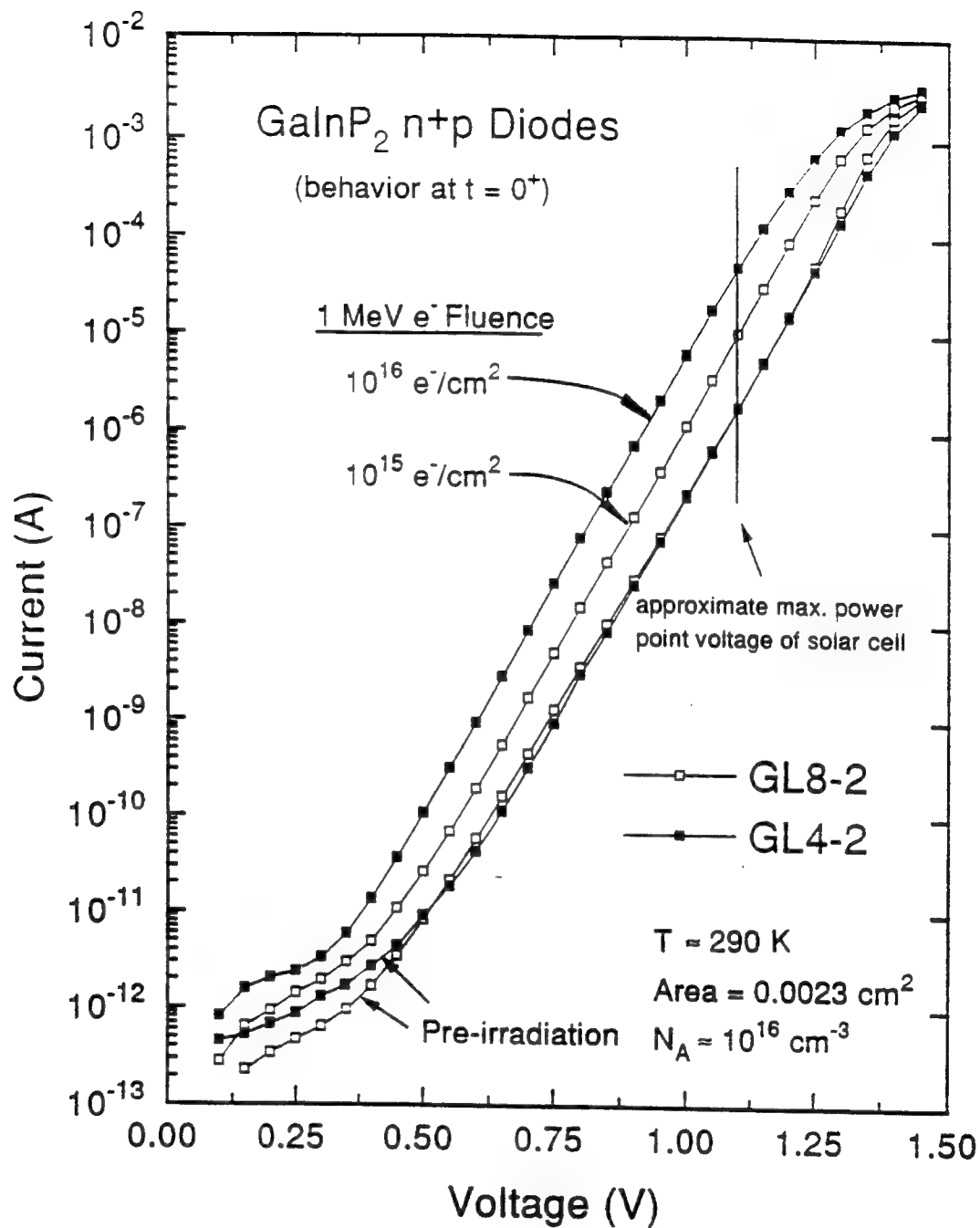


**Figure 68.** A comparison of forward-bias dark I-V curves for GaInP<sub>2</sub> n<sup>+</sup>p diodes following exposure to 1 MeV electron irradiation of fluence of  $10^{15}$  and  $10^{16} \text{ e}^-/\text{cm}^2$ .



current in the diodes increased by a factor of  $\sim 5$  and 30 following the irradiation fluence of  $10^{15}$  and  $10^{16}$  electrons/cm<sup>2</sup>, respectively, compared to a factor of  $\sim 4$  and 40, respectively, for the solar cells. The difference in the factor of 5 and 4 at the lower fluence is within the experimental error. However, the 30% difference in the factor of 30 and 40 resulting at the higher fluence is significant. This may be due to the fact that  $\sim 50\%$  of the dark current in the diodes originates from the junction perimeter (Chapter 4), and that electron irradiation may affect the junction perimeter differently than the bulk. The data would seem to indicate that the perimeter recombination current degrades less than that from the bulk. However, the exact reason for this difference is not understood at this time. As in the case of the solar cells, the increase in dark current can be explained through reductions in  $\tau_n$  and  $\tau_p$  in accordance with Eq. (5.8), where  $J_{\text{rec}} \propto (\tau_n \tau_p)^{-1/2}$ . Making the same assumption that  $\tau_n \approx \tau_p = \tau$ , the increase in dark current can be explained by a reduction in  $\tau$  by a factor of 5 and 30 at the low and high fluences, respectively.

The thermal annealing behavior of the GaInP<sub>2</sub> diodes was also examined. In Figure 69, the dark I-V curves for a low doped diode are shown before and after exposure to  $10^{16}$  electrons/cm<sup>2</sup>, and following hotplate thermal annealing at 250°C. As in the case of the solar cells, a significant reduction in dark current results after the first 10 min., 250°C pulse anneal, followed by a slight further reduction in dark current after the second anneal. A comparison between the reduction (recovery) in current in the diodes and solar cells subjected to a fluence of  $10^{16}$

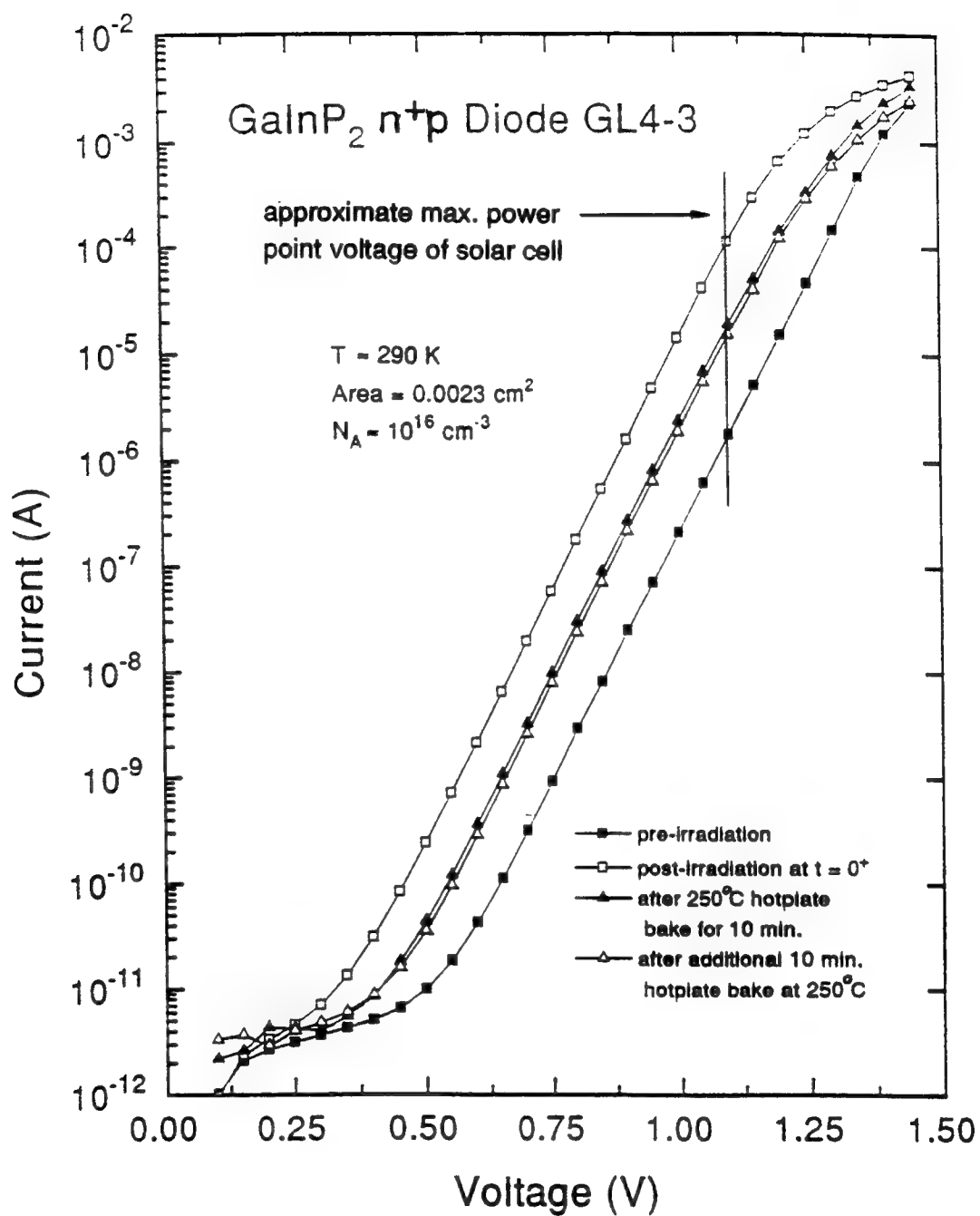
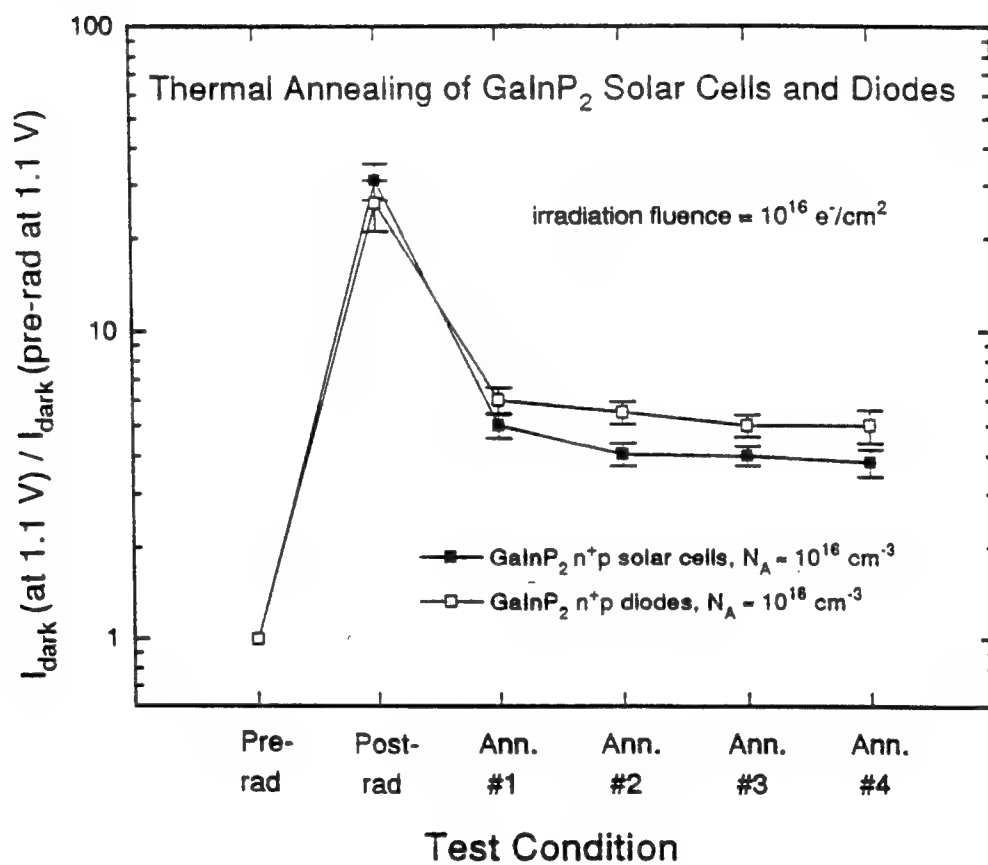


Figure 69. Forward-bias dark I-V curves for a low doped GaInP<sub>2</sub> n<sup>+</sup>p before and after 1 MeV electron irradiation and thermal annealing at 250°C.

electrons/cm<sup>2</sup> is shown in Figure 70. Similar trends in annealing behavior are observed. However, a larger reduction in solar cell dark current occurred. This is surprising considering the fact that the initial increase in solar cell dark current exceeded that in the diodes following irradiation. However, the amount of recovery in both devices is still quite similar, and nearly all recovery in both devices occurred during the first 10 min. These results indicate that the response of the GaInP<sub>2</sub> diodes and solar cells exposed to 1 MeV electrons are very similar. It is probable that the nature and behavior of the 1 MeV-defects in both devices are also very similar. The GaInP<sub>2</sub> diodes should, therefore provide a useful tool for analyzing radiation induced defects in the solar cells. For example, data on how the diode p-base doping density affects the junction's response to electron irradiation and thermal annealing can be used to predict how the value of  $N_A$  in the solar cells affects the cell junction's response to irradiation and annealing.

In Figure 71, dark I-V curves for a mid doped GaInP<sub>2</sub> diode ( $N_A \approx 10^{17} \text{ cm}^{-3}$ ) before and after exposure to irradiation of  $10^{16} \text{ electrons/cm}^2$  are compared to the dark I-V curve for a pre-irradiated low doped diode. Dark current due to (a) tunneling, (b) recombination, and (c) diffusion are seen in the pre-irradiated I-V characteristics of the mid doped diode, whereas dark current due to recombination is seen to dominate in the low doped diode. These current mechanisms were discussed in detail in Chapters 3 and 5. A substantial increase in dark current resulted in the mid doped diode following electron irradiation, i.e., the I-V curve is



**Figure 70.** A comparison of dark current annealing behavior in GaInP<sub>2</sub> n<sup>+</sup>p solar cells and diodes following 1 MeV electron irradiation, and multiple thermal annealing at 250°C for 10 min.

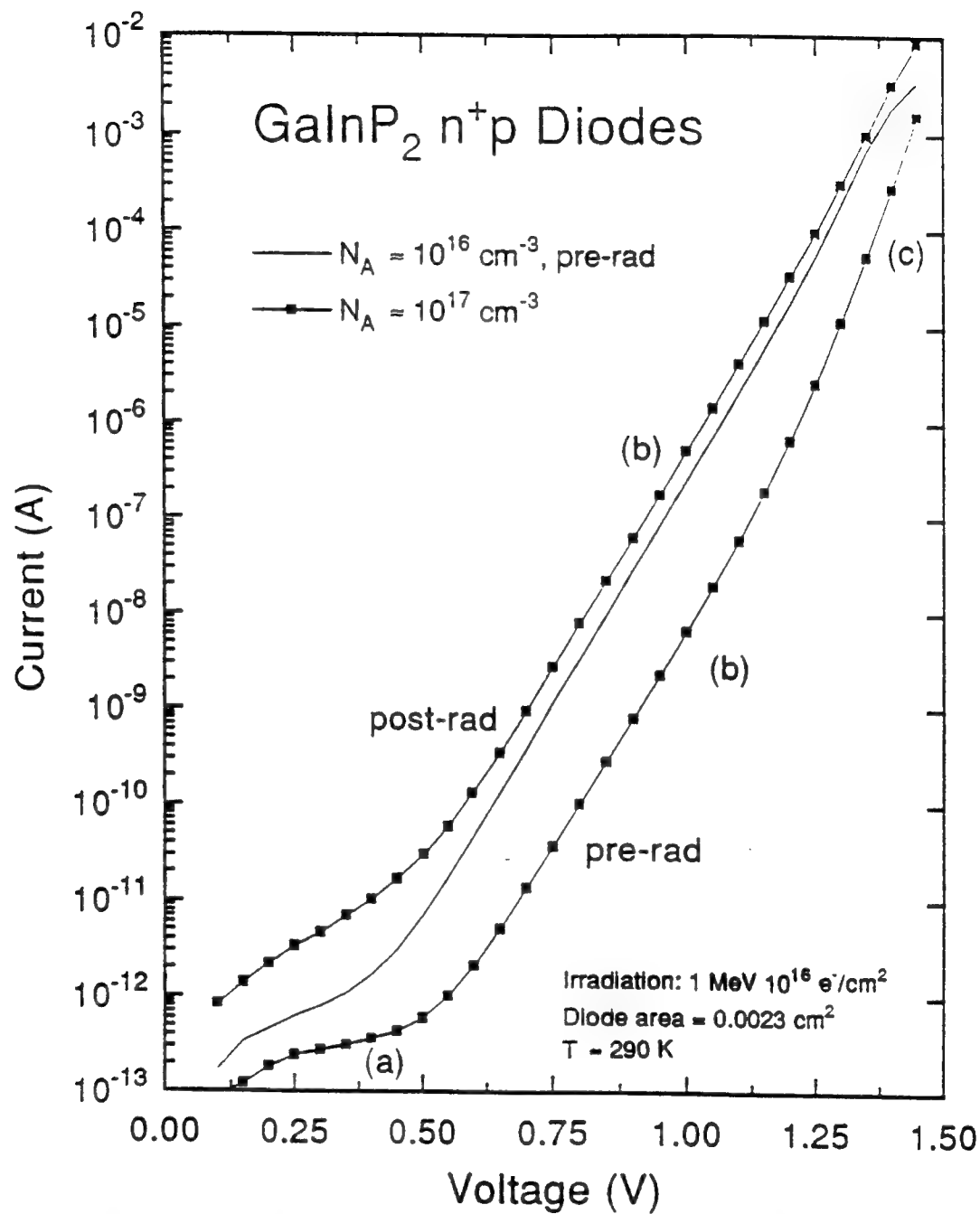


Figure 71. Comparison of dark I-V curves for a mid doped GaInP<sub>2</sub> n<sup>+</sup>p diode before and after 1 MeV electron irradiation, and the dark I-V curve for a pre-irradiated low doped GaInP<sub>2</sub> n<sup>+</sup>p diode.

displaced upward by more than an order of magnitude in dark current. However, the shape of the resulting I-V curve is very similar to that of the pre-irradiated low doped diode. The  $A \approx 1$  diffusion current is no longer observable at the high voltages due to the large increase in the  $A \approx 2$  recombination current. As discussed earlier, this behavior can result from an increase in  $I_{rec}$  through the reduction in carrier lifetimes, in accordance with Eq. (5.8). Similar behavior was observed in the high doped GaInP<sub>2</sub> diodes ( $N_A \approx 2 \times 10^{17} \text{ cm}^{-3}$ ) following electron irradiation.

A comparison study between room temperature and hotplate annealing in the diodes was conducted for the electron irradiated GaInP<sub>2</sub> diodes and the results are shown in Figures 72 and 73. In Figure 72, dark I-V curves are shown for a high doped diode before (1) and after (2) exposure to irradiation of  $10^{16} \text{ electrons/cm}^2$ , and after a series of room temperature ( $\sim 290\text{K}$ ), and  $250^\circ\text{C}$  (523 K) hotplate anneals. The I-V curve was initially displaced upward by more than an order of magnitude in dark current following electron irradiation. The dark I-V characteristics were then monitored every 10 - 12 hrs. over the course of the first 4 days, and every  $\sim 24$  hours during days 5 - 10. The ambient temperature during device storage and measurement was  $\sim 290 \text{ K}$ . As shown in curves (3) and (4) of Figure 72, a sizeable reduction (recovery) in dark current occurred during the first 2 days (45 hrs.) for the high doped diode.. The dark current was then found to change very little between days 2 - 10. Following day 10, additional recovery was

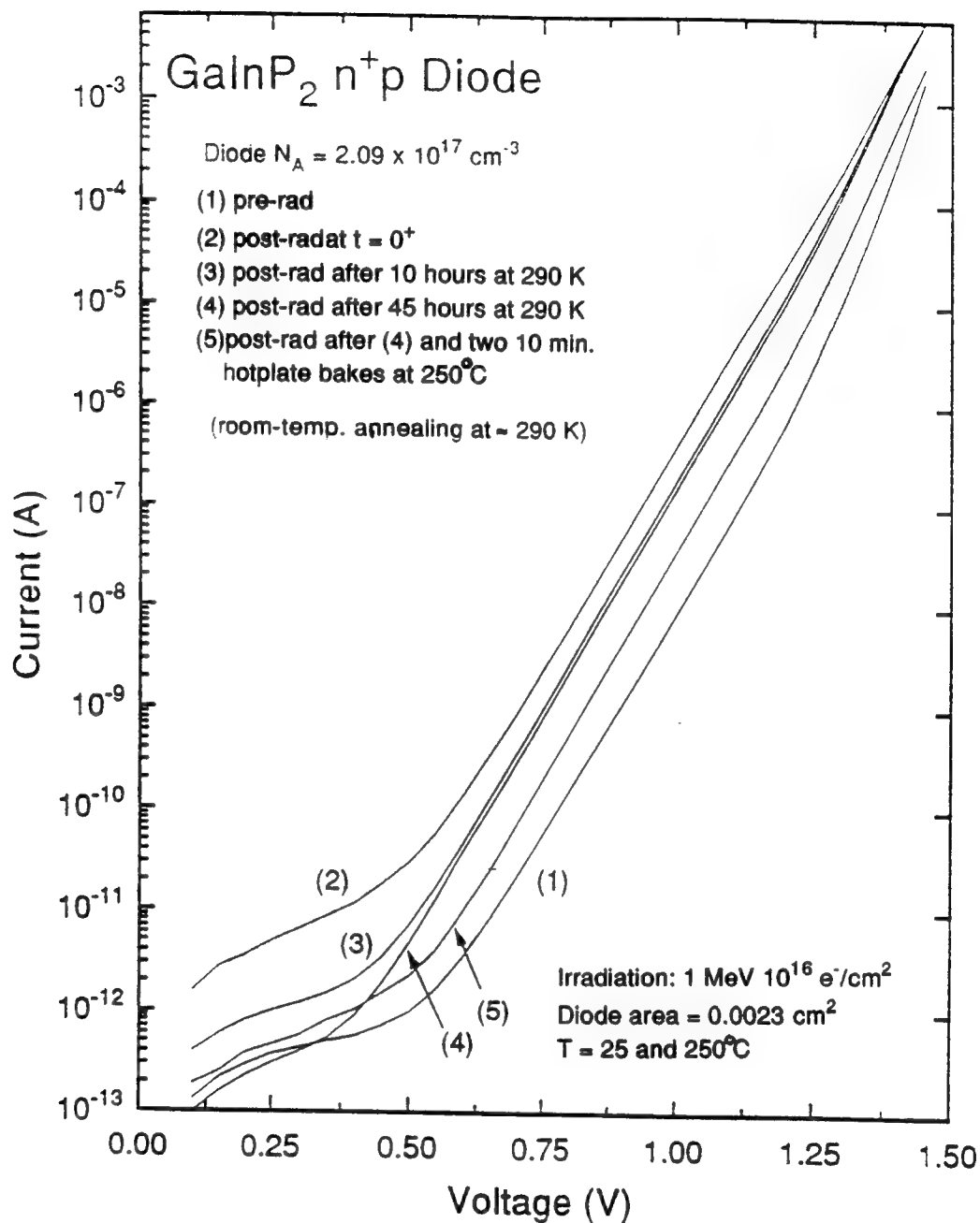


Figure 72. Comparison of forward-bias dark I-V curves for a high doped GaInP<sub>2</sub> n<sup>+</sup>p diode before and after 1 MeV electron irradiation, and after room temperature ( $\sim 25^\circ\text{C}$ ) and hotplate annealing ( $250^\circ\text{C}$ ).

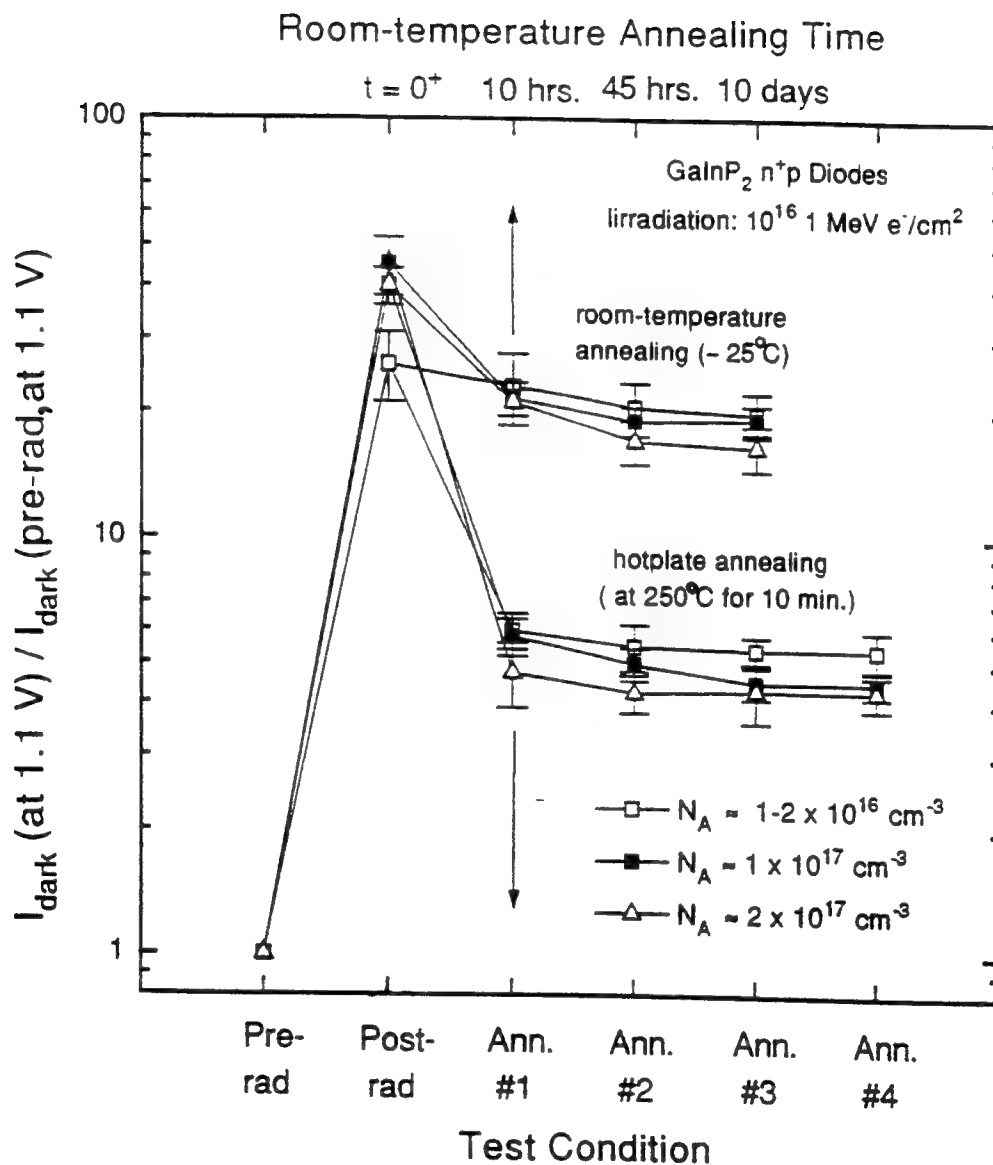


Figure 73. A comparison of dark current annealing behavior in GaInP<sub>2</sub> n<sup>+</sup>p diodes versus doping density following 1 MeV electron irradiation and thermal annealing at  $\sim 25$  and  $250^\circ\text{C}$ .



induced via hotplate annealing at 250°C in steps of 10 min. As was the case for the GaInP<sub>2</sub> solar cells and low doped diodes, a large reduction in dark current resulted after the first 10 min. anneal, followed by only a slight reduction in current after a second 10 min. anneal. The I-V curve labeled (5) in Figure 72 shows the resulting current after a second 10 min. 250 C anneal and after 45 hours at room temperature. It is noted that in many diodes, room temperature annealing did not appear to significantly affect the amount of recovery incurred by hotplate annealing, i.e., the final values of dark current that resulted after hotplate annealing remained about the same when the diodes were kept at room temperature or not.

A comparison between room temperature and hotplate (250°C) annealing in the diodes versus pre-irradiation doping density is shown in Figure 73. The average reduction in dark current following annealing at ~25 C was ~ 50%, compared to a reduction of ~ 85% at 250°C. This result indicates that 1 MeV induced defects in GaInP<sub>2</sub> are unstable and mobile at elevated temperatures, as was found in the case of 1 MeV electron induced defects in InP. Further, the data tends to indicate that the amount of recovery is greater with increased doping density. Similar behavior also occurs in InP, where the minority carrier diffusion length, L, and conversion efficiency in p-InP and n<sup>+</sup>p-InP solar cells degrade less after 1 MeV electron irradiation with increased p-doping density (Yamaguchi and Ando, 1988:5556). The minority carrier lifetime,  $\tau$ , is related to L according to the relation  $L = (D\tau)^{1/2}$ ,

where  $D$  is the diffusion coefficient. The reduction of  $\tau$  following electron irradiation was used earlier to explain the observed increase in GaInP<sub>2</sub> diode and solar cell dark current. The greater apparent recovery of GaInP<sub>2</sub> diode current with increased doping density suggests a greater recovery of both  $\tau$  and  $L$  with increased doping density after electron irradiation. This is consistent with the lower reduction of  $L$  in p-InP with increased doping density. However, the initial increase in current at  $t = 0+$  in Figure 73 is smaller in the low doped diodes compared to the higher doped devices. A cross-over in recovery is seen to occur after the first set of annealings. On the other hand, in Si and GaAs solar cells, the reduction of  $L$  following 1 MeV electron irradiation increases with increased doping density (Uemura and Yamaguchi, 1985:604; Yamaguchi and Nagai, 1972:1016). However, in most space and terrestrial applications, the temperature of the cells will exceed 25°C, and room temperature-type annealing will occur. Hence, if changes in GaInP<sub>2</sub> diode dark current induced by 1 MeV electrons are a good indicator of how GaInP<sub>2</sub> solar cells will respond to similar radiation (i.e., a good correlation between dark current and GaInP<sub>2</sub> solar cell efficiency is shown in Figure 66), then these results indicate that a p-base doping density of  $\sim 10^{17} \text{ cm}^{-3}$  in GaInP<sub>2</sub> solar cells will yield better radiation resistance than a density of  $\sim 10^{16} \text{ cm}^{-3}$  will.

Irradiation induced defects can also result in carrier removal that will enhance dark current. A reduction in carrier density,  $N_A$ , following electron irradiation will

increase dark current through an increase in junction depletion width,  $W_d$ , where  $I_{\text{dark}} \propto I_{\text{rec}} \propto W_d$  in accordance with Eqs. (2.11) and (2.55). From Eq. (5.1), the depletion width for an abrupt  $n^+p$  junction goes as approximately  $W_d \propto N_A^{-1/2}$ . In Figure 74, plots of  $1/C^2$  vs. voltage are shown for typical mid and high doped GaInP<sub>2</sub> diodes before 1 MeV electron irradiation of fluence of  $10^{16} \text{ e}^-/\text{cm}^2$ , and after irradiation and two 10 min., 250°C hotplate anneals. As described in Chapter 5, the slope of  $1/C^2$  vs voltage gives the p-base carrier density. The slope of the  $1/C^2$  vs.  $V$  curves in Figure 74 increases following electron irradiation and annealing, indicating a reduction in carrier density. A reduction in  $N_A$  of 8 - 11% was measured in the mid and high doped diodes, and the reduction rate did not appear to depend on the value of pre-irradiated  $N_A$ . Similar shifts in  $1/C^2$  vs.  $V$  curves resulted in the low doped diodes following irradiation, but due to the graded doping profile in these devices, reliable values for changes in  $N_A$  could not be obtained. Eqs. (5.1) and (5.8) predict that a reduction in  $N_A$  of ~10% in the mid and high doped diodes will increase  $W_d$  (and  $I_{\text{dark}}$ ) by only ~5 and 6%, respectively, which is less than a factor of 1.1. In Figure 73,  $I_{\text{dark}}$  is roughly a factor of 5 larger following electron irradiation and annealing at 250 C. Therefore, carrier removal alone can not be used to explain the large increase in dark current. In the next section, several effects of electron irradiation on the dark current recombination centers will be examined.

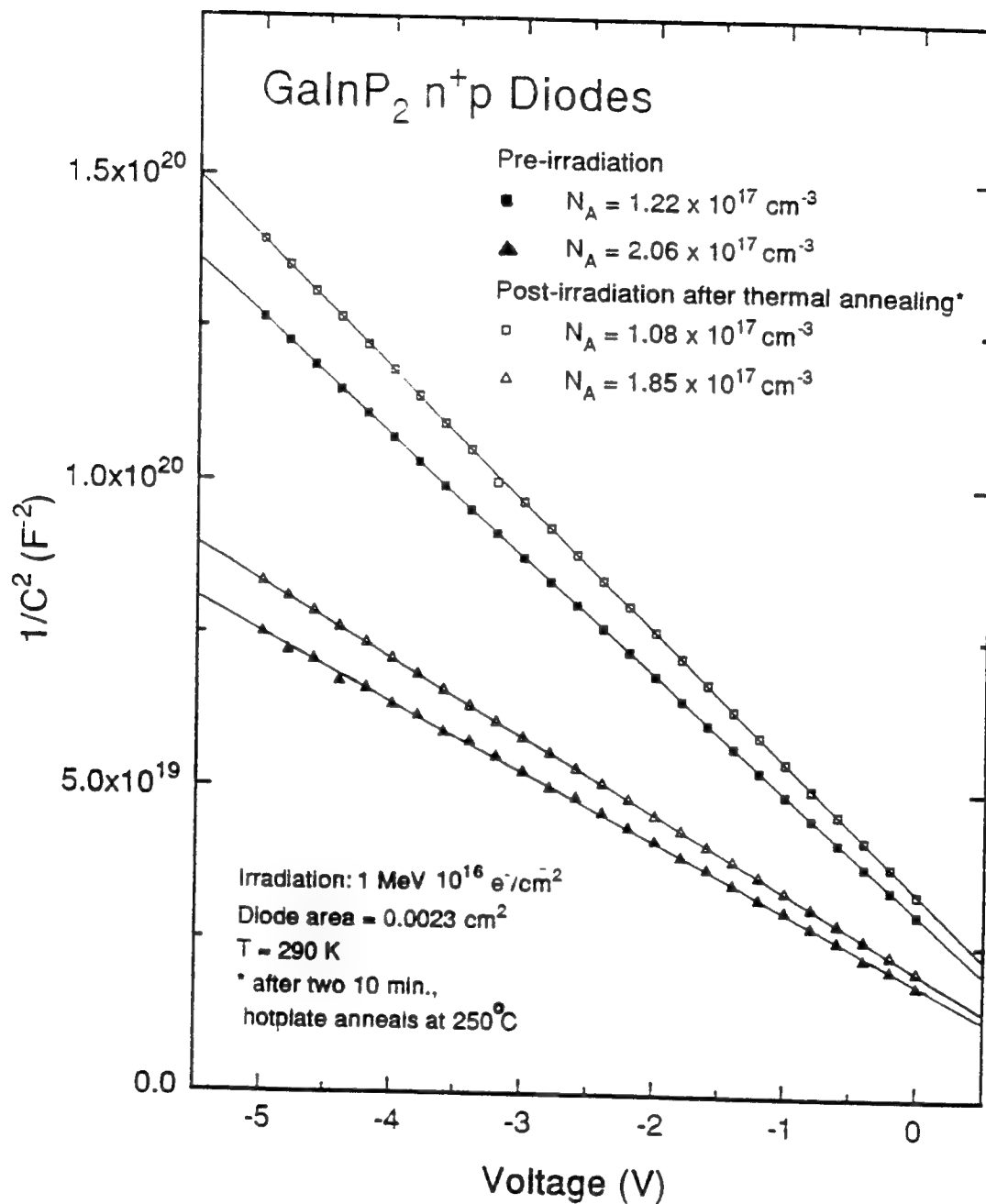


**Figure 74.** A plot of  $1/C^2$  vs. reverse-bias voltage for a mid and high doped GaInP<sub>2</sub> n<sup>+</sup>p diode before and after 1 Mev electron irradiation and thermal annealing at 250 C twice for 10 min.

## **The Response of GaInP<sub>2</sub> n<sup>+</sup>p Junction Dark Recombination Current to 1 MeV Electron Irradiation and Thermal Annealing**

The effect of 1 MeV electron irradiation on recombination activation energy,  $E_A$ , was first examined. In Figure 75, an Arrhenius plot of  $\ln(I_{rec})$  vs.  $1000/T$  is shown before and after 1 MeV electron irradiation to a fluence of  $10^{16} \text{ e}^-/\text{cm}^2$  for low, mid and high doped diodes. The post-irradiated curves resulted after two 10 min., 250°C hotplate anneals. Values for  $E_A$  were calculated from the slope of the Arrhenius plots as described in Chapters 3, 4 and 5. Pre-irradiated values of  $E_A$  for the diodes varied between 0.97 and 1.01 eV in agreement with earlier results and recombination theory, where  $E_A = E_{g0}/2 \approx 0.99 \text{ eV}$ . The situation becomes more complicated after electron irradiation, where two different trends in the slope of the curves are seen. For  $T > 150^\circ\text{C}$ , the slope of the pre- and post-irradiation curves are similar, and values of  $E_A$  ranged from 0.93 - 0.97 eV. These values are within ~5% of  $E_A = E_{g0}/2 = 0.99 \text{ eV}$  predicted by recombination theory, showing that SRH-type recombination dark current continues to dominate following electron irradiation. However, for  $T < 150^\circ\text{C}$  a different situation occurs. Values of  $I_{rec}$  drop off substantially slower with decreasing temperature than predicted by recombination theory, i.e.,  $I_{rec} \propto \exp(-E_{g0}/2kT)$ , and values obtained for  $E_A$  ranged from 0.30 - 0.60 eV. This indicates that a mechanism other than recombination dominates at low temperatures following irradiation. It is noted that no absolute correlation between values for  $I_{rec}$  at low temperatures and  $N_A$  was found, although

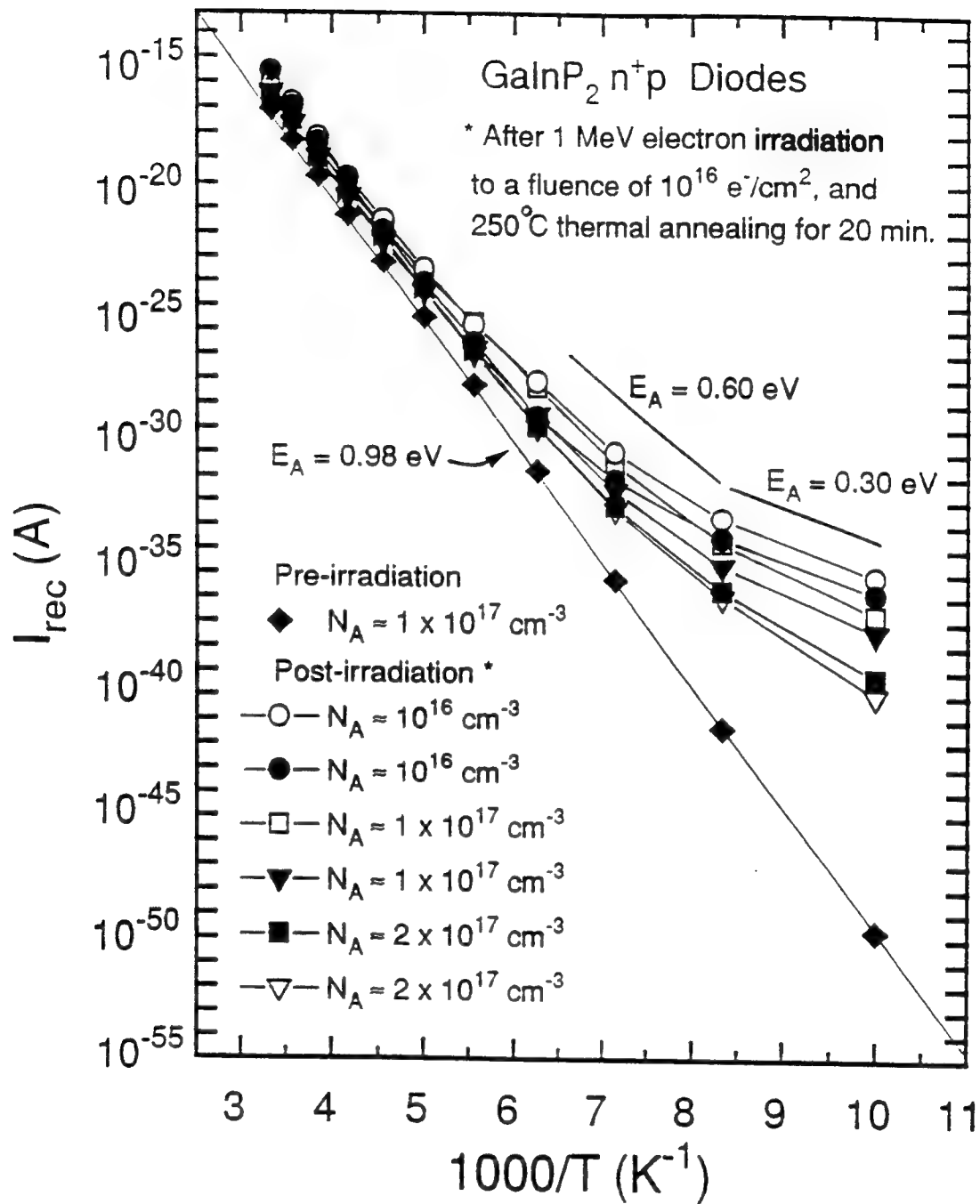


Figure 75. Arrhenius plots of  $I_{\text{rec}}$  vs.  $1000/T$  for GaInP<sub>2</sub> n<sup>+</sup>p diodes before and after 1 MeV electron irradiation and thermal annealing at 250°C twice for 10 min.

the low doped diodes did generally have slightly larger values of  $I_{\text{rec}}$  compared to the mid and high doped diodes.

The low slopes in the Arrhenious plots of Figure 75 at low temperatures indicate a much weaker dependence of  $I_{\text{rec}}$  on temperature. This behavior was observed in the "leaky" GaInP<sub>2</sub> diodes dominated by tunneling current in Chapter 5, where  $I_{\text{rec}}$  was found to decrease slowly with decreasing temperature. Further, in Figure 76, the dark current ideality factor,  $A$ , is plotted as a function of temperature before and after electron radiation for low, mid, and high doped diodes. Prior to irradiation, values of  $A$  are close to 2 and relatively constant with temperature as predicted in recombination theory. However, following irradiation and thermal annealing at 250°C two 10 mins., values of  $A$  increase with decreasing temperature and substantially deviate from 2 for  $T < 150^\circ\text{C}$ . This is also the approximate temperature at which  $I_{\text{rec}}$  starts to appreciably deviate from recombination theory. In fact, an interesting qualitative relationship was found between the anomalous increase in  $I_{\text{rec}}$  and the corresponding increase in values of  $A$ . In Figure 77, an Arrhenious plot of  $\ln(I_{\text{rec}})$  vs.  $1000/T$  and  $1000/(A/2)T$  for a mid doped diode is shown. The post-irradiation plot of  $\ln(I_{\text{rec}})$  vs.  $1000/T$  is not linear, however, when the graph of  $\ln(I_{\text{rec}})$  vs.  $1000/(A/2)T$  is plotted, a straight line is obtained yielding a value for activation energy of  $E_A = 0.96$  eV. This type of result has been observed for a variety of Schottky metal-semiconductor devices, and has been used on a purely empirical basis (Tuck *et al.*, 1983:1099). Similar

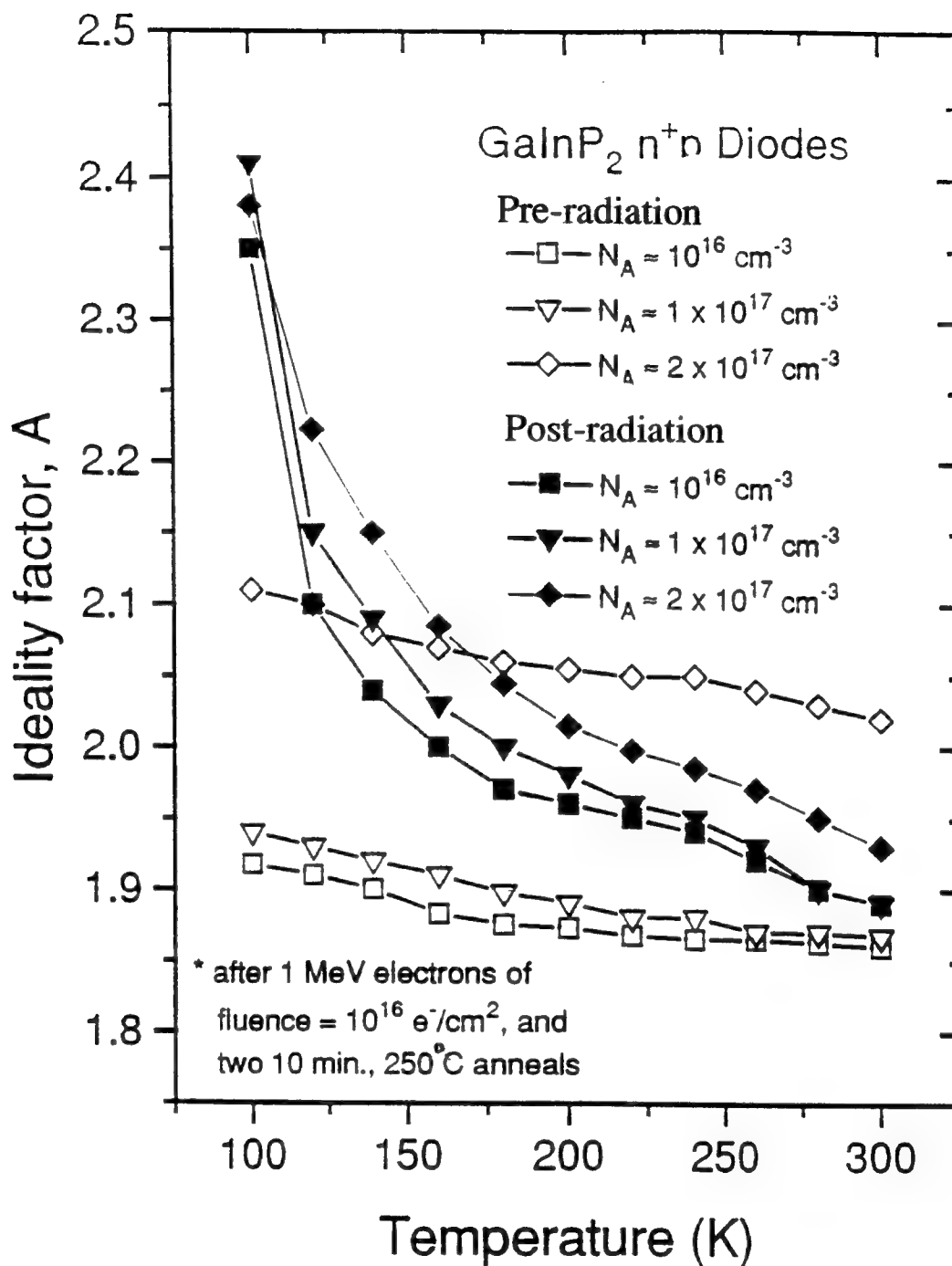


Figure 76. Forward-bias dark current ideality factor versus temperature for low, mid, and high doped GaInP<sub>2</sub> n<sup>+</sup>p diodes before, and after 1 MeV electron irradiation and thermal annealing at 250°C twice for 10 min.



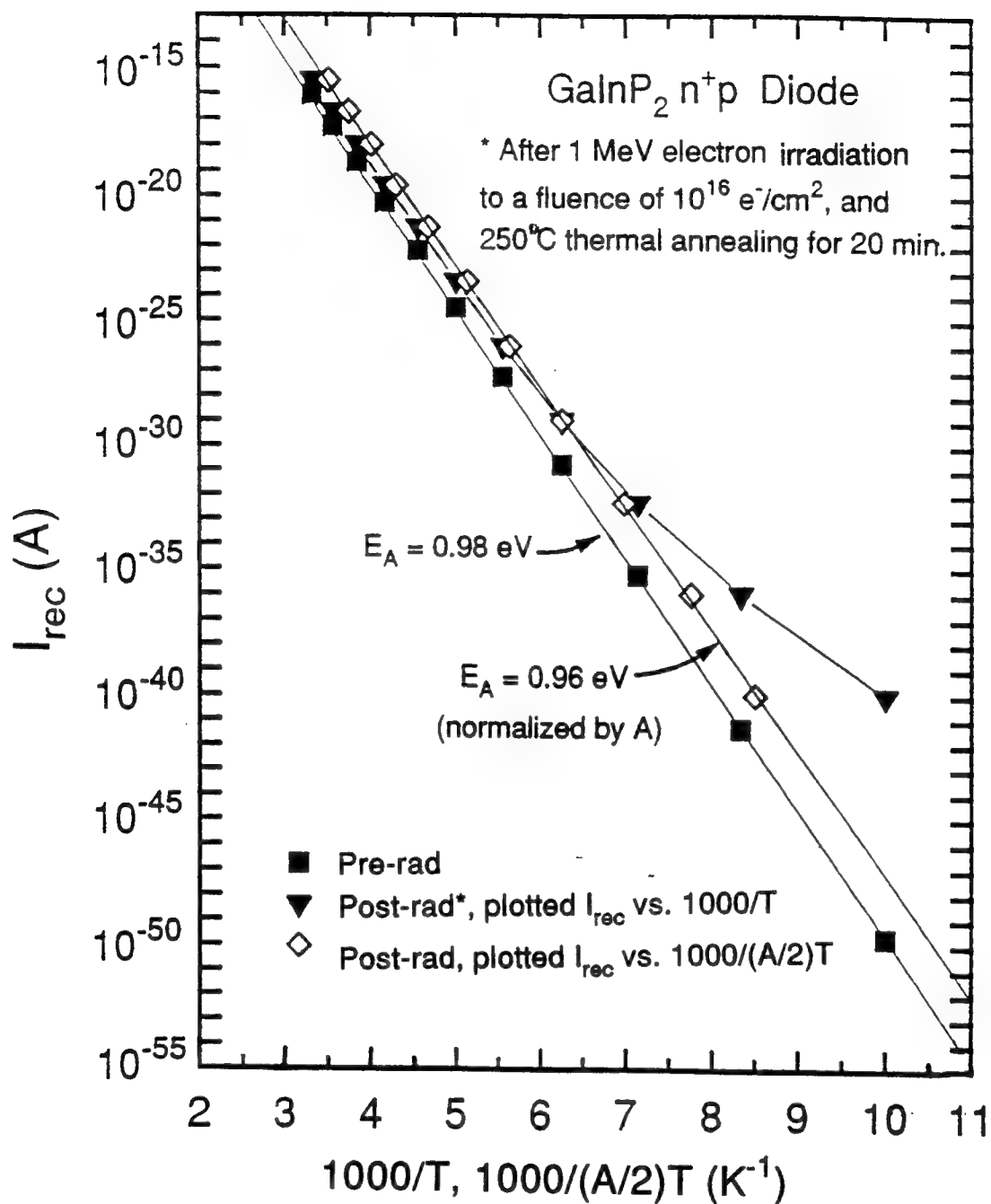


Figure 77. Arrhenius plot of  $I_{\text{rec}}$  vs.  $1000/T$  and  $1000/(A/2)T$  for a GaInP<sub>2</sub> n<sup>+</sup>p diode before and after 1MeV electron irradiation and thermal annealing.

behavior has been reported in InP Schottky diodes (Reinhardt, 1988:95; Tuck *et al.*, 1983:1099).

The extremely weak temperature dependence of  $I_{\text{rec}}$  at low temperatures and the values of  $A$  much greater than 2 strongly suggest the presence of tunneling current (Hovel, 1973:34). The two probable tunneling mechanisms are field enhanced tunneling and defect state tunneling (Fowler and Nordheim, 1928:173; Chynoweth *et al.*, 1962:684). The former mechanism is bias dependent, whereas the latter is practically independent of bias. However, considering Figure 75, it is doubtful that this tunneling current will be appreciable for  $T > 150^\circ\text{C}$ . Hence, it can be expected that tunneling current induced by 1 MeV electron irradiation will not significantly affect dark current behavior in the  $\text{GaInP}_2$  diodes and solar cells operating near room temperature. However, considering the value of  $E_A$  obtained ( $\sim 0.98$  eV) for dark current at  $T > 150^\circ\text{C}$  following irradiation, it is clear that other deep SRH-type recombination centers induced by 1 MeV electrons are responsible for the enhancements in dark current.

## **VII. Summary of Results, Contributions, and Recommendations for Future Work**

### **Summary of Results**

The GaInP<sub>2</sub>/GaAs tandem solar cell currently exhibits the greatest potential of achieving AM1.5 solar conversion efficiencies in excess of 30%. Although the electrical behavior of the bottom GaAs solar cell in the tandem is well understood, this dissertation was the first detailed investigation into the current conduction mechanisms of the top GaInP<sub>2</sub> n<sup>+</sup>p solar cell. Solar cell current mechanisms play a crucial role in limiting conversion efficiency; excess junction dark current limits the maximum obtainable solar cell photocurrent and photovoltage.

The dominant current mechanism in GaInP<sub>2</sub> n<sup>+</sup>p solar cells, with p-base doping density of  $\sim 10^{16} \text{ cm}^{-3}$ , was identified and correlated with solar cell photovoltaic performance. Forward-bias junction currents due to carrier diffusion, recombination, and tunneling were identified through voltage, temperature, and device geometry dependences. Recombination current was found to dominate at the maximum-power point voltage ( $\sim 1.1 \text{ V}$ ) of "well-behaved" GaInP<sub>2</sub> solar cells, and was shown to limit solar cell open-circuit voltage,  $V_{oc}$ . This current was dominant in the solar cells, as well as in GaInP<sub>2</sub> diodes of similar structure, over many orders of magnitude between voltages of 0.75 and 1.2 V. Measured values of both current ideality factor ( $A \approx 1.8 - 1.9$ ) and current activation energy

( $E_A \sim E_g(0 \text{ K})/2$ ) were consistent with Sah-Noyce-Shockley recombination theory. Measured values of solar cell  $V_{oc}$  were consistent with calculated  $V_{oc}$  determined from recombination current theory, confirming that the photovoltage was indeed limited by carrier recombination. The magnitude of recombination current was reduced by a factor of 10 ~ 15 with increased p-base doping density from  $1 \times 10^{16}$  to  $2 \times 10^{17} \text{ cm}^{-3}$  in smaller GaInP<sub>2</sub> n<sup>+</sup>p diodes. This and modeled data suggests that the GaInP<sub>2</sub> solar cell's photovoltage can be increased with increased p-base doping density.

Recombination current transport was found to occur via defect states at the perimeter and within the bulk of the GaInP<sub>2</sub> n<sup>+</sup>p junction. Using the measured value of GaInP<sub>2</sub> intrinsic carrier concentration ( $n_i \approx 2400 \text{ cm}^{-3}$ ) determined from capacitance-voltage measurements, the perimeter surface recombination rate was determined to be  $\sim 3.3 \text{ cm}^2/\text{sec}$ . However, perimeter recombination was found to be dominant only in devices with junction perimeter-to-area (P/A) ratios larger than  $\sim 40$ , indicating that perimeter recombination current will be negligible in practical larger area solar cells, for example, of 2 cm x 2 cm (P/A = 2). The contribution of perimeter recombination current in the GaInP<sub>2</sub> solar cells (P/A ratio  $\sim 9$ ) was estimated to be about 15%. Hence, in these cells the photovoltaic degradation due to dark current was controlled by carrier recombination via centers in the n<sup>+</sup>p junction bulk.

Two deep level recombination centers were identified in the GaInP<sub>2</sub> junction using deep-level-transient spectroscopy, reverse-bias current-voltage-temperature, and capacitance-frequency-temperature measurement techniques;  $E_{a1} = E_t - E_v \approx 0.45$  eV and  $E_{a2} = E_t - E_v \approx 0.05$  eV. These centers were both determined to be majority-hole traps, and the level at  $E_{a1}$  is believed to be the dominant recombination center at room temperature because a difference in  $E_{a1}$  and  $E_{a2}$  of  $\sim 0.40$  eV predicts that the lifetime of the majority carriers will be dominated by  $E_{a1}$  even if the concentration of  $E_{a2}$  is 6 orders of magnitude larger than that of  $E_{a1}$ . Further, since the maximum recombination rate drops off exponentially with  $E_t - E_a$ , a negligible amount of carrier recombination can be expected to occur via  $E_{a2}$ . The deep center at  $E_{a1}$  was also found to exhibit a phenomenon known as Frenkel-Poole barrier (emission) lowering, where the measured value  $E_{a1}$  was lowered as much as 0.20 eV with increased junction reverse-bias.

Dark current due to tunneling was found to dominate in GaInP<sub>2</sub> solar cells and diodes exhibiting "leaky" behavior. In several "leaky" solar cells and diodes, a good correlation between GaInP<sub>2</sub> surface line-defect density and excess current-shunting of the form  $V/R_{sh}$  or  $I_0 \exp(BV)$  was observed. Current of this form has been shown to be due to carrier tunneling and trapping-detrapping through states in the junction. Electroluminescence measurements showed that these line-defects were regions of intense nonradiative recombination and/or tunneling. In several "leaky" diodes, low temperature measurements yielded values of  $I_0$  that were

extremely insensitive to temperature, which is also indicative of tunneling current. The source of line-defects is believed to be related to the strain induced by lattice mismatch between GaInP<sub>2</sub> and GaAs, where GaInP<sub>2</sub> is lattice matched to GaAs over a very narrow compositional range. As a result of the line-defects and related "leaky" device behavior, it was concluded that a practical limitation on the production yield of large area GaInP<sub>2</sub>/GaAs wafers suitable for fabrication of larger area, high efficiency solar cells may exist. Tunneling current was also observed at the junction perimeter in several diodes. Diodes exposed to water vapor experienced an increase in  $I_0$  by almost an order of magnitude, where in these devices only the perimeter of the junction was exposed.

Measurements of GaInP<sub>2</sub> n<sup>+</sup>p solar cell photovoltaic parameter temperature coefficients were obtained between temperatures of 250 - 400 K. These data are important to solar array system designers for modeling the photovoltaic performance of cells operating in space where large solar array temperature excursions frequently occur. An average value for the AM0 conversion efficiency temperature coefficient,  $d\text{Eff}/dT$ , of  $(-1.88 \pm 0.07) \times 10^{-2} \text{ \%}/\text{K}$  was obtained, which is less (better) than that reported for GaAs and InP solar cells.

A series of 1 MeV electron irradiation tests were conducted on GaInP<sub>2</sub> solar cells and diodes. Good agreement in the response between the solar cells and diodes was found. The average reduction in solar cell  $V_{oc}$ , short-circuit current,  $I_{sc}$ , fill-factor,  $ff$ , and AM0 conversion efficiency,  $\text{Eff}$ , following exposure to  $10^{15}$

electrons/cm<sup>2</sup> was ~3, 8, 1, and 10%, respectively, compared to a reduction of 11, 18, 8, and 33%, respectively, for solar cells exposed to 10<sup>16</sup> electrons/cm<sup>2</sup>. The radiation resistance of the GaInP<sub>2</sub> solar cells was found to be greater than that of Si and GaAs solar cells, but less than that for InP, where InP solar cells yield the highest radiation resistance reported to date. The high radiation resistance of GaInP<sub>2</sub> is believed to be due to highly mobile phosphorous related defect centers that are also responsible for the high radiation resistance in InP solar cells. A significant amount of GaInP<sub>2</sub> solar cell recovery resulted following thermal annealing at 250°C. An average increase in solar cell conversion efficiency of 11 and 26% resulted after two 10 min., 250°C hotplate anneals for cells irradiated with 10<sup>15</sup> and 10<sup>16</sup> electrons/cm<sup>2</sup>, respectively. This recovery demonstrates a good potential for extending the operational lifetime of GaInP<sub>2</sub>/GaAs tandem solar cells operating in space using on-orbital thermal annealing. A good correlation between initial solar cell degradation and thermally induced recovery, and changes in solar dark current was found. Changes in solar cell photocurrent and photovoltage were explained through changes in minority carrier lifetime as observed in the dark current data. A minimal amount of carrier removal resulted following electron irradiation and annealing, confirming that changes in minority carrier lifetime were most responsible for changes in the solar cell parameters. The recovery in minority carrier lifetime following annealing was explained in terms of defect annihilation.

A comparison between room temperature ( $\sim 25^\circ\text{C}$ ) and hotplate annealing at  $250^\circ\text{C}$  was conducted for  $\text{GaInP}_2$  diodes following  $1\text{ MeV}$  electron irradiation of fluence of  $10^{16}\text{ electrons/cm}^2$ . The average reduction (recovery) in dark current following annealing at  $\sim 25^\circ\text{C}$  for 24 hours was  $\sim 50\%$ , compared to a reduction of  $\sim 75\%$  following thermal annealing at  $250^\circ\text{C}$  for 20 mins. The amount of recovery was found to increase with increased p-base doping density from  $1 \times 10^{16}$  to  $2 \times 10^{17}\text{ cm}^{-3}$ . Since a good correlation was found between solar cell efficiency and magnitude of cell dark current following electron irradiation, it is believed that a further improvement in  $\text{GaInP}_2$  solar cell radiation resistance can be achieved with increased p-base doping density. As suggested earlier, an increase in doping density will also increase solar cell  $V_{\infty}$  and conversion efficiency.

At temperatures greater than  $\sim 150^\circ\text{C}$ , values of dark current activation energy,  $E_A$ , following electron irradiation were found to be within  $\sim 5\%$  of the value predicted by recombination theory. The commensurate increase in  $A \approx 2$  dark current magnitude and the resulting increased dominance in voltage range were explained through an increase in the density of SRH recombination centers,  $N_t$ . This was in agreement with the observed reduction in solar cell photocurrent, which is due to reduced carrier lifetimes,  $\tau$ , where  $\tau \propto 1/N_t$ . At temperatures less than  $150^\circ\text{C}$ , a substantial reduction in  $E_A$  was found, and a large corresponding increase in the diode ideality factor resulted. An empirical relationship was found between the anomalous large values of dark current coefficient,  $I_{\text{rec}}$ , and the diode



ideality factors. The small and large values of  $E_A$  and  $A$ , respectively, are indicative of tunneling current. However, the increase in tunneling current was very small, and should not adversely affect solar cell performance over the temperature range of interest.

In summary, the basic behavior of dark current mechanisms in  $\text{GaInP}_2$   $n^+p$  diodes and solar cells have been examined for the first time, and the influence of recombination and tunneling current on  $\text{GaInP}_2$  solar cell photovoltaic performance has been established. The  $\text{GaInP}_2$  solar cell was shown to exhibit very high 1 MeV electron radiation resistance, greater than that for Si and GaAs solar cells, and a significant amount of post-electron irradiation thermal annealing was demonstrated at  $250^\circ\text{C}$ .

## Summary of Contributions

In this work, the basic electrical characteristics of the GaInP<sub>2</sub> n<sup>+</sup>p junction diode and solar cell have been studied. In particular, the following electrical properties/behaviors have been identified in the GaInP<sub>2</sub> n<sup>+</sup>p junction for the first time:

- 1) The presence of junction dark current due to carrier diffusion, and recombination and tunneling via defect states in the junction.
- 2) The dependence of recombination current on p-base doping density.
- 3) The presence of perimeter recombination current.
- 4) The dominance of recombination current at the maximum-power point voltage of the GaInP<sub>2</sub> solar cell.
- 5) The influence of dark current on GaInP<sub>2</sub> solar cell photovoltaic parameters.
- 6) Measured values for GaInP<sub>2</sub> intrinsic carrier concentration and surface recombination rate.
- 7) The presence of deep levels in p-GaInP<sub>2</sub>.
- 8) The Poole-Frenkel barrier lowering effect in p-GaInP<sub>2</sub>.
- 9) The influence of GaInP<sub>2</sub>-GaAs line-defects on device dark current and solar cell photovoltaic performance.
- 10) The presence of perimeter tunneling current.
- 11) Measurement of solar cell photovoltaic parameter temperature coefficients.

12) The response of GaInP<sub>2</sub> n<sup>+</sup>p junction dark current to 1 MeV electron irradiation.

13) The 1 MeV electron radiation resistance of the GaInP<sub>2</sub> solar cell was found to be greater than that reported for Si and GaAs solar cells, but less than that for InP solar cells.

14) Dark current recovery (reduction) in diodes and solar cells following 1 MeV electron irradiation via room temperature (~25°C) and hotplate (250 C) thermal annealing.

15) Dependence of dark current recovery on diode p-base doping density.

16) Recovery of 1 MeV electron induced GaInP<sub>2</sub> solar cell degradation resulting from hotplate annealing at 250°C.

17) Empirical relationship between increased tunneling current and diode ideality factor at low temperatures following electron irradiation.

## **Recommendation for Future Work**

Continuous efforts are being made to improve the efficiency and radiation resistance of solar cells. The studies carried out in this work are but the first step towards achieving the long term goal of optimizing the GaInP<sub>2</sub>/GaAs solar cell for utilization in space and terrestrial applications. To continue in this pursuit, some suggestions for future work will be helpful.

During this work, dark current due to recombination was found to dominate at the GaInP<sub>2</sub> solar cell maximum power-point voltage, and a reduction in this current was demonstrated in the diodes with higher p-base doping density. GaInP<sub>2</sub> solar cell with higher doping densities, i.e.,  $N_A \approx 1 - 5 \times 10^{17} \text{ cm}^{-3}$ , need to be evaluated. The affect of doping density on minority carrier diffusion length and spectral response also needs to be measured. This would allow for the optimum value of p-base doping density in the solar cell to be determined. As was shown in this work, an increase in doping density should also improve the radiation resistance of the cell.

The presence of the line-defects responsible for excess shunting/tunneling current and poor solar cell performance also needs to be further examined. Similar shunting behavior was also seen by researchers at NREL, and lattice mismatch between GaInP<sub>2</sub> and GaAs layers may confound the future development of larger area GaInP<sub>2</sub>/GaAs solar cells. A detailed study into the structure and electrical

behavior of the line-defects, as well as any other possible lattice mismatch induced defects in the GaInP<sub>2</sub>/GaAs system, would be very useful.

In this study, possible additional defect levels resulting from 1 MeV electron irradiation could not be uniquely determined from reverse-bias I-V-T techniques due to the overlap of different current mechanism at a given temperature range, and DLTS facilities were unavailable immediately following device irradiation. Therefore, an important research area that still requires attention is the identification of radiation induced recombination centers. Study into the atomic structure and electrical behavior of radiation induced defect centers versus doping specie and density in n- and p-type GaInP<sub>2</sub> would be very useful to the eventual optimization of the GaInP<sub>2</sub> solar cell.

## **APPENDIX A: Derivation of Solar Cell Photocurrent**

Several expressions for monochromatic photocurrent in solar cells have been developed, which are solutions to the continuity equations for the case of optical generation in a p-n junction (Tada, 1963). When light of wavelength  $\lambda$  is incident on the surface of a semiconductor, the generation rate of electron-hole pair photocarriers as a function of distance  $x$  from the surface is

$$G(\lambda) = a(\lambda)F(\lambda)[1-R(\lambda)] \exp(-a(\lambda)x) , \quad (A1)$$

where  $F(\lambda)$  is the number of incident photons per  $\text{cm}^2$  per sec per bandwidth, and  $R$  is the number reflected from the surface. The photocurrent that these carriers produce can be determined for low injection level conditions using the minority carrier continuity equations

$$G_p - (p_n - p_{no})/t_p - D_p d^2(p_n - p_{no})/dx^2 = 0 \quad (A2)$$

for holes in n-type material, and

$$G_n - (n_p - n_{po})/t_n + D_n d^2(n_p - n_{po})/dx^2 = 0 \quad (A3)$$

for electrons in p-type material. The first term in Eqs.(A2) and (A3) accounts for generation of carriers, the second term accounts for recombination of carriers to restore equilibrium, and the third term represents the diffusion of carriers in the presence of a carrier gradient. These equations can be solved for the solar cell in Figure 29 using the appropriate boundary conditions to find the minority carrier concentrations ( $n_p - n_{p0}$ ) and ( $p_n - p_{n0}$ ) at the edge of the space-charge region. The current density entering the space-charge region can then be calculated by evaluating the equations for hole and electron current density,

$$J_p = q\mu_p p_n E - qD_p(dp_n/dx) \quad (A4)$$

and

$$J_n = q\mu_n n_p E + qD_n(dn_p/dx), \quad (A5)$$

respectively, at the edge of the space-charge region. In the case of the abrupt epitaxially grown p-n junction, where both sides of the junction are assumed to be uniform in doping density, carrier mobility, and lifetime, Eqs.(A1) through (A5) can be combined to yield (Tada, 1962)

$$J_p(\lambda) = \frac{qN_0(1-R)\alpha L_p}{1-\alpha^2 L_p^2} \frac{\left[ \left( \alpha L_p + \frac{D_p}{SL_p} \right) \sinh \frac{a}{L_p} + \left( 1 + \frac{\alpha D_p}{S} \right) \cosh \frac{a}{L_p} \right] \exp\{-\alpha a\} - \left( 1 + \frac{\alpha D_p}{S} \right)}{\sinh \frac{a}{L_p} + \frac{D_p}{SL_p} \cosh \frac{a}{L_p}} \quad (A6)$$

for the n-type surface layer, and

$$J_n(\lambda) = \frac{pN_0(1-R)\alpha L_n}{1-\alpha^2 L_p^2} \frac{\left( \sinh \frac{b-a}{L_n} - \alpha L \cosh \frac{b-a}{L_n} \right) \exp\{-\alpha a\} + \alpha L_n \exp\{-\alpha b\}}{\cosh \frac{b-a}{L_n}} \quad (A7)$$

for the p-type base assuming the solar cell front and back surface recombination velocity  $S$  is  $\infty$ , where

$a$  = absorption coefficient for light of wavelength  $\lambda$ , ( $\text{cm}^{-1}$ ),

$F_o$  = photon flux density,

$R$  = reflection loss,

$a$  = junction depth (cm),

$b$  = cell thickness (cm),

$q$  = the hole charge (coul), and

$S$  = surface recombination velocity (cm/sec) .

The total monochromatic photocurrent density  $J_L(\lambda)$  is  $J_n(\lambda) + J_p(\lambda)$ . To calculate the total photocurrent produced when the solar cell is exposed to the full solar spectrum, we need to consider the quantum efficiency of the solar cell. The internal quantum efficiency  $Q(\lambda)$  of the absorber layer of the cell is defined as the ratio of the photon-generated carrier current density to the photon flux incident just inside the light-incident boundary of the layer,

$$Q(\lambda) = J_L(\lambda)/qF_o \quad (A8)$$

The total photocurrent density  $J_{ph}$  is given by the integration of the product of  $Q(\lambda)$  and the solar photon flux spectrum  $dF_o/d\lambda$ ,

$$J_{ph} = q \int Q(\lambda)(dF_o(\lambda)/d\lambda)d\lambda \quad (A9)$$



# APPENDIX B: Tables of Annual Equivalent 1 MeV Electron Fluences

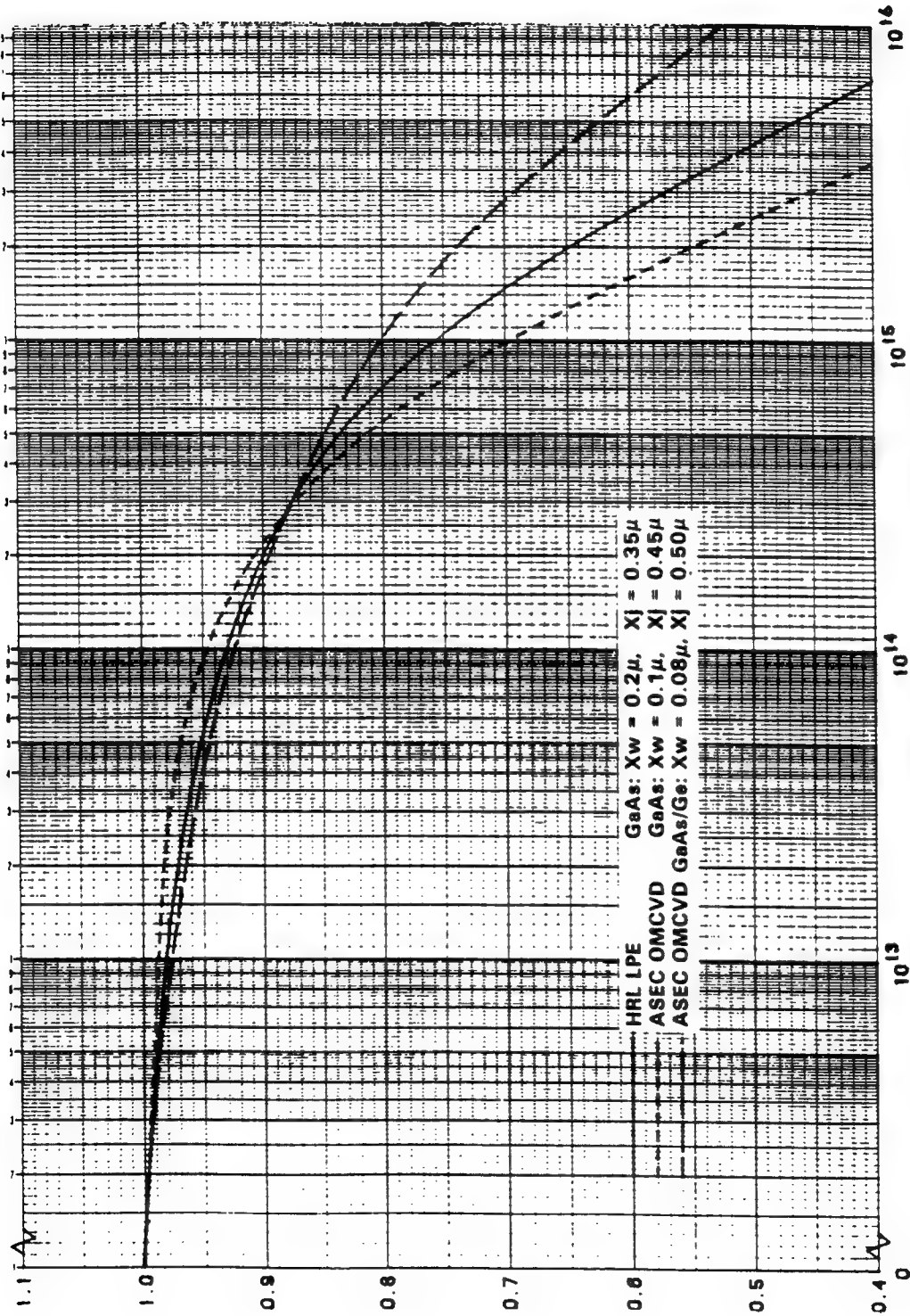
Annual Equivalent 1 MeV Electron Fluence from Trapped Electrons, 30° Inclination  
(Infinite Backshielding)

EQUIV. 1 MEV ELECTRON FLUENCE FOR ISC - CIRCULAR ORBIT DUE TO GEOMAGNETICALLY TRAPPED ELECTRONS - MODELS AEGMAX, AE17LO		ELECTRONS - ISC, VOC, AND PMAX				INCLINATION = 30 DEGREES.			
ALTITUDE (N.M.)	(KM)	Ø		Ø		SHIELD THICKNESS, CM (MILS)		Ø	
		2.54E-3 (1)	7.64E-3 (3)	1.52E-2 (6)	3.05E-2 (12)	6.09E-2 (20)	7.64E-2 (30)	1.52E-1 (60)	
150	277	3.47+09	2.64+09	1.89+09	1.30+09	7.63+08	4.79+08	3.14+08	1.29+08
250	463	4.34+10	3.29+10	2.33+10	1.68+10	9.27+09	6.68+09	3.69+09	1.48+09
300	566	5.68+10	7.34+10	6.20+10	3.66+10	2.05+10	1.25+10	8.10+09	3.25+09
450	833	6.60+11	4.25+11	3.01+11	2.06+11	1.17+11	7.11+10	4.67+10	1.80+10
600	1111	2.00+12	1.53+12	1.08+12	7.37+11	4.22+11	2.65+11	1.63+11	6.42+10
800	1481	7.23+12	6.64+12	3.96+12	2.73+12	1.69+12	9.79+11	6.36+11	2.54+11
1000	1852	1.01+13	1.39+13	1.00+13	6.93+12	4.09+12	2.64+12	1.66+12	6.68+11
1250	2315	3.70+13	2.86+13	2.07+13	1.46+13	8.71+12	5.49+12	3.63+12	1.48+12
1500	2778	6.44+13	4.20+13	3.03+13	2.11+13	1.25+13	7.74+12	5.05+12	2.05+12
1750	3241	6.78+13	5.17+13	3.67+13	2.49+13	1.40+13	8.26+12	6.17+12	2.01+12
2000	3704	7.64+13	6.76+13	4.01+13	2.64+13	1.67+13	7.61+12	4.41+12	1.67+12
2250	4167	8.23+13	6.14+13	4.20+13	2.69+13	1.33+13	6.56+12	3.42+12	1.06+12
2500	4630	8.19+13	6.07+13	4.11+13	2.63+13	1.22+13	6.67+12	2.63+12	7.06+11
2750	5093	7.79+13	5.75+13	3.87+13	2.41+13	1.10+13	4.69+12	2.01+12	4.71+11
3000	5556	6.95+13	5.13+13	3.44+13	2.13+13	9.68+12	4.06+12	1.71+12	4.18+11
3500	6482	6.30+13	3.90+13	2.63+13	1.65+13	7.94+12	3.72+12	1.88+12	6.85+11
4000	7408	4.18+13	3.15+13	2.20+13	1.47+13	8.04+12	4.64+12	2.80+12	1.25+12
4500	8334	3.88+13	3.07+13	2.30+13	1.68+13	8.04+12	6.89+12	4.70+12	2.23+12
5000	9260	3.85+13	3.24+13	2.62+13	2.07+13	1.47+13	1.05+13	7.58+12	3.70+12
5500	10186	4.35+13	3.85+13	3.29+13	2.76+13	2.11+13	1.69+13	1.19+13	6.95+12
6000	11112	6.35+13	4.86+13	4.28+13	3.71+13	2.95+13	2.31+13	1.77+13	9.18+12
7000	12964	8.13+13	7.49+13	6.71+13	5.91+13	4.82+13	3.85+13	3.01+13	1.60+13
8000	14816	1.06+14	9.76+13	8.76+13	7.73+13	6.31+13	5.05+13	3.95+13	2.08+13
9000	16668	1.31+14	1.21+14	1.09+14	9.55+13	7.77+13	6.17+13	4.78+13	2.45+13
10000	18520	1.60+14	1.38+14	1.24+14	1.09+14	8.76+13	6.88+13	6.25+13	2.58+13
11000	20372	1.48+14	1.36+14	1.22+14	1.06+14	8.62+13	6.62+13	4.99+13	2.36+13
12000	22224	1.33+14	1.22+14	1.09+14	9.48+13	7.63+13	6.79+13	4.31+13	1.97+13
13000	24076	1.14+14	1.05+14	9.26+13	8.00+13	6.29+13	4.78+13	3.52+13	1.67+13
14000	26928	9.37+13	8.51+13	7.46+13	6.38+13	4.94+13	3.69+13	2.67+13	1.15+13
15000	29780	7.17+13	6.45+13	5.69+13	4.71+13	3.66+13	2.60+13	1.84+13	7.49+12
16000	29632	5.34+13	4.75+13	4.07+13	3.38+13	2.50+13	1.79+13	1.24+13	4.77+12
17000	31484	3.93+13	3.46+13	2.92+13	2.39+13	1.73+13	1.21+13	8.17+12	2.97+12
18000	33336	2.77+13	2.40+13	1.99+13	1.60+13	1.13+13	7.63+12	5.00+12	1.68+12
19327	35793	1.65+13	1.40+13	1.13+13	8.80+12	6.94+12	3.86+12	2.42+12	7.27+11

Annual Equivalent 1 Mev Electron Fluence from Trapped Protons ( $V_{oc}$ ,  $P_{max}$ ), 30° Inclination  
(Infinite Backshielding)

PROTONS - VOC AND P <sub>MAX</sub>									
EQUIV. 1 MEV ELECTRON FLUENCE FOR VOC AND P <sub>MAX</sub> CIRCULAR ORBIT									
DUE TO GEOMAGNETICALLY TRAPPED PROTONS, MODEL AP8MAX									
ALTITUDE (N.M.)	Ø (Ø)	SHIELD THICKNESS, CM (MILS)				INCLINATION = 30 DEGREES.			
		1.52E-2 (6)	3.05E-2 (12)	5.09E-2 (20)	7.64E-2 (30)	1.52E-1 (60)	1.52E-2 (1)	2.54E-3 (3)	5.12E-3 (6)
150	277	8.78+10	5.12+10	4.54+10	3.82+10	3.19+10	2.87+10	2.52+10	2.13+10
250	463	1.67+12	1.14+12	1.03+12	8.92+11	7.68+11	6.95+11	6.00+11	5.15+11
300	555	4.02+12	2.92+12	2.60+12	2.22+12	1.90+12	1.70+12	1.43+12	1.22+12
450	833	2.96+13	2.06+13	1.78+13	1.45+13	1.16+13	9.91+12	8.44+13	7.22+12
600	1111	1.26+14	8.21+13	6.80+13	5.24+13	3.97+13	3.26+13	2.37+13	1.91+12
800	1481	5.96+14	4.63+14	3.64+14	2.16+14	1.66+14	1.23+14	8.44+13	6.72+12
1000	1852	2.35+15	1.66+15	9.62+14	6.76+14	4.63+14	3.39+14	2.13+14	1.51+13
1250	2316	9.40+15	4.24+15	3.16+15	2.09+15	1.26+15	8.68+14	4.70+14	3.26+13
1500	2778	2.75+16	1.12+16	8.20+15	6.15+15	2.84+15	1.79+15	8.00+14	5.44+13
1750	3241	6.39+16	2.33+16	1.64+16	9.73+15	4.98+15	3.75+15	1.08+15	7.22+12
2000	3704	2.47+17	4.02+16	2.68+16	1.47+16	6.93+15	2.85+15	1.22+15	8.44+13
2250	4167	4.16+17	6.68+16	4.10+16	2.01+16	8.62+15	4.25+15	1.23+15	8.44+13
2500	4630	6.79+17	9.29+16	6.29+16	2.34+16	9.07+15	4.25+15	1.13+15	7.72+12
2750	5093	1.01+18	1.23+17	6.46+16	2.56+16	9.15+15	4.04+15	1.00+15	6.92+10
3000	5556	2.12+18	1.77+17	6.96+16	1.97+16	8.37+15	3.56+15	8.39+14	5.45+14
3500	6482	8.21+18	1.74+17	6.99+16	1.36+16	6.22+16	2.51+15	3.15+14	1.68+14
4000	7408	3.72+18	1.66+17	4.86+16	9.08+15	2.39+15	1.61+15	1.68+14	8.32+13
4500	8334	6.80+18	1.45+17	3.62+16	5.56+15	1.35+15	4.55+14	3.77+13	3.77+13
5000	9260	1.10+19	1.22+17	2.55+16	3.12+15	3.30+14	2.32+14	1.39+13	1.11+12
5500	10186	1.26+19	8.71+16	1.58+16	1.59+15	4.47+13	1.07+13	6.92+10	8.70+09
6000	11112	1.44+19	3.40+16	4.41+15	2.83+14	4.76+12	9.16+11	0.00	0.00
7000	12964	1.23+19	9.93+15	9.48+14	4.01+13	2.58+11	5.15+10	0.00	0.00
8000	14816	7.82+18	1.76+15	1.13+14	2.82+12	1.83+03	0.00	0.00	0.00
9000	16668	4.60+18	1.56+14	8.61+12	2.81+10	0.00	0.00	0.00	0.00
10000	18520	3.08+18	1.15+13	3.21+11	1.11+09	0.00	0.00	0.00	0.00
11000	20372	2.12+18	1.48+11	9.53+03	0.00	0.00	0.00	0.00	0.00
12000	22224	1.56+18	4.09+13	1.42+07	0.00	0.00	0.00	0.00	0.00
13000	24076	1.09+18	6.45+12	7.11+06	0.00	0.00	0.00	0.00	0.00
14000	25928	6.98+17	1.29+12	3.88+05	0.00	0.00	0.00	0.00	0.00
15000	27780	4.68+17	1.09+10	0.00	0.00	0.00	0.00	0.00	0.00
16000	29632	3.18+17	8.11+09	0.00	0.00	0.00	0.00	0.00	0.00
17000	31484	2.02+17	6.29+09	0.00	0.00	0.00	0.00	0.00	0.00
18000	33336	6.60+16	4.05+09	0.00	0.00	0.00	0.00	0.00	0.00
19327	35793								

# **APPENDIX C: Plot of Normalized GaAs Solar Cell Power Output versus 1 MeV Electron Fluence**



Normalized  $P_{max}$  vs 1 MeV Electron Fluence for Three Types of GaAs Solar Cells

#### APPENDIX D: Solar Insolation

The efficiency of solar cells depends critically on the spectral distribution of incident radiation coming from the sun. The sun is a radiator whose spectrum can be approximated by a 6050 K blackbody (Fahrenbruch and Bube, 1983:26). In outer space, 98% of the total energy radiated by the sun lies between 0.25 and 3.0  $\mu\text{m}$ . A quantity called the solar constant is defined as the rate at which energy is received on a unit surface, perpendicular to the sun's direction. In free space, at the earth's mean distance from the sun, the most accepted value for the solar constant is  $1353 \text{ W/m}^2$  (Tada *et al.*, 1982). On the surface of the earth, both the intensity and spectral distribution of the sun's radiation are attenuated. This attenuation depends on the composition of the atmosphere, as well as the path length of the radiation through the atmosphere. The path length through the atmosphere is conveniently described in terms of an equivalent relative air mass  $m_r$ . The path length for a zenith angle  $z$  is  $\sec(z)$  times the path length for  $z = 0$ , and this air mass is defined as  $m_r = \sec(z)$ . Specific solar spectra are labeled  $\text{AM}m_r$  (read: air mass  $m_r$ ). **AM0** corresponds to the solar spectrum in outer space ( $1353 \text{ W/m}^2$ ). The average solar spectrum at the earth's surface corresponds to  $\text{AM1.5} - \text{AM2}$ . **AM0** and **AM2** spectra are compared in **Figure 78**. It is interesting to note that nearly all radiation with  $\lambda < 0.29 \mu\text{m}$  is absorbed by ozone and nearly all radiation with  $\lambda > 3.0 \mu\text{m}$  is absorbed by  $\text{H}_2\text{O}$  and  $\text{CO}_2$  in the atmosphere.

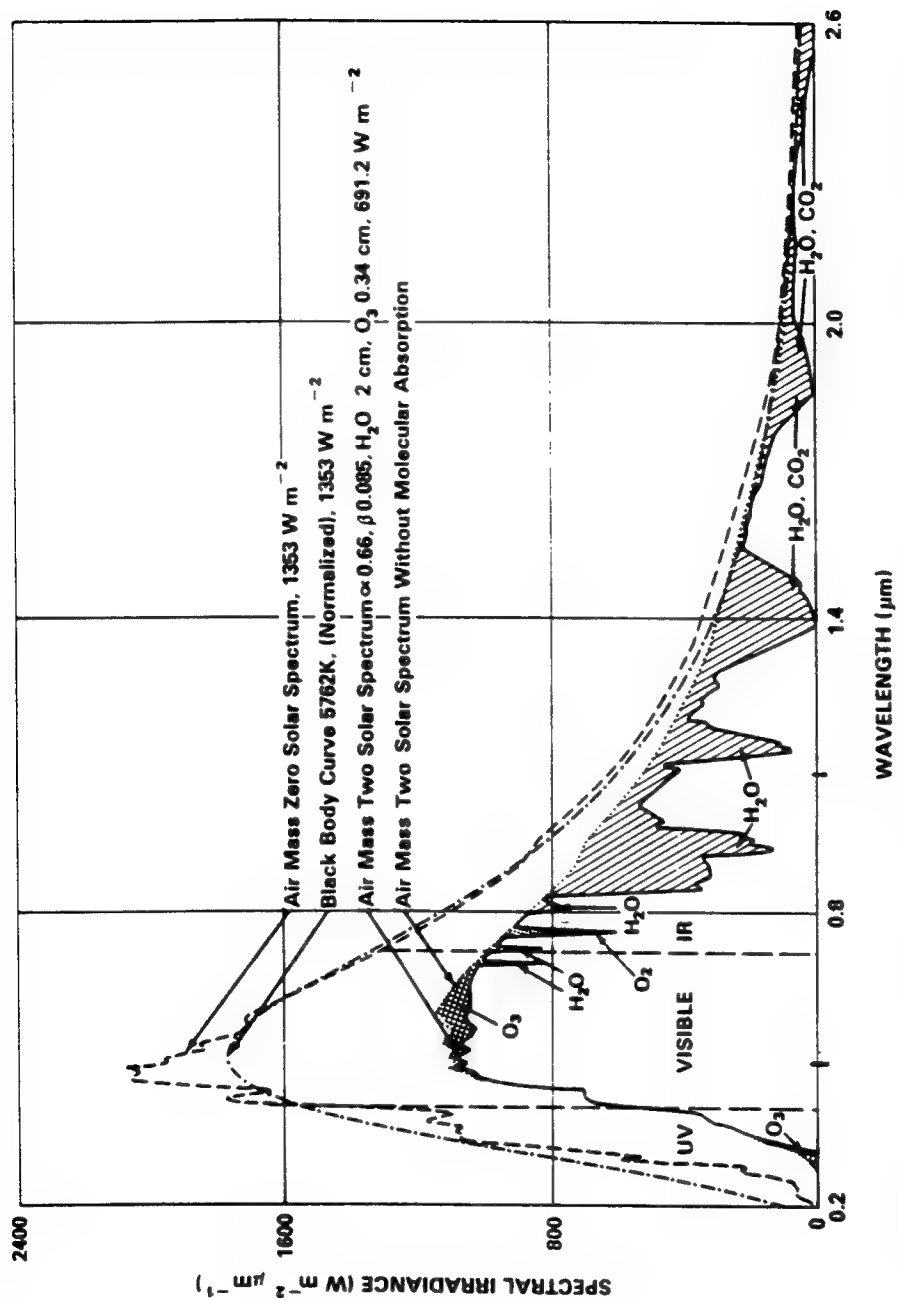


Figure 78. Comparison of AM0 and AM2 solar spectra, showing the various atmospheric absorption bands in AM2. The  $\alpha$  and  $\beta$  for the AM2 spectrum are turbidity coefficients. (After M. P. Thekaekara, Data on incident solar energy. *In* "The Energy Crisis and Energy From the Sun." Inst. Environ. Sci., Mt. Prospect, Illinois, 1974.)

### Bibliography

- Anspaugh, B. E., "Characterization of Production GaAs solar Cells for Space," JPL Publication 88-39, (1988).
- Alferov, Z. I., Andreev, U. M., Kagan, M. B., and Tofin, V. G., Soviet Physics-Semiconductor, 4: 2047 (1971).
- Ando, C., Yamaguchi, M., and Uemura, C., Physics Review B, 34: 3041 (1986).
- Banerjee, S., and Anderson, W. A., Applied Physics Letters, 49: 38 (1986).
- Brennan, K. F., and Chaing, P. K., Journal of Applied Physics, 71: 1055 (1992).
- Cavicchi, B. T., Krut, D. D., Lillington, D. R., Kurtz, S. R., and Olson, J. M., Proceedings of the 22<sup>nd</sup> IEEE Photovoltaics Specialists Conference. New York: IEEE, 1993.
- Cavicchi, B. T., "Lightweight Low Cost, High Efficiency Solar Cell for Space Planar Array," PRDA 91-01-PKRNPOC Report (1991).
- Chapin, D. M., Fuller, C. S., and Pearson, G. L., Journal of Applied Physics, 25: 676 (1954).
- Chiang, P. K., Vijayakumar, P. S., and Cavicchi, B. T., Proceedings of the 23<sup>rd</sup> IEEE Photovoltaics Specialists Conference. New York: IEEE, 1993.
- Choo, S. C., Solid State Electronics, 11: 1069 (1968).
- DeMoulin, P. D., Kyono C. S., Lunstrom, M. S., and Melloch, M. R., Proceedings of the 19<sup>th</sup> IEEE Photovoltaics Specialists Conference. New York: IEEE, 1987.
- DeMoulin, P. D., Tobin, S. P., Lunstrom, M. S., Carpenter, M. S., and Melloch, M. R., IEEE Transactions on Electron Devices, 9: 368 (1988).
- Fran, J. C. C., GaAs Shallow Homojunction Solar Cells, Final Report, NASA CR-165167 (1980).
- Fran, J. C. C., Tsaur, B. Y., and Palm, B. J., Proceedings of the 16<sup>th</sup> IEEE Photovoltaics Specialists Conference. New York: IEEE, 1982.
- Fahrenbruch, A. L., and Bube, R. H., in Fundamentals of Solar Cell. New York: Academic Press, 1983.
- Frenkel, J., Physics Review, 54: 657 (1938).

- Freidman, D. J., Kurtz, S. R., Kibbler, A. E., and Olson, J. M., Proceedings of the 22<sup>nd</sup> IEEE Photovoltaics Specialists Conference. New York: IEEE, 1993.
- Hall, R. N., Physics Review, 87: 387 (1952).
- Hall, R. N., Physics Review, 86: 600 (1952).
- Henry, C. H., Logan, R. A., and Merrit, F. R., Journal of Applied Physics, 49: 3530 (1978).
- Henry, C. H., and Logan, R. A., Journal Vacuum Science Technology, 15: 1471 (1978).
- Hovel, H. J., in Semiconductors and Semimetals (R. K. Willardson and A. C. Bear, eds.), Vol. II solar Cells. New York: Academic Press, 1975.
- Huggins, R. A., Bube, R. H., and Roberts, R. W., in Annual Review of Material Science, Vol. 7. 1977.
- Lang, D. V., Journal of Applied Physics, 45: 3023 (1974).
- Lang, D. V., Institute of Physics Conference Series, 31: 70 (1977).
- Linden, K., Spire Proposal Number , Lightweight, Low-Cost, High-Efficiency Solar Cell for Space Planar Array, 1991.
- Loferski, J. J., Journal of Applied Physics, 27: 777 (1956).
- Markvart, T., Journal of Material Science: Materials in Electronics, 181: 12 (1990).
- Messenger, S. R., Walters, R. J., and Summers, G. P., Journal of Applied Physics, 71: 4201 (1992).
- Meulenberg, A., Mauer, R. H., and Kinnison, J. D., NASA Conference Publication 3121, Space Photovoltaic Research and Technology, p. 39-1 (1991).
- Muller, R. S., and Kamis, T. I., in Device Electronics for Integrated Circuits. New York: John Wiley and Sons, 1977.
- Olsen, G. H., Nuese, C. J., and Smith, R. T., Journal of Applied Physics, 49: 5523 (1978).
- Olson, J. M., Kurtz, S. R., Kibbler, A. E., and Paine, P., Applied Physics Letters, 56: 623 (1990).
- Paloura, E. C., Ginoudi, A., Kiriakadis, G., Grangis, N., Scholz, F., Moser, M., and Christou, A., Applied Physics Letters, 60: 2749 (1992).

- Rao, B. B., Banerjee, S., Anderson, W. A., and Han, M. K., IEEE Transactions on Electronic Devices, 32: 817 (1985).
- Riben, A. R., and Feucht, D. L., Solid State Electronics, 9: 1055 (1966).
- Ringel, S. A., Rohatgi, A., and Tobin, S. P., IEEE Transactions on Electronic Devices, 36: 1230 (1989).
- Sah, C. T., Noyce, R. N., and Shockley, W., Proceedings of IRE, 45: 1228 (1957).
- Sah, C. T., IRE Transactions on Devices, 9: 94 (1962).
- Schmitz, O., Hergeth, J., Strauch, G., and Juergensen, H., Proceedings of the 22<sup>nd</sup> IEEE Photovoltaics Specialists Conference. New York: IEEE, 1993.
- Shaw, G. J., Messenger, S. R., Walters, R. J., and Summers, G. P., Journal of Applied Physics, 73: 7244 (1993).
- Shockley, W., Bell System Technology Journal, 435 (1949).
- Shockley, W., and Read, W. T., Physics Review, 87: 835 (1952).
- Statz, H., Erikson, W. T., and DeMars, G. A., Journal of Applied Physics, 28: 133 (1957).
- Stim, R. J., Proceedings of the 9<sup>th</sup> IEEE Photovoltaics Specialists Conference. New York: IEEE, 1972.
- Stone, J. L., Physics Today, 22 (1993).
- Sze, S. M., Physics of Semiconductor Devices, 2nd ed. New York: John Wiley and Sons, 1981.
- Tada, H. Y., Carter, J. R., Anspaugh, B. E., and Downing, R. G., in Solar Cell Radiation Handbook, JPL Publication 82-69, 1982.
- Takeda, Y., Araki, S., Takemi, M., Noda, S., and Sasaki, A., Journal of Crystal Growth, 107: 351 (1991).
- Tan, C., and Xu, M., Solid State Electronics, 32: 25 (1989).
- Timmons, M. L., in RTI Proposal Number P831-010, Lightweight, Low-Cost, High-Efficiency Solar Cell for Space Planar Array (1991).
- Timmons, M. L., Research Triangle Institute, RTI, NC. Personal interview. January 1994.



- Uemura, C., Yamaguchi, M., Journal of Applied Physics, 57: 604 (1985).
- Wolf, M., Energy Conversion, 11: 63 (1971).
- Wolf, M., Noel, G. T., and Stirn, R. J., IEEE Transactions on Electronic Devices, 24: 419 (1977).
- Wolff, G., Ralph, E., and Powe, J., Technical Report WL-TR-92-2073, High Efficiency Solar Panel Experiment, (1992).
- Yamaguchi, M., and Amano, C., Journal of Applied Physics, 57: 537 (1985).
- Yamaguchi, M., and Ando, K., Journal of Applied Physics, 63: 5555 (1988).
- Yamaguchi, M., Itoh, Y., and Ando, K., Applied Physics Letters, 45: 1207 (1984).

### Vita

Kitt Christopher Reinhardt was born on December 15, 1963 in Cheektowaga, New York, to David and Elaine Reinhardt. He grew up in Cheektowaga, which is just east of Buffalo, where he attended elementary and high school, and enjoyed ice hockey, football, science, and the stars. In September, 1982, he entered the State University of New York (SUNY) at Buffalo as an engineering student, and graduated in September 1986 Magna Cum Laude with a BS degree in Electrical Engineering. He was a research assistant his senior year where he fabricated and tested Si and InP solar cells. He continued his education at SUNY at Buffalo, where he graduated with honors in April 1988 with a MS degree in Electrical Engineering. During his graduate studies, he co-authored two journal articles in the area of InP-Schottky contacts. In April 1988, he joined the Electronics Directorate, Wright Laboratory, WPAFB, OH, and assumed the role of device process engineer for the Microwaves Division. There, he helped develop the Air Force's first in-house X-band GaAs MESFETs. In October, 1989, he transferred to the Aerospace Power Division of the Aero Propulsion and Power Directorate, Wright Laboratory, where he returned to studies in Si, GaAs/Ge, and AlGaAs/GaAs solar cells and survivable rigid and flexible space solar arrays. In September, 1991, he entered the AFIT doctorate program in Engineering Physics. He is currently the co-author of 5 journal articles, and is the first student to graduate from AFIT with a doctorate of philosophy under the Wright Laboratory-AFIT work study full-time (WSF) training program.

REPORT DOCUMENTATION PAGE			Form Approved OMB No. 0704-0188	
Public reporting burden for this collection of information is estimated to average 1 hour per response, including the time for reviewing instructions, searching existing data sources, gathering and maintaining the data needed, and completing and reviewing the collection of information. Send comments regarding this burden estimate or any other aspect of this collection of information, including suggestions for reducing this burden, to Washington Headquarters Services, Directorate for Information Operations and Reports, 1215 Jefferson Davis Highway, Suite 1204, Arlington, VA 22202-4302, and to the Office of Management and Budget, Paperwork Reduction Project (0704-0188), Washington, DC 20503.				
1. AGENCY USE ONLY (Leave blank)		2. REPORT DATE December 1994	3. REPORT TYPE AND DATES COVERED Doctoral Dissertation	
4. TITLE AND SUBTITLE The Junction Characteristics and Current Conduction Mechanisms of GaInP <sub>2</sub> n <sup>+</sup> p Diodes and Solar Cells			5. FUNDING NUMBERS	
6. AUTHOR(S)  Kitt C. Reinhardt				
7. PERFORMING ORGANIZATION NAME(S) AND ADDRESS(ES)  Air Force Institute of Technology WPAFB OH 45433-6583			8. PERFORMING ORGANIZATION REPORT NUMBER  AFIT/WSF/ENP/94-05	
9. SPONSORING/MONITORING AGENCY NAME(S) AND ADDRESS(ES)  WL/POOC-2 Building 18A 1950 Fifth Street WPAFB OH 45433-7251			10. SPONSORING/MONITORING AGENCY REPORT NUMBER	
11. SUPPLEMENTARY NOTES				
12a. DISTRIBUTION / AVAILABILITY STATEMENT  Approved for Public Release; Distribution Unlimited			12b. DISTRIBUTION CODE	
13. ABSTRACT (Maximum 200 words)  This work involves an investigation of GaInP <sub>2</sub> n <sup>+</sup> p diode and solar cell dark current mechanisms, the defect centers that affect these mechanisms, and the response of dark current and solar cell photovoltaic parameters to 1 MeV electron irradiation and thermal annealing. Dark current due to carrier diffusion, recombination, and tunneling were identified, and recombination current was found to dominate at the maximum power-point voltage of the GaInP <sub>2</sub> solar cells. Carrier recombination was found to occur via defect centers at the perimeter and within the bulk of the junction. Two deep majority-hole trap centers were found at $E_{a1} = E_t - E_v \approx 0.45$ eV and $E_{a2} = E_t - E_v \approx 0.05$ eV. Dark current due to carrier tunneling was dominant in "leaky" diodes and solar cells that contained line-like morphological defects believed to be due to lattice mismatch between GaInP <sub>2</sub> and GaAs. The effects of 1 MeV electron irradiation and thermal annealing on solar cell and diode dark current mechanisms and efficiency were also studied.				
14. SUBJECT TERMS Photovoltaic cells, Solar cells, GaInP <sub>2</sub> , Current conduction mechanisms, Dark currents			15. NUMBER OF PAGES 252	
			16. PRICE CODE	
17. SECURITY CLASSIFICATION OF REPORT Unclassified	18. SECURITY CLASSIFICATION OF THIS PAGE Unclassified	19. SECURITY CLASSIFICATION OF ABSTRACT Unclassified	20. LIMITATION OF ABSTRACT UL	

## GENERAL INSTRUCTIONS FOR COMPLETING SF 298

The Report Documentation Page (RDP) is used in announcing and cataloging reports. It is important that this information be consistent with the rest of the report, particularly the cover and title page. Instructions for filling in each block of the form follow. It is important to *stay within the lines* to meet optical scanning requirements.

**Block 1. Agency Use Only (Leave blank).**

**Block 2. Report Date.** Full publication date including day, month, and year, if available (e.g. 1 Jan 88). Must cite at least the year.

**Block 3. Type of Report and Dates Covered.** State whether report is interim, final, etc. If applicable, enter inclusive report dates (e.g. 10 Jun 87 - 30 Jun 88).

**Block 4. Title and Subtitle.** A title is taken from the part of the report that provides the most meaningful and complete information. When a report is prepared in more than one volume, repeat the primary title, add volume number, and include subtitle for the specific volume. On classified documents enter the title classification in parentheses.

**Block 5. Funding Numbers.** To include contract and grant numbers; may include program element number(s), project number(s), task number(s), and work unit number(s). Use the following labels:

C - Contract	PR - Project
G - Grant	TA - Task
PE - Program Element	WU - Work Unit Accession No.

**Block 6. Author(s).** Name(s) of person(s) responsible for writing the report, performing the research, or credited with the content of the report. If editor or compiler, this should follow the name(s).

**Block 7. Performing Organization Name(s) and Address(es).** Self-explanatory.

**Block 8. Performing Organization Report Number.** Enter the unique alphanumeric report number(s) assigned by the organization performing the report.

**Block 9. Sponsoring/Monitoring Agency Name(s) and Address(es).** Self-explanatory.

**Block 10. Sponsoring/Monitoring Agency Report Number.** (If known)

**Block 11. Supplementary Notes.** Enter information not included elsewhere such as: Prepared in cooperation with...; Trans. of...; To be published in.... When a report is revised, include a statement whether the new report supersedes or supplements the older report.

**Block 12a. Distribution/Availability Statement.** Denotes public availability or limitations. Cite any availability to the public. Enter additional limitations or special markings in all capitals (e.g. NOFORN, REL, ITAR).

DOD - See DoDD 5230.24, "Distribution Statements on Technical Documents."

DOE - See authorities.

NASA - See Handbook NHB 2200.2.

NTIS - Leave blank.

**Block 12b. Distribution Code.**

DOD - Leave blank.

DOE - Enter DOE distribution categories from the Standard Distribution for Unclassified Scientific and Technical Reports.

NASA - Leave blank.

NTIS - Leave blank.

**Block 13. Abstract.** Include a brief (*Maximum 200 words*) factual summary of the most significant information contained in the report.

**Block 14. Subject Terms.** Keywords or phrases identifying major subjects in the report.

**Block 15. Number of Pages.** Enter the total number of pages.

**Block 16. Price Code.** Enter appropriate price code (*NTIS only*).

**Blocks 17. - 19. Security Classifications.** Self-explanatory. Enter U.S. Security Classification in accordance with U.S. Security Regulations (i.e., UNCLASSIFIED). If form contains classified information, stamp classification on the top and bottom of the page.

**Block 20. Limitation of Abstract.** This block must be completed to assign a limitation to the abstract. Enter either UL (unlimited) or SAR (same as report). An entry in this block is necessary if the abstract is to be limited. If blank, the abstract is assumed to be unlimited.